**Title**

Influence of Electric Current on Efficiency of Field Assisted Consolidation of Powder Materials

**Author**

Lee, Geuntak

**Publication Date**

2018

UNIVERSITY OF CALIFORNIA SAN DIEGO
SAN DIEGO STATE UNIVERSITY

# Influence of Electric Current on Efficiency of Field Assisted Consolidation of Powder Materials

A dissertation submitted in partial satisfaction of the
requirements for the degree Doctor of Philosophy

in
Engineering Sciences (Mechanical and Aerospace Engineering)
by
Geuntak Lee

Committee in charge:

University of California San Diego

- Professor Joanna McKittrick, Chair
- Professor Prabhakar R. Bandaru
- Professor Jian Luo

San Diego State University

- Professor Eugene A. Olevsky, Co-Chair
- Professor Joaquin Camacho

2018

The Dissertation of Geuntak Lee is approved, and it is acceptable in quality and form for publication on microfilm and electronically:

Co-Chair

Chair

University of California San Diego
San Diego State University
2018

# DEDICATION

Dedicated to

My father, Kyonghong Lee

My mother, Keumryung Lee

# TABLE OF CONTENTS

# LIST OF FIGURES

# LIST OF TABLES

# ACKNOWLEDGEMENTS

All my work was fully supported and guided by Prof. Eugene A. Olevsky. Under his careful guidance and inspiration, I could solve research problems one by one progressively. I can say that he is the best advisor in the world. My co-advisor, Prof. Joanna McKittrick, also provided her full support for my research. With my both advisors, my academic life has acquired clear goals.

I would like to thank also my committee members: Professors Prabhakar R. Bandaru, Jian Luo, and Joaquin Camacho.

I also appreciate the help from the colleagues in SDSU Powder Technology Laboratory: Dr. Maximenko, Dr. Manière, Dr. Alvarado-Contreras, Dr. Wei, Dr. Torresani, Dr. Li, Dr. Giuntini, Ms. Carrillo, Ms. Chan, Mr. Hoeffer, and Mr. Singh.

None of this would have been possible to be done without my family. I cannot explain how I appreciate the support and care of my parents. I love them. I respect them. My sister, Sooyoun: I am really thankful for all her support. My wife and best friend, Hyeyeon, gave me the reason and the energy for my life.

Chapter 3, in part, is currently being prepared for submission for publication of the material. G. Lee, C. Manière, J. McKittrick, and E.A. Olevsky. The dissertation/thesis author was the primary investigator and author of this paper.

Chapter 4, in part, is a reprint of the material as it appears in *Acta Materialia*, 2018. G. Lee, E.A. Olevsky, C. Manière, A. Maximenko, O. Izhvanov, C. Back, and, J. McKittrick. The dissertation/thesis author was the primary investigator and author of this paper.

Chapter 4, in part, is a reprint of the material as it appears in *Ceramics International*, 2015. G. Lee, M.S. Yurlova, D. Giuntini, E.G. Grigoryev, O.L. Khasanov, J. McKittrick and E.A. Olevsky. The dissertation/thesis author was the primary investigator and author of this paper.

Chapter 5, in part, is a reprint of the material as it appears in *International Journal of Refractory Metals and Hard Materials*, 2016. G. Lee, J. McKittrick, E. Ivanov and E.A. Olevsky. The dissertation/thesis author was the primary investigator and author of this paper.

Chapter 5, in part, is currently being prepared for submission for publication of the material. G. Lee, C. Manière, J. McKittrick, A. Gattuso, C. Back, and E.A. Olevsky. The dissertation/thesis author was the primary investigator and author of this paper.

Chapter 5, in part, is currently being prepared for submission for publication of the material. G. Lee, C. Manière, J. McKittrick, D. Nishijima, R. Doerner, A. Gattuso, T. Abrams, D. Thomas, C. Back, and E.A. Olevsky. The dissertation/thesis author was the primary investigator and author of this paper.

Chapter 6, in part, is a reprint of the material as it appears in *Scientific report*, 2017. C. Manière, G. Lee, and E.A. Olevsky. The dissertation/thesis author was the secondary investigator and author of this paper.

Chapter 6, in part, is currently being prepared for submission for publication of the material. C. Manière; G. Lee; J. McKittrick; A. Maximenko; E.A. Olevsky. The dissertation/thesis author was the secondary investigator and author of this paper.

# VITA

| | |
|---|---|
| 2007 | Bachelor of Science, Yonsei University, Republic of Korea |
| 2009 | Master of Science, Yonsei University, Republic of Korea |
| 2018 | Doctor of Philosophy, University of California San Diego and San Diego State University |

# PUBLICATIONS

1. G. Lee, E.A. Olevsky, C. Manière, A. Maximenko, O. Izhvanov, C. Back, and, J. McKittrick, “Effect of Electric Current on the Densification Behavior of Conductive Ceramic Powders Consolidated by Spark Plasma Sintering,” *Acta Materialia,* 2018, 144, 524
2. G. Lee, J. McKittrick, E. Ivanov, and E.A. Olevsky, “Densification Mechanism and Mechanical Properties of Tungsten Powder Consolidated by Spark Plasma Sintering,” *International Journal of Refractory Metals and Hard Materials,* 2016, 61, 22.
3. G. Lee, M.S. Yurlova, D. Giuntini, E.G. Grigoryev, O.L. Khasanov, J. McKittrick, and E.A. Olevsky, Densification of Zirconium Nitride by Spark Plasma Sintering and High Voltage Electric Discharge Consolidation: A Comparative Analysis, *Ceramics International*, 2015, 41, 14973.
4. C. Manière, G. Lee, T. Zahrah, and E.A. Olevsky, “Microwave Flash Sintering of Ti-6Al-4V: From the Experimental Evidence to the Multiphysics Simulation of the Phenomenon,” *Acta Materialia,* 2018, 147, 24.

5. C. Manière, G. Lee, and E.A. Olevsky, "All-Materials-Inclusive Flash Spark Plasma Sintering," *Scientific Reports*, 2017, 7, 15071.

6. C. Manière, G.Lee, and E.A. Olevsky, "Proportional Integral Derivative, Modeling And Ways Of Stabilization For The Spark Plasma Sintering Process", *Results in Physics.*, 2017, 7, 1494.

7. G. Lee, C. Manière, J. McKittrick, and E.A. Olevsky, "Deconvolution of Thermomechanical and Electric Current Effects in Spark Plasma Sintering," *Scripta Materialia,* prepared for publication.

8. G. Lee, C. Manière, J. McKittrick, A. Gattuso, C. Back, and E.A. Olevsky, "Effect of Oxidation on Densification Behavior and Mechanical Properties of Molybdenum Nanopowders Compacted by Spark Plasma Sintering," *Journal of the American Ceramic Society,* prepared for publication.

9. G. Lee, C. Manière, J. McKittrick, R. Doerner, D. Nishijima, A. Gattuso, T. Abrams, Dan Thomas, C. Back, and E.A. Olevsky, "Consolidation of Molybdenum Nanopowders by Spark Plasma Sintering: Densification Mechanism and First Mirror Application" *Journal of Nuclear Materials,* prepared for publication.

10. C. Manière, G. Lee, J. McKittrick, A. Maximenko and E.A. Olevsky, "The creep of graphite in All-Materials-Inclusive Flash Spark Plasma Sintering," *Carbon,* prepared for publication.

11. G. Lee, J. McKittrick and E.A. Olevsky, "Field-assisted Consolidation of Zirconium Nitride Powder," *Proceedings of the PM2014 World Congress on Powder Metallurgy & Particulate Materials,* Orlando, USA, 18-22 May, 2014 (p. 1522-1525). New Jersey: Princeton.

12. G. Lee, M.S. Yurlova, E.G. Grigoryev, J. McKittrick, and E.A. Olevsky, “Comparative Study of Spark Plasma Sintering and High Voltage Electric Discharge Consolidation for Densification of Zirconium Nitride,” *Proceedings of the PM2015 World Congress on Powder Metallurgy & Particulate Materials*, Orlando, USA, 15-19 March, 2015 (08-112 - 08-116). New Jersey: Princeton
13. G. Lee, J. McKittrick, and E.A. Olevsky, “Spark Plasma Sintering Of Molybdenum Nanopowders,” *Proceedings of the PM2016 World Congress on Spark plasma sintering*, Hamburg, Germany, 9-13 Oct, 2016 (978-1-899072-47-7). New Jersey: Princeton.

## FIELD OF STUDY

Major Field: Engineering Sciences (Mechanical and Aerospace Engineering)

Studies in Sintering and Powder technologies, and Mechanical Behavior of Materials
Professors Eugene A. Olevsky

Studies in Solid State Diffusion and Reaction Kinetics
Professor Joanna McKittrick

# ABSTRACT OF THE DISSERTATION

# Influence of Electric Current on Efficiency of Field Assisted Consolidation of Powder Materials

by

Geuntak Lee

in

Engineering Sciences (Mechanical and Aerospace Engineering)

University of California San Diego, 2018
San Diego State University, 2018

Professor Joanna McKittrick, Chair
Professor Eugene A. Olevsky, Co-Chair

Spark plasma sintering (SPS) has clear advantages of fast densification and lower grain growth compared with other powder consolidation techniques such as hot pressing (HP). Many researchers studied intrinsic electric current effects during the SPS process, yet the results of these studies are still controversial due to the complexity of the SPS technology.

In this study, we investigate various consolidation methods with and without electric current assistance to achieve the deconvolution of the electric current effects from the temperature effects. The spatial distribution of the electric current passing through the powder during SPS is modeled using the finite element method. The porosity-interparticle neck area geometrical relationship is utilized to estimate the electric current density inside the powder volume subjected to SPS. For the first time, by taking into account the explicit influence of the electric current effect on the SPS densification mechanisms, the governing equations describing hot pressing are modified to enable an SPS-specific constitutive analysis. The densification mechanisms of various ceramic (ZrN) and metallic (W and Mo) powders are determined by the inverse regression of the new SPS constitutive equations and by utilizing the experimental results on powder consolidation with and without the participation of the electric current effect.

We show that the electron backscatter diffraction (EBSD) technique can be a useful tool to demonstrate the densification mechanism of the powders during the sintering. The grain size and grain growth factors are incorporated into the sintering constitutive equation too to elucidate the grain growth effect on the material behavior governing parameters.

Additionally, the known but controversial intrinsic electric current effects such as surface cleaning and retardation of the grain growth are analyzed for the consolidation of the Mo nanopowders using SPS.

Finally, an energy efficient and fast consolidation technique utilizing the highly concentrated electric current flow through a conductive powder by manipulating the electric current trajectory is developed.

# CHAPTER 1 Introduction

## 1.1. Influence of Field Effects on SPS of Conductive Materials: Survey of the Studies Carried out in the Past

During the last 20 years, there were many efforts of scientists and engineers to use the electric current for the fast and energy efficient consolidation of materials [1].

The electric current assisted sintering (ECAS) method could be subdivided into two main groups depending on the electric current path trajectory during sintering [2]: 1. electric discharge sintering (EDS) and 2. resistance sintering (RS). First, EDS is used generally for the electric conductive materials since the capacitor bank generates the high voltage electric pulsed discharge applied to the powder inside of the insulating die [3, 4]. Various machine setups have been developed to conduct EDS, with different process names such as high voltage electric discharge consolidation (HVEDC), high-energy high-rate (HEHR) consolidation, pulse plasma sintering (PPS) and capacitor discharge sintering (CDS): yet the general principle of the process is the same. The sintering mechanism of EDS was studied and proposed as follows: high voltage helps to destruct the surface contaminating layer of the metal powder, leading to the interparticle neck formation. The conductive interparticle necks dissipate heat energy by Joule heating through the powder volume, inducing sintering [5, 6]. Grigoryev and Olevsky showed the simulation of the thermal process happening between the interparticle contacts of the powder under HVEDC, enabling the optimization of the electric current parameter values used in the experiments [7]. A detailed review of the EDS process can be found elsewhere [4].

Otherwise, RS flow low voltage (1~10 V) and high electric current through the conducting die to indirectly heat the powders. Among RS techniques, spark plasma sintering (SPS) has been widely studied and used for densification of powders ranging from polymers to ultra-high temperature materials [8].

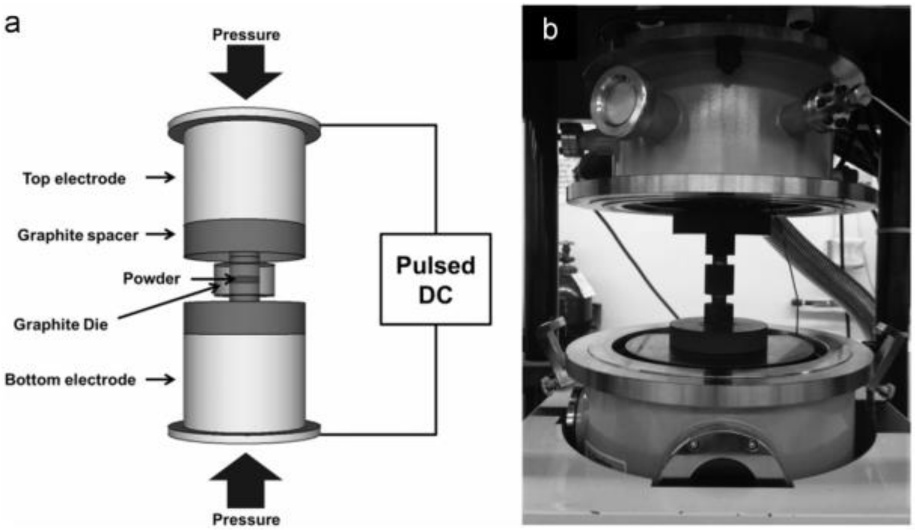

Figure 1.1 (a) Schematic representation of spark plasma sintering process, (b) spark plasma sintering machine before an experiment.

SPS is a low-voltage field-assisted sintering method which utilizes a pulsed direct electric current for the consolidation of powders under elevated temperatures and pressures [9, 10]. SPS is also known as a field-assisted sintering technique (FAST) [11] and pulsed electric current sintering (PECS) [12]. Figure 1.1(a) shows a schematic diagram of the tooling setup assembly. Figure 1.1(b) shows a photograph of the setup, located in the SPS chamber, before an experimental procedure was run. A powder specimen placed in an electrically conductive die is subjected to an external pressure applied by electrically conductive punches, and the specimen's temperature is controlled by Joule heating generated in the die-punch tooling and in the powder material itself if the electrical conductivity of the material is high enough.

In comparison with conventional powder consolidation methods like hot pressing (HP), the SPS can lower the sintering temperature and reduce sintering times, thus favoring the reduction of the grain size of compacted pellets and saving the energy spent.

In general, it is known that the difference between the SPS and HP results can be ascribed to the two groups of physical phenomena: (a) of thermal and (b) of electric current-related [13].

(a) phenomena of thermal nature:

    (1) high heating rates;

    (2) temperature local non-uniformity and thermal diffusion;

(b) electric current-related phenomena:

    (1) surface cleaning;

    (2) electromigration;

    (3) electroplasticity;

    (4) change of the material’s densification mechanism

In this study, we concentrate on the electric current effects influencing the consolidation of electronically or ionically conductive powders. The influence of thermal effects on SPS has been analyzed elsewhere [14, 15].

One of the chronologically first, among the electric current-related phenomena, the surface cleaning effect was considered. This mechanism generally occurs at the initial stages of SPS. Munir [16] reported that the existence of surface oxide films in the metal particles may cause the delay of the densification. In SPS, the electric current may lead to the breakdown of insulating layers at the surface of powder particles during the initial stage of sintering. Induced plasma can remove the diffusion barrier such as surface impurities and oxide layers, resulting in fast densification during SPS [17-19]. Using in situ transmission electron microscopy(TEM), Bonifacio et al. [20-22] studied the dielectric breakdown of a NiO layer on Ni nano particle during field-assisted sintering. After breaking these oxide layers, the electric current conducting path was present and consequently the inter-particle necks have been formed. Also, the threshold electric current density was required to break the oxide layer. Marder et al. [23] showed that insulating ceramic material can have faster densification kinetics with the existence of the plasma during SPS compaction of LiF with pressure below the yield stress. The SEM analysis confirmed the local melting and material jets between the LiF microcrystals presumably due to the sparks and plasma formed. Otherwise, Hulbert et al.[24] was unable to find the indication of plasma formation or glow discharge during SPS using an in situ atomic emission spectroscopy. They introduced the quartz window near the powder in the SPS setup. The plasma was not observed from the powder visually. Also, the authors could not observe the high-frequency radiation of the plasma using ultrafast in situ voltage measurements.

Later, the diffusion of atoms powered by the momentum transfer between ions and conducting electrons, referred to as electromigration, has been suggested as one of the reasons for the accelerated mass transport under SPS conditions. Vacancy formation and diffusion by electromigration effect were first proved by using the positron annihilation spectroscopy (PAS) [25]. PAS uses the properties of positively charged positrons which have a tendency to locate in the open lattice space defects such as vacancy, void, and dislocation, where the atom nuclei are not present. Also, the defect location can be revealed by the gamma rays when the positrons and electrons annihilate each other. Kumar et al. [25] first showed the dynamic formation of point defects in Al-Cu system when an electric current was applied. Vacancy concentration increase due to the passage of an electric current is much larger than that from the pure thermal vacancy generation. Garay et al. also showed the enhanced vacancies mobility in the Ni-Ti intermetallic material by demonstrating the 24% decrease in the activation energy of the mobility when the electric current is applied during annealing [26].

In the SPS process, electromigration effect was studied by observing the growth rate of the reaction layer between two metals with and without an electric current. It was shown that the pulsed DC current accelerated the inter-particle neck growth between Cu or W spheres and plates [27, 28]. In addition, Chen *et al*. [29], indicated that the direction of the current or pulse pattern had no effect on the reactivity between the layers of Si and Mo. Anselmi-Tamburini *et al*. [30], showed that the electric current affected the growth rate of the product phase between layers of Si and Mo under long holding times (up to 75min) which are not normally used for SPS experiments. Olevsky and Froyen [31] developed a constitutive model for SPS taking into account electromigration effect, and compared its predictions with the experimental data on the sintering behavior of aluminum powders, showing that electromigration can be one of the important factors to enhance the current assisted diffusion. However, Trzaska *et al*. [32], showed no dependence of the new phase growth rate on the electric current density in the Ag-Zn system during the SPS process.

Electroplasticity was generally studied by measuring the required stress to deform the fully dense metal specimens with and without electric current at low or high temperatures. Increasing the electric current reduces the flow stress of the metal: – this phenomenon was termed “electro plastic effect” (EPE). For the first time, in 1959, Machlin et al. [33] showed that electric current affects the flow stress, ductility and yield stress of NaCl. Troitskii et al. indicated that pulsed currents can reduce the flow stress of tin, zinc, lead, indium alloys, and explained these results by the interaction between electrons and dislocation motion. Conrad et al. [34, 35], studied the electric current effect on the flow stress of metals and ceramics, and indicated that plastic properties and phase composition can be changed by them. Salandro et al. [36], showed that the direct Joule heating can transfer energy directly to dislocations more efficiently than by oven heating, and local Joule heating at dislocation cores is the main reason for the reduction of flow stress of metals during a passage of an electric current.

During deformation, most of the dislocations are located in the neck area between the grains. Also, the neck region can have high electric current density due to the small electric contact area [37]. Siopis et al. [38] studied the microstructure effect on the EPE, and showed that fine grain materials which have more necks or grain boundaries have the enhanced EPE. Also, Siopis et al. [39] showed that cold worked materials have higher EPE due to the increased dislocation density. Jabbar et al. [40], showed that TiAl alloys densified by SPS have severely deformed the neck area and recrystallized grains near the neck.  Grosdidier et al. [41], showed that the overheating at the neck area favored the recrystallization and grain growth, which rendered large grains near grain boundaries of the nanograin FeAl consolidated by SPS.

It was shown also that the densification mechanisms of the processed powders may be altered by an electric current. Conventionally, it is known that powder materials have certain densification mechanisms depending on the powder particle size, temperature and pressure applied [42]. By and large, three main methodologies have been used in the past to elucidate the densification mechanisms during SPS.

First, the MSC approach had been originally proposed for free sintering by Su and Johnson [43, 44] and was adapted for SPS by Guillon [45]. Within this approach, the whole densification curve is analyzed including the temperature ramping stage, and the apparent activation energy for sintering is estimated. However, the major concepts of MSC, assuming that a single densification mechanism governs the whole sintering process as well as that there exists the grain size direct dependence on the relative density, are not well correlated with actual sintering behavior.

Second, Bernard-Granger and Guizard (B-G) [46, 47] approach assumed that SPS is controlled by the high-temperature creep of a porous material. The activation energy and creep exponent used for the determination of the creep mechanism, can be found using a number of SPS experiments conducted under fixed pressure and different temperatures (for creep exponent) and fixed temperature and different pressures (for activation energy) conditions. However, this approach is based on the uncertain evaluation of the effective stress and shear modulus, which renders the main parameters of the densification mechanism [48, 49].

Third, Olevsky's approach uses the constitutive equation for high-temperature creep of a non-linear viscous porous material to find the densification mechanism of materials subjected to SPS [50]. Combining this constitutive equation with the power-law creep equation for a non-porous material enables the estimations of the activation energy and of the strain rate sensitivity (which is the inverse of the creep exponent). This constitutive equation for sintering is applicable to describe a broad range of powder consolidation techniques such as the pressure-assisted approaches (SPS and HP) and pressureless sintering. Olevsky and Froyen [31] adapted the constitutive equation for sintering for the description of SPS by modifying it to take into account the electromigration effect.

Few attempts have been undertaken to find the effect of electric current on the densification mechanism of various materials using MSC and B-G approach, yet yielding conflicting results. Langer *et al*. [51-53], compared the densification behavior of ionic conductor, semiconductor, and insulator with the same pressure and temperature experimental conditions of the SPS and HP, and showed no difference in the densification mechanism using master sintering curve (MSC) approach [44]. In contrast, Maryse *et al*. [54], utilizing the MSC and Bernard-Granger methods [46], indicated that the electric current changes the densification mechanism of alumina possibly by affecting the grain boundaries of powder particles.

With Olevsky's approach, a few attempts have been undertaken for the investigation of the role of the electric current in the SPS process. Multi-step pressure dilatometry method was used to compare the densification mechanism of copper powders with and without electric current assistance using alumina components inside of the SPS tooling setup [55]. It was shown that the relative density of the densified copper pellets in the current assisted mode was higher than that of the current-insulated mode, yet the densification mechanism was the same for both cases. A limitation of this approach was that, instead of using the temperature of the powder, the temperature of the graphite die was used for controlling the SPS regime and for analyzing the experimental data, thereby leading to the inaccurate deduction of the densification mechanism of the copper powder. More sophisticated deconvolution of the temperature from the electric current was implemented by the sinter-forging setup in SPS [56]. The sample temperature was directly measured by a thermocouple introduced through a hole in the graphite die. *In situ* axial punch displacement was recorded by SPS, and the lateral deformation of the powder specimen was recorded by a video camera taking the images of the radially inserted push-rod's movement during SPS. It was revealed that the electric current-assisted case leads to a higher degree of densification compared to the current-insulated case. However, the electric current effects on the densification mechanism of copper were not quantitatively assessed.

## 1.2. Energy Efficient and Fast Consolidation Methods using Electric Current: Survey of the Studies Carried out in the Past

Among fast densification methods using the electric current, there has been growing interest in flash sintering from the first report by Cologna et al. in 2010 [57]. This original method allows the ultra-rapid sintering of the specimen in few seconds. While conventional oven heats the pre-compacted sample, the constant voltage is applied to the sample at the same time. When furnace reaches the critical onset temperature, the specimen's temperature exhibits runaway profile and the sample densifies quickly. After discovery, the flash sintering of a wide range of materials was studied ($ZrO_2$ [58, 59], $SnO_2$ [60] , ZnO [61], $Y_2O_3$ [62], $Al_2O_3$ [63], $TiO_2$ [64] and SiC [65]).

The electrical conductivity dependence on the temperature is the crucial parameter in the flash sintering [66]. Materials can show a positive temperature coefficient or negative temperature coefficient (PTC or NTC) of electrical resistivity. Most of ceramics display a NTC of electrical resistivity. The electric conductivity of ionic conductors (YSZ) and insulators ($BaTiO_3$, a wide-band gap insulator) increases rapidly with increasing the temperature, while the electric conductivity of semiconductors (SiC and $B_4C$) increases at a slower rate. At the same time, the electric conductivity of metals (Ni, Cu, and W) decreases with increasing temperature and exhibits a PTC dependence of electrical resistivity.

The exact mechanisms of flash sintering are currently a controversial topic of research [67-70]. This is mostly due to the difficulty of measuring the sample volume temperature during thermal runaway. On the other hand, numerical estimations of the sample temperature are challenging because the sample temperature is the net result of the sample Joule heating and heat dissipation, which depend on the electric conductivity and relative density of the sample. At the same time, some attempts of modeling have been undertaken to find the mechanism of the rapid densification during flash sintering [71, 72].

Raj et al. [67, 73] suggested that the nucleation of Frenkel pairs under electric field resulting in the formation of vacancies is the main reason for fast densification during flash sintering. Also, Naik proposed the defect nucleation model based on the difference of incubation time before flash onset temperature with the applied field amount, so that possible electron gas can be induced from a large amount of Frenkel defects by high electric fields during flash sintering, which explains the extra electronic conductivity of the sample and contributes to further Joule heating above the estimations from only ionic conduction mechanism [74].

On the other hand, Todd et al. suggested that flash sintering is simply an ordinary consequence of the NTC of electric resistivity inducing Joule heating at a constant voltage; they derived a model clearly showing the relation between Joule heating and thermal runaway [75]. Similarly, Zhang et al., developed the model to predict the thermal runaway conditions that are coincidental with the observed onset flash temperatures in the ZnO powder densification by flash sintering, and concluded that the flash starts as a thermal runaway without the need of introducing an avalanche of the vacancy formation [76].

Although flash sintering showed promising results for fast densification sintering, there are some limitations on the industrial applications. First, net shape sample fabrication was not achieved. Flash sintering normally uses the dog bone shape specimens to maximize the density of electric power. Second, flash sintering requires long preparation steps before flash event happen which offsets the advantage of fast densification. In the beginning, it needs the pre-compaction of the powder to make a dog bone shape specimen. After making the dog bone shape sample, the sample is to be heated by the conventional furnace which takes a long time [77].

On the other hand, the manipulation of the electric current path inside the graphite die setup in SPS was shown to be the energy efficient way to densify net shape components. An SPS-based approach involving intense heating of initially (from room temperature levels) conductive materials at the maximum power capacity of an SPS device, applied to consolidate an initially electrically conductive $ZrB_2$ specimen or to partially consolidate SiC specimen inside a permanently conductive layer of graphite felt was explored by Grasso et al [77-79]. Flash Hot Pressing or Ultra-Fast Spark-Plasma Sintering (FSPS) has been invented by Olevsky et al [80] for an ultra-fast 1 sec densification of SiC using a copper sacrificial SPS tooling component.

However, net shape sample cannot be obtained by FSPS due to the removal of the graphite die making this approaches closer to fast sinter-forging techniques. Therefore, various approaches were investigated to make net shape samples with full density by fast densification methods using SPS machine.

Niu et al. used a thin die for the preheating of boron carbide ($B_4C$) powder in SPS setup. When electric resistance of the $B_4C$ powder is smaller than that of the thin graphite wall, current starts to flow into the powder, resulting in the density of 99.2% within 1 min sintering time [81]. However, the low-pressure process limitation due to the thin wall die setup restricts the application of this method to other refractory materials.

Roman-Manso et al. used the electrically insulating boron nitride (BN) coating on the inner wall of the graphite die to force the electric current to flow through the inner graphite paper contacting the sample and graphite punches to carry out the liquid sintering of beta-SiC mixed with 2 wt% of $Al_2O_3$ and 5 wt% of $Y_2O_3$ in SPS. Forced localized heating induced by BN coating reduced the power consumption, and accelerated the SiC densification [82]. However, coarser microstructure was obtained compared with the grain size of the normally SPSed sample due to the slow heating rate (50 °C/min).

Zapata-Solvas et al. showed that the manipulation of the path of the electrical current flow can be obtained by the insertion of the alumina film instead of BN between the graphite die and the graphite punches in the SPS setup, enabling the achievement by SPS of the results similar to those obtainable by EDS (for the compaction of $ZrB_2$, $MoSi_2$ and $ZrB_2$/20 vol% $MoSi_2$) and RS processes (for alumina). They state that this setup allows the sintering of any refractory ceramic material in less than 60 sec starting from room temperature with heating rates higher than 2000 °C/min and an energy saving up to 100 times more efficient than that of the SPS [83]. However, the full density was not achieved for all the tested samples possibly due to the low pressure (15MPa) and porous edge formation in the specimens.

# CHAPTER 2 Research Objectives

## 2.1. Research Incentives

The above-mentioned analysis of the previous studies indicates that SPS is a rapid method for the production of dense ceramic materials. However, the SPS mechanisms of rapid densification have not been clearly identified, especially in terms of the effect of electric current, and mainly due to a number of obstacles, including: (i) the complexity of the deconvolution of the Joule heating and possible non-thermal field phenomena, (ii) the difficulty of the accurate experimental measurements of the specimen's temperature and electric current parameters during SPS. At the same time, addressing the obstacles (i) and (ii) can provide a better understanding of SPS-specific factors distinguishing SPS from conventional powder consolidation techniques. To achieve this goal, a consistent research program should be focused on the following problems:

(i): Deconvolution of the electric current effect from the temperature effect is required. For electrically conductive powders, the source of the densification in SPS are the pressure, heat and electric current, while in HP those are pressure and heat by the external heating elements. Heating in HP is transferred by radiation and conduction, which induce certain spatial temperature distributions during the HP operation. However, the heat generation in SPS stems from the Joule heating of the graphite SPS tooling set and of the powder too. If the powder is electrically conductive, a significant fraction of the electric current can pass through it, so that the temperature of the powder becomes higher than that of the die. Usually, during SPS, the control temperature is measured at a selected point in the die wall, therefore special techniques are required to determine the real temperature of the powder for electrically conductive materials subjected to SPS.

(ii): Quantification of the electric current density in conductive powders during SPS process is required. The electric current value recorded during SPS process is not the same as the value of the electric current directly flowing into the powder. The portion of the electric current flowing into the powder is mainly dependent on the electrical and thermal contact resistance, temperature, and the electric resistivity of each material in the die set. During SPS, the necks between particles evolve, so that the electric current density changes respectively.

For addressing the problem (i), various deconvolution techniques can be utilized enabling the comparison of the densification mechanisms with and without electric current under the same sintering conditions. For addressing the problem (ii), FEM simulations of the SPS specimen-tooling setup can be implemented for the assessment of the fraction of the electric current flowing directly into powders. Here the inter-particle neck area evolution should be taken into account for the correct estimation of the local electric current density evolution.

Based on the solution of the problems (i) and (ii), one can find whether the presence of electric current can change the densification mechanism of the powder. In the present study, we use the Olevsky's approach utilizing the constitutive equation for high-temperature creep of a non-linear viscous porous material to find the densification mechanism of powder materials subjected to SPS.

We employ three strategies to analyze the electric current effects on the densification mechanism during the current-assisted powder consolidation.

First, the conventional constitutive equation describing the behavior of powders compacted by HP [84], is used to study the densification behavior of a conductive powder during SPS. If, as a result of the regression of the experimental data, based on the above-mentioned constitutive equation, the value of the power-law creep exponent (corresponding to the non-linearity of the material constitutive behavior) is found to be the same for the sintering with or without electric current (carried out under the same pressure and temperature conditions), then the densification mechanism is not changed by the presence of the electric current. Otherwise, if the value of the power-law creep exponent is found to be different for the pressure and temperature-identical sintering with or without electric current, then the densification mechanism is changed due to the presence of the electric current.

Second, following the results of the electroplasticity theory and experiments from Conrad [85-87] we assume that other power-law creep parameters like frequency factor or deformability of material can be changed due to the presence of the electric current.

Third, the presence of other dissipative mechanisms introducing extra terms in the SPS constitutive equation in addition to the traditional power-law creep expression due to the influence of electric current is assumed. The extra terms can be possible influences of additional dissipative mechanisms, such as electromigration, oxide reduction, defect generation, grain growth and grain orientation, etc. To support the theoretical assessment of the contributions of these phenomena into the intensity of mass transfer during SPS, additional experimental procedures have to be carried out including microscopic analysis of the structure and phase composition of the materials subjected to SPS.

Previously, MSC, B-G, and Olevsky's methods analyzed the densification mechanisms by studying the porosity evolution curves. In particular, grain boundary sliding (GBS) is associated with grain rotation, resulting in the suppression of the grain orientation. In this connection, EBSD technique can give the experimental proof of the densification mechanism of tungsten powders during the sintering by assessing the degree of the grain orientation.

From the conducted literature survey, it can be concluded that SPS possibly can remove surface oxide layers or slower the grain growth. The influence of these electric current effects has been analyzed in the present study for the SPS of surface-oxidized Mo nanopowders.

One advantage of the SPS process is the fast heating rate which enabling the prevention of the grain growth. Using this advantage, for nuclear application, Mo metal mirror with submicron grain size can be fabricated by the Mo nanopowders compaction by SPS.

Flash sintering showed that increasing the electric voltage applied to an ionic conductive powder compact initiated the thermal runaway, and achieved the densification in less than 10 sec. However, Todd and Zhang showed that flash sintering is simply a usual consequence of the negative temperature coefficient of electric resistivity. The results of our studies indicate that high electric current can change the densification mechanism, inducing the fast densification. Based on these facts, we developed a novel NFSPS (net-shape flash spark plasma sintering) process enabling the high electric current flow into a powder within the short time period. The high density of the electric current turns out to be beneficial in terms of decreasing the energy spent and fast densification.

## 2.2. Major Research Objectives

In the previous chapters, we provided an overview of the past studies and possible concepts to explore on how electric current can affect sintering behavior. We have explained that electric current can increase the efficiency of sintering in terms of process energy and time. In this connection, two major research objectives of the present work can be formulated:

a. Investigation of the electric current effects on the densification behavior of the powders consolidated by spark plasma sintering. This objective is aimed at the development of the new SPS-specific constitutive equations describing electric current-assisted powder densification.
b. Utilization of electric current for sintering of refractory materials. This objective is aimed to show the advantages of SPS and to develop novel SPS-based approaches for the consolidation of metal or ceramic components using the advantages of the electric current assisted mass transfer.

## 2.3. Major Research Tasks

In order to achieve the two formulated research objectives, the following three main tasks have to be carried out:

a. Theoretical determination of electric current effects. This task includes all the efforts to find the electric current effects on the densification mechanisms of the tested powders. First, the constitutive equation of HP has to be modified to take into account the influence of the electric current during the SPS. At the same time, the evolution of the electric current density during SPS should be taken into consideration. Secondly, the regression methods to find the thermal, mechanical or electric current affected parameters in the constitutive equation of HP and SPS have to be designed. Finally, the quantification of electric current flow during the SPS process has to be estimated by FEM simulations taking into consideration the inter-particle neck area evolution during the powder specimen's overall density increase.
b. Experimental determination of electric current effects. The sophisticated experimental setup is designed to deconvolute the intrinsic electric current effects from the temperature

effects. Using the theoretical background provided by the outcomes of the research task a), the consolidation experiments of ZrN powder with deconvolution of electric current effects from the temperature effects, are to be carried out to achieve the research objective a). ZrN is a ceramic material with metal-like properties. First, the fine ZrN powders should be consolidated using different electric current densities under the same temperature conditions during SPS. Second, the densification kinetics of the micron size ZrN powder using HP (without electric current) or SPS (with electric current) are to be compared. Third, previous two experiments should indicate whether high electric current density enhances the densification kinetics of ZrN powders. Therefore, the micron-sized ZrN powders have to be consolidated with using SPS (lower voltage) or HVEDC (higher voltage), and the densification behavior and microstructures between SPS and HVEDC are to be comparatively analyzed. By fitting the constitutive equations to the respective experimental porosity evolutions of ZrN powder, the power-law creep parameters can be evaluated. The tasks a) and b) address the research objective a).

c. Consolidation of nano or micron sized powders using electric current effect. The research tasks a) and b) should reveal what changes of the densification behavior are imposed by electric current, and, in particular, by high electric current density. W powders which have higher electric conductivity than ZrN have to be densified by SPS checking whether densification mechanism is affected by comparing the consolidation results from the HP. In addition, other intrinsic electric current effects such as surface cleaning or retarded grain growth should be considered to optimize the fabrication of nano grain sized Mo mirror using SPS. Finally, the novel net shape flash SPS (NFSPS) process intensifying the electric flow by manipulation of the electric current trajectory in the SPS die, is to be explored to consolidate metal or ceramic powders. Tasks b) and c) address research objective b).

Above-mentioned research objectives and task were completed during my Ph.D. study and shown in the flowchart (Figure 2.1).

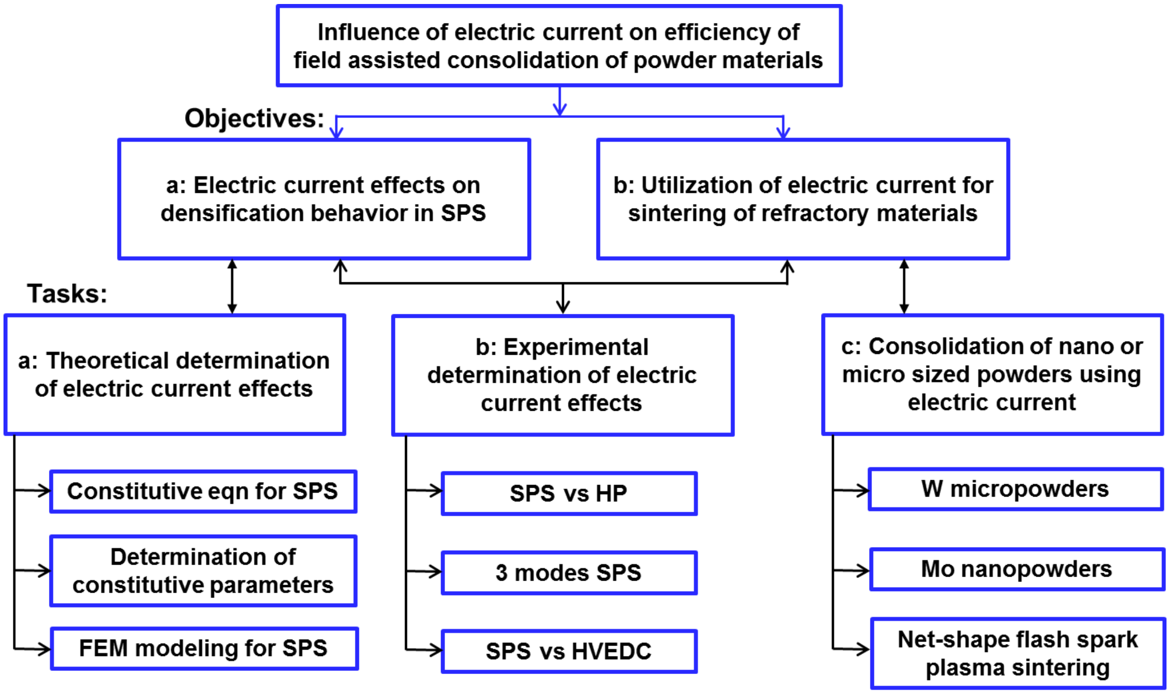

Figure 2.1 Flowchart of formulated research objectives and tasks.

# CHAPTER 3 Effect of Electric Current on Densification during SPS of Conductive Materials

## 3.1. Theoretical Analysis

### 3.1.1. Constitutive equation of the continuum theory of sintering used for the description of HP

The stress for high-temperature deformation of crystalline materials can be described as a function of strain rate ( $\dot{\varepsilon}$ ) and absolute temperature (*T*) as expressed by the Dorn equation [88]:

$$\left(\frac{\sigma}{G}\right)^n = \frac{\dot{\varepsilon}kT}{A_{Cr}DGb}\left(\frac{d}{b}\right)^p \tag{3.1}$$

where $\dot{\varepsilon}$ is the steady-state creep rate (*1/s*), *k* is the Boltzmann's constant (J/K), *D* is the diffusion coefficient (cm$^2$/s), *G* is the shear modulus (MPa), *T* is the absolute temperature (K), *b* is the Burgers vector (m), *σ* is the applied stress (MPa), $A_{cr}$ is the material creep constant (unitless), *d* is the grain size (m), *p* is the grain size exponent, and *n* is the stress exponent (*n* is equal to *1/m*, where *m* is the strain rate sensitivity).

The dependence of the diffusion coefficient *D* on temperature *T* can be expressed through:

$$D = D_0 \exp\left(\frac{-Q}{RT}\right) \tag{3.2}$$

where $D_0$ is the diffusion constant (cm$^2$/s), *Q* is the creep activation energy (KJ/mol), and *R* is the gas constant.

For a porous material [50], Dorn equation can be converted to the power-law relationship in terms of the strain rate as follows:

$$\sigma(W) = G\left\{\frac{A_0T}{G}\exp(\frac{Q}{RT})\right\}^m (\frac{d}{b})^{pm} W^m \tag{3.3}$$

Here, $A_0$ (Pa·s/K) is given by:

$$A_0 = \frac{k}{A_{Cr} b D_0} \tag{3.4}$$

where $\sigma(W)$ is the effective stress, and $W$ is the effective equivalent strain rate of the porous material [50, 55].

Based on the continuum theory of sintering [50] the constitutive equation describing hot pressing of a nonlinear viscous porous material in a rigid die is expressed as:

$$\sigma_z = \frac{\sigma(W)}{W}[\varphi \dot{\varepsilon}_z + (\psi - \frac{1}{3}\varphi)\dot{e}] \tag{3.5}$$

where $\sigma_z$ is the applied axial stress (MPa), $\varphi$ is the normalized shear modulus, $\psi$ is the normalized bulk modulus, $\dot{\varepsilon}_z$ is the axial strain rate component (1/s), and $\dot{e}$ is the volumetric strain rate (1/s).

The above-mentioned constitutive parameters are defined as follows [50]:

$$\psi = \frac{2}{3}\frac{(1-\theta)^3}{\theta} \tag{3.6}$$

$$\varphi = (1-\theta)^2 \tag{3.7}$$

The parameter is expressed as follows.

$$\dot{e} = \dot{\varepsilon}_z + 2\dot{\varepsilon}_r \tag{3.8}$$

Where $\dot{\varepsilon}_r$ is the radial strain rate component.

The evolution of porosity can be defined by the continuity equation:

$$\dot{e} = \frac{\dot{\theta}}{(1-\theta)} \tag{3.9}$$

Where $\dot{\theta}$ is the densification rate (1/s).

Therefore, by substituting (3.3), (3.6) - (3.9) into (3.5) and taking into account that $\dot{\varepsilon}_r = 0$ (uniaxial die compaction boundary condition), the constitutive equation describing hot pressing of a nonlinear viscous porous material in a rigid die can be written as [50, 55]:

$$\dot{\theta} = -\left[\frac{G}{A_0 T}\left(\frac{b}{d}\right)^p \exp\left(\frac{-Q}{RT}\right)\right]\left(\frac{3\theta}{2}\right)^{\frac{m+1}{2m}}(1-\theta)^{\frac{m-3}{2m}}\left(\frac{\sigma_z}{G}\right)^{\frac{1}{m}} \tag{3. 10}$$

### 3.1.2. Constitutive equation of SPS

The constitutive equation for hot pressing (3.10) can be modified to include the electric current effect term based on the recent results of the electroplasticity theory [36, 89, 90].

A) Metal deformation in electroplasticity theory

Assuming that the plastic deformation of the material is thermally activated, the strain rate $\dot{\gamma}$ can be expressed as follows [69, 89]:

$$\dot{\gamma} = \dot{\gamma}_0 \exp\left(\frac{-\Delta G}{kT}\right) = \rho_m b \nu_d s \exp\left(\frac{-\Delta G}{kT}\right) \tag{3.11}$$

where $\rho_m$ is the mobile dislocation density, $b$ is the magnitude of the Burgers vector (m), $\nu_d$ is the frequency of the vibration of the dislocation segment involved in the thermal activation (1/s), $s$ is the average distance of the dislocation travel (m), $\Delta G$ is the activation energy (KJ/mol) $T$ is the absolute temperature (K), and $k$ is Boltzmann constant (J/K).

Conrad [89] studied the electric field effect on the flow stress of metals (Ni, Ti, Al, Cu, and Zn) at low temperatures and showed that there is the interaction between the drift electrons and dislocations. He showed that the most significant effect of the electrons is on the pre-exponential factor $\dot{\gamma}_0$ in (3.11), which was shown to be proportional to the square of the electric current density

(J). This means that the electric current can affect $\rho_m$, $v_d$, $A_s$, or $\Delta S$. However, it was not determined yet which factor is the most affected by the electric current.

B) Ceramics deformation in electroplasticity theory

Ceramic materials manifest their brittle nature at low temperatures. However, they can have ductile properties at high temperatures [86]. Plastic deformation of ceramic materials is described by (3.1). Conrad and Yang studied the electric field effect on the flow stress of oxide ceramics (MgO and $Al_2O_3$) at high temperatures. Like in the case of metals, the application of the electric field during tensile deformation of oxides reduces their flow stress and the increase of the elongation. They tested the rate controlling constants $A_{cr}$, $n$, and $p$ in (3.1) with and without an electric field, and found that the electric current did not change the major deformation mechanism of the material [85-87]. Instead, they assumed that the electric current affected the values of $D_0$ or $Q$. Also, Conrad and Yang explained that the reduction of the flow stress by an electric current is due to the decrease in the electrochemical potential of the rate-limiting vacancies in the space charge cloud near grain boundaries [89].

Also, we assume that the reduction of the particle material yield stress by an electric current is a major mechanism of the rapid densification of conductive powders compacted via an electric current-assisted consolidation method. The reduction of the yield stress can be achieved mainly by the two effects induced by the electric current: (i) local Joule heating, (ii) electron wind effect.

(i) Local Joule heating effect

When the electric current flows through a powder during deformation, the local "hot spots" caused by the greater electron scattering at defects such as dislocations, voids, impurities and grain boundaries, largely enhance the lattice vibration energy in the defect vicinity. As a result, dislocations can move more easily along the slip plane bypassing lattice obstacles with smaller resistance. Therefore, the stress required to move dislocations is reduced. This heating occurs at the atomic level within the lattice contributing to the total heating of the sample, and expanding the lattice locally [36, 91]. Hence, the local Joule heating increases parameters $v_d$ and $\rho_m$ in (3.1). This effect can lead to faster defect motion under SPS compared with HP conditions. While HP needs external energy input that has to heat the entire material to allow for the dislocations to diffuse to a sink such as grain boundaries, SPS provides a greater amount of energy in a faster mode and directly to the dislocations. Also, recently, using the modified Williamson-Hall method [92, 93], the XRD method indirectly showed that an increasing electric current density decreased the dislocation density of a tungsten pellet compacted by SPS, which indicated the dislocation mobility enhanced by the electric current influence [94].

(ii) Electron wind effect

The direct momentum transfer from flowing electrons through the electric conductor can help the mobility of dislocations in the lattice structure [35, 95]. However, some researchers showed that the electron wind effect is not sufficient to affect the dislocation activities [96, 97]. In particular, Salandro et al. [36], showed that the added energy to a dislocation core by the electron wind effect is much less than that by the local Joule heating effect.

Therefore, one can assume that the main source of the reduction of the flow stress by the electric current is from the indirect local vibration energy from electron scattering, not from the direct momentum transfer to the dislocation.

In (3.10), we define the function in the square bracket as $A_{TD}$ (1/s) which indicates the thermal deformability of the powders during the sintering.

$$A_{TD} = \frac{G}{A_0 T}\left(\frac{b}{d}\right)^p \exp\left(\frac{-Q}{RT}\right) \tag{3.12}$$

With (3.12), (3.10) can be simply written as follows:

$$\dot{\theta} = -A_{TD}(\frac{3\theta}{2})^{\frac{m+1}{2m}}(1-\theta)^{\frac{m-3}{2m}}(\frac{\sigma_z}{G})^{\frac{1}{m}} \tag{3. 13}$$

Total equivalent effective strain rate (*W*) should be the sum of the strain rate from thermal and electric current assisted effect during the SPS process.

$$W = W_{Thermal} + W_{Electric\,current\,assisted} \tag{3.14}$$

Using (3.3), (3.14) is converted with the introduction of $A_{ECAD}$ (1/s) which indicates the electric current assisted deformability of the powders as follows:

$$W = (A_{TD} + A_{ECAD})(\frac{\sigma_z}{G})^{\frac{1}{m}} \tag{3.15}$$

By substituting (3.15), (3.6) - (3.9) into (3.5) and taking into account that $\dot{\varepsilon}_r$ = 0 (uniaxial die compaction boundary condition), the constitutive equation for SPS can be written as

$$\dot{\theta} = -\left[A_{TD} + A_{ECAD}\right](\frac{3\theta}{2})^{\frac{m+1}{2m}}(1-\theta)^{\frac{m-3}{2m}}(\frac{\sigma_z}{G})^{\frac{1}{m}} \tag{3.16}$$

Also, (3.16) is validated based on the electroplasticity theory which indicates that the electric current affects the pre-exponential factor for metals, and $D_o$ or *Q* for ceramic materials [69, 85, 86, 89].

To find $A_{ECAD}$, the following analysis is used. Local Joule heating can provide the vibration energy to the dislocation movement [36]. Also, the high temperature of the locally overheated region may be sufficient to activate additional intrinsic defects [98]. These generated defects can enhance the mobility of dislocations by interacting with elastic and electronic fields of the dislocations [26, 69, 99], but more interestingly, can be also the source of the local Joule heating, making the local temperature to increase again, and thereby starting the cascade effects. However, due to the relatively low electric current density under regular SPS conditions and being coupled with vacancy annihilation by dislocation movement, these cascade effects are limited compared to flash sintering [64, 67].

Therefore, we assume that the energies of the local Joule heating are the original source for the electric current effects. The actual temperature of the sample was calibrated previously in the experiments, but the additional Joule heating effects like the defect generation should be accumulated with sintering time during SPS due to the cascade characteristics. The localized energy provided to the dislocation core due to the Joule heating effect (per dislocation core volume) is given by [36]:

$$E_J = J^2 \lambda_d \Delta t \tag{3.17}$$

where $J$ is electric current density, $\lambda_d$ is electrical resistivity of the dislocation core and $\Delta t$ is the time duration when the electric current is applied. Parameter $\lambda_d$ was determined to be around 6~8 times the electric resistance of the defect-free lattice ($\lambda$) [100]. Also, the dislocation movement by Joule heating can be hindered by Peiers-Nabarro stress ( $\tau_{PN}$ ) of each material. For the FCC material like ZrN, experimental results showed that $\tau_{PN}$ is approximately $(10^{-6} \sim 10^{-5})G$ [101].

Including the terms that affect the dislocation movement considered above, $A_{ECAD}$ can be written as:

$$A_{ECAD} = \left[ \int_{t_0}^{t_f} \frac{J^2 \lambda_d}{\tau_{PN}} dt \right]^{\omega} \tag{3.18}$$

where $t_0$, $t_f$ are the starting and final time for SPS and $\omega$ is the electric current sensitivity exponent (material constant).

By including the electric current effect coefficient (*β*), which involves the relationships between $J_{OL}$ vs. actual $J$ in the sample, $\lambda_d$ vs. actual $\lambda$, and $\tau_{PN}$ vs. $G$, (3.18) can be written as:

$$A_{ECAD} = \beta^{\omega}\left[\int_{t_0}^{t_f}\frac{J_{OL}{}^{2}\lambda}{G}\,dt\right]^{\omega} \tag{3.19}$$

Therefore, the constitutive equation for SPS, (3.16) can be expressed as:

$$\dot{\theta} = -\left[\frac{G}{A_0 T}\left(\frac{b}{d}\right)^{p}\exp\left(\frac{-Q}{RT}\right) + \beta^{\omega}\left[\int_{t_0}^{t_f}\frac{J_{OL}{}^{2}\lambda}{G}\,dt\right]^{\omega}\right]\left(\frac{3\theta}{2}\right)^{\frac{m+1}{2m}}(1-\theta)^{\frac{m-3}{2m}}\left(\frac{\sigma_z}{G}\right)^{\frac{1}{m}} \tag{3.20}$$

### 3.1.3. Determination of the creep parameters: in situ method

The direct *in situ* method based on the continuum theory of sintering is used here to identify the sintering mechanism.

Initially, the regression analysis renders the temperature-dependent creep parameters ($A_0$, $Q$ and $n$) based on the SPS experiment at the ramping temperature and assuming the traditionally used expressions of the normalized shear and bulk moduli [102]. When $n$ value cannot be unambiguously determined from the regression analysis, the SPS multistep pressure approach is used [55]. The detailed derivation of the sintering parameters can be found elsewhere[102, 103].

The linearization of the constitutive equation of the pressure-assisted sintering[84] can be expressed as follows:

$$n\ln\left(\frac{|\sigma_z|}{\left(\psi+\frac{2}{3}\varphi\right)^{\frac{n+1}{2n}}(1-\theta)^{\frac{n-1}{2n}}|\dot{\varepsilon}_z|^{\frac{1}{n}}}\right) - \ln(T) = -\ln(A_0) + \frac{Q}{RT} \tag{3.21}$$

where, $|\sigma_z|$ is the applied axial stress (Pa), $|\dot{\varepsilon}_z|$ is the strain rate of the sample (s$^{-1}$). Parameters $A_0$ and $Q$ can be obtained for different values of $n$.

Various [84] $n$ values can be found by the comparison of the experimental and theoretical porosity curves. However, in many cases, when using this method, the determination of the parameter $n$ value is [103] difficult due to the low accuracy; therefore the SPS multistep pressure dilatometry approach is a more reliable approach to utilize.

For the SPS multistep pressure dilatometry[55] approach, the $n$ value can be determined by the following equation:

$$n = \frac{\ln\left( \frac{\exp(-|\varepsilon_{z2}|) - (1-\theta_0)}{\exp(-|\varepsilon_{z1}|) - (1-\theta_0)} \frac{|\dot{\varepsilon}_{z1}|}{|\dot{\varepsilon}_{z2}|} \right)}{\ln\left( \frac{\sigma_{z1}}{\sigma_{z2}} \exp(|\varepsilon_{z2}| - |\varepsilon_{z1}|) \sqrt{\frac{\exp(-|\varepsilon_{z2}|) - (1-\theta_0)}{\exp(-|\varepsilon_{z1}|) - (1-\theta_0)}} \right)} \tag{3.22}$$

where $\theta_0$ is each initial porosity just before the pressure jump.

After finding the $n$ value from this multistep pressure approach, parameters $Q$ and $A_0$ can be obtained. Therefore, the creep parameters ($A_0$, $Q$, and $n$) which identify the densification mechanism can be obtained using only one or two (when SPS multistep pressure dilatometry is required) experiment.

### 3.1.4. Overall local electric current density (OLECD) estimation for powder samples

Current density in a powder sample is mainly affected by the neck area between particles during the SPS. The neck area changes with porosity evolution, has been studied by Helle, Artz, and Ashby [104, 105]. Current density can be large at the initial stage of sintering (small neck) and reduces with decreasing porosity (large neck) during sintering.

For an irregular packing of the spherical particles, the neck area evolution with porosity can be estimated as shown by Helle *et al*. [105]:

$$\frac{SZ}{4\pi R^2} = \frac{(\theta_0 - \theta)(1-\theta)}{\theta_0} \tag{3.23}$$

where $S$: average area of contacts between two particles, $Z$: coordination number, $R$: particle radius, $\theta_0$: initial porosity and $\theta$: porosity. When $R$ is constant, the $AZ/4\pi R^2$ value is increased from 0 to 1 when porosity is changed from $\theta_0$ to 0 (Fig.1 in Ref [105] ). We assume that the neck area evolution of one particle is proportional to the total contact area change of the total powder specimen's volume. Therefore, we consider $AZ/4\pi R^2$ to be the ratio of the total neck area to the total powder surface area. Overall local electric current density (OLECD) is the summation of the electric current density of all necks in the powder volume.

Using the previous consideration, $J_{OL}$ (OLECD) of the sample can be calculated as follows:

$$J_{OL} = \frac{I_s}{A_{cross-section}} \times \frac{4\pi R^2}{SZ} \tag{3.24}$$

where $A_{cross\text{-}section}$: cross-sectional area of the full density sample.

### 3.1.5. Dislocation density analysis by modified Williamson-Hall method

The modified Williamson-Hall method was used to estimate the dislocation densities in the compacted pellets. Assuming that the strain broadening is generated by the existence of the dislocations, the full width at half maximum (FWHM) obtained from each peak is substituted into the quadratic form of the modified Willamson-Hall equation:

$$\left(\Delta K\right)^2 \simeq \left(0.9/D\right)^2 + (\pi M^2 b^2/2)\rho K^2 \overline{C} \pm O(K^4 \overline{C}^2) \qquad (3.25)$$

where $\Delta K = 2\cos\theta(\Delta 2\theta)/\lambda$, $K = \sin\theta/\lambda$, θ is diffraction angle (rad), *Δ2θ* is FWHM) (rad), $\lambda$ is the wavelength of X-rays ( Cu Kα1 = 0.15406 nm), *D* is the average particle size (nm), *b* is the magnitude of Burgers vector, *M* is a constant depending on both the effective outer cut-off radius of dislocations and dislocation density, $\rho$ is the average dslocation density (nm$^{-2}$), *C* is the average contrast factor of dislocation, correspondoing to (hkl) reflection, and *O* is non-interpreted higher order terms which can be ignored. In FCC and BCC, *C* can be written as:

$$\overline{C} = \overline{C}_{h00}(1 - q\left(\frac{h^2l^2 + h^2k^2 + l^2k^2}{\left(h^2 + k^2 + l^2\right)^2}\right)) \qquad (3.26)$$

where $C_{hoo}$ is an elastic constant, h,k, and l are the Miller's indices of each peak, and q is a parameter indicating the dislocation characteristic in the samples. For ZrN [106], parameters $C_{hoo}$ and $q$ are 0.135 and -0.636 calculated from the equation provided by Ungar et al [93]. Parameter *M* for is taken as 2.3 [107].

In the modified Williamson-Hall equation, the slope ($\beta$) of the fitted curves from the plot $\Delta K^2$ vs $K^2C$ provides the average dislocation density as follows:

$$\rho = \frac{2\beta}{\pi M^2 b^2} \qquad (3.27)$$

## 3.2. Experimental Analysis

In the conducted study, special 3 experimental modes were developed to find the electric current effect on the densification mechanism of ZrN. All the 3 modes were conducted at same sample temperature with different electric current density, which enables the deconvolution of the electric current effects from the thermal factors such as Joule heating and heating rate. The electric current effects were quantified by finding the electric current passing through ZrN powder using a FEM simulation and considering the local neck area evolution during sintering. The effect of the electric current flow on the material's deformability and dislocation density during ZrN powder densification process are analyzed by three special SPS mode experiments enabling the deconvolution of the electric current effects from the thermal effects' contributions.

### 3.2.1. Experimental procedures

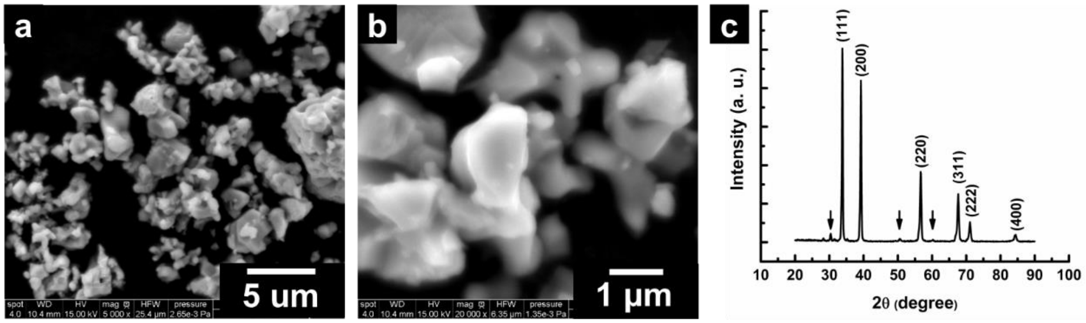

Figure 3.1 (a) and (b) SEM images of as received ZrN powder: 5000X, 20000X, respectively. (c) XRD of ZrN powder. Arrows in Figure 3.1(c) indicate oxide phase.

ZrN powders (Face centered cubic, Fm3m) produced by Sigma-Aldrich (lot number: BCBM0674V) with an average particle size of 2 μm were employed for the 3 modes of SPS experiments. The ZrN powders have an irregular particle shape and agglomeration (Figure 3.1(a) and (b)). The crystal structure and lattice parameters were evaluated by X-ray diffraction (XRD) (Bruker D-8 diffractometer, MA, USA), utilizing CuKα radiation at room temperature (Figure

3.1(c)). The cubic NaCl-type structure dominates, however oxide impurities were found in the ZrN powders ($ZrO_2$, ICSD Collection code # 85322) [108]. From energy-dispersive X-ray spectroscopy (EDS) (Oxford Instruments, UK) analysis, ZrN powder contains on average 8.30 at% of oxygen. Also, the powder showed the presence of hafnium in the amount < 0.3 %.

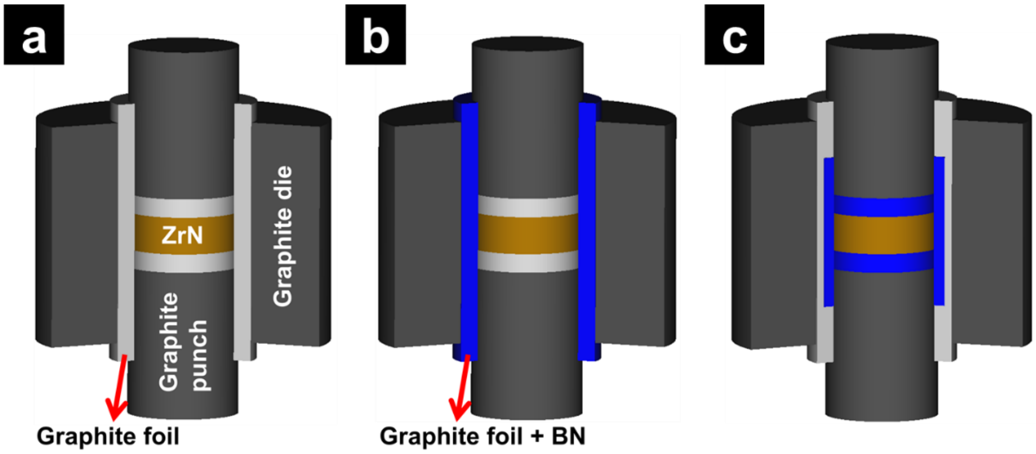

Figure 3.2 Schematics of spark plasma sintering setup enabling the different current density flow into ZrN powders. Black, gray, gold and blue color indicate the graphite component, graphite paper, ZrN, and boron nitride respectively. (a) Normal J (Electric current density) mode, (b) High J mode and (c) Insulation mode.

The sintering experiments were carried out using the SPS device manufactured by SPS Syntex Inc., (Dr. Sinter SPSS-515, USA) with a graphite (EDM-4, Poco Graphite, Inc., TX, USA)) tooling setup. As shown in Figure 3.2, boron nitride (BN, electric insulator) was coated on the graphite paper (0.15 mm-thick) in order to manipulate the electric current path in the SPS setup. The three SPS modes include “normal J  mode” (with J being the electric current density) where the electric current can pass both in the sample and the die (Figure 3.2(a)), the “high J mode” where all the current passes through the sample and not through the die (Figure 3.2(b)) and, finally, “insulation mode” where no electric current passes through the sample (Figure 3.2(c)). For all the 3 modes, the same SPS conditions were used: 1600 °C, 60 MPa, 100 °C/min and 60 min holding time. The relative density was obtained by the Archimedes' immersion method. The fractured specimens were analyzed by the scanning electron microscopy (SEM), (FEI Quanta 450, USA). XRD was used too to analyze ZrN pellets processed via 3 SPS modes.

For the deconvolution of the electric current effect from the thermal effects, the exact temperature of the sample should be measured. Due to the high sintering temperature (1600 °C), a pyrometer was preferred for temperature detecting and PID (proportional–integral–derivative) controlling device [109]. For all the modes, the powders were pre-consolidated by SPS until it had the sufficient binding strength (See Supplementary Methods online). Without removing the ZrN sample from the die in the pre-consolidation experiment, 0.5 mm depth hole at the side of the ZrN sample was drilled through the 2 mm diameter graphite die hole, so that the optical pyrometer directly measured the temperature focused on the side of the pre-consolidated samples. This method guarantees that the temperature of the samples is the same for all the three SPS mode experiments. For all three modes, the same conditions were used: 1600°C, 60 MPa, 100 °C/min and 60 min holding time.

The dependence of ZrN emissivity on porosity and temperature is unknown. Therefore, the pyrometer was calibrated by an additional experiment conducted in the similar conditions where an additional k-type thermocouple was placed in another through hole and contacted with the pre-compacted samples to estimate the true temperature of the samples. The difference between the temperature values measured by the pyrometer and thermocouple was obtained as follows:

$$T_{ZrN\_TC} = 1.121 \times T_{ZrN\_Pyro} - 76.330 \tag{3.28}$$

Where $T_{ZrN\_Pyro}$ and $T\__{ZrN\_TC}$ are the temperatures (in °C) measured by the pyrometer and by the thermocouple, respectively. The maximum holding temperature was found to be 1717 °C while the pyrometer displayed 1600 °C.

### 3.2.2. Experimental results

#### 3.2.2.1. Estimation of the density of the electric current flowing into ZrN powders

Table 3.1 Physical properties of graphite, ZrN and stainless steel 304 (with T in Kelvin).

| Material | Electrical conductivity | Heat capacity | Thermal conductivity | Density |
|---|---|---|---|---|
| | S/m | J/(kgK) | W/(mK) | $kg/m^3$ |
| Graphite [110] | $29.40*10^{3}+208.84T-16.77*10^{-2}T^{2}+5.24*10^{-5}T^{3}-5.90*10^{-9}T^{4}$ | $-280.03+4.16T-2.91*10^{-3}T^{2}+9.30*10^{-7}T^{3}-1.11*10^{-10}T^{4}$ | $161.63-1.79*10^{-1}T+1.07*10^{-4}T^{2}-2.43*10^{-8}T^{3}$ | 1740 |
| ZrN | $3.23*10^{8}T^{-0.804}*(1-(3/2)\theta)$ [111] | $(45.86+6.82*10^{-3}T-5.54*10^{5}/T^{-2})/0.11*(1-\theta)$ [112] | $(28.30+1.2*10^{-2}T-3.7*10^{-6}T^{2})*(1-(3/2)\theta)$ [112] | $7090*(1-\theta)$ |
| Stainless steel 304 [113] | $(50.17+8.38*10^{-2}T-1.75*10^{-5}T^{2})*(1.00*10^{-8})$ | $446.50+1.62*10^{-1}T$ | $9.99+1.75*10^{-2}T$ | 7900 |

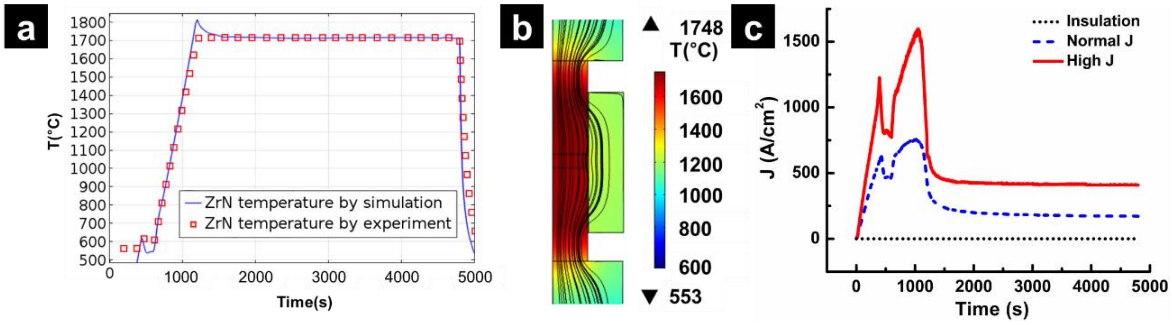

Figure 3.3 (a) Experimentally measured and simulated temperatures of ZrN powder during normal J SPS. (b) FEM simulation map of the die set for temperature (color table) and electric current flow (solid line) for the normal J mode at the final holding time. (c) Overall local electric current density ($J_{OL}$) evolution during whole SPS cycle before cooling stage for 3 SPS modes

Because the processing conditions and measured sample temperature were the same for the three modes, the electric current was the only factor which could additionally affect the densification behavior of the powders.

The total electric current values recorded by the SPS system ($I_t$) are not identical to the amount of the electric current ($I_s$) passing through the samples [114]. The $I_s$ value is evident for the high J (100% of $I_t$) and the insulation modes (0% of $I_t$). However, for the normal J mode $I_s$ is not the same as $I_t$, and is mainly affected by the electrical and thermal properties of the graphite die set. An electro-thermal model based on the finite element code COMSOL$^{TM}$ has been developed within the framework of the present studies to estimate the $I_s$ during SPS. The entire vertical assembly of the SPS tooling setup including the graphite die, punches, sample, and electrodes are analyzed in the model. The properties of the materials considered are given in Table 3.1. The properties of ZrN were obtained from the literature [111, 112], and the electrical and thermal conductivity were modified by the effective medium approximation method [2, 115]. The detailed boundary conditions of the FEM simulations have been previously described [116].

Vertical and horizontal electrical contact resistance (ECR) were obtained from reference [117]. Also, the thermal contact resistance (TCR) were used in accordance with reference [118].

After developing the FEM model, the temperature values measured in the die and inside the powder from the start until the onset of cooling were used to calibrate the ECR and TCR at the ZrN-graphite interfaces. Both contact resistances affect the thermal behavior during the ramping and holding stage. Otherwise, the cooling stage (purely thermal) is suitable for adjusting the TCR. Calibrated ECR and TCR from same die setup in section 4.2.1.2.2. were used

As shown in Figure 3.3(a), the temperatures experimentally measured and simulated by the FEM match well, which indicates that the thermal and electrical parameters in the FEM have been well matched with experimental conditions. Figure 3.3(b) shows the FEM simulation map of the die set for the temperature and electric current flow for the normal J mode, indicating that the electric current (black lines in Figure 3.3(b)) from the top punch is split into the ZrN and the graphite die. Also, the large temperature difference between the ZrN sample and the die is observed (color map in Figure 3.3(b)), and this rationalizes the importance of finding the exact sample temperature instead of the die temperature.

The electric current density of the powders is largely affected by the inter-particle neck area evolution during current-assisted sintering. During sintering, the area between particles increased. The electric current density value dependence on the increasing inter-particle neck area was introduced in section 3.1.4. The summation of the electric current density of all the necks in the powder volume was estimated as the overall local electric current density ($J_{OL}$) shown in (3.27).

With $I_s$ obtained from the FEM simulation and SPS experiment, $J_{OL}$ was estimated for all the 3 SPS modes as shown in Figure 3.3(c). The high J mode (red solid line) has the largest $J_{OL}$ during the ramping and the holding stages due to the electric current concentration within the central column of the SPS tooling setup. The normal J mode (blue dash line) has the lower $J_{OL}$ due to the split of the electric current compared with that of the high J mode. We assume that the insulation mode (black dot line) has no electric current flow into ZrN powder.

#### 3.2.2.2. Densification mechanism of fine ZrN powders for different electric current densities

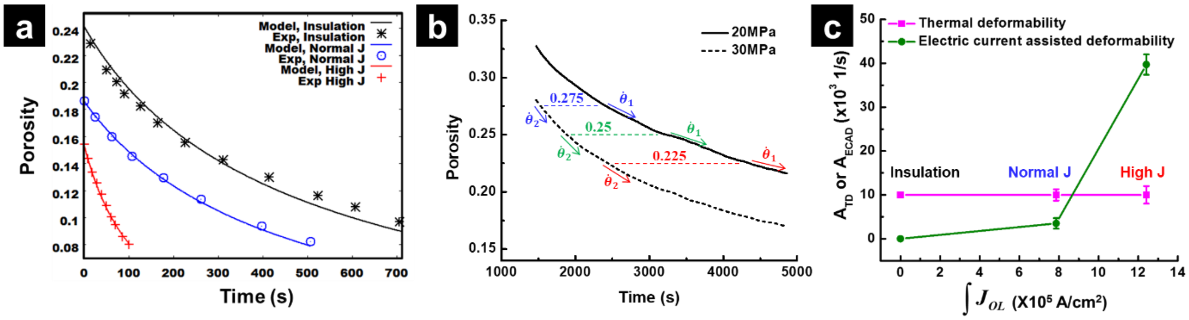

Figure 3.4 (a) Experimental porosity evolution curves of ZrN specimens processed by 3 SPS modes fitted by (3.10). (b) Porosity evolution of ZrN under 20MPa (solid line) and 30MPa (dash line) at 1500 ºC, (c) Comparison of $A_{TD}$ (thermal deformability) and $A_{ECAD}$ (electric current assisted deformability) of ZrN for 3 SPS modes based on the fitting results.

Previously, the sintering for ZrN consolidated by HP was studied by Petrykina and Shvedova [119], indicating that HP has the dislocation climb controlled creep mechanism ($n$ = 4 - 5, $m$ = 0.2 - 0.25) with average $Q$ of 142.26 kJ/mol. Also, in fully dense stoichiometric uranium nitride (UN), which has the same crystallographic structure as ZrN, an analogous value for $m$ was found [120]. A relative density < 92% during the holding stage was chosen for finding the constitutive parameters for the three modes to prevent the possibility of the grain growth effects influencing the densification mechanism [121]. The porosity evolution (scattered symbols; $0.08 < \theta < 0.15$) for the three modes is shown in Figure 3.4(a). The high J mode (red cross line) shows the fastest densification. At the same time, the densification rate for the insulation mode is the lowest (black asterisk line). For the same temperature conditions, a higher the electric current density results in more rapid densification. These results clearly show that the electric current affects the consolidation behavior of the powders during the sintering under the same temperature.

In the constitutive equation, four unknown parameters ($m$, $A_{TD}$, $\beta$, and $\omega$) can be obtained by fitting the porosity evolution curves. For holding conditions at 1717 °C, these parameters are constants. It is assumed that the thermomechanical part of the sintering model ($m$ and $A_0$) is not impacted by the electric current following the theory of electroplascitity[52, 86, 87], $m$ and $A_{TD}$ values should be the same for all the modes. To find the effect of the electric current density on sintering ($A_{ECAD}$), the following experimental-theoretical analysis was performed.

First, the value $m$ was experimentally obtained under the two different pressure values (20 MPa and 30 MPa) at the same temperature (1500°C) (Figure 3.4(b)). The parameters $G$, $A_0$, $Q$, $\beta$, and $d$ for ZrN powders are the same for different pressures ($P_1$ and $P_2$) and for the same porosity in (3.20); therefore $m$ can be obtained as follows [114]:

$$m = \frac{\ln[\frac{P_1}{P_2}]}{\ln[\frac{\dot{\theta}_1}{\dot{\theta}_2}]} \tag{3.29}$$

Where Where $\dot{\theta}_1$ and $\dot{\theta}_2$ are the densification rates for the 20MPa and 30MPa cases at specified porosity levels ($\theta = 0.225$, 0.25 and 0.275), respectively. The average $m$ value is found to be 0.504.

Secondly, having determined $m$ value from the first step, $A_{TD}$ remains the only unknown parameter and is determined to be $1\times10^5$ (1/s) by applying (3.20) without electric effect term ($\beta = 0$) to fit the porosity evolution curve for the insulation mode (black curve and asterisk symbols in Figure 3.4(a)). The parameter $A_{ECAD}$ for the insulation mode is equal to zero because no current is applied ($J_{OL} = 0$). All the three modes should have the same $A_{TD}$ value due to the same temperature imposed during SPS.

Lastly, with $m$ and $A_{TD}$ determined at the previous two steps, and obtaining $J_{OL}$ from (3.20), parameters $\beta$ and $\omega$ values can be identified through (3.20) fitting to the porosity data for the normal J (blue curve and circle symbols in Figure 3.4(a)) and high J modes (red curves and cross symbols in Figure 3.4(a)). Especially, the electric current sensitivity exponent, $\omega$ is accurately identified thanks to the different level of local current density of normal J and high J mode. The accurate estimation of $\omega$ has not been achieved with general comparison experiment with hot pressing ($J_{OL} = 0$) and SPS ($J_{OL} \neq 0$) due to lack of the current density level [51, 114]. This step provides the $A_{ECAD}$ values for each normal J and high J, as shown in Figure 3.4(c). The obtained $\omega$ and $\beta$ are 2 and $1.10 \times 10^8$ respectively. The expression $\int J_{OL}$ in Figure 3.4(c) indicates the accumulated sum of the overall local electric current densities ($J_{OL}$) from the starting porosity up to 8 % porosity. As shown in Figure 3.4(c), $A_{TD}$ is of the same value for all three modes, and, in contrast, $A_{ECAD}$ has different values and increases with the amount of the electric current density ($\int J_{OL}$). These results clearly point out that electric current can affect the deformability or plasticity of the ZrN powders at high temperature.

The creep mechanism of some materials requires a non-linear ($m \neq 1$) behavior which is defined by a power law. By analogy, this study gives the clear evidence that the current effect term of the deformability requires a power law as the value of $\omega = 1$ fails to explain the results obtained in different current regimes. $A_{ECAD}$ in (3.20) was introduced based on the theory of the electroplasticity which explains that the reduced flow stress of the material under an electric current passage is the result of the enhanced dislocation motion due to the local Joule heating in the vicinity of defects located in the crystalline lattice [114]. Therefore, it should be verified whether the different levels of the electric current density corresponding to the respectively different levels of the dislocation density.

### 3.2.2.3. Dislocation densities and mechanical properties of ZrN specimens for the 3 SPS mode experiments

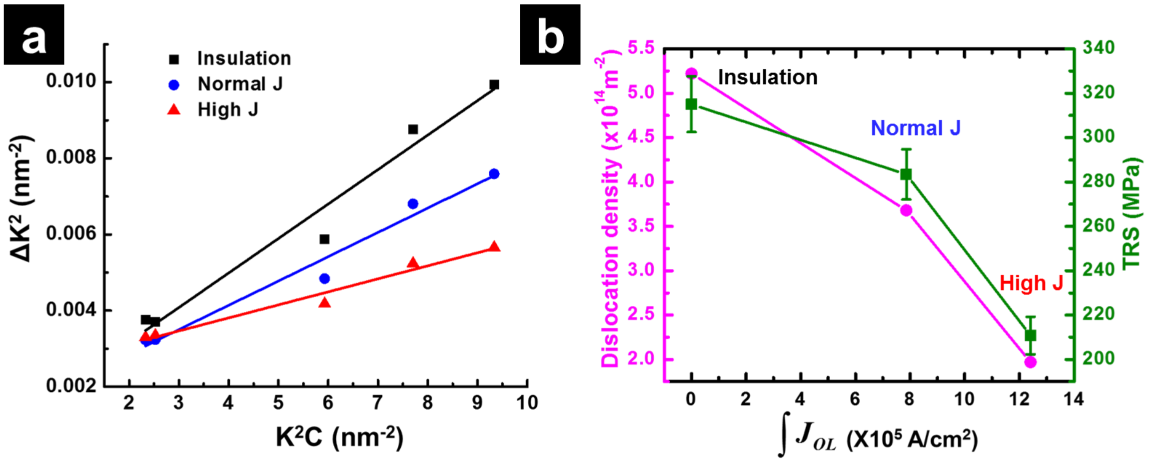

Figure 3.5 (a) $\Delta K^2$ vs $K^2C$ plot from the modified Williamson-Hall method, and (b) Relationship between electric current density, dislocation density and transverse rupture strength (TRS) for 3 SPS modes.

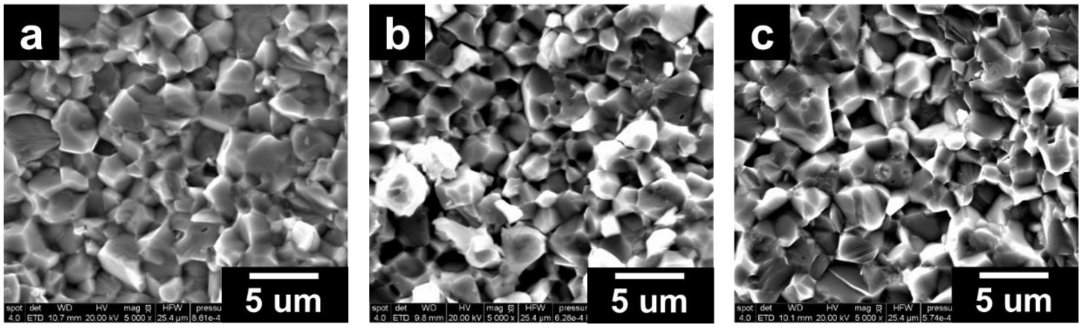

Figure 3.6 SEM Images of fractured surfaces of ZrN specimens densified by 3 SPS modes, (a) insulation, (b) normal J, and (c) high J mode.

Parameter $A_{ECAD}$ in (3.20) was introduced based on the electroplasticity theory which explains that the reduced flow stress of the material under an electric current passage is the result of the enhanced dislocation motion due to the local Joule heating in the vicinity of defects located in the crystalline lattice [114]. Therefore, it should be verified whether the different levels of the electric current density corresponding to the respectively different levels of the dislocation density in the ZrN powder pellets.

The modified Williamson-Hall method as described in section 3.1.5 was used to estimate the dislocation densities in ZrN pellets [93]. It is clear that the slope of the plot is decreased with increasing electric current density, as shown in Figure 3.5(a), which indicates that the dislocation density was reduced with larger electric current density. The calculated average dislocation densities under insulation, normal J and high J modes, are $5.22 \times 10^{14}$, $3.68 \times 10^{14}$, and $1.97 \times 10^{14}$ ($m^{-2}$), respectively (Figure 3.5(b)). The enhanced dislocation motion from local Joule heating at defects [36] or defect generation [26, 69, 99] by the electric current can be the reasons for the reduction of the dislocation density for the higher electric current density levels. Also, it was observed that with increasing the electric current density, the transverse rupture strength (TRS) [122] also decreased (Figure 3.5(b)). ZrN samples processed by the three modes have a similar relative density (98%) and grain size (~3 μm) (Figure 3.6), therefore, the TRS results also validate the above-mentioned explanation of the reduction of the dislocation density when increasing the electric current density. The enhanced dislocation motion decreases the number of dislocations inside (due to their annihilation), inducing lower mechanical strength.

In summary, the fitting by the SPS constitutive equation of the three mode experiments conducted under different electric current density levels demonstrated that the electric current influences the deformability of the powders during electric current assisted sintering. The reduction of the dislocation density corresponding to the increasing electric current density, as evidenced by the XRD analysis, and supported also by the mechanical strength and microstructural characterization data, strongly indicates that electron flow affects the dislocation motion in conductive specimens during electric current assisted sintering.

### 3.3. Chapter Conclusions

Thus, in Chapter 3, we described the theoretical and experimental assessment of the electric current effects on the densification kinetics of a fine ZrN powder during SPS. The deconvolution of the electric current effects from the temperature effects is achieved by controlling the flow of the electric current inside the graphite tooling – powder specimen setup.

For the first time, a constitutive equation of SPS was developed taking into consideration the enhanced dislocations motion by local resistive heating. The 3 SPS mode experiments with different electric current trajectories clearly indicated that the electric current affects the densification kinetics. The electric current density was quantified by finding the fraction of the electric current flowing through a conductive powder using a FEM simulation taking into consideration the inter-particle neck area evolution during SPS. The derived constitutive equation fitting to the porosity evolution curves from 3 SPS mode experiments conducted under different electric current density levels showed that the local Joule heating at defects increases the dislocation motion, which induces the increase of the deformability of the powders (or reduction of flow stress). Also, an increase of the dislocation motion was confirmed by the XRD, SEM and TRS measurement of compacted ZrN specimens under different electric current density.

In the next chapter, we compare the sintering behavior of micro-size ZrN by HP, SPS, and HVEDC.

First, the densification kinetics of the ZrN powder using HP (without electric current) or SPS (with electric current) are to be compared. Compared with the experiments in section 3.2, the main differences are the following:

a. The assumption that electric current can change the parameter *m* value is also explored. In Chapter 3, we assume that parameter *m* value is not changed with the flow of electric current during sintering. In chapter 4, the above-mentioned two situations will be considered separately.

b. Micro-size ZrN powder is used. Parameter *m* value for HP of ZrN from literature [119] can be directly compared with that for the HP conducted in this research.

c. The effects of the heating rate (10 °C/min vs 100 °C/min) on OLECD and densification behavior during SPS are compared.

d. The conducted experiments (3 modes of SPS and HP vs SPS) indicate that high electric current density enhances the densification kinetics of ZrN powders. Therefore, the micron-sized ZrN powders are consolidated using SPS (lower voltage) or HVEDC (higher voltage), and the densification behavior and microstructures between SPS and HVEDC are to be analyzed.

Chapter 3, in part, is currently being prepared for submission for publication of the material. G. Lee, C. Manière, J. McKittrick, and E.A. Olevsky. The dissertation/thesis author was the primary investigator and author of this paper.

# CHAPTER 4 Electric Current Assisted Consolidation of ZrN

## 4.1. Consolidation of ZrN: Literature Survey

Zirconium nitride (ZrN) is a material that has been attracting increasing attention over the last decades, due to the combination of excellent thermal, mechanical and electrical properties, even though there are significant difficulties in its synthesis and processing methodologies. In particular, the mechanical strength of ZrN retained at high temperatures and chemical inertness, with the exception of a limited tendency to oxidize [123, 124], render it a suitable material for a variety of applications, such as coatings for thermal barrier layers and tooling setups for material processing. Another application is as a model surrogate system for the highly radioactive materials used in nuclear reactors: for fuel pellets (UN) [125, 126], as an inert matrix for actinide fuels [127-129] or as an additive for PuN pellets, with which it can form a solid solution [130, 131]. However, it is difficult to obtain ZrN fully dense bodies due to ZrN high melting temperature (2980˚C), the low self-diffusion coefficient (~0.026 $m^2/s$ at 2400~2600˚C), strong covalent bonding [132], and the existence of an oxide layer ($ZrO_2$) on the surface of the starting powders.

A few studies report on the consolidation of ZrN powders by pressureless oven sintering, HP, HIP, and SPS. With pressureless oven sintering method, Pshenichnaya et al. [133] investigated the sintering behavior of submicron-sized ZrN in a vacuum or nitrogen atmosphere. 95% relative density ZrN pellet was produced with at 2100˚C for one hour in a vacuum, yet having decreased nitrogen contents. To retain the dense ZrN pellet with the stoichiometric composition, it is suggested either to do sintering above 2000 °C with nitrogen environment or to put vacuum sintered ZrN pellets into annealing oven in the nitrogen gas. In order to reduce the sintering temperature of pressureless vacuum sintering, various conditions such as particle milling, cold pressing with high pressure and inserting sintering aid were utilized. Wheeler et al. milled the particles followed by cold pressing of 250 MPa for 10 min. 92 % of ZrN pellets were obtained at 1600 °C for 10 hours with sintering aids in Ar atmosphere [125].

In order to reduce the sintering temperature, pressure assisted sintering was used. Petrykina and Shvedova showed that a slightly substoichiometric ZrN0.95, ceramics with 99% density could be obtained by HP at 2500 °C for 5 min under 45 MPa. Also they stated that the densification mechanism of ZrN for HP is a dislocation-climb controlled creep (m = 0.2 - 0.25) with $Q$ equal to 142.26 kJ/mol [119]. To increase the sinterability of ZrN powder using HP method, ZrN ceramics doped with Zr or Ti have been investigated at 1500 ~1700 C, and 98% of ZrN with 20 mol% Zr or Ti with a high level of hardness and fracture toughness was achieved with the sintering temperature of 1700 °C [134]. The solid solution of Zr or Ti into ZrN to form non-stoichiometric $ZrN_{1-x}$ or $(Zr,Ti)N_{1-x}$, and the increased nitrogen-vacancy can give rise to the improvement of mass transport process through solid-state diffusion to enhance the densification.

Alexandre et al. [135], studied the influence of powder properties on the sintering behavior, the microstructural development and the mechanical properties of hot isostatically pressed (HIPed) ZrN. > 99% density ZrN pellet was obtained with 1950 °C, 195 MPa and 2 hrs holding time. They show that the densification behavior is dependent on the grain shape and size, and oxygen, carbon, and metallic impurity contents. Finer and more-spherical powder was densified at the lower temperature compared to the powder with large size distribution and particle irregular shape. The mechanical properties of ZrN showed large dependence on the porosity. Tang et al., showed that 99% relative density of ZrN was obtained, which required spherical shape powders and a pre-sintering stage of cold pressing (250 MPa), followed by 2 hours of HIP at a temperature of 1950 ˚C and pressure of 195 MPa [135].

Ryu et al. [136], first used the SPS to densify ZrN as a surrogate for inert matrix fuels in nuclear applications, and fabricated low density of 65% ZrN pellets. The SPS conditions were not clearly stated and had the ranges of 1500 ˚C~1727 ˚C, 30 MPa, 75 ˚C/min, 1 ~ 4 min holding time and vacuum atmosphere. Large powder particle size, low temperature, pressure and holding time can be the possible factors for low density. Muta et al. [126] dramatically decreased the sintering time and showed high Vickers hardness due to the grain size reduction by high heating rates using SPS. They showed that 89.8% relative density of ZrN can be processed at 1800 ˚C and 100MPa for 5 min without any milling process and sintering additive. They also indicated that the impurity layers on particle surfaces can be removed in the SPS process. Tang et al. [137] used 0.5 um sized powder and achieved 95% relative density of ZrN at 1600˚C and 50 MPa for 5min with a heating rate of 100˚C /min. In particular, when they used BN to block the electric current, the grains of ZrN pellets exhibited a loosely bonded interface between the ZrN grains. Otherwise, ZrN pellets without using BN, showed grains tightly stuck together, which possibly indicated the effect of the pulsed magnetic and electric fields during SPS.

## 4.2. Consolidation of ZrN: Comparative Analysis of Various Field Assisted Technologies

### 4.2.1. SPS vs HP

SPS and HP consolidation experiments of ZrN have been carried out under the same pressure and temperature conditions. In order to identify the actual temperature during SPS, an independent experiment has been performed with a thermocouple directly inserted into ZrN powder during SPS. The parameters of the electric current passing through ZrN powder were calculated using a FEM simulation. For finding the densification mechanism of ZrN, the constitutive equations for the hot pressing of powders have been modified to take into account the explicit electric current effect on SPS.

#### 4.2.1.1. Experimental procedures

For all the SPS and HP experiments, ZrN powders (Fm3m) produced by Sigma-Aldrich with an average particle size of 6.71 μm were employed. Detailed properties of ZrN powder was described in section 4.2.2.1.1.

The SPS and graphite die information can be found in section 3.2.1.

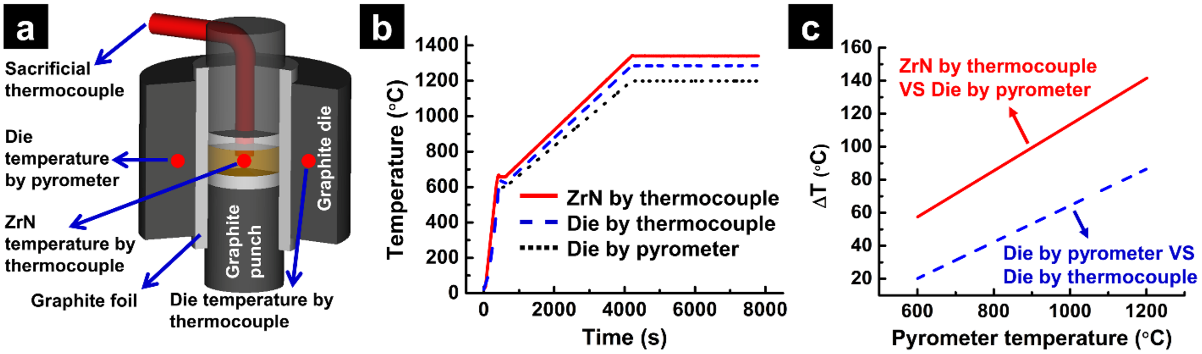

Figure 4.1 (a) Schematics of SPS setup with temperature measurement points, (b) Temperature evolution of different measurement spots, (c) Differences (ΔT) between ZrN temperature measured by thermocouple and die temperature measured by pyrometer, and between die temperature measured by pyrometer and die temperature measured by thermocouple.

Optical pyrometer and k-type thermocouple can measure temperature within the ranges from 570 °C to 3000 °C and from room temperature to 1200°C respectively. However, the pyrometer generally showed non-accurate temperature values compared with those measured by the thermocouple; also it could not be used within the low-temperature range. At the same time, the exact temperature of ZrN powders during SPS should be identified to ensure the correct determination of the densification mechanism. Firstly, the graphite die temperature was measured by an optical pyrometer and a k-type thermocouple at the same time. PID (proportional–integral–

derivative) control of the SPS system was accomplished using the pyrometer aimed at the 2.5 mm deep hole in the die, and, at the same time, another k-type thermocouple detected the die temperature in another hole of the same die which was recorded by the extra thermometer (die temperature by pyrometer and thermocouple in Figure 4.1(a)). Secondly, for obtaining the exact temperature inside the specimen, the sheath protected k-type thermocouple was directly inserted into the powder (ZrN temperature by thermocouple in Figure 4.1(a)) and, at the same time, SPS machine was operated by the temperature of the die hole measured by pyrometer (die temperature by pyrometer in Figure 4.1(a)) [138]. The thermocouple was inserted through a center hole in the upper graphite punch. Another SPS experiment under the same temperature and pressure conditions was conducted without inserting the thermocouple to obtain the densification curve of the powder and thus, without eventual disturbances of the electrical and temperature fields imposed by the thermocouple inserted in the powder.

HP of the powders was carried out by a 1000 kg hot press furnace (Oxy-Gon Industries, Epsom, NH, USA). The heating in HP is transferred by radiation and conduction from the heating element outside of the graphite setup, resulting in more homogenized temperature distribution between the die and powder. Therefore, we assumed that the temperature of ZrN and the graphite die are the same for the HP process.

The measured initial green density of the powder compacts was ~ 58 % for 60 MPa uniaxial pressure in the SPS and HP chambers before starting the sintering. The same heating cycle was used to compare the HP and SPS densification behaviors of ZrN. The experimental conditions and the representative results of the SPS and HP experiments are listed in Table 4.1. All experiments were conducted with purged argon gas.

The relative density was estimated by the Archimedes' immersion method. The fractured or polished specimens were analyzed by the scanning electron microscopy (FEI Quanta 450, USA).

#### 4.2.1.2. Results and discussion

Table 4.1 The experimental conditions and physical properties of ZrN specimens prepared by SPS and HP

| Name | Set T* | T(ZrN)** | Pressure | Holding time | Heating rate | Relative density | Grain size |
|---|---|---|---|---|---|---|---|
| Exp. setup | °C | °C | MPa | min | °C/min | % | μm |
| SPS | 1100 | 1225 | 60 | 60 | 10 | 92.74 | 7.7 |
| SPS | 1200 | 1340 | 60 | 60 | 10 | 96.45 | 11.88 |
| SPS | 1200 | 1340 | 60 | 60 | 100 | 98.05 | 13.69 |
| SPS | 1300 | 1453 | 60 | 60 | 10 | 98.92 | 24.34 |
| SPS | 1500 | 1683 | 60 | 30 | 10 | 99.81 | 36.55 |
| HP | 1200 | 1200 | 60 | 60 | 10 | 80.44 | 7.67 |
| HP | 1500 | 1500 | 60 | 60 | 10 | 98.19 | 21.79 |
| HP | 1900 | 1900 | 60 | 60 | 13 | 99.42 | 59.71 |

*Set T is the maximum programmed temperature at the die hole in the SPS or HP devices

** T(ZrN) is the temperature measured or estimated by inserting the thermocouple into ZrN during SPS

The experimental conditions and physical properties of the ZrN specimens compacted by SPS and HP are listed in Table 4.1. Full density was achieved under both SPS and HP with different maximum temperatures, 1500 °C for SPS and 1900 °C for HP, which means that SPS showed faster densification and lower densification temperature. However, this result may have been caused by the direct Joule heating of the electrically conductive ZrN powder. Also, the densification could have been affected by a possible electric current effect.

The following two experimental factors should be accurately determined for elucidating the electric current effect on the powder densification mechanism: (a) the powder temperature and (b) the electric current density in the powder, located inside of the graphite die during SPS. In addition, one needs (c) a modeling concept for the evaluation of the densification mechanism considering the electric current effect.

#### 4.2.1.2.1. Temperature calibration for SPS

The pyrometer measured the temperature until the final temperature was reached, and the sacrificial k-type thermocouple embedded in ZrN powder was melted and finally broken at 1250 °C. Temperatures > 1250 °C were estimated by the fitting equation based on the calibration experiments (T > 600 °C).

Compared with the die temperature readings from the pyrometer, the die and powders measured by thermocouple showed higher temperatures during the SPS cycle: 1200 °C under 60 MPa and 10 °C/min (Figure 4.1(b)). For example, at 1200 °C, ΔT between ZrN and die is 141 °C (Figure 4.1(c)). The location of the sample in the SPS die set is more favorable to heat accumulation compared with the die surface, which is the heat dissipation area. Ceramic material like alumina also showed similar temperature differences supporting our observations [118]. The concentrated current flow in the center of the powder specimen should increase the direct Joule heating, which can be another factor causing the temperature difference between the die and specimens.

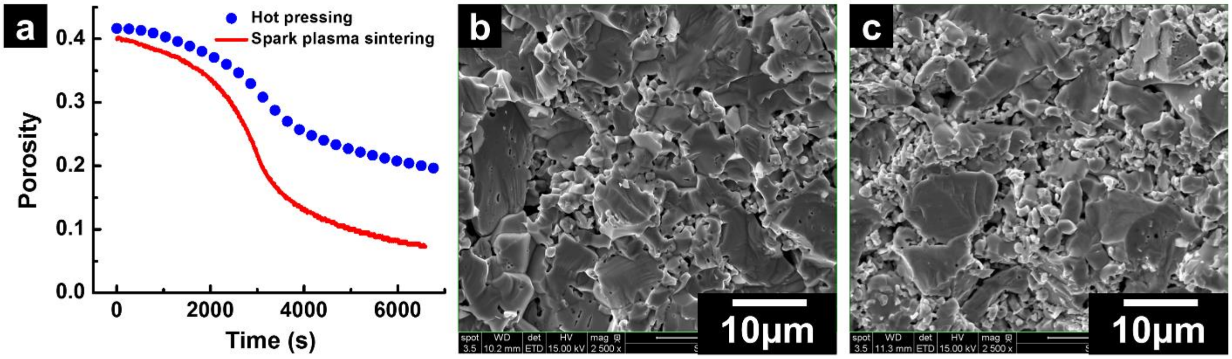

Figure 4.2 (a) Porosity variation of ZrN powder densified (60MPa and 10 °C/min) by SPS (1100 °C) and HP (1200 °C); images of the fractured surface of samples densified by (b) SPS at 1100 °C and (c) HP at 1200 °C.

Figure 4.2 shows porosity evolution during the whole processing cycle for the sintered specimens obtained from the two experiments: SPS at 1100 °C and HP at 1200 °C. Experimental conditions, including heating rate, applied uniaxial pressure, and atmosphere, as well as the amounts of powder utilized per specimen, were the same. For the SPS, the actual ZrN temperature inside of the die at the holding stage is 1225 °C; that was 25 °C higher compared with the HP case (1200 °C). SPS showed faster densification (Figure 4.2(a)) and a more consolidated structure compared with HP (Figure 4.2(b) and (c)). The 25 °C temperature difference is not sufficient to explain the final density difference of 12.30 % between SPS and HP. Therefore, the electric current flowing into ZrN powder during SPS can be a possible factor contributing to the difference in porosity evolution shown in Figure 4.2(a).

#### 4.2.1.2.2. Assessment of the electric current density in the powder specimen’s volume

An electro-thermal model based on the finite element code COMSOL$^{TM}$ has been developed within the framework of the present studies to estimate $I_s$ during SPS. The details of the FEM simulations have been previously described in section 3.2.2.1.

After developing the FEM model, the temperature values measured in the die and inside the powder from the start until the onset of cooling were used to calibrate the ECR and TCR at the ZrN-graphite interfaces.

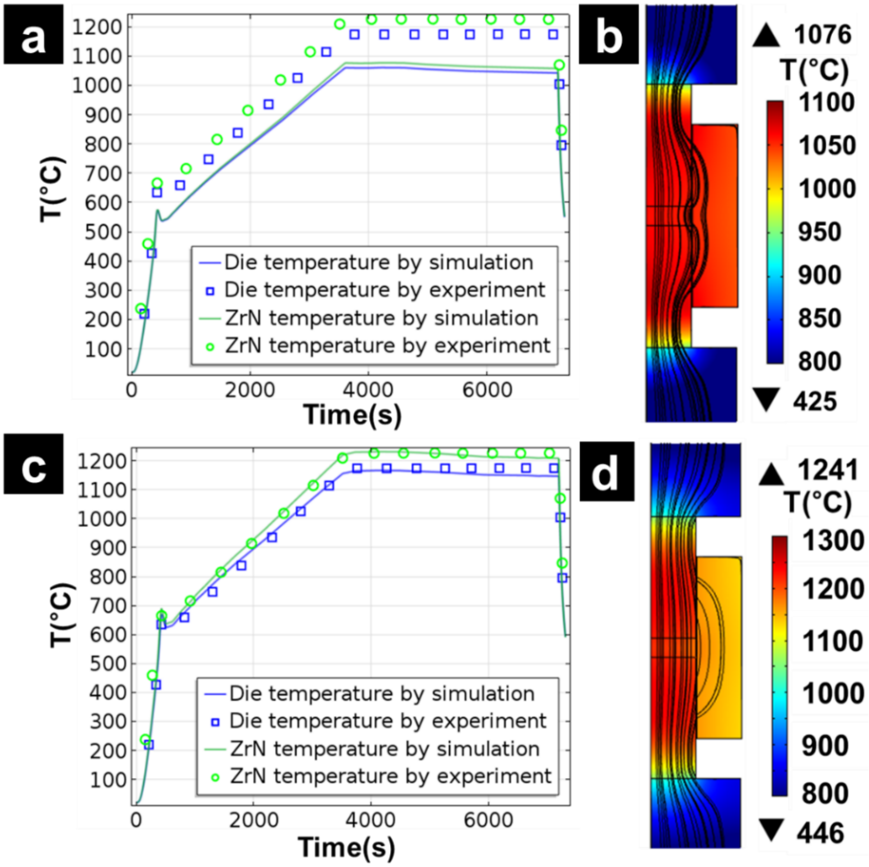

Figure 4.3 Experimentally measured and FEM-simulated temperatures of ZrN powder and graphite die during SPS (a) without contact resistance, (c) with electrical and thermal contact resistance. FEM simulation map of the temperature and electric current flow at the end of the holding time (b) without contact resistance, (d) with electrical and thermal contact resistance.

The vertical and horizontal contact resistances were disregarded in previous studies [139, 140]. However, the vertical contact resistance has an important impact on the magnitude of the fraction of the electric current passing through the conductive powder. Without the consideration of the vertical ECR and TCR, the simulated temperatures for the die and sample during the holding stage are 138 °C and 172 °C lower than the experimentally measured temperatures (Figure 4.3(a)), which means that the ECR- and TCR-related heat dissipation should be considered. Also, the major fraction of the electric current appears to flow through the die (Figure 4.3(b)).

As shown in Figure 4.3(c), the results of the modeling considering the vertical ECR and TCR and their calibration are close to the experimentally measured and simulated temperatures. The calibrated ECR and TCR equations are shown in the (4.1) below. The electric current from the top punch was split, and the high portion of electric current passed through the powder during the holding stage (Figure 4.3(d)). Also, a non-homogenous temperature distribution between the die and the central column of the tooling set (punches and powder) was observed due to the presence of the contact resistance (Figure 4.3(d)).

$$ECR_{ZrN/graphite} = ((-5.70 * 10^{-3} * (T - 273) + 18.6) * (-7.90 * 10^{-3}P + 1.14) * (1.00 * 10^{-7})) * 0.3\ (Ohm \cdot m^2)$$
$$TCR_{ZrN/graphite} = 1.50 * 10^{-4}/(162 - 0.179T + 1.07 * 10^{-4}T^2 - 2.43 * 10^{-8}T^3)\ (K \cdot m^2/W)$$

(4. 1)

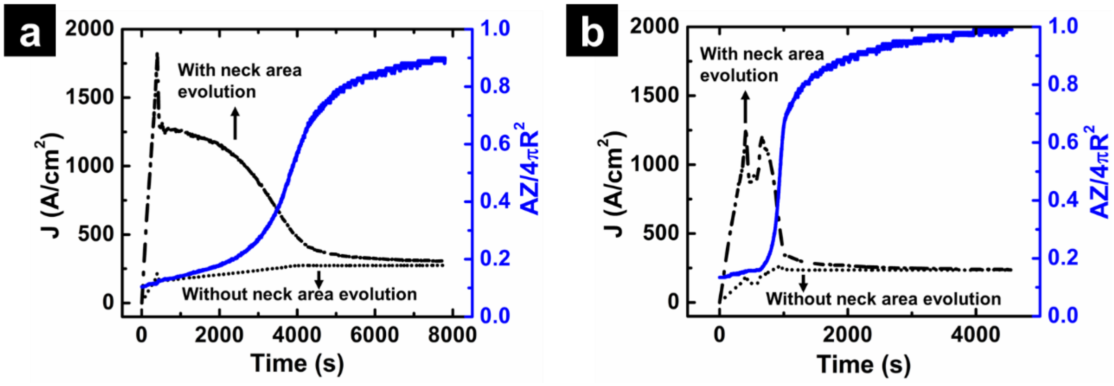

Figure 4.4 Current density evolution with (black dash-dot line) and without (black dot line) consideration of the neck area change during the whole SPS cycle. Neck area evolution is shown with respect to the right y-axis (blue solid line). (a) SPS, 1200 °C, 60MPa and 10 °C/min and (b) SPS, 1200 °C, 60MPa and 100 °C/min.

Parameter OLECD which was described in section 3.1.4. was calculated during the SPS process of ZrN. Compared with 3 modes experiment which uses the same heating rate (100 °C/min) in chapter 3, the sum of the OLECD dependence on the heating rate (10 °C/min vs 100 °C/min) was analyzed. Figure 4.4 shows the electric current density change during SPS experiments for (a) 1200 °C, 60 MPa and 10 °C/min and (b) 1200 °C, 60 MPa and 100 °C/min. The black line represents the electric current density evolution with (dash-dot line) and without (dot line) consideration of the neck area change. The blue solid line represents $AZ/4\pi R^2$ . For all the conducted SPS experiments, the temperature stabilization steps during SPS runs include the ramping from room temperature to 580 °C for 6 min (93 °C/min), ramping from 580 °C to 600 °C for 1 min, and soaking at 600 °C for 3 min. After these steps, the ramping to the maximum temperature at 10 °C/min or 100 °C/min and holding step is used.

The low heating rate SPS showed the highest OLECD peak with the overheating around 580 °C and decreased OLECD during ramping to the maximum temperature and holding stage (black dash-dot line in Figure 4.4(a)). Higher heating rate SPS showed two high OLECD peaks at 580 °C and 1200 °C due to overheating at the end of the ramping stage (Figure 4.4(b)). Especially, the integral of OLECD (area under the black solid line) is small for high heating rate SPS, which implicates that overall electric current effects can be small.

#### 4.2.1.2.3. Sintering "trajectory"

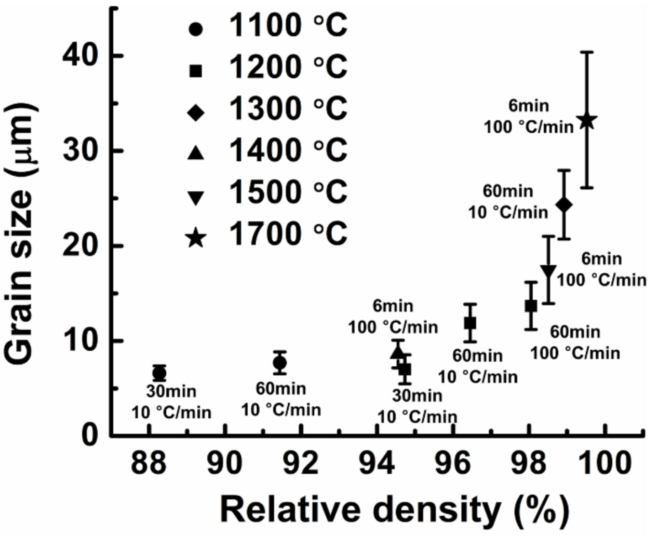

Figure 4.5 Grain size as a function of the relative density of ZrN powder pellets obtained by SPS under 60 MPa.

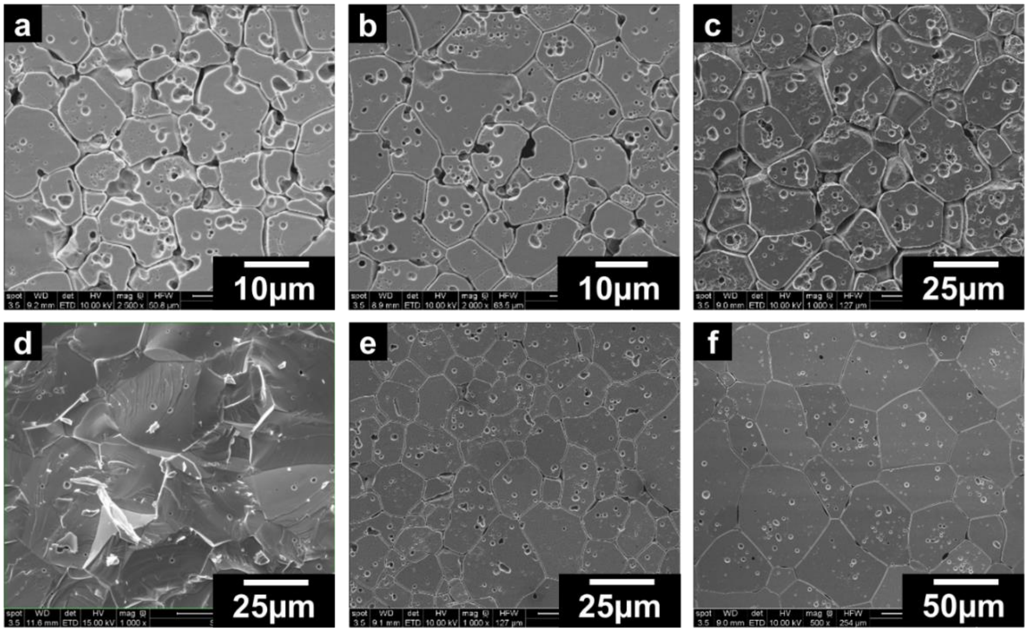

Figure 4.6 SEM images of ZrN samples (a) SPS under 1200 °C, 10 °C/min and 60 min, (b) SPS under 1200 °C, 100 °C/min and 60 min, (c) SPS under 1300 °C, 10 °C/min and 60 min, (d) SPS under 1500 °C, 10 °C/min and 30 min, (e) HP under 1500 °C, 10 °C/min and 60 min, (f) SPS under 1900 °C, 10 °C/min and 60 min. 60 MPa is used for all the experiments.

Grain growth can affect the densification behavior of a powder during sintering [46, 55]. Figure 4.5 shows the variation of the grain size as a function of relative density for the different heating rates, holding temperatures and times (data are also taken from the previous ZrN SPS consolidation studies [26]). The SEM images of the polished or fractured ZrN specimens are shown in Figure 4.1 and Figure 4.6. Densification is favored when no grain growth is present until the relative density value of ~ 92% is achieved and when the grain size is ~ 7 μm, similar to the average size of the raw powder particles. Thus, when the relative density is less than ~ 92 %, p = 0 in (3.1), (3.10) and (3.20).

#### 4.2.1.2.4. Densification mechanism of ZrN consolidated with and without electric current effect

If it is assumed that $G$, $A_{cr}$, $D_0$, and $m$ are the same for different temperatures ($T_1$ and $T_2$), $Q$ can be obtained by:

$$Q = \frac{R\ln\left[ (\frac{\dot{\theta}_{T_1}}{\dot{\theta}_{T_2}}\frac{T_1}{T_2})/(\frac{d_2}{d_1})^p \right]}{\left[ \frac{1}{T_2} - \frac{1}{T_1} \right]} \text{ [kJ/mol]} \qquad (4.2)$$

To confirm the HP results from Petrykina and Shvedova [119], the range of the parameters $m$ *and* $Q$ were also calculated by (3.30) and (4.2) respectively.

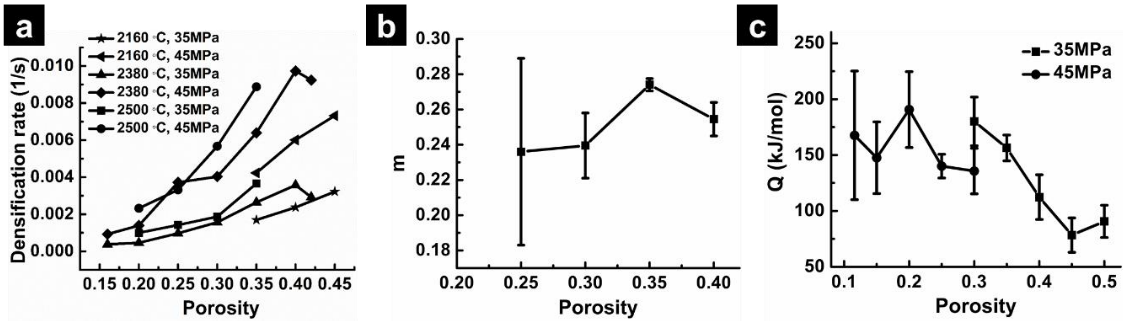

Figure 4.7 (a) Densification rate of ZrN powders as a function of porosity with various hot pressing conditions, (b) *m* values and (c) activation energy variation with porosity. ZrN porosity evolution with time was obtained from the literature data for hot pressing [119].

The porosity evolution data for ZrN consolidated by HP obtained by Petrykina and Shvedova [119] were used. By substituting *T*, *P* and densification rate (Figure 4.7(a)) into (3.30) and (4.2), the holding stage average *m* and *Q* were found to be 0.26 and 137.41 kJ/mol (35 MPa) and 153.95 kJ/mol (45 MPa) as shown in Figures 4.7(b) and (c). Petrykina and Shvedova stated that the densification mechanism of ZrN for HP is a dislocation-climb controlled creep (*m* = 0.2 - 0.25) with *Q* equal to 142.26 kJ/mol. Therefore *m* and *Q* values determined using the previous method agree well with the results from Petrykina and Shvedova [119].

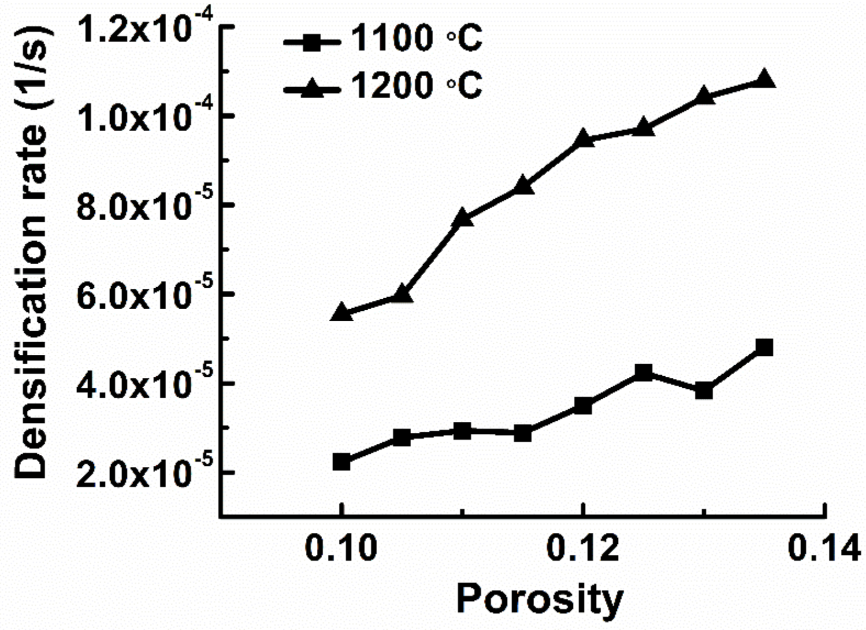

Figure 4.8 Densification rate of ZrN powders subjected to SPS at 1100 °C and 1200 °C.

For ZrN compaction using SPS, $Q$ was estimated using (4.2) similarly to the HP case. Values of $Q$ calculated based on the results of the SPS conducted under different temperatures are shown in Figure 4.8 and have an average of 173.48 kJ/mol, which is the similar range to the constitutive equation fitting results described in the following section.

Table 4.2 Summary of the fitting parameters for hot pressing and spark plasma sintering of ZrN. R$^2$ is the correlation coefficient.

|  | Fitting equation | m | Q (kJ/mol) | A$_0$ (Pa·s/K) | $\int J_{OL}$ (A/cm$^2$) | A$_{TD}$ (1/s) | A$_{ECAD}$ (1/s) | R$^2$ |
|---|---|---|---|---|---|---|---|---|
| HP, 1200 °C and 10 °C/min | (3.10) | 0.23 - 0.24 | 114.25 - 220.73 | 1.35x10$^{-10}$ – 4.13x10$^{-7}$ | - | 1.59x10$^{10}$ - 2.31x10$^{10}$ | - | 0.9997 |
| SPS, 1100 °C and 10 °C/min | (3.10) | 0.33 | 109.12 – 207.04 | 3.83x10$^{-7}$ – 4.37x10$^{-3}$ | 4.47x10$^{6}$ | 1.67x10$^{7}$ | - | 0.9994 |
|  | (3.20) | 0.24 | 114.25 | 4.13x10$^{-7}$ |  | 2.69x10$^{10}$ | 2.80x10$^{11}$ - 4.16x10$^{11}$ | 0.9942 |
| SPS, 1200 °C and 10 °C/min | (3.10) | 0.35 – 0.36 | 132.38 – 195.01 | 8.92x10$^{-6}$ – 5.41x10$^{-3}$ | 5.36x10$^{6}$ | 4.72x10$^{6}$ - 5.05x10$^{6}$ | - | 0.9984 - 0.9985 |
|  | (3.20) | 0.24 | 114.25 | 4.13x10$^{-7}$ |  | 4.76x10$^{10}$ | 1.08x10$^{12}$ - 1.20x10$^{12}$ | 0.9943 |

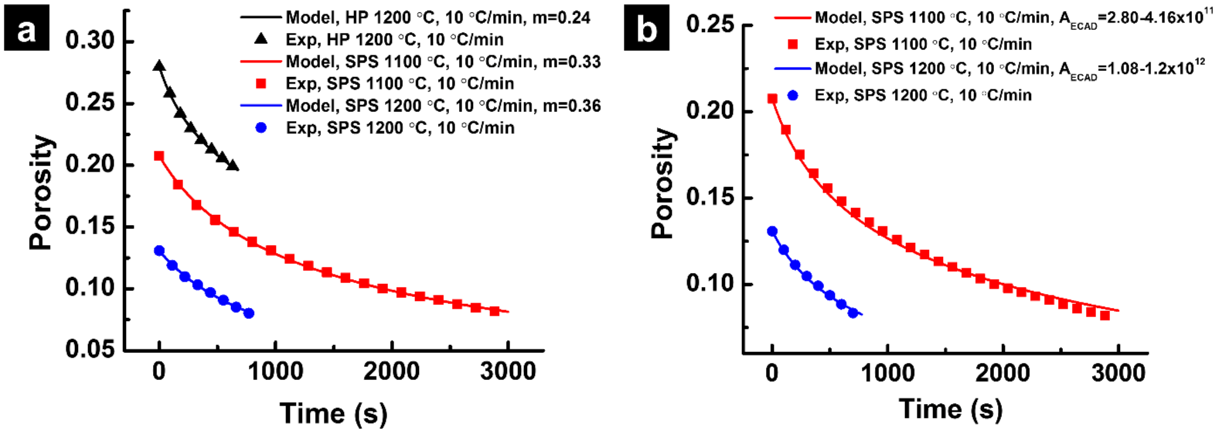

Figure 4.9 (a) Experimental porosity evolution curves of ZrN specimens processed by HP or SPS fitted by (3.10), (b) experimental porosity evolution curves of ZrN specimens processed by SPS fitted by (3.20). Applied compaction pressure was a 60 MPa. Detailed fitting parameters are shown in Table 4.2.

When fitting (3.10) (constitutive equation of HP) into experimental porosity evolution data from HP and SPS, if the *m* value from SPS is not the same as during HP, then these results indicate that the densification mechanism is affected by electric current effects.

Table 4.2 summarizes the range of the obtained fitting parameters (*m*, *Q*, and $A_0$) and the correlation parameter ($R^2$), using the constitutive equation fitting (3.10) into the experimental porosity time evolution curve during holding stages of HP and SPS. Figure 4.6(a) shows the representative fitting results. The experimental densification curves were drawn by the scattered symbols, while the curves defined by a solid line denote the fitting curve.

HP results showed *m* = 0.23 - 0.24 and *Q* = 114.25 - 220.73 kJ/mol, and SPS rendered *m* = 0.33 – 0.36 and *Q* = 109.2 – 207.04 kJ/mol (Table 4.2). The obtained *m* and *Q* in the HP study indicate that ZrN consolidation using HP is based on the dislocation climb controlled creep mechanism which agrees with results from Petrykina and Shvedova [119]. In contrast, *m* and *Q* values for SPS show that the densification mechanism is close to the glide controlled creep (*m* =

0.33). Creep deformation of ZrN during HP is controlled by the climb of dislocations over physical obstacles in the glide/climb sequential mechanism [88]. The electric current effect such as localized heating at defects and defects generation may facilitate the diffusion of the number of barriers encountered by a mobile dislocation, which assists the removal of the obstacle [141]. Also, a mobile dislocation that obtains energy from local Joule heating or an elastic field effect from vacancies generated by an electric current, can overcome obstacles more easily. The bulk vacancy concentration is important for the climb controlled creep [142]. Vacancy formation by local Joule heating can promote the dislocation climb. As a result, the overall rate-limiting step of ZrN powder deformation during SPS can be transferred from the climb controlled to the dislocation glide controlled mechanism.

Alternatively, some previous studies showed that the densification mechanism is not changed by the electric current effect as explained in the section 3.1.2 [51-53]. Therefore, we assume that the creep parameters ($A_0$, $m$, and $Q$) are the same for both HP and SPS, and verify whether the electric current term in (3.20) can fit the experimentally observed porosity evolution corresponding to the SPS results.

Figure 4.9(b) represents the best fitting results of the constitutive equation (3.20) taking into account the electric current effect based on the SPS experimental results and using the same values of $m$, $Q$, *and* $A_0$ as those found for HP. We use OLECD (section 4.2.1.2.2), the temperature dependent $\lambda$ and $G$ of ZrN for the fitting. We found the best values of ω and $\beta$ rendering a good agreement with the porosity evolution experimentally determined during SPS.

One can see from Table. 4.2 that, due to the similar ZrN temperature for HP (1200 °C) and SPS (1100 °C), parameter $A_{TD}$ is in the same range for both HP and SPS. That is why it is parameter

$A_{ECAD}$, related to the electric current effect, which accelerates the densification during SPS compared with HP case. In SPS, higher temperature is obtained by applying higher electric current to the sample and the graphite die, which causes higher values of parameters $\int J_{OL}$ , $A_{TD}$ and $A_{ECAD}$ corresponding to SPS (1200 °C) case compared to SPS (1100 °C) case.

Due to the narrow density range during the holding stage under 92 % relative density, we cannot evaluate the densification mechanism of ZrN for the fast heating rate SPS (1200 °C and 100 °C/min) case. However, the smaller $\int J_{OL}$ value for the fast heating rate SPS (100 °C/min) compared to that of the slow heating rate SPS (10 °C/min), as shown in Figure 4.4, may indicate that the densification mechanism of ZrN is not changed.

Therefore, the conducted experiments point out that the electric current affects the densification behavior of ZrN powder, which can be related to the current influence on the dislocation motion (electroplasticity phenomena). From the constitutive equations' fitting results, two conclusions can be derived. The accelerated dislocation mobility by electric current can change the densification mechanism (Figure 4.9(a)). In contrast, the dislocation motion mechanism for ZrN is not changed (dislocation climb controlled creep), but the electric current can affect other parameters to assist the dislocation motion during SPS (Figure 4.9 (b)).

### 4.2.2. SPS vs high voltage electric discharge consolidation (HVEDC)

In previous results, it was shown that electric current enhances the densification kinetics by either shifting the densification mechanism itself or changing the other creep parameters. Therefore, the comparison of densification behavior and microstructure between SPS and HVEDC is desired.

During HVEDC (developed in Moscow Engineering Physics Institute in Russia), a single pulse of electric current flows through the source powder, leading to an ultra-intense energy release inside the powder volume, which is sufficient to allow consolidation up to high-density levels for a variety of materials. The high-voltage discharge (up to 30 kV), obtained by a capacitor bank and released with an extremely short pulse (the pulse length increases with the applied voltage: 500 ~ 1300 μs for 1.5 ~ 5 kV), creates a significant current density passing through a powder compact, while an external pressure is being applied. As a result, an ultra-rapid temperature increase is attained at the contact points between powder particles and almost instantaneous micro-welding occurs during the electric discharge. Because of such short sintering times, densification is accompanied only by minimal changes in the microstructure, a factor of merit when aiming at achieving high mechanical strength characteristics.

In the present study, the sinterability and final mechanical properties of the two commercial ZrN powders processed through the two different field-assisted sintering methods (SPS and HVEDC) have been tested and compared. With fixed holding time and heating rate, a systematic densification map of SPS ZrN was built. Also, the influence of high pressure by double die SPS setup was evaluated. A constitutive model of powder hot pressing (3.10) was subsequently applied to the obtained experimental results for the description of the densification kinetics during both SPS and HVEDC.

### 4.2.2.1. Experimental procedures

#### 4.2.2.1.1. Materials investigated

Two ZrN powders were employed for this study, one produced by Sigma Aldrich (SA) and the other by Alfa Aesar (AA). The main powder utilized for the consolidation by both SPS and HVEDC was AA, while SA was utilized for the SPS processing only, in order to compare the behavior of slightly different materials when undergoing this type of electric field-assisted technology. The powder data are reported in Table 4.3.

Table 4.3 ZrN powders' characteristics.

| Name | SA* | AA** |
|---|---|---|
| Vendor | Sigma Aldrich | Alfa Aesar |
| Lot # | BCBC1256V | L27X042 |
| Purity | ≥99% (trace metals basis) | 99.5% (metal basis excluding Hf), Hf<3% |
| Size | Particle size: 6.71± 0.5μm | Particle size: 6.02± 0.42μm |
| Melting temperature (˚C) | 2980 | 2980 |
| Composition | $ZrN_{0.86}O_{0.18}$ | $ZrN_{0.87}O_{0.28}Hf_{0.01}$ |

* Sintered by spark plasma sintering

** Sintered by spark plasma sintering and high voltage electric discharge consolidation

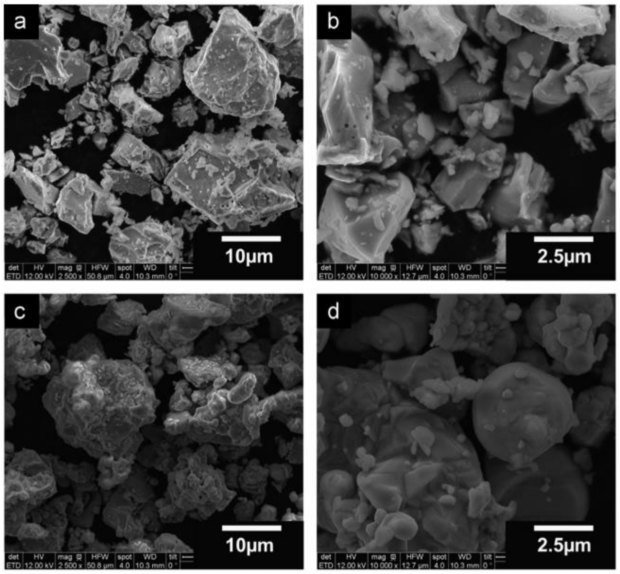

Figure 4.10 As-received ZrN powders, (a),(b) SA and (c),(d) AA powders.

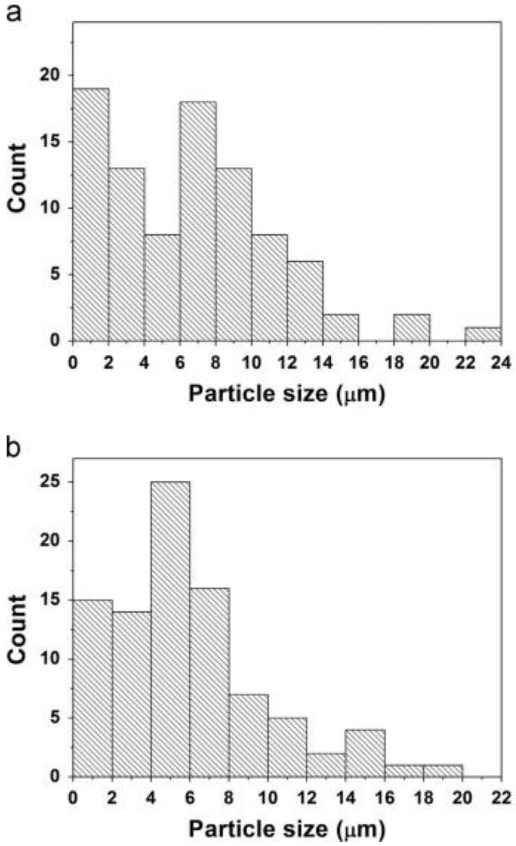

Figure 4.11 Particle size distribution of ZrN powders, (a) SA and (b) AA powders.

As shown in Figure 4.10, the SA powder particles show sharp edges and the absence of agglomeration, while the AA powders are well-rounded, almost spherical particles with a tendency to form agglomerates. The particle size was derived by manual measurements of 90 particles for each powder, resulting in an average value of 6.71 ± 0.5 µm for SA and 6.02 ± 0.42 µm for AA, as shown in Figure 4.11.

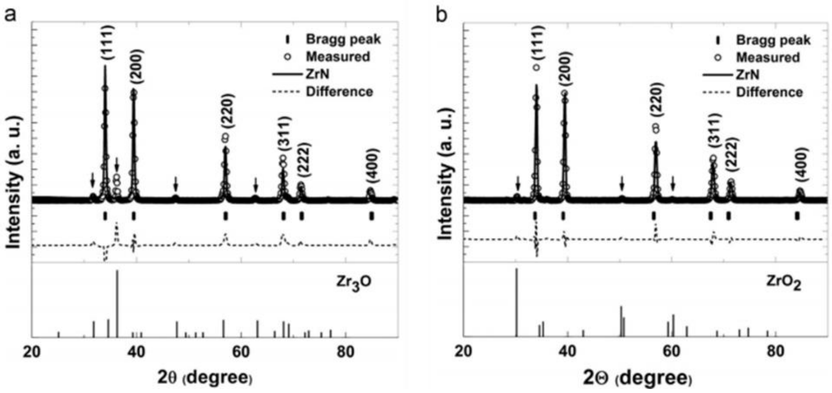

Figure 4.12 X-ray diffraction results of SA (a) and AA powders (b), arrows indicate the oxide impurity positions. $Zr_3O$ (a) and $ZrO_2$ (b) peak location and relative intensity were shown at the bottom of each plot.

The crystal structure and lattice parameters were evaluated by X-ray diffraction (XRD) (Bruker D-8 diffractometer, MA, USA), utilizing $CuK_\alpha$ radiation at room temperature. In Figure 4.12, measured and reference ZrN (ICSD collection code # 167851) [143] XRD plot is represented by hollow circles and solid line, respectively. Also, the dashed line shows the intensity difference between the measured and reference peak. Diffracted (h,k,l) planes are shown on the top of each peak. From the XRD data, in Figure 4.12, the cubic NaCl-type structure dominates, however oxide impurities were found in both powders. Comparing these results with the zirconium oxide peak locations shown in Figure 4.12 (a) and (b), the SA powder has oxide in the $Zr_3O$ form (ICSD Collection code # 88320) [144], while AA includes $ZrO_2$ (ICSD Collection code # 66781) [145].

The lattice parameter for the two powders was found to be 0.4563 nm, a value close to the one reported in the literature (0.457 nm) [143].

Table 4.4 Energy-dispersive X-ray spectroscopy results for SA and AA powders.

| Element | Shell | SA | AA |
|---|---|---|---|
| N | K | 42.26% | 40.19% |
| O | K | 8.72% | 13.03% |
| Zr | L | 49.02% | 46.26% |
| Hf | M | 0% | 0.53% |

From the energy-dispersive X-ray spectroscopy (EDS) (Oxford Instruments, UK) analysis as shown in Table 4.4, a different oxygen content was detected between the two powders: 8.72% for SA and 13.03% for AA, even though the two powders have almost analogous non-stoichiometric compositions, *i.e.* $ZrN_{0.86}$ and $ZrN_{0.87}$, respectively, when atomic % of each powder by the EDS converts to the composition of that. AA also showed the presence of hafnium in amount < 3%.

#### 4.2.2.1.2. SPS processing regimes

Two different pressure conditions were selected. For low-pressure (< 90 MPa) experiments, 3.76 g of powder was placed into a 15.4 mm-diameter graphite die and compressed between two 20 mm-long graphite punches. For the high-pressure (> 90 MPa) experiments, a double die setup was used [146]. In this case, the tooling additionally had an internal 7 mm-diameter graphite die and two SiC 7 mm-high punches. This double die setup contained 0.82 g of powder. Schematics of used double die setup can be found elsewhere [147].

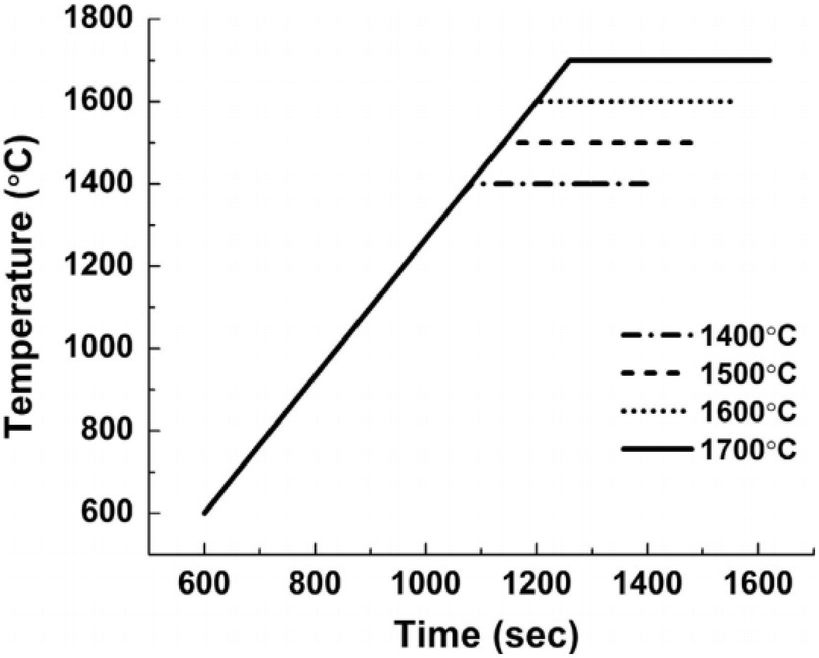

Figure 4.13 Temperature regime for the consolidation of ZrN (SA) powders by spark plasma sintering.

For the SA powders, the measured green densities of the powder compacts were ~ 57%, 59%, and 66%, for the pre-SPS cold compaction at 30 MPa, 60 MPa and 120 MPa, respectively. The sintering regime consisted of heating at 100˚C/min from room temperature to the maximum temperature (1400, 1500, 1600 or 1700˚C) with a dwell time of 6 min as represented in Figure 4.13.

For the AA powders, the measured green densities of the powder compacts were ~ 47%, 62%, 63% and 64%, for the pre-SPS cold compaction at 20 MPa, 120 MPa, 150 MPa and 180 MPa, respectively. The maximum sintering temperature was set at 1700˚C. A broader range of pressures, compared to the processing conditions of SA powder, was applied to AA powder: 0, 20, 120, 150 and 180 MPa, while the other experimental conditions were analogous. For the free pressure-less SPS a cold compaction step with a 50 MPa load was applied, reaching the green density of 49%.

For the control experiment of high-pressure SPS, three SiC punches were inserted, instead of the conventional two, because the total length of the two SiC punches used with the powders was smaller than the overall axial dimension of the die.

For both SA and AA powders, the selected pressure was applied during the entire process and was concluded within 30 minutes. The SPS machine provided a periodic sequence of 12 ms of DC pulses followed by a pause of 2 ms during the whole process. All the experiments were conducted under ~20 Pa atmospheric pressure.

Once the SPS process was complete, the densified specimens were extracted from the graphite die, ground by a 75 µm diamond disk and subsequently by a series of progressively finer SiC grinding papers (36 µm, 21.8 µm and 15.3 µm). To remove the carbon paper residuals from the specimen surface the samples were dried in an oven at 120˚C for 20 min.

#### 4.2.2.1.3. HVEDC processing regimes

As for the materials employed, the information relative to powder AA given in section 4.2.2.1.1 is valid in this case too and will not be reiterated.

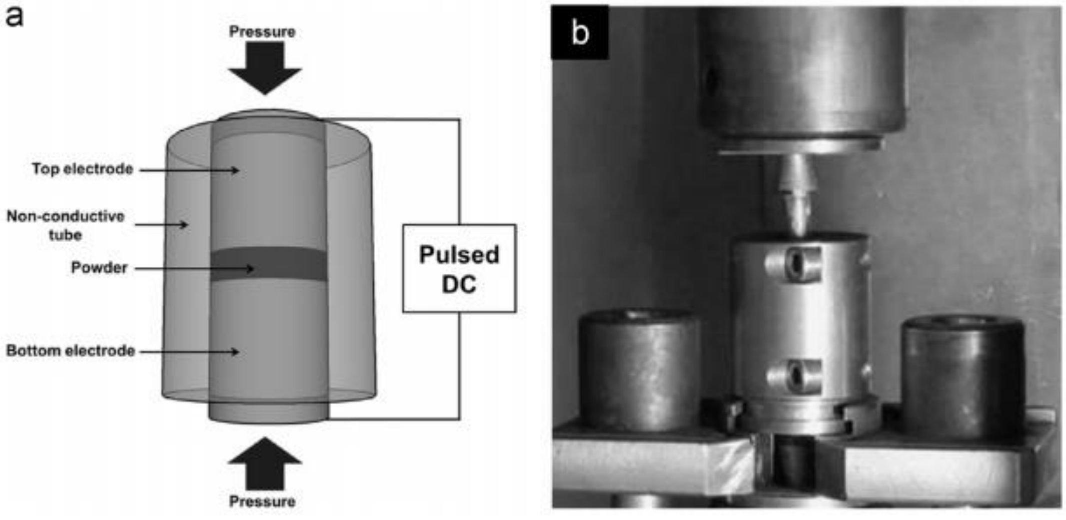

Figure 4.14 (a) Schematic representation of the high voltage electric discharge consolidation process, (b) high voltage electric discharge consolidation machine before an experiment [4].

The schematics of the apparatus for HVEDC (Impulse-BM, Russia) and a photograph of this setup are shown in Figure 4.14 [4]. The overall system consists of the energy storage unit, switch-board, pressure and temperature measurement systems, electric current parameters' recording system and powder material sealing registration system. The energy storage unit includes a capacitor bank with a stored energy of 75 kJ, which provides an intense energy discharge to the powder compact and the charging unit. The apparatus uses a pulsed current generated by the capacitor bank, for rapid processing of the powder under constant pressure during the whole process.

Table 4.5 Green density of AA specimens after applying the pressure for the high voltage electric discharge consolidation

| **Pressure (MPa)** | 75 | 100 | 125 | 150 | 175 | 200 | 225 | 250 | 275 | 300 |
|---|---|---|---|---|---|---|---|---|---|---|
| **Green relative density (%)** | 53.5 | 54.5 | 56 | 57 | 58 | 59 | 60.5 | 60.5 | 61 | 61 |

The tooling setup employed in the HVEDC procedures consisted of a mold and two molybdenum punches. The mold was a metal cage fixed to an insulating mullite liner with an inner diameter of 10 mm and an outer diameter of 20 mm. The consolidation of the powders was conducted at pressures of 75 MPa to 300 MPa and at a voltage of 2 kV to 4 kV. Measured green densities after applying the pre-sintering pressure ranged from 53.5% to 61.0% under pressures of 75 MPa to 300 MPa, respectively, as shown in Table 4.5.

#### 4.2.2.2. Processed specimen characterization results

Final density was evaluated, together with the role of temperature and pressure on consolidation, and the influence of porosity on the mechanical and morphological characteristics of the sintered material. The employed technologies and methodologies involved various density measurement techniques, imaging by SEM, analysis by EDS, and hardness obtained from Vickers micro-hardness testing. All measurements were taken at room temperature.

#### 4.2.2.2.1. Characterization of specimens processed by SPS

##### 4.2.2.2.1.1. Sigma Aldrich powders

All the sintered specimens were fractured or etched and characterized by SEM and EDS. The high-quality surface was obtained by etching for a few seconds in a solution containing concentrated HF, Aqueous (49%) / $HNO_3$, Aqueous (70%) / $H_2O_2$, Aqueous (30%) with a ratio of 4.5:4.5:1 respectively [148].

Vickers micro-hardness tests were performed at room temperature by applying a 1 kg load on the standard diamond indenter (M-401-H1 Hardness testing machine, Leco, Michigan). A total of 12 indents per specimen from edge to center over the sample cross-section were realized and their diagonal was measured using an optical microscope, so that the Vickers micro-hardness could be calculated as follows:

$$HV = 1.854\frac{F}{D^2} \tag{4.3}$$

in which F is the load (kgf) and D is the arithmetic mean of the two diagonals (mm).

Table 4.6 Physical, chemical and mechanical properties of ZrN (SA and AA) specimens prepared by spark plasma sintering

| Specimen | Sintering temperature (˚C) | Sintering pressure (MPa) | Relative density (%, Archimedes ) | Grain Size (μm) | HV1 ($kgf/mm^2$) | Composition (Atom %) |
|---|---|---|---|---|---|---|
| SA1403 | 1400 | 30 | 89.73 | 6.99 | 959.59 | $ZrN_{0.76}O_{0.10}$ |
| SA1503 | 1500 | 30 | 93.18 | 12.47 | 1234.02 | $ZrN_{0.87}O_{0.11}$ |
| SA1603 | 1600 | 30 | 95.36 | 17.59 | 1435.89 | $ZrN_{1.03}O_{0.13}$ |
| SA1703 | 1700 | 30 | 98.34 | 32.70 | 1413.85 | $ZrN_{0.88}O_{0.10}$ |
| SA1406 | 1400 | 60 | 94.55 | 8.62 | 1249.33 | $ZrN_{0.93}O_{0.11}$ |
| SA1506 | 1500 | 60 | 98.51 | 17.47 | 1561.46 | $ZrN_{0.94}O_{0.10}$ |
| SA1606 | 1600 | 60 | 98.94 | 24.67 | 1507.16 | $ZrN_{0.90}O_{0.10}$ |
| SA1706 | 1700 | 60 | 99.52 | 33.26 | 1528.58 | $ZrN_{0.88}O_{0.10}$ |
| SA1412 | 1400 | 120 | 96.22 | 9.14 | 1419.09 | $ZrN_{1.21}O_{0.14}$ |
| SA1512 | 1500 | 120 | 97.90 | 16.71 | 1473.06 | $ZrN_{0.81}O_{0.10}$ |
| SA1612 | 1600 | 120 | 99.12 | 24.09 | 1480.54 | $ZrN_{1.15}O_{0.13}$ |
| SA1712 | 1700 | 120 | 98.12 | 22.79 | 1498.11 | $ZrN_{0.89}O_{0.10}$ |
| AA1700 | 1700 | 0 | 54.07 | - | - | - |
| AA1702 | 1700 | 20 | 75.58 | 3.61 | 546.30 | $ZrN_{0.82}O_{0.17}Hf_{0.01}$ |
| AA1712 | 1700 | 120 | 93.19 | 3.77 | 1183.6 | $ZrN_{0.90}O_{0.36}Hf_{0.01}$ |
| AA1715 | 1700 | 150 | 96.95 | 5.99 | 1446.71 | $ZrN_{1.06}O_{0.37}Hf_{0.01}$ |
| AA1718 | 1700 | 180 | 97.42 | 6.30 | 1422.46 | $ZrN_{1.16}O_{0.31}Hf_{0.02}$ |

The physical and mechanical properties of the specimens are listed in Table 4.6, showing that the highest values of relative density (~100%) were achieved with the SA powder at 1700˚C under 120 MPa.

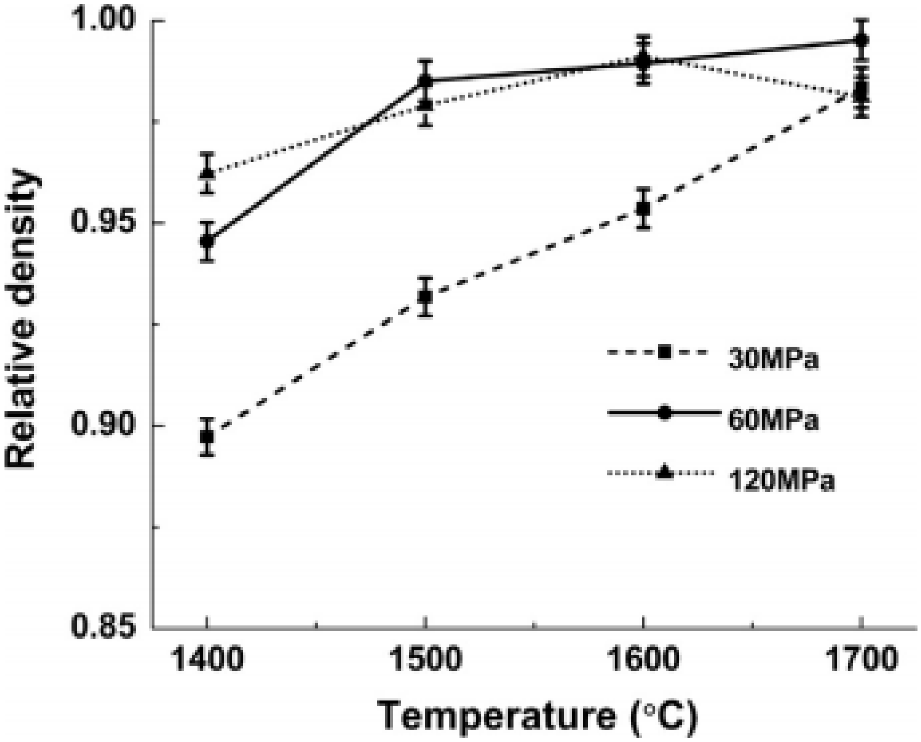

Figure 4.15 Relative density plot of ZrN (SA) specimens prepared by spark plasma sintering measured by Archimedes immersion method.

The final relative densities of these samples are reported in Figure 4.15. For a fixed value of pressure, relative density is increased with increasing maximum final temperature with the only exception of the 1700 °C /120 MPa case (explained below). For the temperature and pressure ranges used in this study, these are the highest relative density values attained with a commercial powder. It is worth noting that the powders were not milled and sintering agents were not used. Such relative density values are significantly higher than the 63.5 % we obtained by means of high-temperature vertical dilatometer (Unitherm 1161, Anter corporation, USA), with a maximum sintering temperature of 1500 ˚C, a heating rate of 10 ˚C /min and 2-hours holding time.

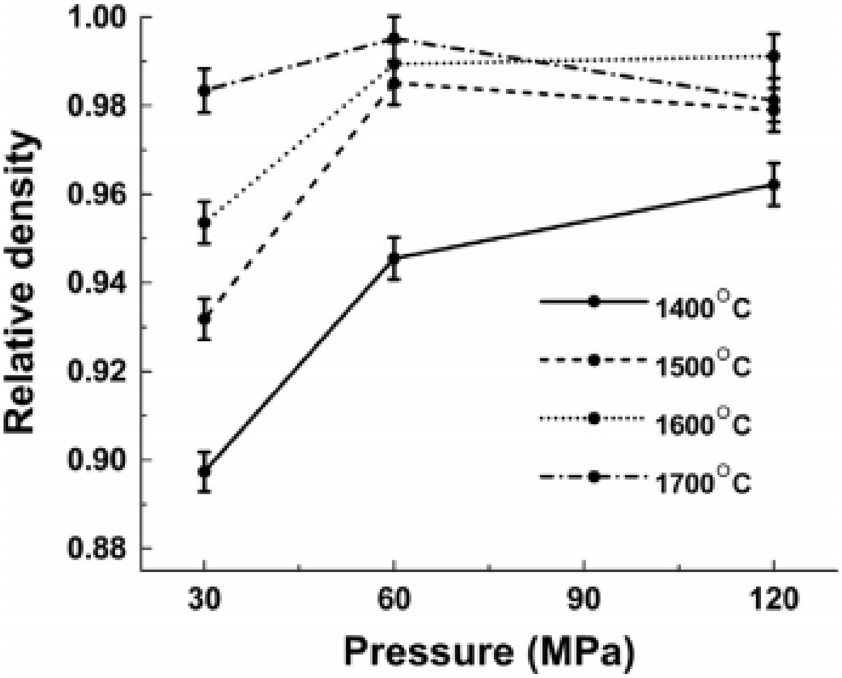

Figure 4.16 Effect of the pressure on the final relative density of SPSed ZrN (SA) specimens sintered at different temperatures.

One of the main influencing factors during SPS is pressure, whose significant role in powders has been widely investigated [1, 12, 146]. Quach *et al*. [146] pointed out in yttria-stabilized $ZrO_2$ that pressure prevails diffusional mechanisms at low temperatures, while this trend tends to be less effective once higher temperatures are reached. Analogous conclusions were reached in the present investigation. Figure 4.16 plots relative density as a function of temperature. Densification is significantly enhanced when increasing pressure from 30 MPa to 60 MPa at relatively low temperatures (1400°C and 1500˚C). However, a further increase of pressure up to 120 MPa did not appear to have a noticeable influence on the relative density. A slightly lower final density was observed for 1500°C and 1700°C when increasing pressure from 60MPa to

120MPa. Including previous relative density result of 1700 °C/120 MPa in Figure 4.16, such small decrease could be attributed to measurement errors in the Archimedes' method or to a discrepancy in the application of a high pressure (in this case, 120 MPa) when using SiC punches instead of the graphite components employed for the low-pressure cases. The SiC punches present lower thermal and electrical conductivity compared with those of graphite, which results in slow heat transfer to specimens compared with regular graphite punches.

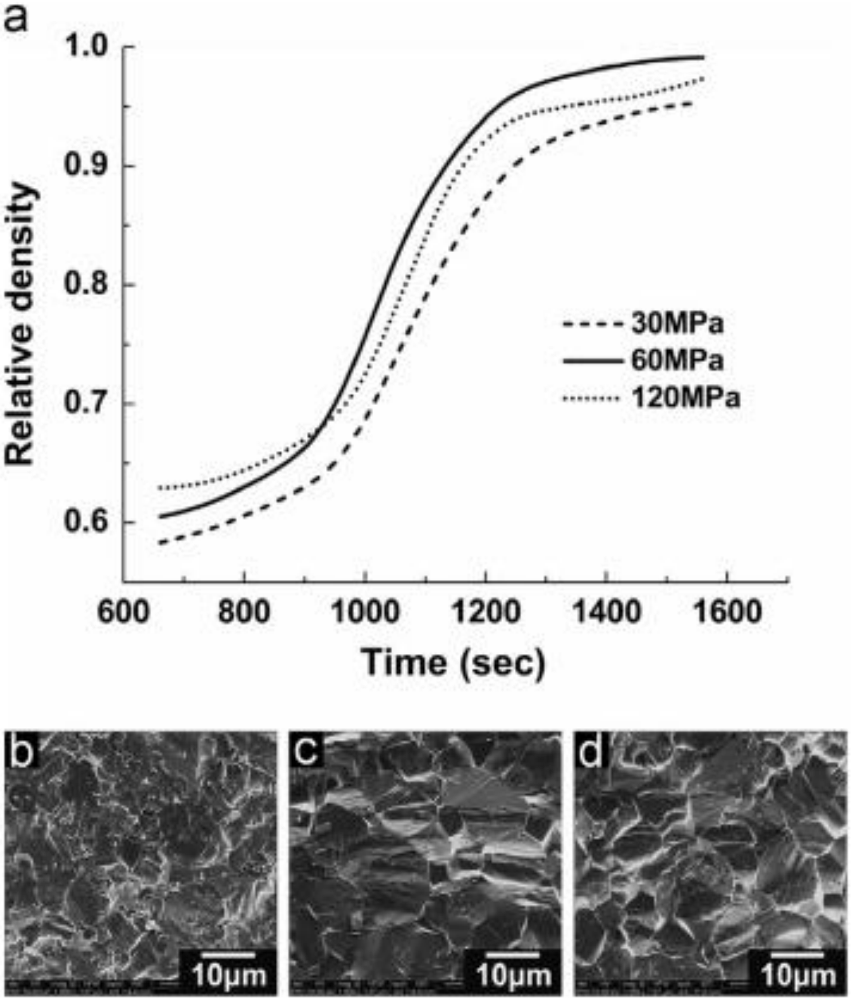

Figure 4.17 Relative density variation with time at fixed maximum temperature of 1600 ˚C and scanning electron microscope image of SPSed ZrN (SA) specimens (b) 30MPa, (c) 60MPa and (d) 120MPa.

Figure 4.17 shows the relative density as a function of time for a maximum temperature of 1600˚C for different pressures. The 30 MPa and 60 MPa curves present the same shape, with the latter being shifted to higher values of density, while the 120 MPa case has a different shape. Even though the 120 MPa curve has the highest initial relative density, the corresponding densification rate is lower with respect to the other two cases. Such trend is confirmed by considering the temperature at which the highest densification rate (slope of the curve) is reached for the various levels of pressure. While the 30 and 60 MPa curves behave as expected, with peak densification rates at 1359˚C and 1290˚C respectively, for the 120 MPa one this peak is reached only at 1370˚C. Nevertheless, in both 60 and 120 MPa cases a final relative density of ~99% is attained, according to the Archimedes' immersion method (Table 4.6). Figure 4.17(b) - (d) shows the microstructure of the fractured specimens consolidated under different pressures of 30MPa, 60MPa and 120MPa respectively. Generally, an increase of the applied pressure results in the reduction of the grain size of the specimen with the same density [146]. In our results, the 60MPa and 120MPa under 1600 ˚C conditions have similar density (~ 99%) and grain size (~24 μm) (Table 4.6). This may be attributed to the low thermal conductivity of the SiC punches.

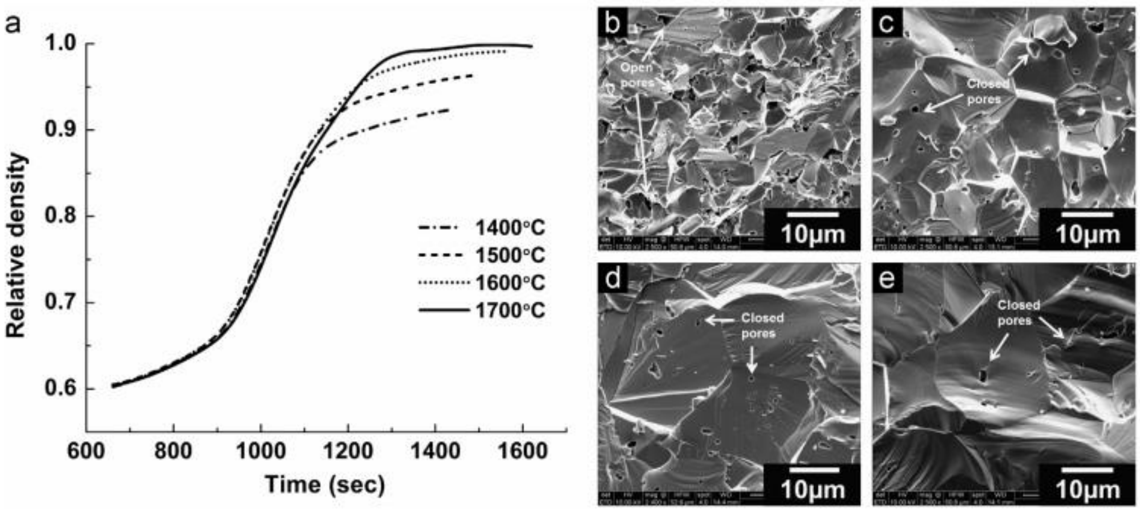

Figure 4.18 Relative density variation with time at fixed pressure of 60MPa and scanning electron microscope image of the fracture surface of SPSed ZrN (SA): (b) 1400 ˚C, (c) 1500 ˚C, (d) 1600 ˚C and (e) 1700 ˚C. Open and closed pores are indicated by white arrows.

Figure 4.18 shows the effect of the maximum sintering temperature on the relative density as a function of time under 60 MPa pressure and shows SEM fractured images of the specimens. Higher sintering temperatures lead to an augment of the final density. As a drawback, the more elevated temperatures promote the increase in grain size from 8.62 μm to 33.26 μm, as shown in the micrographs. Figure 4.18(b) shows the presence of several open pores for a specimen with 94.55% final relative density, while solely closed porosity, with voids characterized by small dimensions and a spherical shape, is encountered in the > ~ 98%-density samples depicted in Figure 4.18(c) – (e).

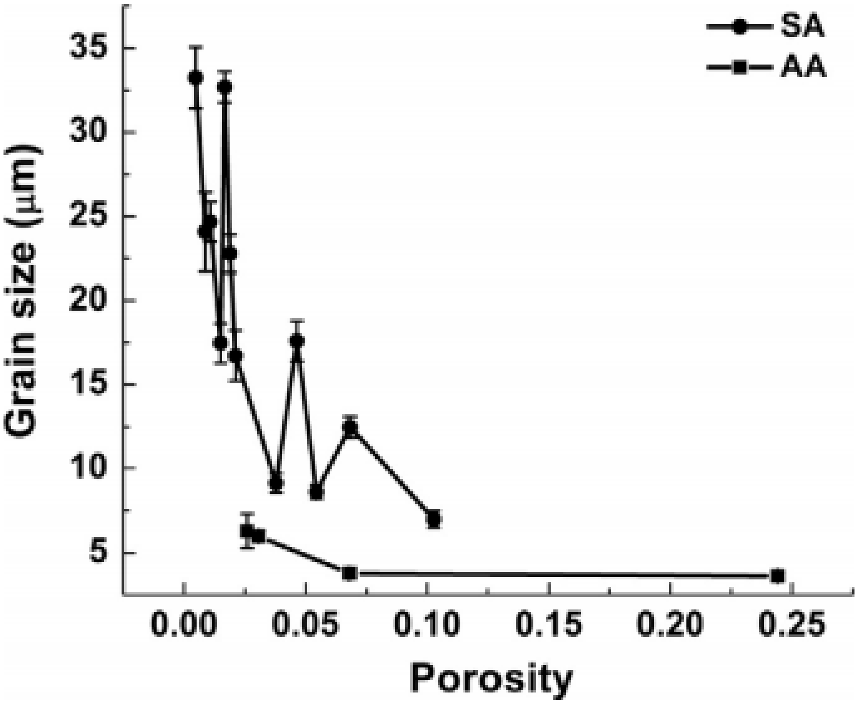

Figure 4.19 Grain size dependence on porosity of SA and AA specimens consolidated by spark plasma sintering. 1400~1700 ˚C, 30~120MPa for SA specimens and 1700 ˚C, 0~180MPa for AA specimens.

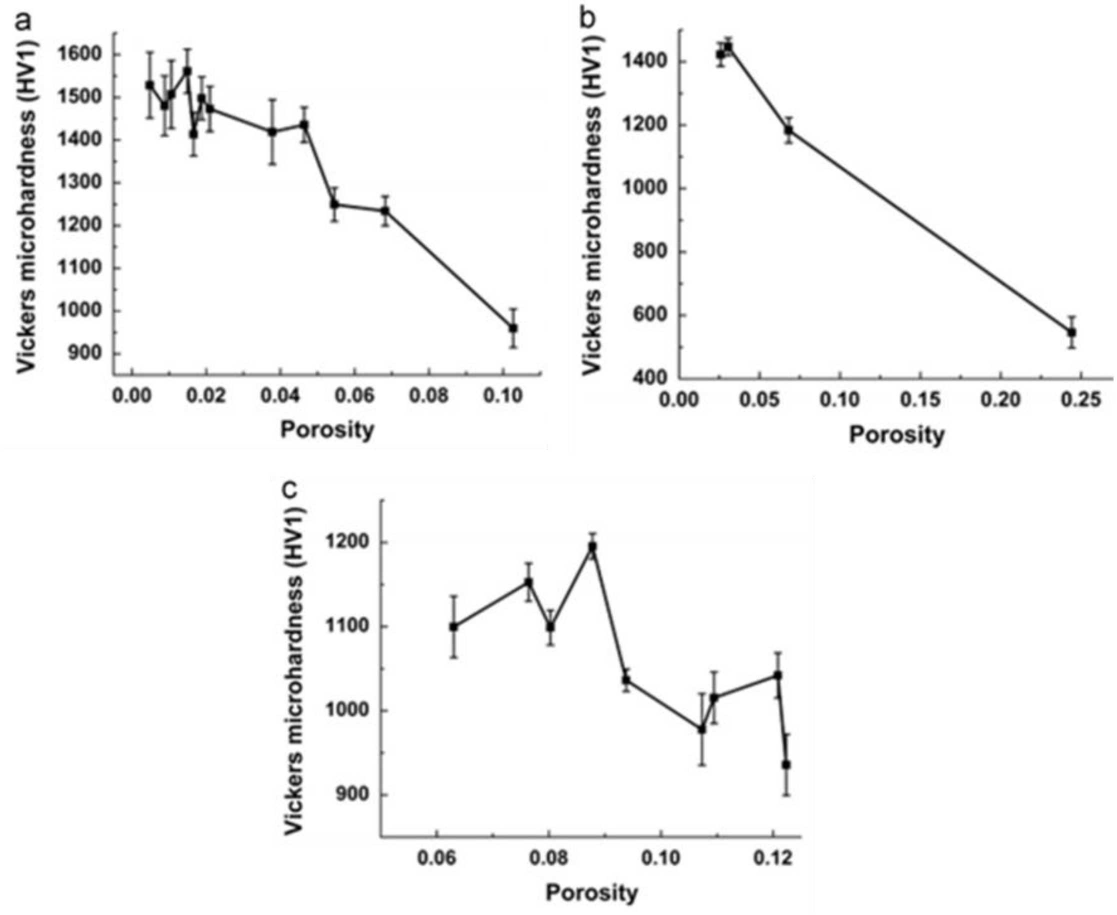

Figure 4.20 Vickers microhardness dependence on porosity of ZrN specimens (a,b) SA, AA consolidated by spark plasma sintering and (c) AA consolidated by high voltage electric discharge consolidation.

Figure 4.19 shows the grain size dependence on the porosity of the SA specimens. The general trend is an increase in grain size with decreasing porosity, with the exception of a few data points. Finally, Vickers micro-hardness measurements were performed. This parameter's dependence on porosity for the SA specimens is shown in Figure 4.20(a), revealing a strong correlation. Several previous studies measured the Vickers micro-hardness of ZrN samples consolidated by SPS [137, 149] or other techniques, such as hot pressing and hot isostatic pressing [129, 135, 150], and reported average values of Vickers micro-hardness between 1000 kgf/mm$^2$ and 1500 kgf/mm$^2$, which is in a good agreement with our data.

### 4.2.2.2.1.2. Alfa Aesar powders

Figure 4.19 and Table 4.6 present the relationship between the porosity and grain size of the AA samples.

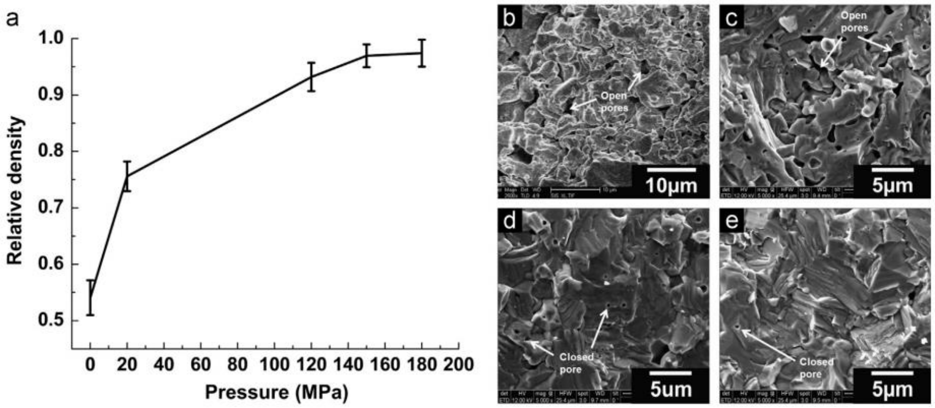

Figure 4.21 Relative density variation with pressure at fixed maximum temperature of 1700˚C (a) and SEM image of (b) 20MPa, (c) 120MPa, (d) 150MPa and (e) 180MPa for the ZrN (AA) consolidated by spark plasma sintering. Open and closed pores are indicated by white arrows.

Figure 4.21 shows the effect of pressure on relative density and also shows the images of fractured specimens sintered at 1700˚C under four different pressures (20, 120, 150 and 180MPa). Relative density appears to increase with growing pressure, and this influence of pressure is more prominent than that for the SA cases (Figure 4.16). It is noted that a maximum relative density of 97.42% is achieved with the highest pressure (180MPa), a value that can be compared with fully dense specimens of SA powders in terms of sinterability, as shown in Table 4.6.

Additionally, from the analysis of the microstructure shown in Figure 4.21(b)-(e), we notice that pores start to be closed at 93~97% relative density.

The Vickers micro-hardness measurements outcomes, represented in Figure 4.20(b), proved that the hardness dependence on porosity is analogous to the SA case.

#### 4.2.2.2.2. Characterization of specimens processed by HVEDC

The relative density of the specimens processed by HVEDC was evaluated by means of hydrostatic weighing in a pycnometer. It is found that the maximum specimen density of ZrN did not exceed 93%.

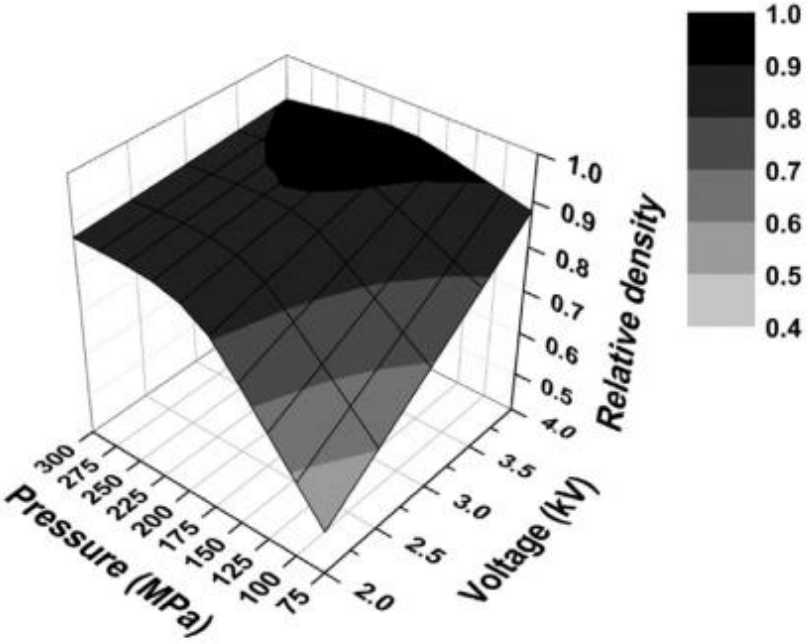

Figure 4.22 The densification map of ZrN (AA) consolidated by high voltage electric discharge consolidation. The relative density of the specimens is given as a function of pressure and voltage. The legend indicates the relative density.

Since the governing parameters of the HVEDC technology are pressure and voltage, the densification map describing the density dependence on these two quantities was built and is pictured in Figure 4.22. The map is constructed by fitting the experimental data in the test parameters intervals, with an error < 12%. The density of the specimens increases with the load applied in the pre-pressing stage. This trend appears, nevertheless, to have an upper bound. Given a value of electric current, a densification enhancement is observed up to a certain value of the cold-pressing load, after which any further increase affects density only slightly. Figure 4.22 also shows that the dependence of the relative density on the voltage is linear. The electric power is proportional to the squared voltage. If the voltage is applied for more than a few seconds, the zirconium nitride specimens can reach a thermodynamically stable structure. In this context we expect the ZrN relative density to depend on the squared voltage. However, the extremely short duration of HVEDC processes leads to kinetically trapped structures, which renders the relative density linearly dependent on the applied voltage. A raise in the electric current density that flows through the powder compact leads to an increase in the density of compacts [151]. However, beyond a certain critical value, the powders will release a significant amount of voltage through the matrix. Quantitatively, the dependence between the energy and the voltage is complex, since the material resistance depends on the relative density of the material, which evolves during processing. In general, the dependences between the process energy and the instant values of system internal parameters, such as density, can be described by rather complex relationships, including exponential/logarithmic terms [55, 152]. Therefore it may be expected, that if explored over wider ranges of applied voltages, the relationship between the relative density and the voltage may become non-linear.

It should be noted also that for the completeness of the conducted analysis, it is highly desirable to know the temperature of specimens according to the applied voltages. However, in its current apparatus' configuration, the temperature of specimens could not be measured during HVEDC process due to the very short pulse duration. Theoretically, the correlation between electric discharge parameters and the localized temperature field developed during HVEDC has been analyzed in earlier publications [4, 7].

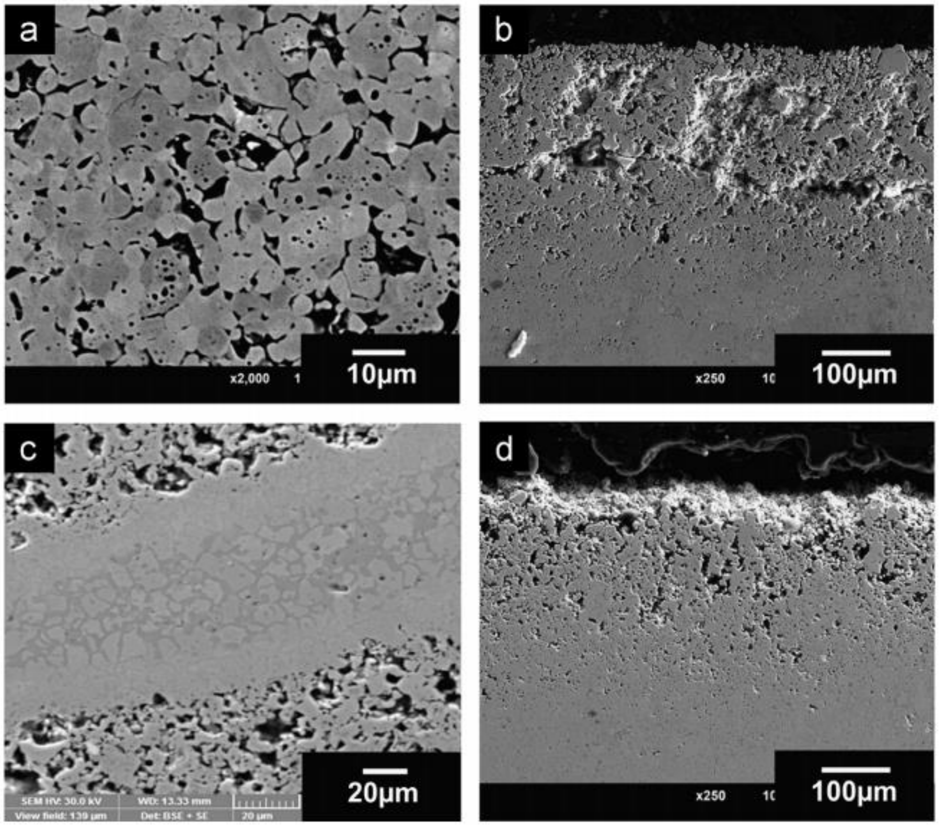

Figure 4.23 Scanning electron microscope images of ZrN (AA) specimens consolidated by high voltage electric discharge consolidation. (a) central and ((b) and (c)) edge of the specimen (3kV and 175MPa) and (d) edge of the specimen (3kV and 200MPa).

Figure 4.23 shows the typical microstructure of a sample prepared under 3kV and 175MPa for the (a)~(c) and 3kV and 200MPa for the (d). Figure 4.23(a) shows that the particle size in the center does not exceed the initial values of the powder particle size, which indicates an absence of grain growth, as such rapid densification process was expected to guarantee.

On the other hand, the final porosity of the compact with density > ~ 75% includes a certain amount of open porosity, primarily located in the peripheral layer (Figure 4.23(b). Having a compact core and a porous periphery may be related to a radially heterogeneous distribution of the green density. This effect is due to a gradient in the lateral pressure caused by the friction of the mold walls against the powder particles movement. The magnitude of this lateral pressure is not constant along the height of the specimen, and it has a tendency to decrease when moving from the punches to the powder, therefore causing a heterogeneous density distribution in the axial direction within the specimen.

A consequence of the uneven distribution of the lateral pressure is a lower green density at the center of the powder compact, combined with a reduced contact area among the particles, which leads to an increased electrical resistivity and therefore enhanced Joule effect and localized peak temperatures.

Apparently with a decrease in the density of electric current (at constant pressure) or the level of applied pressure (at constant current density), the size of the densified central zone is reduced and a corresponding increase in the volume occupied by the porous peripheral zone is obtained, which ultimately leads to a lower overall relative density of the specimen.

An improvement against such non-homogeneities can be reached by applying more elevated (axial) pressures, responsible for the expansion of the dense central zone. If, instead, the current density is increased, the raise in electrical power is focused on the central area. Consequently, localized heating occurs in the region that is already the most compacted, causing a grain size increase in the central zone.

When an electrical current pulse passes through the compact, the peripheral zones can be heated at a temperature relatively lower than the ones in the central part, which results in the friable structure at the edge of specimens (Figure 4.23(b)). The thickness of the porous layer was reduced by increasing the applied pressure, which can be seen by comparison between Figure 4.23(b) and Figure 4.23(d).

However, it should be noted that in some areas of the end pressing parts (Figure 4.23(c), apparently strong energy is released after formation of the individual grains by dissociation of nitride, constituting a eutectic solid solution of zirconium nitride and zirconium (large grains of Figure 4.23(d)).

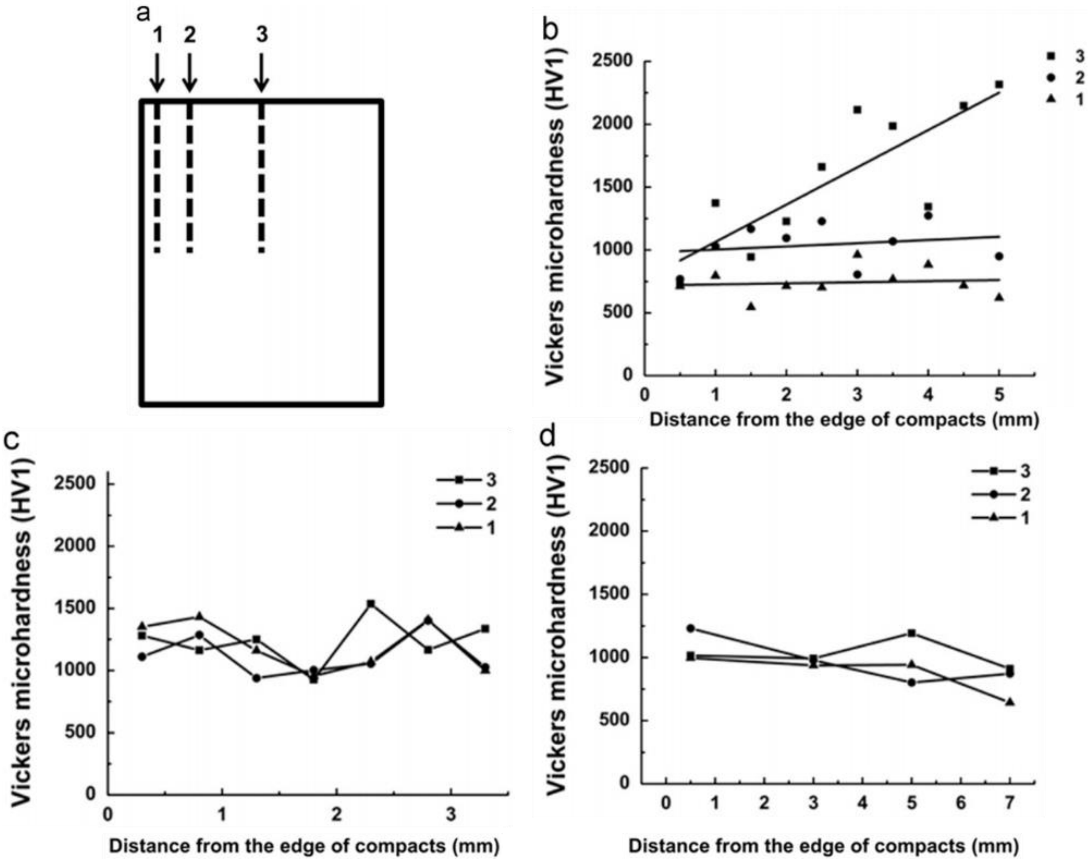

Figure 4.24 Vickers micro-hardness of ZrN specimens after sectioning, (a) schematics of analyzed areas, from edge (Location 1) to center( location 3), Vickers micro-hardness plot as a function of the radial position of (b) AA specimen consolidated by HVEDC, (c) AA specimen consolidated by SPS and (d) SA specimen consolidated by SPS

In order to confirm the discussion above, we checked the Vickers micro-hardness measured with a load of 1kgf. These measurements along the longitudinal direction of the samples' cross-section confirmed that the central part was endowed with the most densified material, as shown in

Figure 4.24(a). The internal area of the specimen exhibits micro-hardness values four times greater than the peripheral areas as shown in Figure 4.24(b).

### 4.2.2.3. Discussion: processing – structure – properties correlation and modeling of densification kinetics

#### 4.2.2.3.1. Processing – structure – properties correlation

The processing of SA powders resulted in higher relative densities consolidated under SPS compared to AA powders, even though they share similar properties in terms of particle size and distribution. Such behavior can be explained by considering that AA powders are more agglomerated and have higher levels of impurities (Hf < 3%), which typically hamper the sinterability of this material. Another possible reason may be the higher initial oxygen content in the AA powders. The average composition was $ZrN_{0.94}O_{0.11}$ for SA and $ZrN_{0.99}O_{0.3}Hf_{0.01}$ for AA (Table 4.6), which can be compared with the respective initial compositions of $ZrN_{0.86}O_{0.18}$ and $ZrN_{0.87}O_{0.}28Hf0.01$ (Table 4.4). In both cases, the starting powder oxide ratio was retained, which implies that the initial oxide content affects the composition of the densified specimens.

ZrN is characterized by a broad range of non-stoichiometry ($ZrN_{1-x}$, $0<x<0.35$). The sintering of ZrN is accompanied by the release of weekly bound nitrogen [134, 153]. Interestingly, the application of high pressures makes the nitrogen ratio remained in the AA pellets (Table 4.6). It is inferred that the cold pressing with elevated loads prior to the SPS process renders the contact area of the particle larger, which results in reducing the number of the open pores that act as fast diffusion paths of the dissociated nitrogen. Therefore, nitrogen dissociation is at least partially impeded by a sintering stage of cold pressing.

Both powders share the natural tendency to increase in grain size when porosity is reduced. However, for analogous porosity levels, AA specimens showed a smaller average grain size than SA (Table 4.6).

Concerning mechanical properties, the specimens' hardness also resulted to be dependent on porosity, as Figure 4.20 shows. To evaluate the Vickers hardness of a porous material, the following equation was utilized [154]:

$$H_v(\theta) = H_{v,0} \times \exp(-b\theta) \tag{4.4}$$

where $H_{v,0}$ is the Vickers hardness of the fully dense material, *b* is a constant that depends on the applied load and $\theta$ is porosity.

By applying this equation to our hardness data we obtained *b* and $H_{v,0}$, which resulted to be 4.22 and 1609.96, respectively, for SA samples and 4.53 and 1633.75 for AA, revealing that the hardness dependence on the porosity of the two powders is comparable. The *b* values are in good agreement with the literature [149].

Because of the high electric currents applied, HVEDC allows consolidation of a powder compact within a few seconds, and therefore the retention in the sintered specimens of smaller grain sizes than in the SPS cases is expected. But, interestingly, the specimens processed by the two techniques share analogous average grain sizes.

The maximum relative densities achieved in the experiments are ~93% for HVEDC, ~97% for AA SPS and ~99% for SA SPS. The lower values attained for the HVEDC cases are explainable by the presence of the porous peripheral zone, while the SPS process renders a more homogeneous microstructure.

Figure 4.24(c) and (d) shows the measurements of the Vickers micro-hardness for the cross-section of the SPS-processed specimens (AA1712 and SA1403) along the longitudinal direction. Compared with Figure 4.24(b), which concerns the analogous properties for the HVEDC-processed specimens, the SPS samples present a more uniform structure within the axial cross-section.

Another macro-scale effect of the non-uniformities characterizing HVEDC specimens is found in the presence of cracking and barrel-like shapes in the densified compacts. Additionally, the application of high pressures and voltages create mullite contamination in the samples, The optimal compaction conditions to prevent shape alterations and mullite contamination in the HVEDC of zirconium nitride have been identified in the application of a pressure within the 100~160MPa range and a voltage of 2~3kV, which, on the other hand, limits the final relative density to 83%.

#### 4.2.2.3.2. Modeling of the densification kinetics imposed by HVEDC

Many efforts are currently dedicated to the individuation and modeling of densification mechanisms of ceramic materials under SPS conditions [15, 31, 51-53, 55, 155], while equations capable of reliable describing consolidation kinetics for HVEDC procedures have not been developed.

For HVEDC, a significant aspect to be taken into account for the modeling of the process is the extreme rapidity characterizing this technique, which allows powders to be consolidated within a few seconds. A “zero-order approximation” of such technology, based on its peculiarly short processing time, can disregard the influence of heat on densification and, in view of the applied high pressures, can describe HVEDC as a cold pressing process.

From the constitutive equation for the cold pressing case, the following relationship can be derived [55]:

$$\sigma_z = \sigma_y \sqrt{\frac{2}{3}\frac{(1-\theta)^3}{\theta}} \tag{4.5}$$

where $\sigma_y$ is the yield stress of the bulk material.

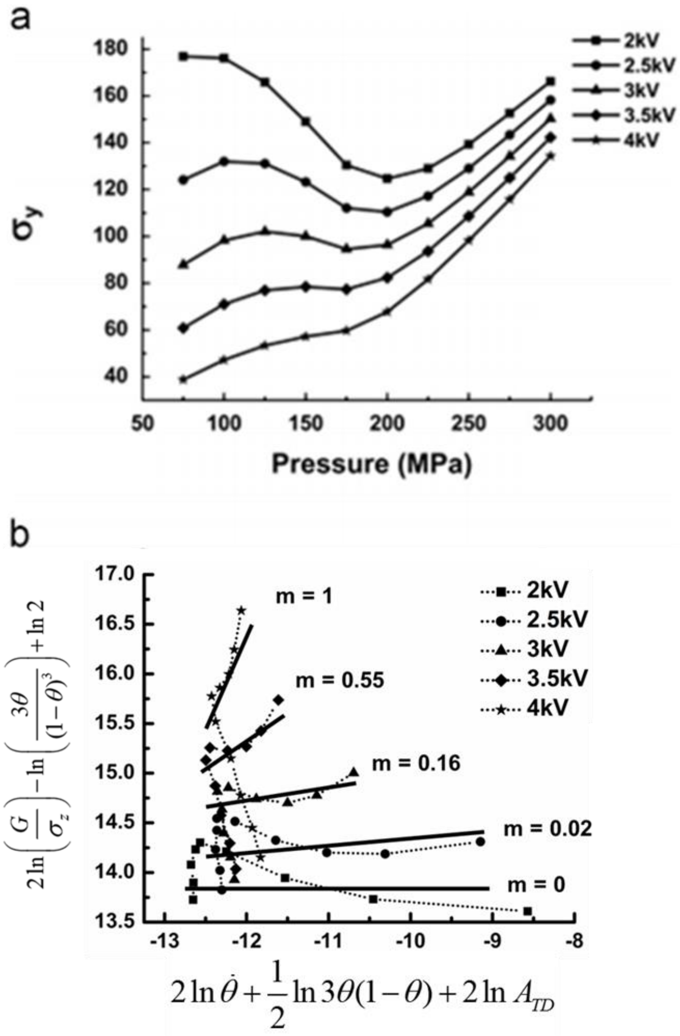

Figure 4.25 Constitutive equation fitting of high voltage electric discharge consolidation results. (a) yield stress variation with pressure and (b) m variation with voltage.

By substituting the experimental data on pressure and final porosity into (4.5), the yield stress for each condition can be calculated, as shown in Figure 4.25(a). It appears that when a low voltage is applied, (4.5) provides good correlations with experimental data for a constant value of the yield stress of the bulk material. Indeed, in low voltage processes, the short sintering time does not allow enough time for the effect of heating to be significant, and the adoption of a cold pressing model can be considered adequate. When the voltage is increased, the high electrical currents are involved, and the consequently increased heat and/or field-related phenomena compromise the validity of the purely plastic material assumption, inducing a pressure-dependent behavior on the "apparent yield stress."

The constitutive equation for a non-linear viscous material, (3.10), was applied to the HVEDC results to determine the densification mechanism (*m* value). Taking the natural logarithm of (3.10) and rearranging:

$$2\ln\left(\frac{G}{\sigma_z}\right)-\ln\left(\frac{3\theta}{(1-\theta)^3}\right)+\ln 2=m\left(2\ln\dot{\theta}+\frac{1}{2}\ln 3\theta(1-\theta)+2\ln A_{TD}\right) \tag{4.6}$$

After inserting the average porosity rate by calculating the slope and pressure given in Figure 4.21 into (4.4), a plot can be generated to determine *m* and $A_{TD}$, as shown in Figure 4.25(b). In the conventional sintering theory, the densification of a powder by means of hot pressing provides one *m* value that is associated with a specific sintering mechanism. However, Figure 4.25(b) shows an increase of the slopes (*m* value) with increased voltage, if excluding the high-pressure points (300 MPa for 2.5kV and 225 ~ 300 MPa for 3 ~ 4 kV). Under low voltage, $m = 0$, which confirms that HVEDC acts like quasi-cold pressing. Increasing the voltage leads to a change of the strain-rate sensitivity value *m* from 0 to 1, which is attributed to the increasing heat generation.

The provisional exclusion of the high pressure data was motivated by the markedly distinct behavior of our curves when shifting from low to high values of pressures, which suggested that the two pressure regimes need to be evaluated separately. It appears that the combination of high pressure and voltage during HVEDC induces a different behavior in the material with respect to the one used for modeling of hot pressing equation (3.10). The obtained first-order approximation provides an impetus for future work on refining the mechanisms underlying the novel and still rare technology of HVEDC.

## 4.3. Chapter Conclusions

The effect of the electric current on spark plasma sintering (SPS) of ZrN powder was examined. For a rigorous comparison of SPS with hot pressing (HP), the processing parameters such as the actual temperature inside the powder, the electric current, and electric current density were measured or calculated. The electro-thermo-mechanical finite element modeling (FEM) of SPS showed that the vertical electrical and thermal contact resistances are crucial factors for obtaining the realistic values of the electric current flowing through the powder during SPS. The inter-particle neck area at the initial stage of sintering is small; therefore high electric current density can be developed and then reduced when the relative density is increased. Fitting the developed constitutive equation to the experimental porosity evolution observed in HP and SPS, showed that the densification mechanism of ZrN can be changed from dislocation climb to dislocation glide by the introduction of the electric current. The constitutive equation of SPS taking into account the effect of the electric current effect was developed taking into consideration the enhanced dislocations motion by local resistive heating. The derived equation shows the possibility of the facilitation of the dislocation movement by an intrinsic current effect other than a change of the densification mechanism.

A comparative study of spark plasma sintering and high voltage electric discharge compaction methods for the consolidation of micro-sized ZrN was conducted. SPS allows the obtainment of the highest relative densities and the formation of more uniform microstructures with respect to HVEDC. In this more successful case of SPS, two different ZrN powders were utilized, so that the significant impact of powder agglomeration and oxide content on the physical and mechanical properties of the sintered specimens could be evidenced. The sintering temperature is the critical variable; on the other hand, pressure gives serious effect only with low sintering temperature for the densification of the ZrN powder (SA). Densification of AA powder depends strongly on the pressure and, nitrogen dissociation from ZrN was reduced with increasing pressure. Specimens densified by HVEDC have porous structure at the edge and non-uniform shape due to the non-homogenous temperature distribution and short soaking time (<1 sec). A constitutive model of the densification behavior was proposed and verified based on the experimental data of HVEDC, and showed that the univocal underlying sintering mechanism could not be individuated in which modeling outcomes are strongly dependent on the applied voltage.

Chapter 5 is focused on the densification of the metal powder using a general SPS setup, possibly largely affected by electric current compared with semiconducting ZrN powders. Chapter 6 is dedicated to the setup and optimization of the high current density consolidation method based on SPS.

Chapter 4, in part, is a reprint of the material as it appears in *Acta Materialia,* 2018. G. Lee, E.A. Olevsky, C. Manière, A. Maximenko, O. Izhvanov, C. Back, and, J. McKittrick. The dissertation/thesis author was the primary investigator and author of this paper.

Chapter 4, in part, is a reprint of the material as it appears in *Ceramics International*, 2015. G. Lee, M.S. Yurlova, D. Giuntini, E.G. Grigoryev, O.L. Khasanov, J. McKittrick and E.A. Olevsky. The dissertation/thesis author was the primary investigator and author of this paper.

# CHAPTER 5 Electric Current Assisted Consolidation of Refractory Metal Powders

In this chapter, the consolidation by SPS of Tungsten (W) or Molybdenum (Mo) powders is considered. In section 5.1, the densification of a micro-sized W powder is analyzed. Due to the higher electric conductivity of W compared with previously considered ZrN, a more intensive electric current can pass through the W powder during SPS. (3.10) is applied to determine whether the densification mechanism of W powder is changed with the application of electric current.

There is much interest focused on sintering of nanopowders to fabricate nano-structured components. However, metal nanopowders are easily oxidized which hinders their sintering. Also, conventional sintering of nanopowders is usually accompanied by significant grain growth. Earlier (see section 1.1) we assumed that the electric current assisted consolidation can reduce the surface oxides or slower the grain growth. Therefore, Mo nanopowders were subjected to SPS, expecting to overcome the above-mentioned problems.

## 5.1. Densification Mechanism and Mechanical Properties of Tungsten Powder Consolidated by SPS

Tungsten (W) components find a broad spectrum of applications in automotive and aerospace industry, in furnace elements, in electronics, in medical devices, in sports equipment, in welding electrodes, and in nuclear power plants. Due to the high melting temperature, manufacturing of tungsten parts is frequently attempted through powder metallurgy routes. However, consolidation of tungsten powders by traditional powder processing technologies, such as sintering and pressing, presents significant challenges. It has been reported that 2.3 μm W powder had to be sintered at 2500 °C for 1 hour in a hydrogen atmosphere to get specimens with the relative density close to 90 % [156]. In a different study, Bewlay *et al*. showed that 50 hours of free sintering were required to obtain 90.2 % density under 1800 °C [157].

Pressure-assisted sintering methods were also utilized for the consolidation of W powders. Karpinos *et al*. reported that W powder could be sintered to 94 % under 2300 °C and 24.52 MPa using hot pressing (HP) [158]. Hot isostatic pressing (HIP) using 14 µm W powder achieved 92.7% with the processing conditions of 1277 °C and 195 MPa [159].

To lower the consolidation temperature and pressure, alternative sintering methods have been pursued to compact the dense W components.

W consolidation by SPS showed that 91.5 % relative density was achieved within 8 min holding time at 2327 °C and 47 MPa in the air [160]. This study indicated clean grain boundaries formed due to the interface cleaning effect by the SPS method [1, 12]. Cho *et al*. tested various SPS sintering conditions and revealed the effects of the powder size, pulsed current, holding temperature and pressure on the final density and microstructure of W specimens [161].

Under free sintering, the densification mechanism of W powders has been investigated for different consolidation approaches for micro- and nano-powders. Hayden and Brophy [162, 163] measured the linear shrinkage of a W powder body as a function of time and concluded using the two-sphere sintering model that grain boundary diffusion was the rate limiting mechanism over the temperature range of 1050 °C to 1200 °C with an activation energy of 380 kJ/mol [164]. Based on the rate of volume change in terms of the diffusion constant, Kothari found the activation energy of 420 kJ/mol for cold-pressed W powders (3 µm) under vacuum conditions [165, 166]. This study revealed that densification occurred by grain boundary diffusion for temperatures between 1100 °C to 1500 °C. Vasilos and Smith studied W sintering kinetics between 1300 °C and 1750 °C and found that the activation energy was 465 kJ/mol, which was in agreement with the activation energy of the grain boundary diffusion [167]. Chen investigated the sintering kinetics with dilatometric analysis and concluded that the rate controlling mechanism was the grain boundary diffusion [168].

There are few reports on the determination of the sintering mechanisms of W by pressure assisted methods (HP and SPS). Karpinos *et al*. [158, 169] investigated W densification using HP and used the sintering kinetics model, which had been earlier employed by Kothari [165]. Densification mechanisms were sub-divided into three regions with respect to the relative density. The dominant mechanisms identified for each region were (i) particle rearrangement (45 - 58%), (ii) plastic flow (58 - 75 %), and (iii) grain boundary diffusion ( > 80%). Gao *et al*. studied the kinetics of W compaction by SPS using an initial stage model of sintering and found that diffusion along the grain boundaries leading into interparticle neck regions was the rate controlling mechanism for W sintering in the temperature range of 1250 °C to 1500 °C and under 16 MPa pressure [170].

It is known that power-law creep is the main mass-transfer mechanism during deformation processing of crystalline powders at intermediate to high temperatures [171]. Robinson and Sherby reported that low temperature ( < 2200 °C) creep of W had a strain rate sensitivity (*m*) of 0.14 (subgrains are not formed during creep) or 0.21 (subgrains are formed during creep). They discovered that the rate controlling step was dislocation diffusion for temperatures in the range 0.4 - 0.65 $T_m$ ($T_m$ = melting temperature of W) and lattice diffusion for temperatures over 0.65 $T_m$ [172].

Superplastic behavior was reported for coarse (> 10 µm) grain size pure W powder subjected to creep test conducted under near 0.5 $T_m$ or higher temperatures [173]. Also, W powder mixture with Re showed superplasticity with $m$ = 0.2 ~ 0.4 rendering substantially larger elongation to failure (200 % ~ 400 %) compared with that of $m$ = 1 [174-177]. Nieh *et al*. indicated that superplasticity in W-Re alloys may be the result of a solid solution behavior governed by the solute atom diffusion with dislocation glide [88]. Kurishita *et al*. controlled the mechanical milling conditions of a mixture of W and TiC powder, which showed superplastic behavior with $m$ = 0.2 and $m$ = 0.5 for in hydrogen and argon atmospheres, respectively [178]. Recently, SPS of powder mixtures containing W (nano-) powder has been reported, where the W-phase was contributing to the overall power-law mechanism of mass transfer [179].

In the present study, micron size W powders were consolidated using SPS. In order to obtain the densification kinetics of W compacted by SPS, for the first time, the constitutive model of powder hot pressing (3.10) was applied assuming the dominance of the power law creep, a mechanism which contributes, and often prevails in HP [171]. The present study indicates that grain boundary sliding controlled by dislocation climb with dislocations moving along grain boundaries is the main densification mechanism of the W powder compaction by SPS method. Also, the microstructure and mechanical properties of the compacted W pellets were examined in close correlation to the powder material processing conditions.

### 5.1.1. Experimental procedures

#### 5.1.1.1. Materials investigated

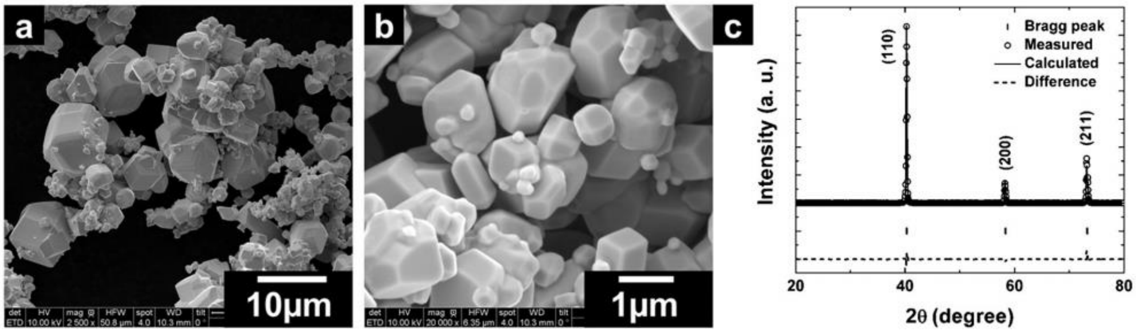

Figure 5.1 (a) and (b) Scanning electron microscope images of W powders : 2500X, 20000X, respectively. (c) X-ray diffraction results for as- received W powders.

W powders (99.999%, body centered cubic, Im-3m) produced by Buffalo Tungsten Inc. were employed. The powder morphology and size (Figure 5.1(a) and (b)) were observed using SEM. The powders had a faceted particle shape with a tendency to form agglomerates. Based on the manual size measurement of 200 particles using an image analysis program (Image J), it was determined that the powders had various size particle distributions, which were composed of about 1 µm to 12 µm size particles. The purity level of the powders was obtained by measuring 12 regions by EDS.

The crystal structure and lattice parameters were evaluated by XRD, utilizing $CuK_\alpha$ radiation at room temperature. In Figure 5.1(c), the measured and reference W (ICSD collection code # 76151) [180] diffracted patterns are presented by hollow circles and a solid line, respectively. The diffracted (hkl) planes are shown on the top of each peak. The dashed lines indicate the intensity difference between the measured and reference peaks. The lattice parameter of the powders is found to be 0.3168 nm, which is very close to the reported value of 0.3165 nm [180].

#### 5.1.1.2. SPS processing regimes

The detailed information on the tooling setup and SPS device can be found in section 3.2.1.

For some specimens, boron nitride was sprayed onto the graphite paper, which surrounds the inner hole of the graphite die in order to block the carbon diffusion from the graphite (specimens W3BNC_1660_H30, W6BNC_1660_H30, and W9BNC_1660_H30 in Table 5.1).

For 60 MPa or 120 MPa, the measured initial green (after pre-cold-compaction) densities of the powder compacts were ~ 54% and ~ 65%, respectively. The sintering conditions were a heating rate of 100 ˚C/min from 600 °C to the maximum temperature (1600 ˚C, 1700 ˚C or 1800 ˚C) with dwell times of 0, 6, 30 or 60 min.

Most experiments were conducted under ~20 Pa, except the experiments carried out at 1800 ˚C when argon gas was purged in the SPS chamber.

### 5.1.2. SPS results

The densified specimens were ground by a 125 μm diamond disk and subsequently by a series of gradually finer SiC grinding papers (36 μm, 21.8 μm, and 15.3 μm). Following this, the specimens were dried in an oven (Neyo 2-1350, USA) at 120 ˚C for 20 min. The relative density was estimated by the Archimedes' immersion method, which required the samples to be coated with paraffin wax.

For electron backscatter diffraction (EBSD) analysis, the specimens were ground and polished using an automatic polishing machine (Struers, Germany). The polished samples were analyzed by scanning electron microscopy (Hitachi S3600N, Hitachi, Ltd., Japan) utilizing the

Hikari Pro series EBSD camera (EDAX, USA). The respective pole figure has been constructed by means of TSL OIM Analysis 5.31 software (EDAX, USA).

### 5.1.2.1. Tungsten powder densification map

The physical and mechanical properties of the W specimens are listed in Table 5.1, which indicates that the highest value of the relative density (~ 95.93 %) was achieved at 1600 ˚C under 60 MPa.

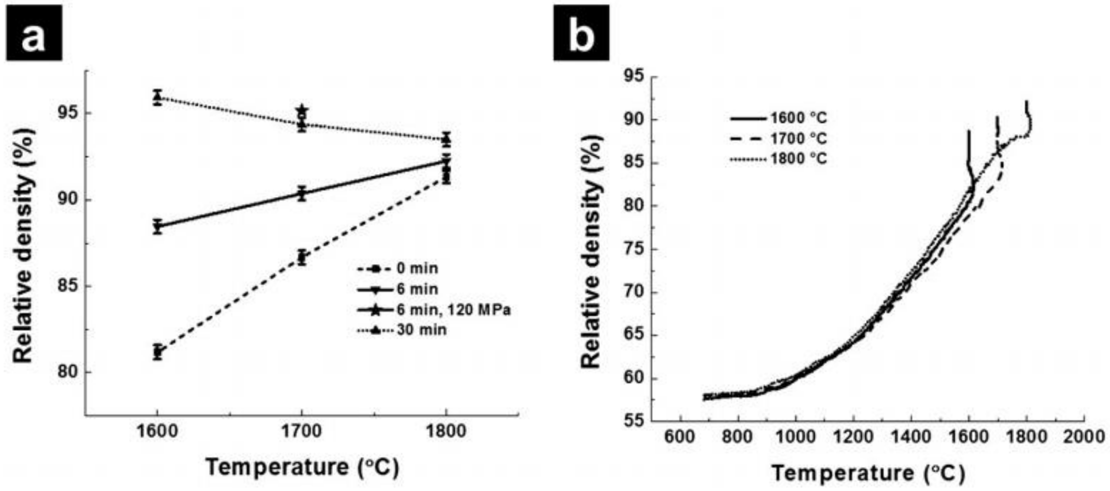

Figure 5.2 (a) Relative density dependence on SPS maximum temperature, holding time and pressure, measured by Archimedes immersion method. (b) Relative density variation with the temperature at a fixed pressure of 60 MPa.

For 60 MPa, the relative density generally increased with increasing temperature and holding time, as shown in Figure 5.2(a). Some experimental conditions such as those used for sintering of W6_1760_H30, W9_1860_H30, and W10_1860_H60, show decreasing relative density with increasing temperature or holding time. This can be explained as follows: during characterization of the samples, a tungsten carbide layer was observed at the periphery of the specimens and the carbide layer thickness increased with the holding time and temperature. Because the theoretical density of W (19.25 g/cm$^3$) is used for the relative density calculations, the lower density of tungsten carbide (15.63 g/cm$^3$) layer renders lower final relative density. Carburization of W is analyzed in section 5.1.3 in more detail.

At a fixed temperature and holding time (1700 °C and 6 min), the pressure effect on the relative density was examined using the double die setup as shown in Figure 5.2 (a). The higher pressure of 120 MPa (Figure 5.2 (a): star shape symbol) renders ~95% relative density which is ~5% higher compared with that obtained when applying 60 MPa. However, considering the different green densities provided by applied pressures of 60 MPa and 120 MPa, respectively, a total increase of the relative density was ~ 36% and ~ 30%, respectively. Specifically, the net density increase is smaller when using the high-pressure double die setup; slower densification at higher relative density may be the reason for this phenomenon. Also, the lower thermal and electrical conductivity of SiC punch can affect the densification environment during SPS, which has been discussed in our earlier study [3]. Figure 5.2(b) shows the effect of the maximum sintering temperature on the relative density as a function of temperature under 60 MPa and 6 min holding time. The fast heating rate (100 °C/min), results in ~ 15 °C of overheating are shown on the plots at each final sintering temperature. The vertical portions of the curves show the increase of the relative density during the holding stage. All the three plots show similar densification rate during the ramping stage. Figure 5.2(b) indicates that the final sintering temperature is the major factor controlling the final relative density of the processed specimens.

Table 5.1 Physical, chemical and mechanical properties of W specimens prepared by spark plasma sintering.

| Name | **T** | **P** | **Holding time** | **Atmosphere** | **Relative density** | **Grain size** | **Vickers micro-hardness of W (HV1)** | **Vickers micro-hardness of $W_2C$ (HV0.5)** |
|---|---|---|---|---|---|---|---|---|
| | **˚C** | **MPa** | **min** | | **%** | **µm** | **Kgf/mm$^2$** | **Kgf/mm$^2$** |
| W1_1660_H0 | 1600 | 60 | 0 | Vacuum | 81.18 | 8.56 | 354 | - |
| W2_1660_H6 | 1600 | 60 | 6 | Vacuum | 88.46 | 6.96 | 311 | - |
| W3_1660_H30 | 1600 | 60 | 30 | Vacuum | 95.93 | 6.48 | 292 | - |
| W4_1760_H0 | 1700 | 60 | 0 | Vacuum | 86.68 | 6.03 | 278 | - |
| W5_1760_H6 | 1700 | 60 | 6 | Vacuum | 90.37 | 7.91 | 323 | - |
| W6_1760_H30 | 1700 | 60 | 30 | Vacuum | 94.38 | 11.06 | 358 | 1755 |
| W7_1860_H0 | 1800 | 60 | 0 | Argon | 91.33 | 5.82 | 220 | - |
| W8_1860_H6 | 1800 | 60 | 6 | Argon | 92.25 | 16.13 | 359 | 1671 |
| W9_1860_H30 | 1800 | 60 | 30 | Argon | 93.50 | 30.15 | 363 | 1875 |
| W10_1860_H60 | 1800 | 60 | 60 | Argon | 92.98 | 39.46 | 397 | 1885 |
| W11_1712_H6 | 1700 | 120 | 6 | Vacuum | 95.18 | - | 394 | 1890 |
| W3BNC_1660_H30 | 1600 | 60 | 30 | Vacuum | 94.11 | 19.11 | - | - |
| W6BNC_1760_H30 | 1700 | 60 | 30 | Vacuum | 94.61 | 22.38 | - | - |
| W9BNC_1860_H30 | 1800 | 60 | 30 | Argon | 95.04 | 85.09 | - | - |

### 5.1.2.2. Tungsten powder densification kinetics

In the present study, the constitutive equation of the continuum theory of sintering (3.10) is used to determine the densification kinetics of W powder subjected to SPS.

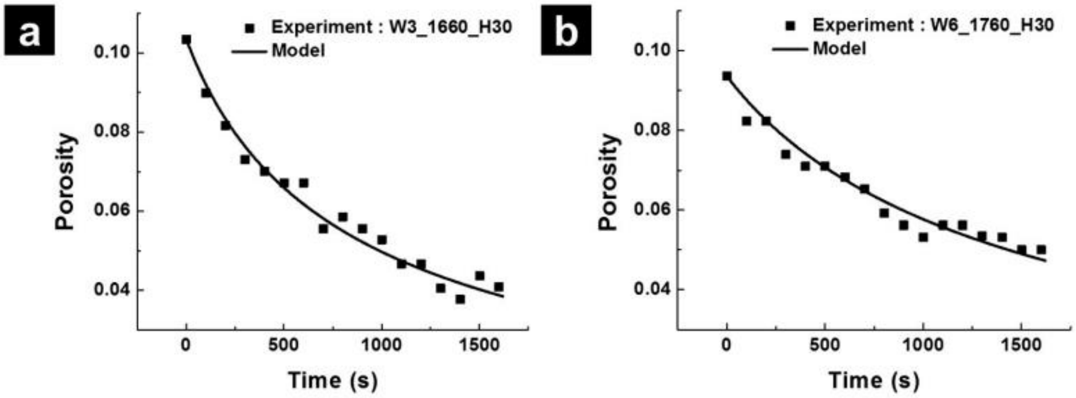

Figure 5.3 Experimental porosity evolution curves of W specimens ((a) W3_1660_H30 and (b) W6_1760_H30) processed by spark plasma sintering fitted by the constitutive equation.

All experiments with 30 min holding time were chosen for finding the densification kinetics. Figure 5.3 shows constitutive equation-based fittings of the porosity time evolution under (a) 1600 ˚C and (b) 1700 ˚C with 60 MPa during holding the stage. The experimental densification curves were drawn by the scattered square symbols, while the curves defined by a solid line denote the fitting curve using (3.10). The best fit corresponds to m = 0.39 and Q = 412.27 kJ/mol.

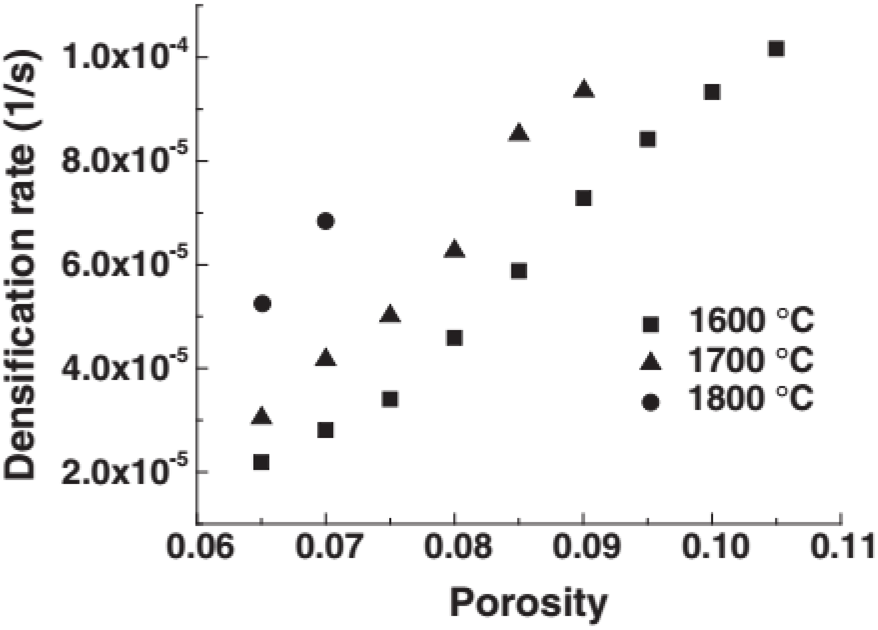

Figure 5.4 W powder densification rate as a function of porosity, conducted at 1600 °C (squares), 1700 °C (triangles) and 1800 °C (circles).

To confirm the sintering mechanism, the activation energy was also calculated by (4.2). In (4.2), $p$ will be zero when grain growth is not significant. The powders show the grain growth when relative density is > 90%, so $p$=2 was used to include the grain growth effect [88]. By comparing the densification rate for the three different sintering temperatures of 1600°C, 1700 °C and 1800 °C, the apparent activation energy $Q$ for powder consolidation was obtained. Grain sizes for each temperature are estimated by (5.1) (see below) [181]. Using the densification rate as a function of porosity and temperature during the holding stage (Figure 5.4), $Q$ was found to be 433.76 kJ/mol. This value is in the same range as the values assessed by Kothari (418 kJ/mol) [165], Vasilos and Smith (463 kJ/mol) [167] and Karpinos *et al*. (418 kJ/mol) [158, 169] and with the activation energy value of the grain boundary diffusion (385 kJ/mol) determined by the tracer diffusion method in the temperature range of 1400 °C to 2200 °C [182]. This finding supports the view of the grain boundary diffusion as the rate limiting mechanism. A number of other studies

[164, 168, 183] also suggested the grain boundary diffusion to be the main sintering mechanism for pressure-less and pressure assisted sintering of W in the vicinity of 0.5 $T_m$.

The obtained in the present study results match well the mechanism of grain boundary sliding accommodated by dislocation slip governed by dislocation climb [88]. The superplasticity of coarse-grained (10 ~ 20 µm) W was reported in the past [173]. Both the obtained from the SPS constitutive equation-based fitting and the value of the activation energy obtained from the Dorn method indicate that the grain boundary diffusion is the rate controlling mechanism. The calculated $m$ is in between the dislocation climb and glide behavior characteristic values ($m$ = 0.1 to 0.33) and superplastic behavior value ($m$ = 0.5 to 1)[184]. This may indicate that SPS of W powder is affected by the contribution of two or more mass transfer mechanisms. Kapinos *et al*. speculated that dislocation climb controlled by diffusion ($m$ = 0.2 to 0.25) was the consolidation mechanism for HP of W during the final stage of sintering [158, 169]. Therefore, one can conjecture that the two mechanisms (dislocation slip and grain boundary sliding) affect the densification of the W powder processed by SPS. The electric current effect during SPS may also affect the plastic deformation of W powder, inducing superplasticity of W.

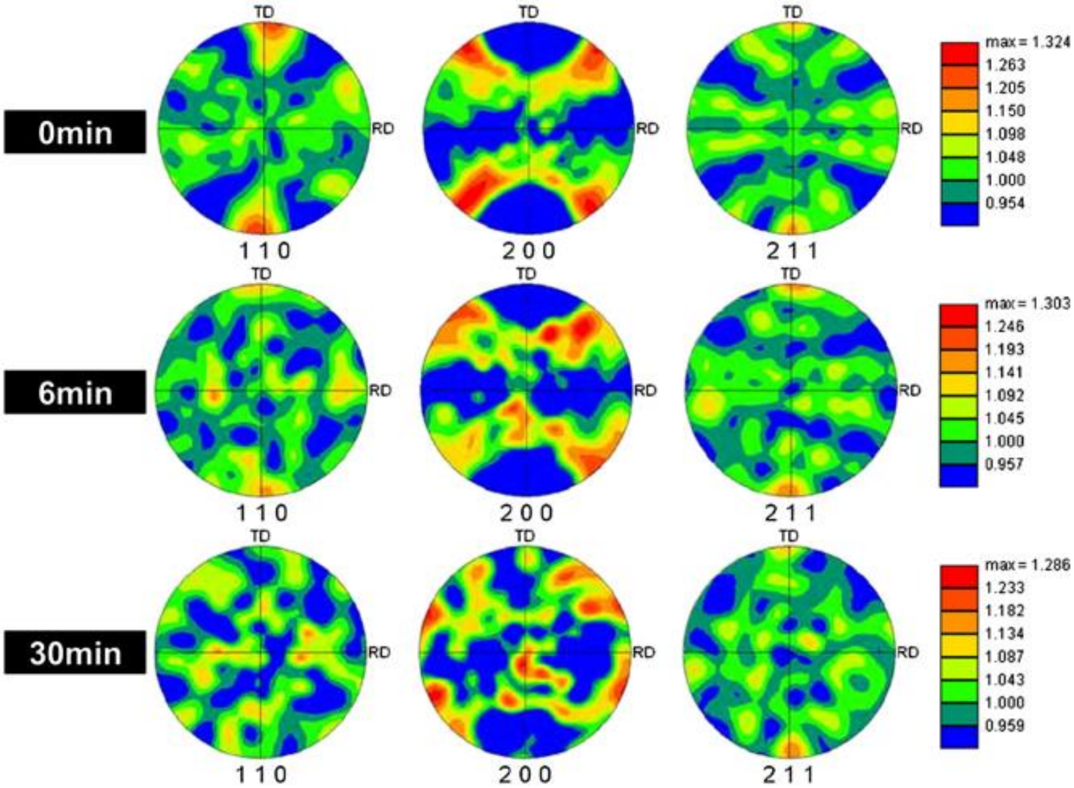

Figure 5.5 Pole figures showing the grain orientation of the sample subjected to SPS at 1700 °C for 0 min, 6 min, and 30 min recorded along the surface perpendicular to the applied uniaxial pressure.

The results of the EBSD texture analysis also support the notion of grain boundary sliding contributing to the densification mechanism. When polycrystalline structures are subjected to largely tensile plastic deformation, close-packed crystallographic planes have the trend to be aligned with the tensile direction. Previous results show that cold pressed or extruded W have (001)<110> texture [185]. In Figure 5.5 the pole figures of the main crystallographic directions of the specimens sintered at 1700 °C for 0 min show a relatively strong (001)<110> texture along the uniaxial pressure direction when EBSD scanned along the surface perpendicular to the applied uniaxial pressure. Pole figures (200) are equivalent to (100). The reduction of the texture by increasing the holding time under 1700 °C is very prominently represented by the pole figures. Most likely the initial cold pressing of the powders in the SPS chamber aligns the (110) grains perpendicular to the specimen axial direction; and this alignment can be retained until the holding stage due to the fast heating conditions. However, it is also possible that the grain orientation by cold pressing is changed during the ramping stage which showed over 25% densification. Grain rotation associated with grain boundary sliding produces predominantly random texture after deformation [186], which would make the degree of texture decrease with increasing holding time. The small equiaxed grain structure of the specimens also support the concept of the grain boundary sliding being one of the components of the overall densification mechanism (Table 5.1 and Figure 5.6). However, there is a low probability of grain boundary sliding under the sintering temperature of 1800 °C, which showed large grain growth, thereby shifting the dominant mechanism from grain boundary sliding to dislocation creep during densification.

Uniaxial compression of 60 MPa renders the normalized shear stress value ($\sigma_s / G$) of $2.58 \times 10^{-4}$. Based on the deformation mechanism map of W with 1 μm grain size [42], this processing condition corresponds to the grain boundary diffusion mechanism. On the other hand, from the deformation mechanism map of W with 10 μm grain size [42], this processing condition matches the low-temperature power-law creep range. The average grain size of 8 μm in the present study is between these above-mentioned two values. Therefore, it appears that the processing conditions utilized in the present work should render densification mechanisms near the boundary between power-law creep and diffusional flow. Indeed, Gao *et al*. [170] studied the W compaction by SPS using 16 MPa applied pressure and pointed out the grain boundary diffusion as the major densification mechanism. However, some studies have shown that the grain boundary sliding region can be at lower stress levels associated with lower creep strain rates in the power law creep region in deformation maps [187-189]. Therefore, according to the values of the normalized shear stress and the average grain size of the processed W specimens, the utilized SPS processing conditions may cause some grain boundary sliding too. It appears that the small particle size of W powders and different processing conditions may result in the change of the major contributing densification mechanism, as demonstrated by the results of the present study.

### 5.1.3. Processed specimens' characterization

#### 5.1.3.1. Microstructure characterization

The morphologies and the grain area distribution of the etched surface of the W samples were extracted from the EBSD scans using OIM software. Mean grain sizes were calculated from the total 0.38 mm$^2$ cross-section area of each of the W samples.

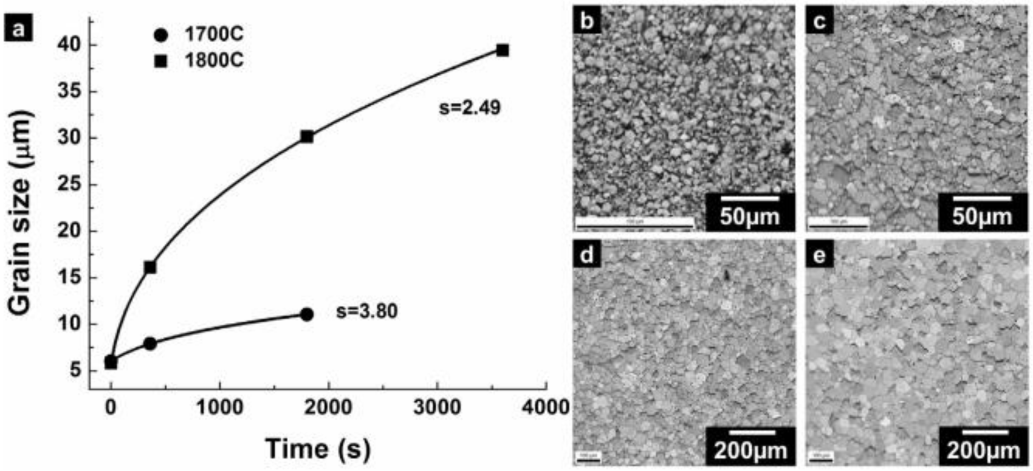

Figure 5.6 (a) Plot of the grain size time evolution for W consolidated at 1700 °C and 1800 °C by SPS. The grain growth exponent(s) for each temperature plot is shown on the right side of the fitting curves. SEM images of W specimens processed at 1800 °C with holding time of (b) 0 min, (c) 6 min, (d) 30 min and (e) 60 min.

The grain growth kinetics can be described as [181]:

$$D^s - D_0^{\,s} = ct \tag{5.1}$$

where $s$ is the grain growth exponent, $D_0$ is the average initial grain size, $D$ is the final average grain size after annealing time $t$, $c$ is the temperature dependent rate constant. The $s$ value can be

2 for normal grain growth conditions (high purity fully dense metal at a high homologous temperature). The *s* value can be deviated from 2, when the grain growth inhibiting factors, such as solute dopants or impurities, the liquid phase at the grain boundaries, and inclusions (pores or second phase particle), are present [166, 170, 190].

Figure 5.6 shows the relationship between the isothermal grain growth and the annealing time. The values for *s* for 1700 °C and 1800 °C are found to be 3.70 and 2.58, respectively. Parameter *s* values are decreased with increasing temperature and tend to converge to 2. This is in a good agreement with previous studies on the grain growth of W using conventional sintering [166] and SPS [176]. The change of the grain growth exponent *s* with sintering temperature implies that grain growth is affected by a combination of a number of various grain growth mechanisms. Decreasing *s* values in the present work are possibly related to the suppression of the grain growth inhibiting factors such as pinning by pores when the sintering temperature is increased.

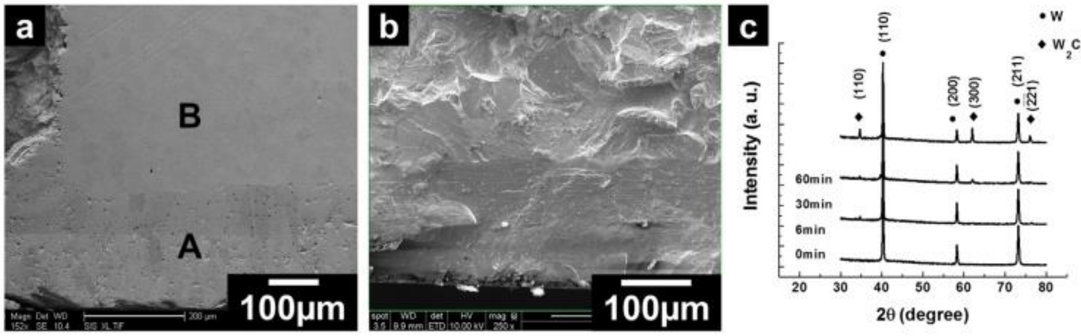

Figure 5.7 A cross-sectional view of W specimen processed by SPS at 1800 °C and 60 MPa for 30 min without (a) and with (b) BN coating. (c) XRD patterns of W processed by SPS at 1800 °C and 60 MPa with different holding times of 0 min, 6min, 30 min, and 60 min. W peaks (circle) and $W_2C_{0.85}$ peaks (diamond).

Although W densification using SPS is carried out during short time compared with conventional sintering methods, diffusion of carbon into specimens is observed. For W powder consolidation by SPS at 1800 °C and 60 MPa for 30 min, the respective SEM image reveals a clear interface between the two different zones (A and B) as shown in Figure 5.7(a). The average thickness of the A zone is about 253 μm. The cross-sectional hardness was measured at both locations. The average Vicker's hardness values were 1875 MPa and 363 MPa in A and B zones, respectively, which indicates that the two zones may contain different material phases. From EDS analysis, the A zone contains W atoms and carbon (2.20 wt%), while B zone is pure W. Figure 5.7(c) showed the diffraction patterns of the cross-section of the W specimens processed at 1800 °C for 0, 6, 30 and 60 min. Circle and diamond symbols indicate W and $W_2C_{0.85}$ peaks, respectively. The tungsten carbide peak increased with the holding time, which shows that the tungsten carbide phase is thickened with time. From the SEM, EDS and XRD results, the carburized zone A can be assumed to contain hexagonal $W_2C_{0.85}$. Carbon can diffuse from the graphite die, punch, and paper, which surrounds the W powder during the SPS. The carburization of W in HP and SPS has been explained also elsewhere [191-194].

The presence of carbon near the processed W powder does not guarantee the carbide layer formed during SPS consolidation. The solubility of carbon in W is the main factor for carbide layer formation [195]. The carburized layer is assumed to grow in a parabolic manner with holding time, which allows an approximate estimation of the diffusion coefficient of carbon in W ($D_C$). If it is assumed that the concentration of carbon at the interface is constant, $D_C$ can be obtained by the following equation.

$$x \sim (D_C\ t)^{0.5} \tag{5.2}$$

where $x$ is the tungsten carbide thickness, $D_C$ is the diffusion coefficient of carbon into W ($cm^2/s$) and $t$ is time. $D_C$ is estimated to be $3.86 \times 10^{-7}\ cm^2/s$, which is in a good agreement with a literature value [193].

To minimize the carbon diffusion, in some experiments (used for fabrication of the specimens W3BNC_1660_H30, W6BNC_1660_H30, and W9BNC_1660_H30, Table 5.1) the graphite paper was coated with a boron nitride spray ((MR-97, ZYP Coating, Inc., Oak Ridge, TN) before the powder was loaded. Boron nitride is known to block carbon diffusion during SPS [196]. However, a large reduction of the thickness of tungsten carbide layer is not achieved in the present study, which may be attributed to the high solubility of carbon in W. The thickness of the tungsten carbide layer was 191 µm (Figure 5.7(b)) when boron nitride coated graphite paper was used, which can be compared with 253 µm (Figure 5.7(a)) of the non-boron nitride coated case.

#### 5.1.3.2. Mechanical properties characterization

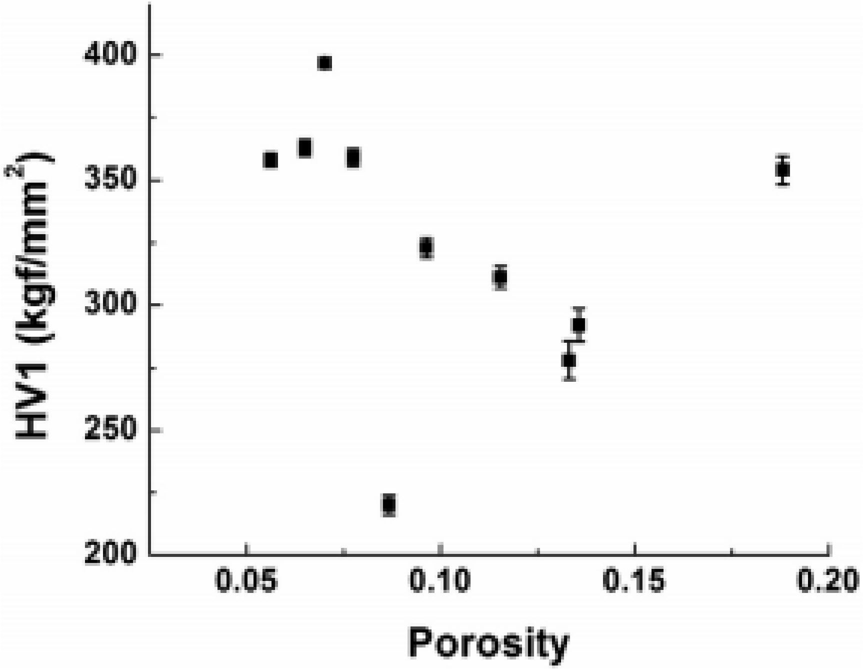

Figure 5.8 Vickers micro-hardness dependence on the porosity of W specimens consolidated by spark plasma sintering.

The polished specimens were subjected to Vickers micro-hardness test (M-401-H1 Hardness testing machine, Leco, Michigan) by applying a load of 1 kg for 10 s. The mean

Vickers hardness of each sample was determined by averaging 4 different indents at different locations of the sample. Figure 5.8 shows that hardness is generally increased with decreasing porosity. The measured maximum hardness is 397 kg/mm$^2$ and this is similar to the reference value (407.9kg/mm$^2$ for 96.10% relative density) [197].

The transverse rupture strength (TRS) was obtained with a Universal Testing System (5982 Instron, USA), by applying a load through a tungsten carbide ball-shaped indenter onto the disk-shaped W specimens. The equation utilized to calculate the TRS is given as follows:

$$\sigma_{\max} = \frac{P}{h^2}[(1+\nu)(0.4851\log\frac{a}{h}+0.52)+0.48] \tag{5.3}$$

where *P* is the measured load, *h* is the specimen thickness, *a is* the specimen radius and *v* the Poisson ratio (0.28 for W, as reported in [198]). A more detailed explanation of the TRS setup and procedures can be found in Ref. [122]. TRS values for 91% and ~ 95% specimens (W7_1860_H0, W6BNC_1760_H30) were found to be 705 MPa and 1006 MPa, which are larger than the three points bending strength value ( < 658MPa for 94.85% to 98.22 % relative density specimens) of W compacted by resistance sintering under ultra-high pressure (RSUHP) [199]. The higher strength found here can be attributed to the longer holding time compared with that (30s to 60s) of RSUHP method which may cause the formation of metastable W-based phases.

## 5.2. Effect of Oxidation on Densification behavior and Mechanical Properties of Molybdenum (Mo) Nanopowders Compacted by Spark Plasma Sintering

Molybdenum (Mo) powder-based components are used for many industrial applications due to the favorable physical, chemical and mechanical properties, such as high melting temperature (2623°C), high corrosion resistance and weldability, low thermal expansion coefficient and high thermal conductivity [200-202]. However, Mo products with large porosity and coarse grain structure exhibit poor mechanical strength. Therefore, studies to produce dense Mo products with small grain size by compaction of Mo nanopowders are in great demand.

A significant challenge in sintering of metal powders is the presence of a natural oxide layer at the surface of particles. In particular, metal nanopowders, which have higher surface area and energy, are easily oxidized compared to micron-sized powders. Particularly, Mo nanopowders generally show the pyrophoric behavior when exposed to an air, so special care is required to avoid the possible formation of a surface oxide during powder handling and storage.

The surface oxide layer in the powders hampers the mass transport and therefore impedes diffusion between the powder particles [203]. Munir et al. [16], studied the role played by surface oxide layers in the kinetics of sintering of metal particles, and showed that the onset of sintering was delayed by the presence of the surface oxide phase. Specifically, palladium particles with surface oxide layers modified the sintering mechanism from grain boundary diffusion to surface diffusion below the oxide dissociation temperature. By applying the sintering temperature higher than the oxide dissociation temperature of palladium, the mechanism of the sintering of palladium converts back to the grain boundary diffusion [204].

The creep parameters of Mo with micron-scale grain size have been studied extensively [42, 205, 206]. The creep exponent ($n$) was determined to be approximately 4.85, indicating the dislocation creep was controlled by the dislocation climb mechanism, generally observed in most polycrystalline metals [88]. The creep tests under 1500 °C – 1600 °C and 62 MPa revealed the $n$ value of 4.5 with an activation energy ($Q$) of 480 kJ/mol, which was slightly higher than for lattice diffusion ($Q_l$, 405 kJ/mol) [207]. From compression and tension tests, Carvalhinhos et al. [208] found $n$ to range from 5.2 to 5.8 with $Q$ ranging from 257 kJ/mol - 369 kJ/mol. However, the creep parameters for nano-grained Mo at elevated temperatures (~0.5$T_m$) cannot be directly experimentally found due to grain growth during the creep test. Also, the oxide effect on the densification mechanism of Mo nanopowders at high temperatures has not been studied. From aid from grain growth inhibitors such as ZrC particles located at the grain boundaries, creep tests of a Mo alloy (300 nm average grain size) with 0.8 mol% dispersed zirconium carbide (ZrC) with the at 1500°C indicated superplastic behavior ($n = 2.44$) [200, 201, 209]. At near ambient temperature, nanoindentation creep data of Mo thin film (30nm – 40 nm grain size) showed that the creep exponent was close to 6.67 – the value related to the thermally activated glide-controlled creep [210, 211].

The phase diagram of Mo-O by Phillips and Chang [212] shows that about four stable oxides exist below the temperature around 820 °C: $MoO_2$, $MoO_3$and two intermediate phases $Mo_4O_{11}$ and $Mo_9O_{26}$ in composition [213]. $MoO_2$ melts around 2327 °C, but can be decomposed to Mo (solid) and $O_2$ (gas) if the oxygen partial pressure in the furnace is equal to or lower than $7.5 \times 10^{-2}$ (Pa) [214]. Otherwise other oxides phase like $MoO_3$, $Mo_4O_{11}$ and $Mo_9O_{26}$ can be melted around 820 °C and can be vaporized at the temperature from 1150 °C to 1450 °C [213, 215].

Lee et al. [216] studied the influence of the oxygen concentration in the micron-sized Mo powders on the grain size and hardness of pellets compacted by spark plasma sintering (SPS). This resulted in a reduced oxygen content, using metallic calcium as a deoxidizer. It was shown that, compared to the samples with a high oxygen content, samples with lower oxygen content had larger hardness values due to the higher density and smaller grain size enabled by the reduction of oxide impurities at the Mo grain boundaries. It was reported that the impurity level of the oxygen can distort the atomic structure near the grain boundaries and therefore facilitate defect or Mo diffusion [217]. However, the removal of the surface oxide layer during *in situ* sintering should provide great benefit to further the production of small grain sized, dense Mo parts.

Some *in situ* oxide removal methods have been attempted for sintering of metal powders. First, sintering under the $H_2$ atmosphere can be performed to reduce the oxide. Majumdar *et al*. removed the oxide phase by holding Mo powders at 900 °C for 15 min in the presence of $H_2$ gas during conventional oven sintering [218]. However, *in situ* oxide reduction during sintering, if possible without using the flammable hydrogen gas, is highly desirable considering the time and safety. Second, the oxide coating of metal powders can be removed by the addition of the carbon powder to the starting powders, which results in the reaction of carbon and oxide (carbothermic reaction). This method has been used to remove the surface oxide during the pressure-assisted or pressure-less sintering of SiC [219-221], $B_4C$ [222, 223] and $ZrB_2$ [224]. Since the oxide is removed via the gas phase, gas diffusion is the rate-limiting step for the complete removal of the oxide phase [222]. Third, during SPS, surface cleaning from the presence of high-temperature plasma between particles can be used for an *in situ* oxide removal [18, 19]. Kim et al. [225] showed that the oxide phase is removed by holding the temperature at 1300 °C for 1 hour in the middle of the SPS process for $B_4C$ sintering. The second and the third above-mentioned methods have not been applied to the sintering of Mo nanopowders.

In the present study, the effect of oxygen on densification kinetics of Mo nanopowders was investigated using *in situ* methods [103]: carbothermic reduction and particle surface cleaning. The efficiencies of each oxide reduction method are compared. The sintering constitutive parameters based on the regression analysis of the experimental data on the porosity evolution using the continuum theory of sintering wss determined [55, 84, 102] The effect of the oxygen content on the density and mechanical properties of the sintered samples is also discussed.

### 5.2.1. In situ oxide removal strategy

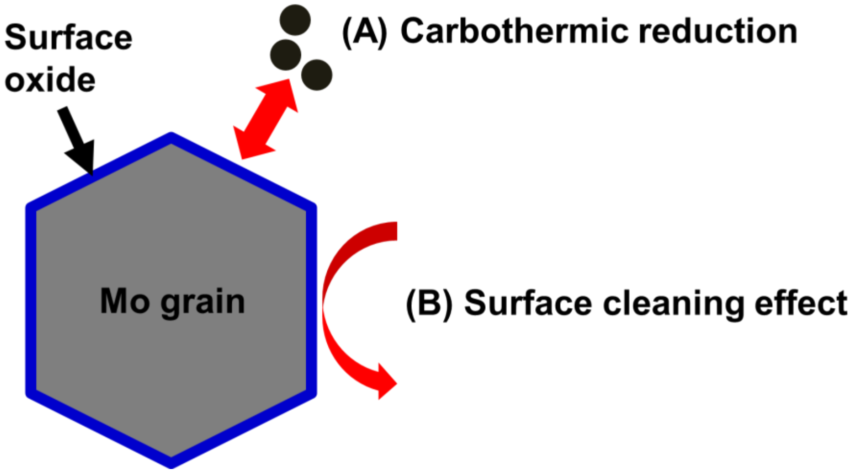

Figure 5.9 *In situ* oxide reduction strategies during sintering. (a) carbothermic reduction and (b) surface cleaning effect

Two strategies were employed to remove the oxide during sintering of the surface-oxidized Mo nanopowders.

In the first strategy, the reaction of Mo oxides with carbon powders was employed during the SPS process (Figure 5.9(a)). The carbothermic reduction of nano-sized $MoO_3$ to Mo was studied by Saghifi et al. [226, 227]. Using differential temperature analysis and temperature gravimetric analyses, the following reactions were suggested:

$$2MoO_3 + C = 2MoO_2 + CO_2,\ \Delta G\ (298K) = -\ 122.3\ kJ/mol \tag{5.4}$$

$$MoO_2 + C = Mo + CO_2,\ \Delta G\ (298K) = 130\ kJ/mol \tag{5.5}$$

Based on this analysis, Saghifi et al. [226, 227] showed two steps for the carbothermic reduction of $MoO_3$ to Mo. First, $MoO_3$ is heated to 600 °C with holding for 1 hour for the complete reduction of $MoO_3$ to $MoO_2$. Next, heating to 1000 °C for 1 hour provides the reduction of $MoO_2$ to Mo.

In the present study, the similar steps were applied during Mo nanopowders compaction by SPS. The carbothermic reduction produces CO or $CO_2$ gases. Since gas diffusion is a critical factor for densification [222], a low uniaxial pressure of ~ 15 MPa was used to facilitate outgassing at the initial and intermediate stages of sintering in the SPS vacuum chamber. At the end of the carbothermic reduction, the pressure was increased to 60 MPa to enhance densification.

For the second strategy, the oxide can be removed by the electric current flow through the Mo particles during SPS, using the surface cleaning effect (Figure 5.9(b)). The high energy electric field generated by high electric current removes the oxide layer [18, 19]. A holding stage at the temperature (800°C) lower than the onset temperature (~ 900°C, section 5.2.3.3) of the densification of the samples was used.

### 5.2.2. Experimental procedures

Commercial Mo nanopowders (US Research Nanomaterials, Inc., Houston, USA, average size 200 nm) with a labeled purity of 99.9% (metal basis) and carbon black nanopowders (MTI Corporation, Richmond, USA, average size 50 nm) were used for this research. The theoretical densities of Mo and carbon nanopowders were measured by the pycnometer (AccuPyc 1330, Micromeritics Instrument Corp., Norcross, USA).

The sintering process was carried out using a SPS system (Dr. Sinter SPSS-515, Syntex Inc., Japan) with a tooling setup made from the EDM4 graphite (Poco Graphite, Inc., Texas, USA). A 0.15 mm-thick graphite paper wrapped the powder to prevent adhesion between the sample and the tooling. An optical pyrometer (IR-AHS2, Chino, Japan) was used to detect the temperature at the 2.5mm depth hole in the graphite die.

SPS conditions to investigate the consolidation behavior of the surface-oxidized Mo nanopowders included initial ramping to 600°C in 10min and sequential heating from 600 °C to the maximum temperature (1100˚C, 1200˚C, 1300˚C or 1800˚C) with 60 MPa applied pressure, 100 ˚C/min with no holding time under vacuum. Control experiments were performed to obtain the thermal expansion coefficient of the graphite die set was carried out under the same SPS conditions without the Mo nanopowders. A k-type thermocouple was directly into the Mo nanopowders to measure the temperature.

For the regression analysis, the data obtained at 1200 °C was used from the above experiments.

For the multistep pressure dilatometry approach, with 100 °C/min and the minimum pressure under vacuum, the surface oxidized nanopowders were heated to 950 °C which is the temperature higher than the melting point of most of the Mo oxides except $MoO_2$ [215]. After stabilization of the temperature during the holding stage, a few successive jumps of the pressure were applied to measure the variation of the strain rate at each pressure jump.

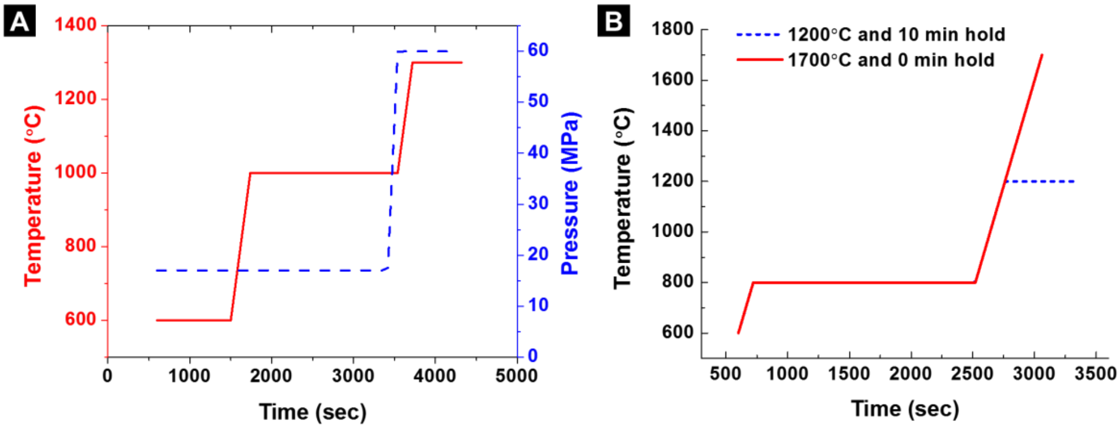

Figure 5.10 Temperature and pressure profile for (a) first strategy: carbothermic reduction and (b) second strategy: surface cleaning effect by SPS

For preparing the carbothermic reduction (Figure 5.9(a)), the Mo nanopowders were mixed with carbon nanopowders in the cyclohexane by ultrasonication for 30 min. Mo + C nanocomposite suspension was frozen by liquid nitrogen for 10 min and subjected to freeze-drying (Freezone 1, Labconco, Kansas City, USA) at -50 ˚C for 24 hours. The following steps were used as shown in Figure 5.10(a): A. ramping to 600°C with 17 MPa pressure, B. holding at 600°C for 15 min (see (5.4)), C. ramping to 1000°C with 100°C/min, D. holding at 1000°C for 30 min then increasing the pressure to 60 MPa during the last 2 min of the holding stage (see (5.5)), E. ramping to 1300°C with 100°C/min. G. holding at 1300°C for 10 min. We used shorter holding time (15 min) compared to the that (60 min) suggested by Saghifi et al. since the pressure makes the diffusion distance between the carbon and oxide shorter in SPS case. For comparison, an SPS test was conducted under the same conditions without the addition of carbon to the Mo powders.

To employ the second strategy (Figure 5.9(b)), the powders were heated to 800 °C under 60 MPa pressure and held for 30 min, and then heated to the final sintering temperatures of 1200°C or 1700°C with 100°C/min and 0 or 10 min holding time as shown in Figure 5.10(b). The 800 °C used for the soaking stage is the temperature before the onset (~900°C in Figure 5.16(a)) of the sintering of Mo to remove the oxide phase. The final sintering temperatures were chosen to see the change of the grain size and density with temperature if the oxide is removed by the second strategy. For comparison, a test was conducted under the same conditions without the soaking stage at 800 °C.

The apparent densities of the sintered samples were measured by the Archimedes method. Since the theoretical density of the sintered Mo pellets is not fixed due to the evaporation of the Mo oxide during the SPS, the apparent densities were presented in this study. For the regression approach (section 5.2.3.3), we assume that there is no evaporation of Mo oxide, and use the relative density calculated with the theoretical density of Mo nanopowders obtained by pycnometer. The powder (or grain) size and composition were assessed by the scanning electron microscopy (SEM), (FEI Quanta 450, Thermo Fisher Scientific, Waltham, USA) and Energy-dispersive X-ray spectroscopy (EDS) (Oxford Instruments, Abingdon, UK). The composition of the powders and pellets were obtained by the average of 6 measurements by EDS. The well-polished samples were etched with Murakami's reagent (Solution of 200mL DI water, 10g KOH and 10g $K_3Fe(CN)_6$) for 30 sec. The transverse rupture strength (TRS) of the compacted Mo pellets was measured. The experimental method to measure the TRS can be found elsewhere [228].

### 5.2.3. Results and discussion

#### 5.2.3.1. Powder characterization

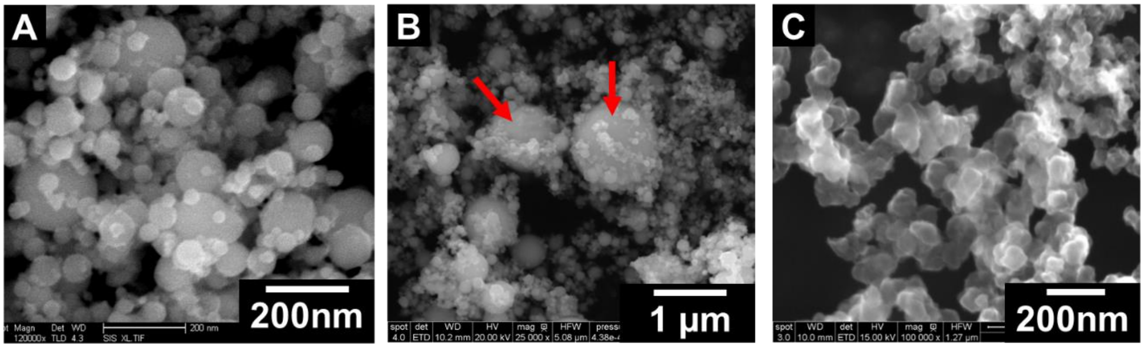

Figure 5.11 Scanning electron microscopy images (a) high magnification of Mo powders, (b) lower magnification of Mo powders. Red arrows indicate large Mo particles, (c) carbon powders.

As shown in Figure 5.11(a) and (b), the powders have a round shape and are agglomerated. By the particle size analysis using image analysis software (ImageJ, National Institutes of Health, USA), the powders showed a broad size distribution from 50 nm to 2 μm with an average particle size of 200 nm. The micron-sized particles (non-agglomerated) are indicated as red arrows shown in Figure 5.11(b). The theoretical density of Mo is 10.2 $g/cm^3$. The carbon nanopowders have an average particle size of 50 nm and show agglomeration (Figure 5.11(c)).

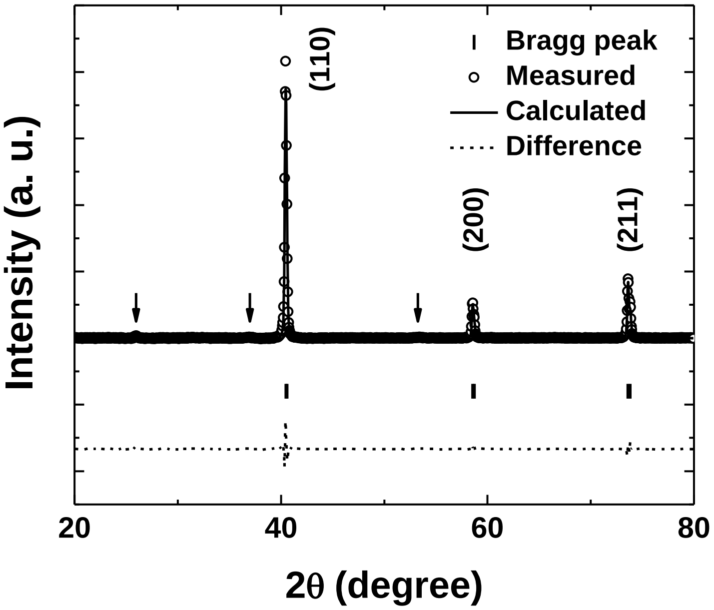

Figure 5.12 X-ray diffraction results for as- received Mo nanopowders

The surfaces of Mo nanoparticles are highly oxidized and showed 27.3 at% of oxygen by EDS. From XRD results in Figure 5.12, the high 3 peaks indicate Mo (ICSD collection code # 00-042-1120). Other small peaks indicated by arrows are from the existence of $MoO_2$ (ICSD collection code # 01-078-1073). The theoretical density of Mo is 10.2 g/cm$^3$. The density measurement by the pycnometer showed 9.68 g/cm$^3$ due to the low theoretical density of Mo oxide ($MoO_2$: 6.47 g/cm$^3$ and $MoO_3$: 4.69 g/cm$^3$).

### 5.2.3.2. Surface oxidized Mo nanopowders consolidated by spark plasma sintering

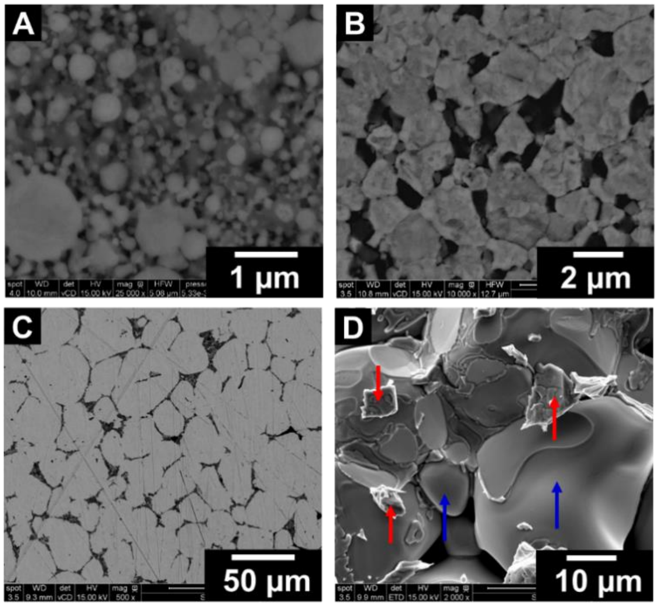

Figure 5.13 SEM image of polished Mo pellets densified at (a) 1100 °C, (b) 1300 °C and (c) 1600 °C respectively. (d) Mo oxide debris (red arrows) and Mo grains (blue arrows) of fractured Mo pellets compacted at 1700 °C. The white and black color in SEM phase images (a to c) indicate Mo and Mo oxide phases, respectively.

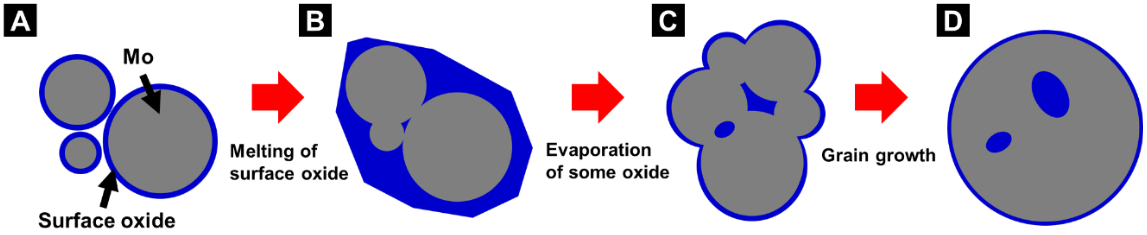

Figure 5.14 Schematics of the behavior of the surface oxide during SPS of Mo nanopowders

Figure 5.13 displays SEM images of Mo pellets compacted at different temperatures under the same conditions of 60 MPa, 100 °C/min, 0 min holding time and vacuum. EDS analysis revealed that the black regions correspond to the Mo oxide, white regions were from Mo (Figure 5.13(a) to (c)) and the oxide debris (red arrows in Figure 5.13(d)) between the grains of the fractured samples. As shown in Figure 5.13(a), the melted oxide was distributed between Mo and some Mo particles are connected by necks. At 1300 °C, the neck areas between the particles are increased and the average grain size is increased up to about 2 μm (Figure 5.13(b)). After the neck area increased, the grain size increases rapidly with increasing the sintering temperature but without densification (Figures 5.13(b) to (d)), which will be discussed later.

We can see the melted Mo oxide phase with SEM and EDS analysis. However, $MoO_2$ which is observed in the starting Mo nanopowders by XRD is known to be melted at 2327 °C. Therefore we think $MoO_2$ was transferred to $MoO_3$ or other non-stoichiometric oxides phase during the SPS by pick up the oxygen other from the chamber or the other powders.

The behavior of the surface oxide is schematically shown in Figure 5.14. The neck formation between Mo powders is inhibited by the liquid film of the oxide, resulting in the retardation of the onset of the sintering and the grain growth [229] (Figure 5.14(a)). After melting of the surface oxide layer, the molten oxide moves to the porous regions between the Mo particles (Figure 5.13(a) and 5.14(b)). Similarly to the Ostwald ripening during liquid phase sintering [230], the shrinkage of nanoparticles and the growth of the large grains occur at this stage through the dissolution and precipitation of atoms. With increasing temperature, most of the oxides are evaporated and diffuse out to the chamber through the open porous path, but some oxides remain due to a block of the diffusion path for the gas due to the densification. Also, the $MoO_2$ was remained due to the high melting point. Due to evaporation, the amount of the oxide in the samples is reduced, and then the neck area between the Mo particles increased, simultaneously resulting in the grain growth and densification. Some oxide is trapped in the grains during the coalescence of the grains (Figures 5.13(b) and (c), and Figure 5.14(c) and (d)). With an increase in the sintering temperature, the grains become larger and then the melted, non-melted or evaporated oxide occupy the grain boundary regions and can recrystallize during the cooling stage (Figures 5.13(c) and Figure 5.14(d)).

The surface oxides have two effects on sintering behavior, depending on the quantity. First, when there are large amounts of the oxide phases near the Mo grains, the oxide can act as a physical obstacle to contact between the Mo grains, resulting in a delay of the neck formation and of the onset of densification [16]. Otherwise, small amounts of oxygen atoms near the grain boundary regions can affect the grain growth behavior. This impurity level of the oxygen can distort the atomic structure near the grain boundaries and therefore facilitate defect or Mo diffusion. Therefore, Mo grains with a small amount of oxygen can grow faster than those of pure Mo [217].

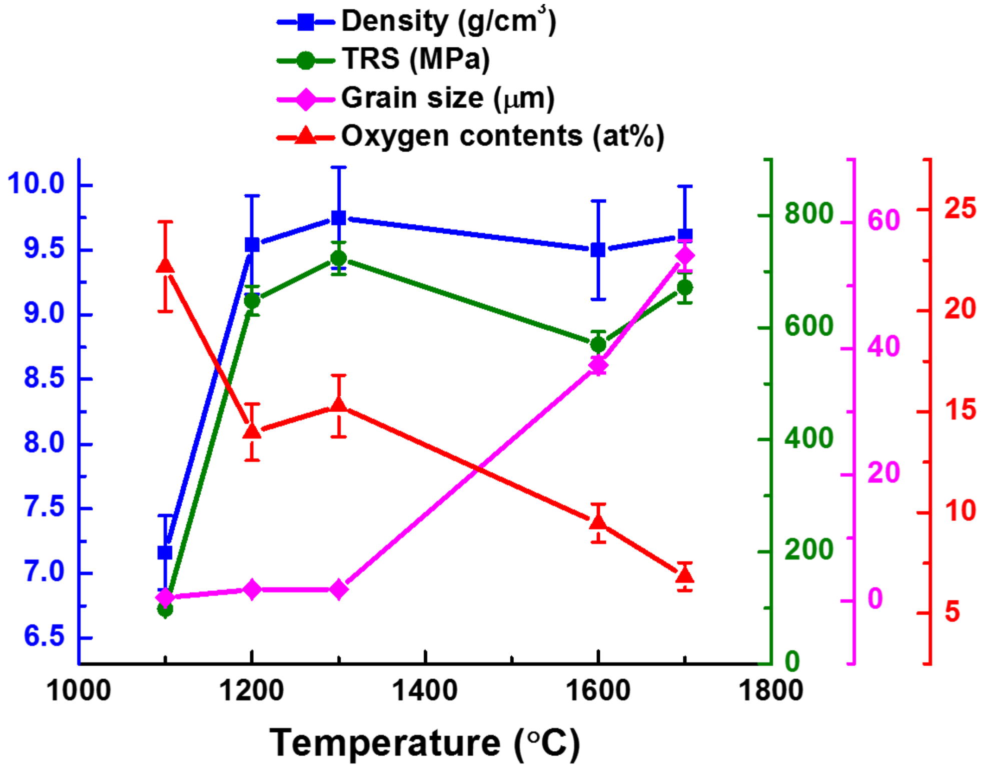

Figure 5.15 The density, TRS, grain size and oxygen content change with sintering temperature 1100˚C, 1200˚C, 1300˚C, 1600˚C and 1700˚C in SPS with 60 MPa, no holding time and vacuum

The densification map indicating the density, TRS, grain size and oxygen content is shown in Figure 5.15. The oxygen content decreased with increasing sintering temperature due to the evaporation of the oxide phase, which induced the rise of the density at temperatures below 1300 °C. However, the density of the samples did not increase at temperatures > 1300 °C due to the slow Mo atom diffusion and interface reaction through the oxide at the grain boundaries, as shown in Figures 5.13 (c) and (d) and Figure 5.14(d). Because of the high density of the Mo pellets, for temperatures > 1300 °C, the fast diffusion path for the oxide gas is almost blocked, so that the samples cannot be densified easily with an increase in the sintering temperature. Although the oxygen content is decreased by the slow diffusion of gas, the density of the samples at 1600 °C and 1700 °C is even lower than that at the 1300 °C, presumably due to carbon diffusion into the edge of the samples from the graphite paper and die [231].

The TRS is dependent on the porosity and grain size. However, the TRS shows a greater dependence on the porosity rather than on the grain size (Figure 5.15). The porous regions are filled with the melted oxide (Figure 5.13 and 5.14), which promotes the embrittlement, and the presence of the oxide phase dominates the overall mechanical behavior.

As analyzed before, the surface oxide limits the densification and increases the grain size enormously during the Mo nanopowder sintering. Therefore, in order to increase the density of the Mo pellets, various in situ oxide reduction methods have been employed, as described in section 5.2.1. and 5.2.2.

### 5.2.3.3. Densification mechanism of oxidized Mo nanopowders

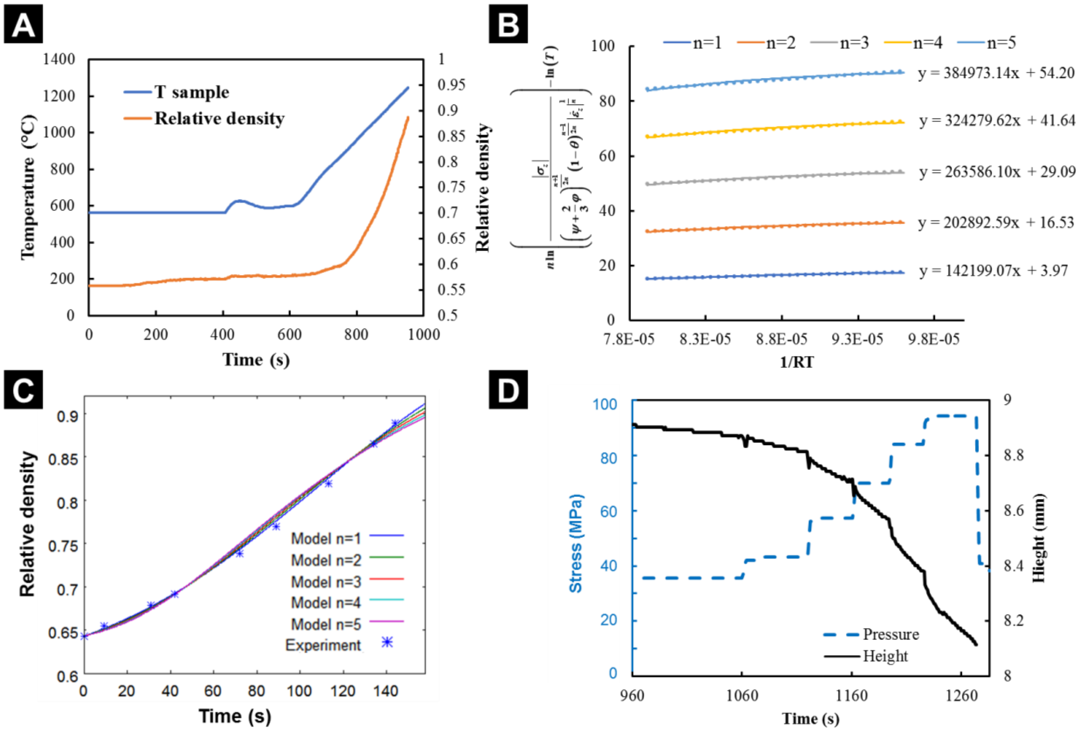

Figure 5.16 The steps to find a sintering mechanism of Mo nanopowders compacted by SPS. (a) Experimental SPS results, (b) Linearization curves for each n values, (c) Modeled/experimental relative density curves using identified parameters from regression approach for each tested n values, (d) Change of pressure and sample height in multistep pressure method

The densification is small (increase in relative density of 4.5%) until 900 °C, which is higher than the melting point of most of Mo oxides except $MoO_2$ (Figure 5.16(a)). This 4.5% increase of density is possibly due to the particle rearrangement and pore filling by the melted oxide. After melting of some oxides, the particles become connected, forming necks and starting densification > 900°C. The experimental densification data (Figure 5.16(a)) were used to plot the linearized densification curves for different *n* values (1 to 5) using (3.21), as shown in Figure 5.16(b). The relative density ranges from 0.64 to 0.89 are used from Figure 5.16(a) to exclude the effect of the grain growth on the sintering kinetics. $A_0$ and Q values for each *n*, using (3.21), are listed in Table 5.2.

Figure 5.16(c) shows the modeled/experimental relative density curves through the regression analysis of the constitutive parameters for each of the tested *n* values (Table 5.2). However, comparison of the experimental and theoretical density curves do not indicate a unique *n* value, therefore the complementary SPS multistep pressure dilatometry was used to find the distinctive *n* value. Figure 5.16(d) shows the change of pressure and sample height during the multistep SPS of for an isothermal stage at 950 °C. When there is a jump of the pressure, the slope of the sample height is altered accordingly, indicating the change of the strain rate for each jump. From Figure 5.16(d), the average *n* value estimated using (3.22) is 4.86. With this average *n* value, one can expect the value of parameter *Q* to be in the range from 324 kJ/mol (n = 4) to 385 kJ/mol (n = 5), as shown in from the Table 5.2 regression-based data.

Table 5.2 Creep parameters identified from regression approach of the porosity evolution curve in Figure 5.16(a)

| n | 1 | 2 | 3 | 4 | 5 |
|---|---|---|---|---|---|
| Q (kJ/mol) | 142.20 | 202.89 | 263.59 | 324.28 | 384.97 |
| $A_0$ (Pa·s/K) | 1.881E-2 | 6.624E-8 | 2.334E-13 | 8.224E-19 | 2.898E-24 |

The *n* and *Q* values indicate that the sintering mechanism after melting of the Mo oxide is dislocation creep controlled by dislocation climb, which is the same mechanism (*n* = 4.85 - 5) identified based on the creep test of Mo with a grain size of 150 μm [42]. The dislocation climb mechanism requires the lattice diffusion [88], and indeed, the activation energy obtained (324.28 kJ/mol to 384.97 kJ/mol) is similar to the reported $Q_l$ of 405 kJ/mol [42]. The smaller particle size of the Mo nanopowders may be the reason for the lower activation energy.

Prior to melting of the oxide, diffusion of Mo atoms is limited and only can be possible via the surface diffusion mechanism from the existence of the surface discontinuity in the surface layer caused by the compaction pressure [204], Mo precipitation from Mo oxide, or via Mo diffusion through Mo oxide from other particles. When the inter-particle necks are formed after the oxide layer melting, dislocation creep may be the most probable sintering mechanism in this temperature range (about $0.4T_m$). Diffusional creep ($n = 1$) requires high temperatures of about $0.9T_m$. Grain boundary sliding ($n = 2$), which is often observed during creep of nanograined materials indicates grain boundary diffusion, is restricted in this case due to the presence of the oxide at the grain boundaries. When the oxide is removed, diffusion through the grain boundary has a critical role due to the large grain boundary area of Mo nanopowders. Since typically the activation energy for grain boundary diffusion ($Q_{gb}$) is lower than $Q_l$, a lower activation energy is expected without the oxide. Indeed, our on-going studies show that the densification mechanism of Mo nanopowders without surface oxide is the grain boundary sliding controlled by the grain boundary diffusion at the same temperature range (of about $0.4T_m$).

### 5.2.3.4. Carbothermal reduction of oxidized Mo nanopowders during SPS

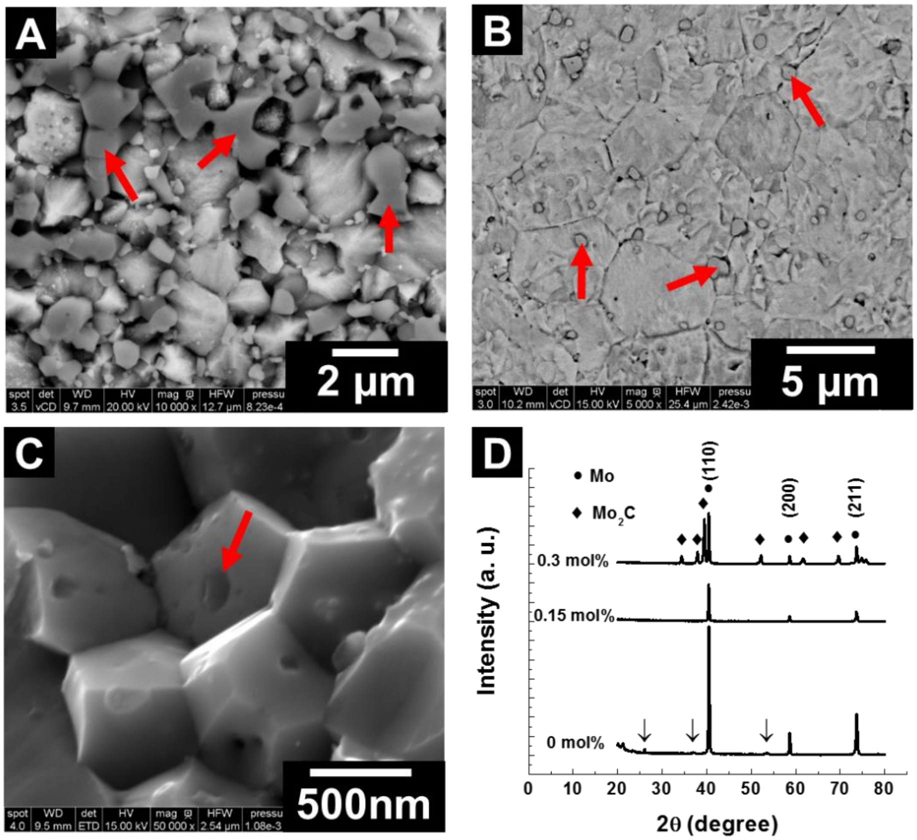

Figure 5.17 SEM images of SPSed Mo pellets consolidated with different carbon contents: (a) No carbon added. (b) 0.15 mol% and (c) 0.3 mol% carbon added. Red arrows indicate the Mo oxide phase. (d) XRD of compacted Mo pellets. The circle and diamond symbols indicate Mo and $Mo_2C$ phases, respectively. Black arrows indicate the peaks corresponding to $MoO_2$

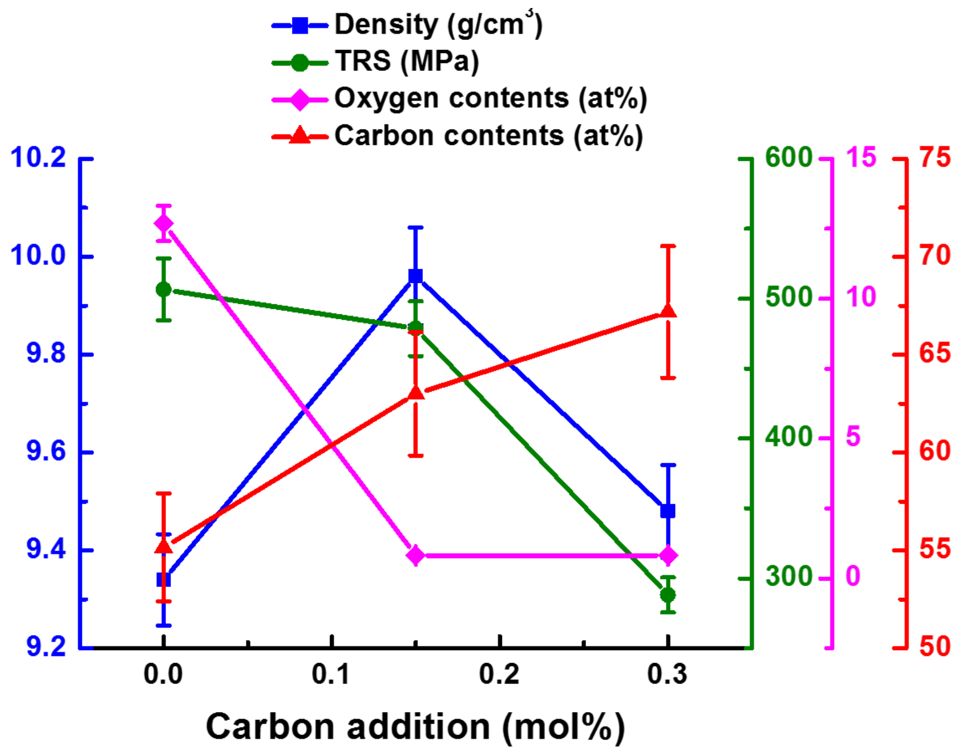

Figure 5.18 Effect of carbon addition on density, TRS, oxygen contents, and carbon contents of Mo pellets compacted by SPS.

Mo with different amount of added carbon was densified by SPS under the same conditions (1300 °C, 60 MPa, 100 °C/min and 10 min holding time, Ar gas). Figures 5.17(a) to (c) show the SEM images of the obtained samples with different additions of carbon. The corresponding XRD pattern from the samples is shown in Figure 5.17(d). Figure 5.18 shows the effect of the carbon addition on the density, TRS, oxygen amount, and carbon contents.

There is a high amount of oxygen without carbon addition, as confirmed by SEM (Figure 5.17(a)) and EDS (Figure 5.18). Black arrows indicate the XRD peaks of the $MoO_2$ phase (Figure 5.17(d)) [232]. Due to the addition of the carbon, oxygen amounts were reduced to almost 1 at%, as shown in Figure 5.18. The oxide peaks are removed when 0.15 mol% of carbon was added, and only Mo peaks were identified (ICSD # 76147) [233]. When carbon additions were increased to 0.3 mol%, the $Mo_2C$ peaks (ICSD # 1326) [234] were identified. However, as shown in Figures

8A to C, the oxygen atoms are still present (red arrows). This means that the oxide was reduced with the addition of carbon, yet was not completely removed. The oxygen impurities can still be present in some amounts as a crystalline or amorphous oxide phases, or dissolved in the Mo lattice, which is below the detection limit of XRD. By reducing the oxide phase at the grain boundaries, the density of Mo samples increased to 9.96 g/cm$^3$ for the 0.15 mol% carbon (Figure 5.18), which is much higher than that compacted at a higher sintering temperature (maximum apparent density: 9.77 g/cm$^3$ as shown in Figure 5.15). Due to the low theoretical density of $Mo_2C$ (9.18 g/cm$^3$) and a possible remaining carbon, which did not react with the oxide, the density of the sample with 0.3 mol% carbon addition is lowered compared to that of the sample with 0.15 mol% carbon (Figure 5.18).

Although the density of the sample increased, and the oxide content decreased by the carbothermic reduction compared to the sample without carbon addition, therefore the TRS value was reduced, which is proposed to be due to the increased amount of the remaining carbon which acts as an internal lubricant (Figure 5.18) [222].

### 5.2.3.5. Surface cleaning of oxidized Mo nanopowders during SPS

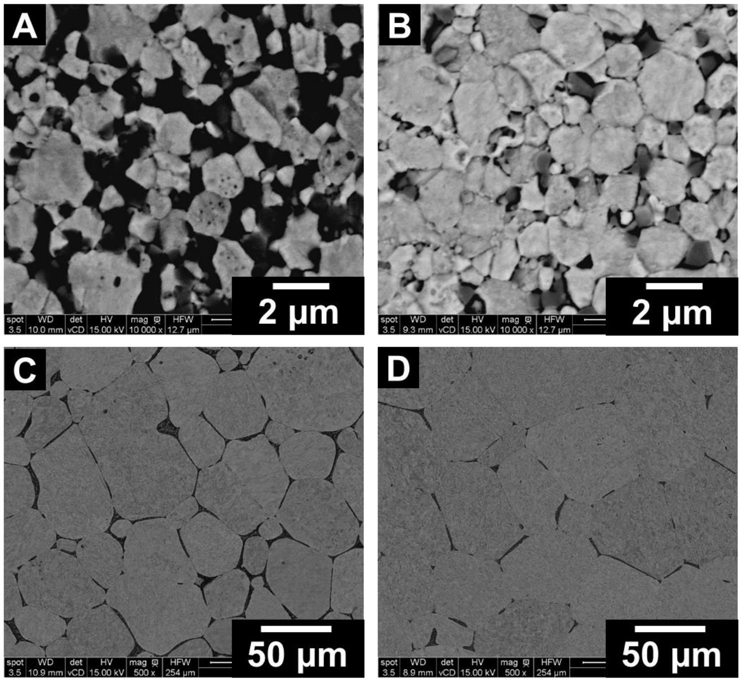

Figure 5.19 SEM phase images of SPSed Mo pellets without (a and c) and with (b and d) soaking stage at 800 °C with the final sintering temperatures of 1200 °C (a and b) and 1700 °C (c and d).

Table 5.3 Properties of sintered samples with or without a holding stage at 800 °C

| Sintering temperature (°C) | Holing at 800 °C | Oxide contents (at%) | Density (g/cm$^3$) | Grain Size (µm) | TRS (MPa) |
|---|---|---|---|---|---|
| 1200 | X | 12.6 | 9.30 | 1.61 | 753.31 |
| 1200 | O | 10.3 | 9.66 | 1.74 | 859.99 |
| 1700 | X | 6.8 | 9.61 | 54.75 | 671.71 |
| 1700 | O | 4.5 | 9.94 | 73.95 | 711.67 |

A holding stage at 800 ˚C was used, after which the temperature was increased to a maximum of 1200 ˚C or 1700 ˚C. As shown in Figure 5.19 and Table 5.3, the oxygen amount in the samples was reduced after holding at 800 ˚C, but not as dramatic as in the carbothermal reduction case (Section 5.2.3.4). The density and TRS with the holding stage at 800 ˚C are of higher values than those of Mo pellets processed without the holding stage (Table 5.3), which can be explained by the reduction of oxygen. The samples sintered at 1700 ˚C with the holding stage at 800 ˚C showed high density (9.94 g/cm$^3$) but large average grain size (73.95 μm). Compared with the samples obtained by the carbothermic reduction with 0.15 mol% carbon, the samples sintered at 1700 ˚C with the holding stage at 800 ˚C have a higher TRS even despite their larger grain size due to the absence of carbon (Figure 5.18 and Table 5.3).

In summary, during SPS, the surface oxide impedes diffusion, which limits the densification. The dissociation of the surface oxide accelerates the diffusion mass transport, but the remaining oxide surrounds the Mo grains, still hindering the densification. In the present study, increasing the sintering temperature did not enhance the density of the samples; instead, the grains of Mo grew rapidly. The sintering mechanism of the Mo nanopowders with an oxide layer was obtained by the regression analysis of the experimental data on the regular SPS-based densification, and the SPS multistep pressure dilatometry. The $n$ and $Q$ values are 4.86 and 324.28 kJ/mol to 384.97 kJ/mol, respectively, indicating dislocation creep controlled by lattice diffusion. The carbothermic reduction method can successfully reduce the oxide amount in the Mo pellets and increase the apparent density to 9.96 g/cm$^3$, yet resulting in a decrease of the TRS due to the increase of the remaining carbon content. Otherwise, having the holding period reduced the oxide amount, but not as dramatic as in the carbothermal reduction case.

## 5.3. Consolidation of Molybdenum Nanopowders by Spark Plasma Sintering: Densification Mechanism and Metal Mirror Application

Metallic mirrors are planned as part of diagnostic systems which relay optical signals from the plasma to measurement devices for the International Thermonuclear Experimental Reactor (ITER) [235]. First mirrors (FM), those in close proximity or direct sight line of the ITER plasma, will be subject to harsh environmental conditions that deteriorate their reflectivity and performance. Molybdenum has been utilized as a FM material due to its low sputtering yield under plasma sputtering conditions [236]. Single crystal (SC) Mo mirrors have shown the best performance under erosion intensive conditions characteristic of fusion plasmas. However, the technology to fabricate large-format SC mirrors (> ~120 mm diameter), needed for ITER, is not commercially available. Eren et al. [237] fabricated nanocrystalline (NC) metallic mirrors with 70 nm to 100 nm grain size by Mo coating (thickness of 1 μm) onto a polished stainless steel substrate using magnetron sputtering. The spectral reflectivity performance of the NC mirror was comparable with a SC Mo mirror[238]. Sintered NC Mo is a candidate process for large-format FMs due to lower cost than SC, comparable performance, and improvement in mechanical performance over coated substrates. Also, a bulk Mo metal mirror made by sintering should have the longer life expectancy than the one made by the coating method which requires long time and price to produce the thick metal mirror. Therefore, the sintering of a Mo metal mirror with nanoscale grain size should be explored.

The fabrication method of Mo metal mirror with a grain size less than 1 μm and with greater than 90% relative density is difficult due to the large grain growth of metal nanopowders during sintering. Srivatsan et al., showed that the densification of Mo nanopowders (100 nm) using plasma pressure compaction method resulted in grain size of 1 μm to 3 μm with 97% relative density. Apparently, only Park et al. [239], obtained the Mo compact with ultra-fine 500 nm grain size with

90% relative density using a two-step sintering method with 20 hours holding time. Also, the description of the fabrication of the Mo mirrors by the sintering route tested for reflectivity is limited in the literature [238, 240, 241]. Voitsenya et al. [242] indicated the possibility to make W and Mo mirror with 250 nm – 350 nm grains size using resistance sintering and provided the reflectivity results, however, only W sintering conditions were described [199]. To advance the research on the fabrication of metal mirrors for nuclear engineering applications and to fabricate bulk metal mirrors with nano-size grains (<100 nm), the study of the densification behavior for Mo nanopowders is required.

The commercial Mo nanopowders made by the wire explosion method [243] suffer from two disadvantages: large surface oxidation during handling and storage and broad particle size distribution from 50 nm to 2 μm. These powder properties prevent the fabrication of Mo pellets with nano-size grains. Kim et al. [229, 244], showed the densification behavior of Mo nanopowders fabricated from the milled $MoO_3$ by $H_2$ reduction. Freshly synthesized Mo nanopowders using this method showed narrow particle size distribution with an average particle size of 100 nm.

In the present study, for the first time, the NC Mo disks with an average grain size of 400 nm were fabricated by SPS. Sintering kinetics was analyzed using the *in situ* methods [103] of the determination of the sintering constitutive parameters based on regression analysis of the porosity evolution curves by the continuum theory of sintering [55, 84, 102]. The reflectivity and microstructure of the SC and NC Mo mirrors were evaluated before and after plasma exposure using the PISCES-A linear plasma device.

### 5.3.1. Experimental procedure

A commercial $MoO_3$ powder with a purity of 99.9% (US Research Nanomaterials, Inc., Houston, USA) was used as raw material. The powder was wet-milled using a high energy ball milling machine (Pulverisette 6, Fritsch, Germany) run at 300 rpm for up to 30 hours in air with SS304 balls (diameter: 5mm) and jar (250ml). The charge ratio is 12:1 for the balls and powders. Due to the small size (< 500 nm) of milled $MoO_3$ nanopowders, the large surface tension induces the agglomeration of powders during the oven drying method. Thus, the freeze-drying method was used to prevent the agglomeration during the drying stage, and Tert-butyl alcohol (TBA) was chosen due to the high melting temperature (25 °C) and miscibility match with $MoO_3$ powders [245]. The milled $MoO_3$ powder with TBA was frozen by liquid nitrogen for 10 min and dried at -50 °C for 48 hours in the freeze drier (FreeZone 1, Labconco, MO, USA). The freeze-dried $MoO_3$ powders were heated to 550 °C with 5 °C/min and holding for 30 min and to 850 °C with 5 °C/min and holding for 50 min or 80 min under the $H_2$ atmosphere, resulting in the synthesis of Mo nanopowders.

The sintering process was carried out using SPS system (Dr. Sinter SPSS-515, Syntex Inc., Japan), with a tooling made from EDM4 graphite (Poco Graphite, Inc., Texas, USA). A 0.15 mm-thick graphite paper was used to prevent adhesion between the sintered specimen and the tooling. An optical pyrometer (IR-AHS2, Chino, Japan) was used to detect the temperature at the 2.5mm depth hole in the graphite die. SPS conditions for the consolidation of the $H_2$ reduced Mo nanopowders included the heating rate of 100 ˚C/min from 600 °C to the maximum temperature (950 °C and 1200 °C) with 90 MPa applied pressure and 13 min holding time. All the experiments were conducted in argon gas. The control experiments to get the thermal expansion of the graphite die set were carried out under the same SPS conditions without Mo nanopowders. Also, the temperature of the Mo nanopowders during SPS compaction was measured by inserting a k-type thermocouple directly into the Mo nanopowder. For the regression approach, SPS data obtained from the compaction of the Mo nanopowder at 1200 °C were used. For the multistep pressure approach, starting with the minimum pressure, Mo nanopowders were heated up to 950 °C with 100 °C/min. After the stabilization of the temperature during the holding stage, a few successive jumps of the pressure were applied to measure the variation of the strain rate at each pressure jump.

X-ray diffraction (XRD) (Bruker D-8 diffractometer, MA, USA), utilizing CuKα radiation at room temperature was used to analyze the powders and compacted pellets. The densities of sintered Mo specimens were measured by the Archimedes method. The particle (or grain) size and composition were assessed by scanning electron microscopy (SEM), (FEI Quanta 450, Thermo Fisher Scientific, Waltham, USA) and Energy-dispersive X-ray spectroscopy (EDS) (Oxford Instruments, Abingdon, UK). The transverse rupture strength (TRS) of the compacted Mo pellets was measured. The experimental method to measure the TRS can be found elsewhere [122].

The plasma irradiation and reflectivity measurement conditions are explained in section 5.3.2.3 with their results.

### 5.3.2. Results and discussion

#### 5.3.2.1. Fabrication of Mo nanopowders and compaction by SPS

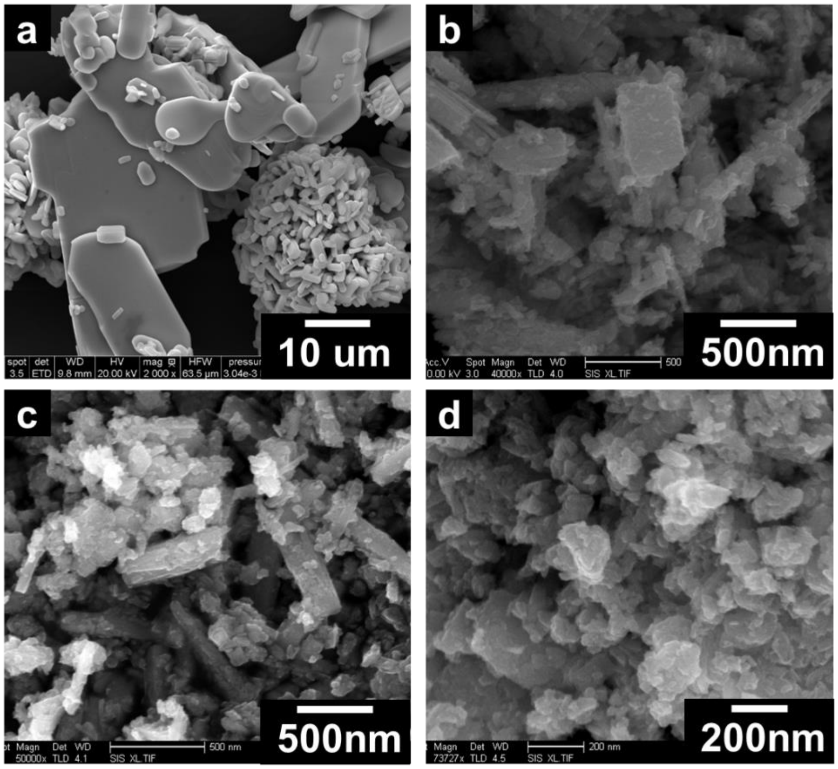

Figure 5.20 SEM images of $MoO_3$ powders (a) without milling and with milling for (b) 3 hours, (c) 10 hours and (d) 30 hours

As shown in Figure 5.20(a), the as-received $MoO_3$ powders display a broad size distribution from 1 μm to 50 μm with plate-like particle shape. SEM images of milled $MoO_3$ powders in TBA are shown in Figure 5.20 (b) to (d) for milling time of 3 hours, 10 hours and 30 hours, respectively. With milling time of 30 hr, an average particle size of less than 200 nm was obtained (Figure 5.20(d)).

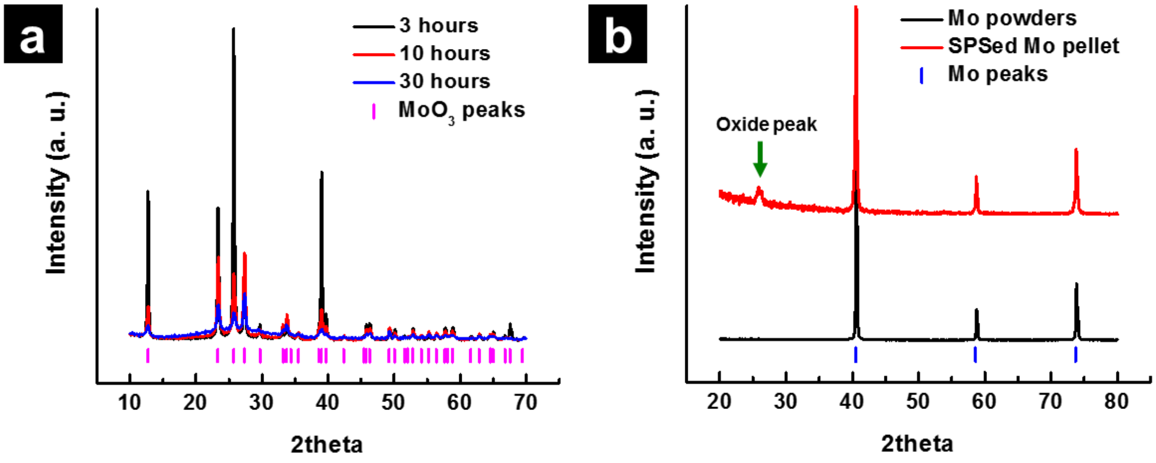

Figure 5.21 (a) XRD of $MoO_3$ powders with different milling time (3 hours, 10 hours and 30 hours). (b) $H_2$ reduced Mo powders (bottom) and SPSed Mo pellet (top). The $MoO_3$ and Mo reference peaks are shown at the bottom of XRD graphs. The green arrow indicates the $MoO_2$ phase.

The intensity drop and the peak broadening from XRD of the $MoO_3$ powders [246] can indicate the decrease of the crystalline size with increasing milling time (Figure 5.21(a)). The bottom graph of Figure 5.21(b) shows the XRD pattern of the $H_2$ reduced Mo powders. Using the $H_2$ reduction method, the $MoO_3$ powders were successfully transformed to Mo (ICSD collection code # 76147) [180]. The compacted Mo pellet by SPS at 950 °C with 13 min holding time, 90MPa and Ar atmosphere shows the oxide peak ($MoO_2$ with ICSD collection code # 01-078-1073) indicated by the green arrow in Figure 5.21(b). Due to the large surface area of the Mo nanopowder, the oxide layer can form quickly during handling of the powders, which is not indicated by XRD when the oxide concentration is less than the XRD detection limit. Also, although Ar gas was purged during the SPS compaction of Mo powders, the remaining oxygen can easily react with Mo nanopowders. SPS of Mo nanopowders in $H_2$ atmosphere can render more homogenous Mo pellets.

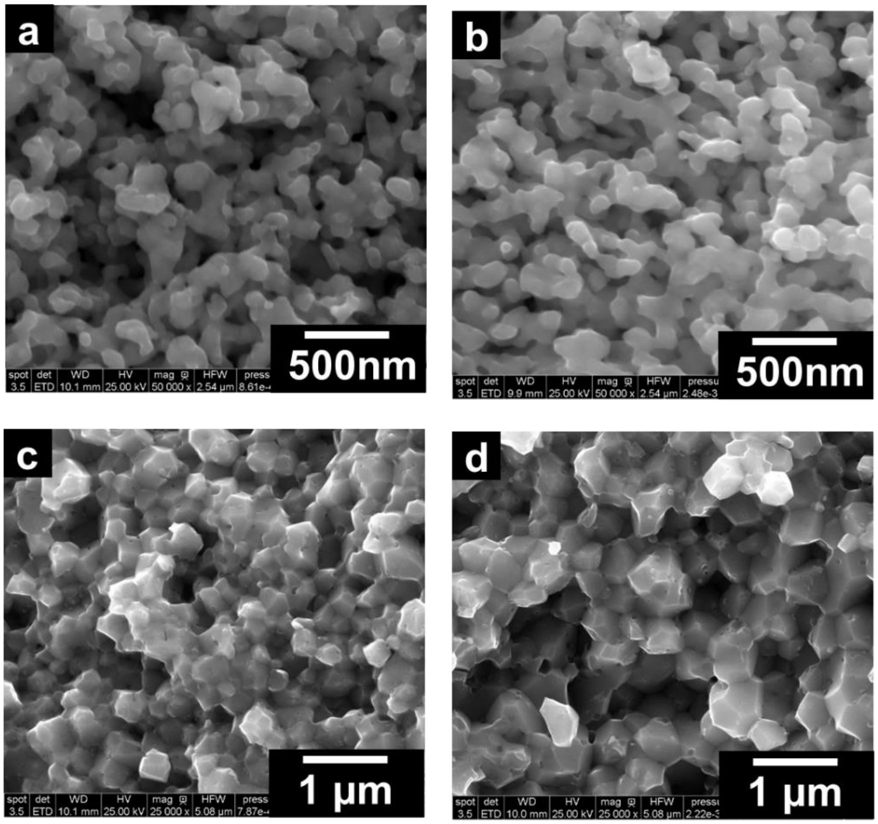

Figure 5.22 SEM images of Mo powders reduced at 850 °C for (a) 50 min and (b) 80 min. SEM images of (c) Mo pellet using powder (a), and (d) Mo pellet using powder (b) compacted by SPS.

The $H_2$ reduced Mo powders have an average grain size of 100 nm as shown in Figure 5.22(a) and (b). During the $H_2$ reduction, Mo particles are connected by necks which are increased with the holding time at 850 °C. The morphology of Mo powders reduced at 850 °C for 80 min (Figure 5.22(b)) represents a more interconnected structure compared to that of the powders $H_2$ reduced at the same temperature for 50 min (Figure 5.22(a)). The large interconnected area in the Mo powders affects the sintering kinetics of Mo compaction by enhancing the diffusion of atoms during SPS. The average grain size and relative density of Mo pellets made from the Mo nanopowders synthesized using the $H_2$ reduction time of 80 min are about 700 nm and 93.89 %, respectively, which are slightly higher values than 400 nm and 92.58 % of the Mo pellet obtained from the Mo nanopowders synthesized using the $H_2$ reduction time of 50 min (Figure 5.22(c) and (d)). TRS values of the Mo pellets made from the Mo nanopowders synthesized using the $H_2$ reduction times of 50 min and 80 min are 486.27 MPa and 472.16 MPa, respectively.

### 5.3.2.2. Mechanism of Densification of Mo nanopowders

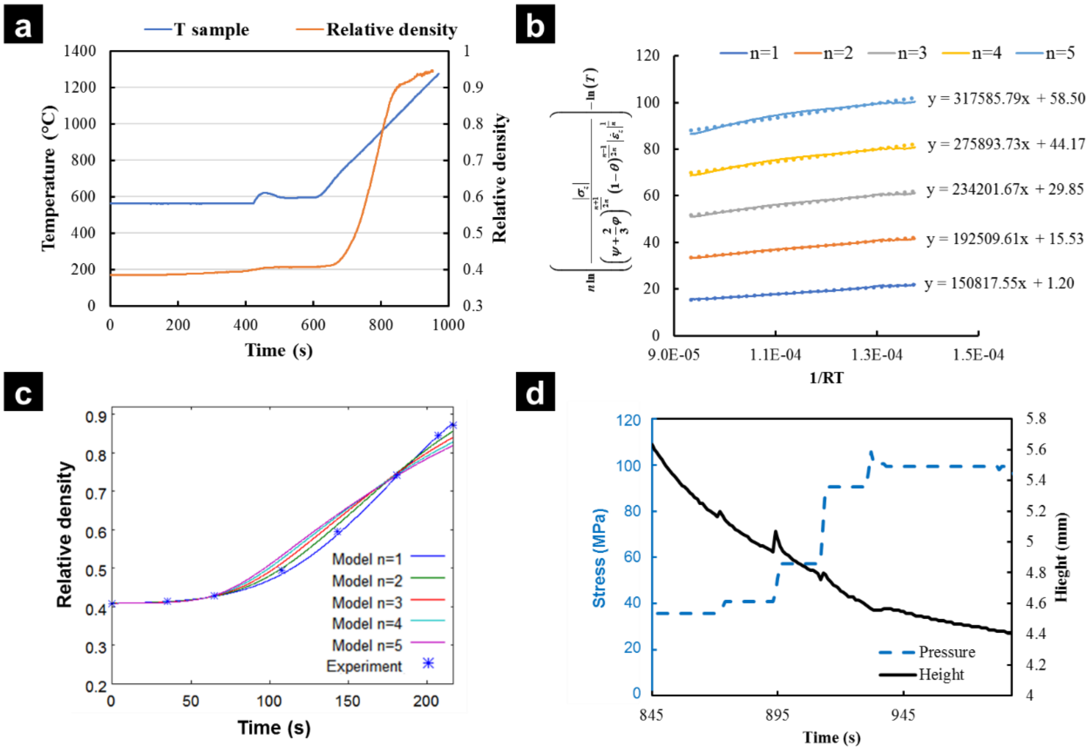

Figure 5.23 (a) Experimental SPS results, (b) Linearization curves for each n values (the fitting equations are shown on the right side of each curve), (c) Modeled/experimental relative density curves using identified parameters from regression approach for each tested n values, (d) Change of applied stress and height of sample in multistep pressure method

The experimental SPS data with the ramping stage (100 °C/min) (Figure 5.23(a)) was used to plot the linearization curve for various *n* values (1 to 5) shown in Figure 5.23(b). The relative density range from 0.41 to 0.87 is used in Figure 5.23(a) to avoid the effect of the grain growth on the sintering behavior. The fitting equations for each *n* value are shown on the right side for each curve in Figure 5.23(b). Table 1 displays the $A_0$ and Q values for each n value for the linear regression fitting using (3.21) in Figure 5.23(b). Figure 5.23(c) shows the modeled/experimental relative density curves using the identified sintering parameters (Table 5.4) and it appears that the *n* value is between 1 and 2. More accurate *n* value can be obtained by the regression of the SPS multistep pressure dilatometry data. Figure 5.23(d) shows the change of the stress and height of a Mo pellet during the multistep SPS of Mo nanopowders during the isothermal holding stage of 950 °C. When there is a jump of the pressure, the slope of the sample height curve is changed accordingly indicating the alteration of the strain rate for each jump. From the data in Figure 5.23(d), the average *n* value, estimated using (3.22), is 1.5. Based on this *n* value, parameter Q value can be expected to be in the range from 150 kJ/mol to 192 kJ/mol (Table 5.4).

Table 5.4 Creep parameters identified from regression approach

| n | 1 | 2 | 3 | 4 | 5 |
|---|---|---|---|---|---|
| Q | 150.82 | 192.51 | 234.20 | 275.89 | 317.59 |
| $A_0$ | 3.007E-1 | 1809E-7 | 1.088E-13 | 6.547E-20 | 3.939E-26 |

Obtained *n* and *Q* values indicate that the sintering mechanism of Mo nanopowders obtained via $H_2$ reduction method can be the grain boundary sliding (GBS) accommodated by dislocation slip (*n* = 1 with dislocation glide, *n* = 2 with dislocation climb) controlled by the grain boundary diffusion ($Q_{gb}$=263 kJ/mol) [88]. Due to a low sintering temperature (0.4$T_m$) imposed during SPS, the Coble creep (*n*=1) which requires high temperatures (0.9$T_m$) is not possible in this case. A Mo compact with average nano-size grains will have larger grain boundary area compared with that of the average micron-size grains. Therefore, the grain boundary related densification mechanism such as GBS is expected for most nanopowders [88]. The *Q* values obtained here

(150.82 kJ/mol to 192.51 kJ/mol) are lower than the $Q_{gb}$ value (263 kJ/mol) obtained from the creep test of the micro-sized grain Mo pellet. The smaller particle size of the Mo powders used in the present study can be a possible reason for the lower $Q$ value.

#### 5.3.2.3. Reflectivity analysis of single crystal and nanocrystal Mo

Materials used in this experiment were SC Mo with (110) crystal orientation and NC Mo made of $H_2$ reduced Mo powders and compacted by SPS (950 °C, 90 MPa, 100 °C/min, 13 min holding time, and Ar atmosphere). The SC and NC Mo were mechanically polished to mirror quality of approximately $< 0.01$ μm and $< 0.03$ μm roughness before the exposure respectively.

The SC and NC Mo disks were exposed to Ar plasma bombardment using the PISCES-A linear plasma device [247]. All samples were exposed to Ar+ plasma fluxes of $3.1 \times 10^{17}$ /cm$^2$s with an ion impact energy of average 85 eV. The reflectivity of the Mo samples was measured before and after exposure by high precision spectroradiometer (GS-1290-2NVIS, Gamma Scientific, USA) with the RadOMA camera and full frame lens. There is maximum 10% measurement uncertainty in the reflectivity measurement induced from the alignment angle and the surface non-uniformity of the samples.

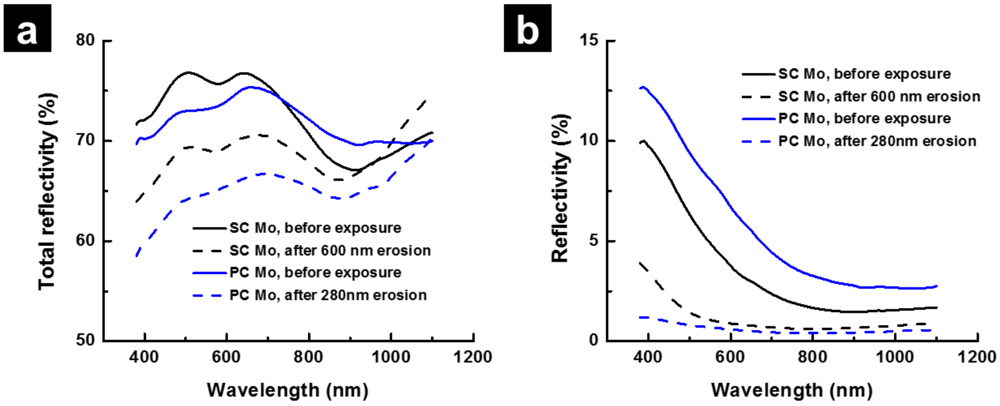

Figure 5.24 (a) Specular reflectivity of single crystal (SC) and nanocrystal (NC) Mo before and after plasma exposure (45° illuminations and 45° collection), (b) Diffuse reflectivity of SC and NC Mo and (45° illuminations and 35° collection)

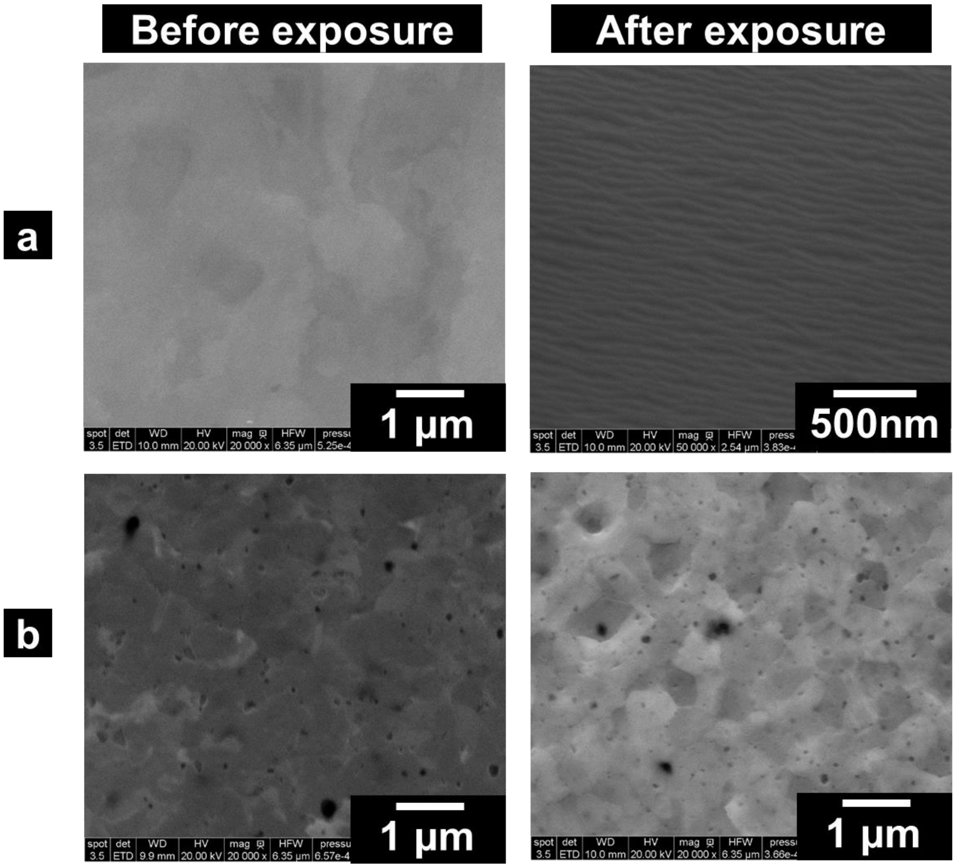

Figure 5.25 SEM images of (a) single crystal (SC) and (b) nanocrystal (NC) Mo before (left) and after (right) plasma exposure

The spectral reflectivity of the SC and NC Mo mirrors before and after exposure are displayed in Figure 5.24(a). Both the SC and NC mirrors have around 70% reflectivity before plasma exposure. Under the same amount of plasma exposure, the spectral reflectivity of the SC and NC Mo mirrors was reduced approximately by 10 %, but showed comparable performance. The total erosion of each sample was also measured via total mass loss. Interestingly, the NC Mo mirror has 2 times higher resistance to erosion (280 nm) by plasma compared to that of the SC mirror (600 nm). The diffuse reflectivity of the NC Mo mirror used in this study is lower than that of the SC Mo mirror under the same plasma conditions, which is unexpected. As shown in Figure 5.24(b), the NC Mo mirror has a low average diffuse reflectivity of less than 1% after exposure. The high diffuse reflectivity of the SC mirror in the range of < 600 nm can be related to the eroded pattern observed after exposure (right image of Figure 5.25(a)). The surface relief formation which is known as the main reason for the high diffuse reflectivity of polycrystalline metal mirror [8] was observed for the SPSed Mo mirror after exposure in this study (right image of Figure 5.25(b)), yet, it was not severe compared with the literature [8]. The obvious reason for the higher erosion resistance and the lower diffuse reflectivity of the NC Mo mirror relative to those of the SC mirror obtained from this study is not determined yet. Although maximum 10% of measurement error make the reflectivity results ambiguous, NC Mo mirror clearly has higher erosion resistance over SC Mo mirror, which was not observed for the NC mirror (100nm grain size) made by magnetron sputtering [3].

In summary, the consolidation behavior of the Mo nanopowders obtained from milled MoO3 powders by H2 reduction was analyzed by the regression of the experimental data on regular SPS and on the SPS multistep pressure dilatometry. Obtained creep parameter values n and Q are 1.5 and 151 kJ/mol to 193 kJ/mol, respectively, indicating the GBS accommodated by dislocation slip-controlled by grain boundary diffusion as the densification mechanism of the Mo nanopowders used in this study. The NC Mo disk shows the promise in approaching the reflectivity of the SC Mo in the as-polished condition. Initial optical test results are not conclusive due to the measurement error of the reflectivity. However, NC Mo showed good resistance to erosion compared to that of the SC Mo. The sintering of Mo alloy with the grain growth inhibitor like ZrC to have smaller grain size, and more accurate optical measurements could be done for the future study.

## 5.4. Chapter Conclusions

The densification mechanism of tungsten consolidated by spark plasma sintering was analyzed by the constitutive equation of sintering (3.10) considering the applied pressure and using the power-law creep model of mass transfer. The strain rate sensitivity of 0.38 - 0.40 and sintering activation energy of ~ 410 ~ 434 kJ/mol were obtained. These values indicate that the densification mechanisms may be grain boundary sliding accommodated by dislocation climb controlled by the grain boundary diffusion, which is also supported by the electron back-scattered analysis. Increasing the sintering temperature causes the reduction of the grain growth exponent and tends to be converged to the ideal grain growth exponent of 2, possibly due to the removal of the grain growth inhibiting factors such as pores at grain boundaries. The tungsten carbide external shell is generated on the specimen’s surface with increasing holding time due to the presence of the carbon wrapping paper and graphite die. The diffusion coefficient of carbon in tungsten was obtained, and it is similar to the literature values. Using BN coating on the graphite paper did not block the carbon uptake from the die and graphite paper, but it slowed down the diffusion of carbon. Vickers micro-hardness was measured for the processed tungsten specimens and showed porosity dependence.

The study of the sintering behavior of the surface-oxidized Mo nanopowders showed that the density of the processed Mo pellets cannot be increased without removing the oxide phase from the starting powders. Also, the mechanical properties (like TRS) of Mo pellets are governed by the presence of the oxide phase at the grain boundaries, which promotes the final product embrittlement. Sintering mechanism of the oxidized Mo nanopowders compacted by SPS after the melting of the oxide phase is the dislocation creep controlled by dislocation climb. Since the grain boundary diffusion of the Mo atoms is limited by the presence of the meted oxide phase at the grain boundaries the dislocation climb, which is operated by the lattice diffusion, seems to be a reasonable densification mechanism for Mo nanopowders. The two *in situ* oxide reduction methods were employed to remove the oxide during SPS. The carbothermal reduction or the particle surface cleaning by electric current have been used. Both methods showed the decrease of the oxide contents and the increase of the final density. It was shown that carbon remaining in the Mo pellets after the carbothermal reduction process negatively affects the TRS, which lends impetus to analyzing the optimization of the concentration of the carbon amount in the Mo+C powder mixture in future studies.

For the first time, the densification mechanism of Mo nanopowders compacted by SPS was analyzed. A NC Mo metal mirror with submicron grain size fabricated by SPS was tested using a spectroradiometer after plasma exposure. The densification mechanism of the Mo nanopowders during SPS is GBS which is expected for the metal nanopowders. The spectral reflectivity of the NC Mo mirror after exposure is comparable with that of the SC mirror. Especially, the NC Mo mirror shows higher erosion resistance over the SC Mo in this study. By further optimizing the $H_2$ reduction and SPS process or Mo powders alloying with the grain growth inhibitor, bulk scale NC

Mo mirrors can be possibly fabricated by SPS, which should provide clear benefits in terms of cost, size and life expectancy of metal mirrors.

In this chapter, we have shown that the presence of the electric current can enhance the densification rate, or remove the surface oxides, or slower the grain growth. Next chapter describes the development of the novel fast powder consolidation processes utilizing these advantages of the electric current assistance for the fabrication of micro- or nano-sized metal and ceramic powders.

Chapter 5, in part, is a reprint of the material as it appears in *International Journal of Refractory Metals and Hard Materials*, 2016. G. Lee, J. McKittrick, E. Ivanov and E.A. Olevsky. The dissertation/thesis author was the primary investigator and author of this paper.

Chapter 5 in part, is currently being prepared for submission for publication of the material. G. Lee, C. Manière, J. McKittrick, A. Gattuso, C. Back, and E.A. Olevsky. The dissertation/thesis author was the primary investigator and author of this paper.

Chapter 5, in part, is currently being prepared for submission for publication of the material. G. Lee, C. Manière, J. McKittrick, D. Nishijima, R. Doerner, A. Gattuso, T. Abrams, D. Thomas, C. Back, and E.A. Olevsky. The dissertation/thesis author was the primary investigator and author of this paper.

# CHAPTER 6 Net Shape Flash Spark Plasma Sintering (NFSPS)

The novel net shape flash spark plasma sintering (NFSPS) based on the SPS process and enabling the achievement of densification rates similar to those in flash sintering is developed. In this method, the electric current is concentrated in the powder sample, and a graphite die is utilized to easily control the shape of the processed component. The newly developed approach employing various direct/hybrid configurations is applicable to a very broad spectrum of material systems from insulative powder materials ($Al_2O_3$) to ionic ($ZrO_2$) or metallic (ZrN) conductive powders. Compared with flash sintering or FSPS, NFSPS can use high pressure (~90 MPa) and high heat conservation without the time-consuming precompaction of the powder, making this approach to be more attractive for industry applications.

## 6.1. Experimental

### 6.1.1. Materials investigated

For NFSPS, various powders were tested depending on their electric conductivity behavior with temperature. A : Ionic conductor and insulator which showed NCT behavior: Tosoh TZ-3YS (99.9 %, 200nm, 3 mol% tetragonal-stabilized zirconia (Tosoh, Shunshi, Japan)), Alumina (99 %, 37nm, (Cerac, USA)) and SiC (beta phase, ~50 nm, (US Nanoresearch, USA)). B: conductor or metallic semiconductor exhibiting PCT behavior: W (99.95 %, ~100 nm (US nanoresearch, USA)) and ZrN (1 μm (Sigma-Aldrich, USA)).

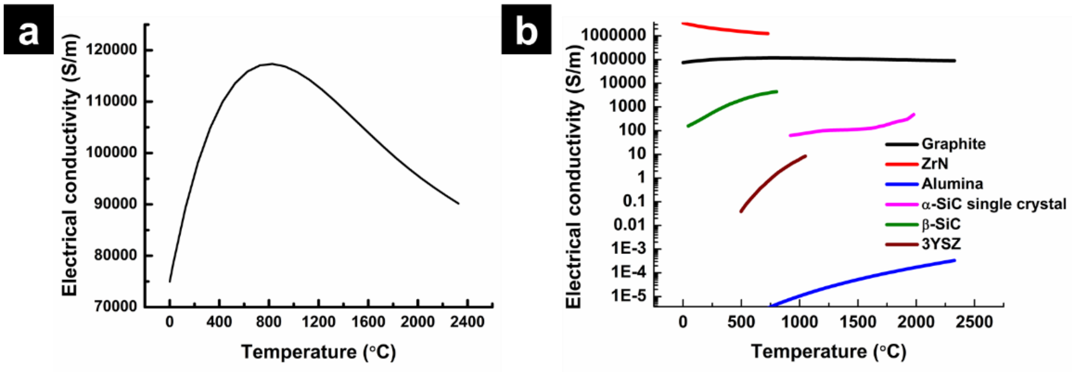

Figure 6.1 Electric conductivity data for (a) graphite [110] and (b) ZrN [111], Alumina [248], alpha -SiC single crystal [249], beta-SiC [250] and 3YSZ [251].

The temperature dependence of the electrical conductivities of the used materials is shown in Figure 6.1. Used graphite has NCT of electric resistivity temperature dependence between 23 °C to 827 °C, and PCT of that after 827 °C (Figure 6.1(a)) [110]. Figure 6.1(b) shows the comparison of the electric conductivity for the powder materials used in this research and the graphite. Y-axis is on a log scale. ZrN [111] has the highest electric conductivity and even higher than the one of graphite. Ionically conductive α and β SiC [249, 250] and 3YSZ [251] show lower electric conductivity than that of the graphite. Insulating alumina has the lowest electric conductivity values.

### 6.1.2. NFSPS processing regimes

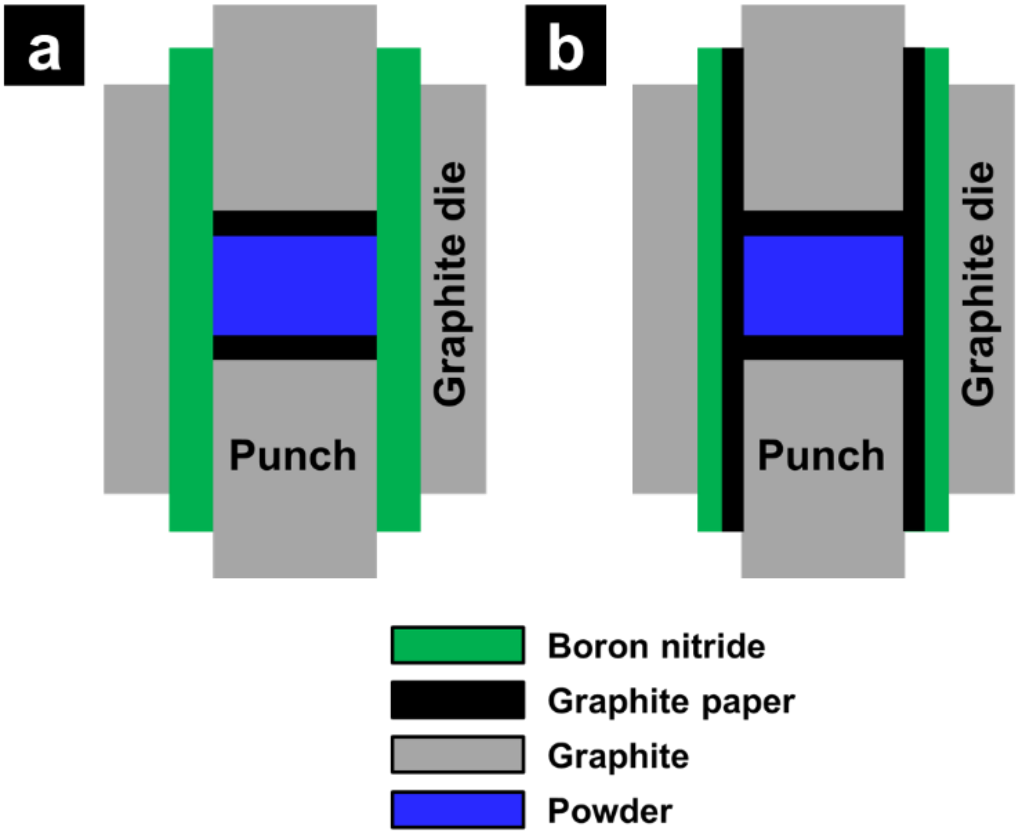

Figure 6.2 Schematics of NFSPS. Green, black, gray and blue color indicate the boron nitride, graphite paper, graphite component, and the powder, respectively. (a) direct heating setup, (b) hybrid heating setup.

SPS machine and die setup are described in section 3.2.1. As shown in Figure. 6.2, a Boron nitride (BN) coating was applied to the graphite paper (0.15 mm-thick) in order to manipulate the electric current path trajectory in the SPS setup.

For the direct heating setup, both sides of the graphite paper inside the die were coated with BN, forcing all the electric current to flow into the conductive powder. For hybrid heating setup, the external (with respect to the powder) surface of the graphite paper which contacted the graphite die was coated with BN, which prevented the electric current flowing into the die but enabled the electric current flow into the graphite paper to heat up the insulating powder at room temperature. Once the powder becomes conductive with increasing temperature, the electric current can flow into the powder providing a fast volume sample heating.

All NFSPS experiments were carried out using the manual mode in SPS. Real-time changes of the electric current, voltage, temperature, Z-axis displacement and vacuum pressure were displayed on the monitor of the SPS system. There were two strategies used to control the electric current: 1. Forced mode: First, the electric current is slowly increased until right before the start of the densification observed on the monitor. When densification is started, the electric current is manually quickly increased until the graph of the Z-axis displacement becomes flat, which means that the densification is completed. 2. Current control mode: from the start of the sintering, the electric current increases until the pre-set current value is reached. The preset current is determined using the relationship between the temperature and the electric current obtained from the forced mode experiments.

To resolve the problem of the graphite creep during NFSPS, a few attempts were tried.

First, the creep behavior of the graphite punch (diameter 10mm, height 20mm, EDM4 grade) was tested using SPS with 100 °C/min under vacuum. The Z-displacement of the graphite punch was recorded under 3 different pressure (50MPa, 80MPa and 100MPa) with increasing temperature up to 2600 °C. After knowing the onset temperature of the creep for each pressure, a two-step pressure approach was applied during NFSPS. Nano SiC powders were compacted by NFSPS under 100 MPa. When the temperature of the punch reaches the onset temperature of creep for 100 MPa, the pressure is reduced to 50MPa to prevent the creep of the graphite while the temperature was increased before the onset temperature of the creep under 50MPa.

Secondly, argon gas flow into the chamber may reduce the temperature of the graphite punch. Thus, the temperature of the graphite punch during SiC compaction by NFSPS was compared for Ar gas flow conditions and vacuum conditions.

Lastly, the height of the graphite punch was reduced to 15.5mm (original 20 mm) to prevent the creep behavior. NFSPS of the nano-SiC powder was conducted to prove this concept.

The crystal structure and lattice parameters of the compacted pellets were evaluated by XRD. The relative density was estimated by the Archimedes' immersion method. The fractured or polished specimens were analyzed by SEM and EDS.

## 6.2. NFSPS Results and Discussion

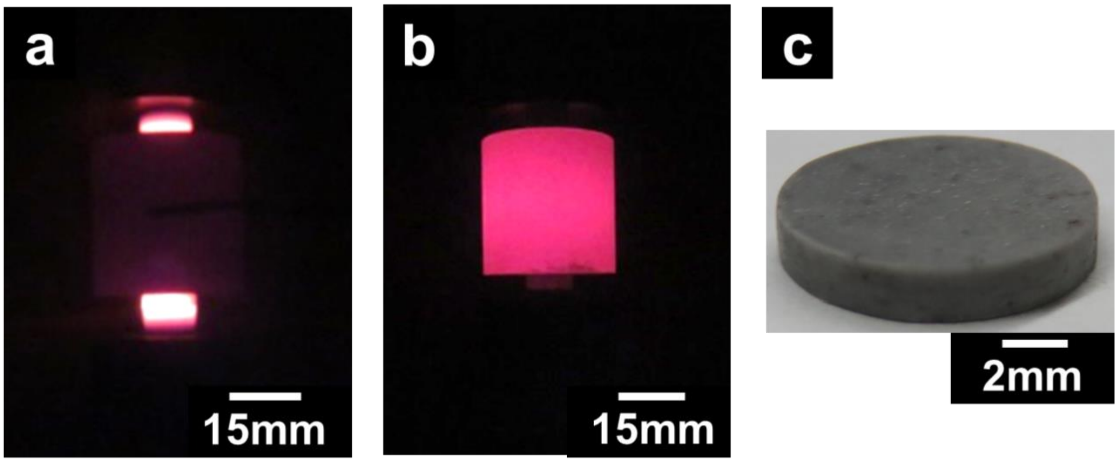

Figure 6.3 Images of the graphite tooling setup at the ramping stage during the net shape flash spark plasma sintering. The image was taken at the moment when the graphite part became visually red-hot. (a) direct heating setup, (b) hybrid heating setup. (c) Alumina pellet compacted by NFSPS

The effects of the graphite paper boron nitride coating can be easily seen during the NFSPS experiments. Figure 6.3 shows the images of the graphite setup at the ramping stage during NFSPS when the graphite setup starts to be heated and becomes visually red-hot. For the direct Joule heating setup, all the electric current flow into the punch and the powder column in the center of the graphite die induces the Joule heating at the area of the punch first (Figure 6.3(a)). On the other hand, the graphite die becomes red-hot first in the hybrid heating setup. The most electrically conductive graphite paper is heated first, then it generates the Joule heating which is transferred to the graphite die by heat conduction (Figure 6.3(b)). Therefore, we infer that BN effectively controls the electric current during the NFSPS experiment. Figure 6.3(c) showed the alumina pellet compacted by NFSPS. Utilizing the graphite die setup helps to fabricate net shape samples.

### 6.2.1. NFSPS of TZ-3YS and Alumina

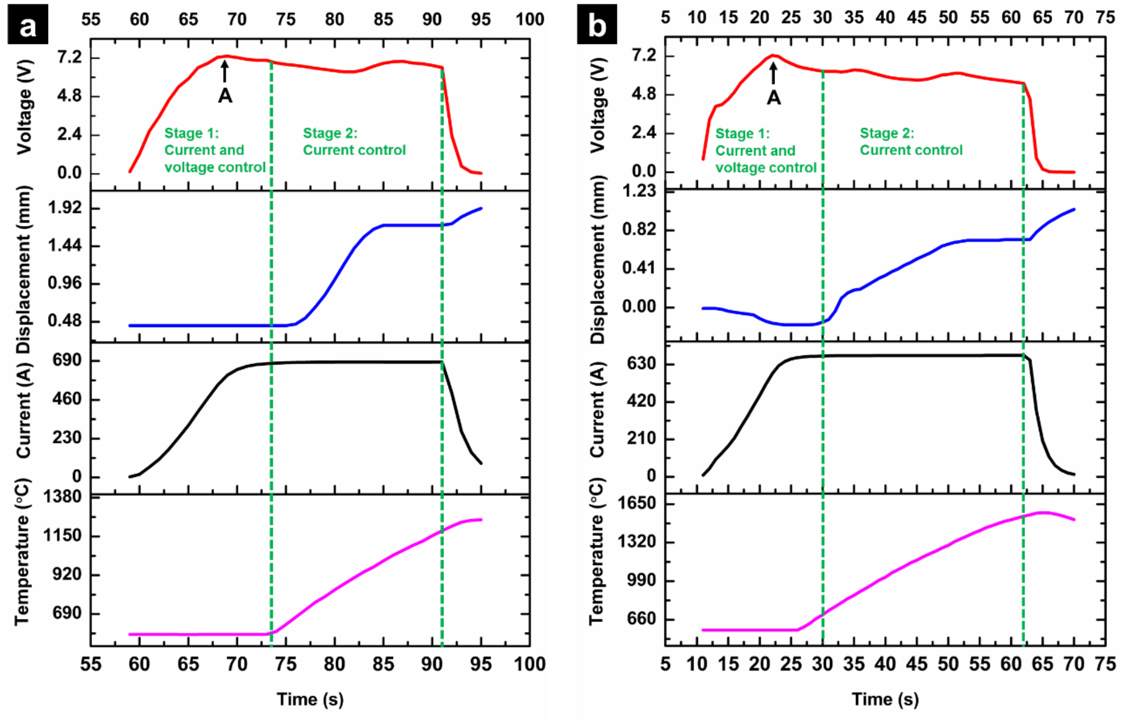

Figure 6.4 The SPS parameter changes during hybrid heating mode NFSPS used with the constant current mode (a) TZ-3YS, (b) Alumina (Red line: Voltage(V), Blue line: Z-axis displacement(mm), Black line: electric current (A) and Magenta line: temperature (C))

During the constant current mode, the electric current quickly increases to the maximum preset value. Under a constant current, the SPS machine records the change of the voltage induced by the resistance change depending on the temperature. The optical pyrometer can measure the temperature within the ranges from 570 °C to 3000 °C, so that the temperature less than 570 °C was not recorded in the graphs (Magenta line in Figure 6.4). Also, the temperature of the powder can be much higher than that of the die measured by the pyrometer.

SPS setup resistance was affected by many factors described below.

A. Electric conductivity: graphite parts (punch and spacer) and the powder. Used graphite punch has NCT or PCT character of the electric resistivity dependence on temperature (Figure 6.1(a)) [110]. Also, the powder showed either NCT or PCT of resistivity (Figure 6.1(b)).

B. Electric contact resistance (ECR): there is vertical ECR which is based on the parallel gap between the punch and the die, and horizontal ECR which is caused by the gap between the sample and the punch. Both ECR has NCT of resistivity. The graphite paper electric conductivity properties can be included in the ECR value.

C. The size of the SPS components: Powder pellet size reduces during SPS, which increases the electric conductivity of the total processing setup. The punch size can be considered to be constant if the graphite tooling creep is insignificant during SPS.

D. The porosity of the powder: Increasing temperature reduces the porosity of the powder resulting in the decreasing electric resistance.

Ionic conductor TZ-3YS powder (Figure 6.4(a)) and insulator Alumina (Figure 6.4(b)) were densified under 90 MPa using hybrid heating NFSPS. The constant current mode was employed to analyze the thermal-electrical response of the die setup. The TZ-3YS sample took about 10 sec to achieve the necessary preheating for flash sintering. After pre-heating stage, it took the powder 26 – 32 sec to become fully dense, which is shown by the plateau of the displacement data. Therefore, totally about 40 sec was required to consolidate a net-shape TZ-3YS pellet using NFSPS. The average heating rate was 2105.65 °C/min during the ramping stage. Alumina also showed similar behavior as demonstrated in Figure 6.4(b). 98 % density was achieved in 51 sec with a heating rate of 1674.36 °C/min.

In Figure 6.4, two stages can be identified. During stage 1, the electric current increased to the maximum preset value, resulting in the increase of the voltage. Abruptly, at point A indicated by the black arrow, the voltage started to decrease due to the increase of the electric conductivity of the die set and powder. When the electric current reached the maximum preset value, the current control mode started (Stage 2). During stage 2, the voltage increased or decreased depending on the material electric resistance temperature dependence. In particular, the graphite, which showed PCT of resistivity above 827 °C, is the reason for the increase of the voltage. During stage 1 or stage 2, it is not easy to determine when electric current flows into the powder. At the Point A, TZ-3YS can be electrically conductive, contrary to alumina.

The absence of the significant drop in the voltage value or even of an increasing voltage during stages 1 and 2 may indicate that there is no thermal runaway of the powder. This is possibly due to the high conductivity of the graphite foil and low voltage utilized by the SPS machine. Therefore, our results may show that thermal runaway may not be required for the consolidation of fully dense TZ-3YS components.

In the flash sintering experiments, the thermal runaway didn't enable the achievement of the full density (From 52% to 82% for TZ-3YB) [252]). After thermal runaway, when current reached the preset current limit, the power supply switched to the current control mode within less than a second from the onset of the flash. The power dissipation in the powders, equal to $I^2R$, where $I$ is the electric current, and $R$ is the resistance, decayed after that point as the resistance of the specimen continued to fall, quickly reaching a quasi-steady-state rate of power dissipation in the specimen. During constant current mode in flash sintering, the density of the sample reached the 95% [252]. At the same time, NFSPS enabled the consolidation of a full density sample without thermal runaway, possibly due to the external pressure assistance.

### 6.2.2. NFSPS of SiC

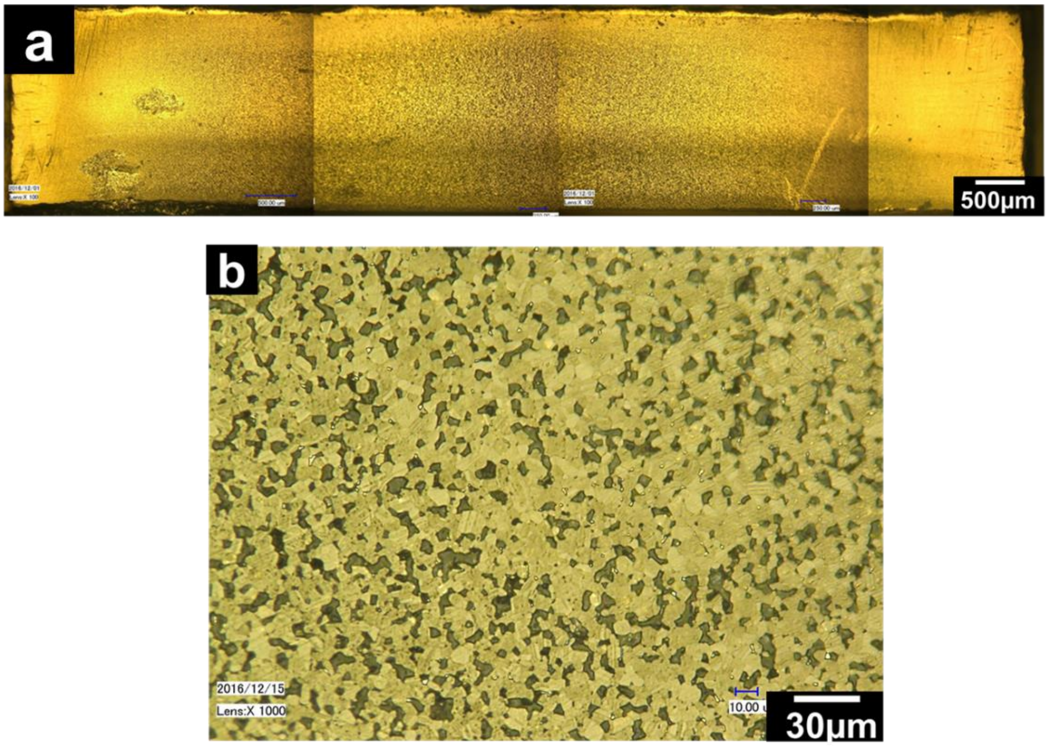

Figure 6.5 Optical microscope images of vertical cross-section of (a) whole sample and (b) 1000X of etched nano SiC pellet processed by NFSPS

Semiconducting nano size SiC powder was densified by NFSPS. Generally, sintering of SiC requires high temperature, pressure and holding time (> 2050 °C, 69 MPa and >5min) [253]. Using NFSPS, the relative density of 87.04% was achieved within 294 sec employing the forced mode. Due to the creep of the graphite punch stating around 1900 °C, the higher density was not achieved. The creep behavior of the graphite is analyzed in last part of this section. Figure 6.5(a) shows the optical microscope images of a vertical cross-section of the whole sample of nano SiC pellet processed by NFSPS. An inhomogeneous density distribution is observed possibly due to the fast densification regime of NFSPS. Etching of the SiC pellet shows a twin boundary in a grain of SiC (Figure 6.5(b)). A high strain rate of NFSPS can favor deformation twinning.

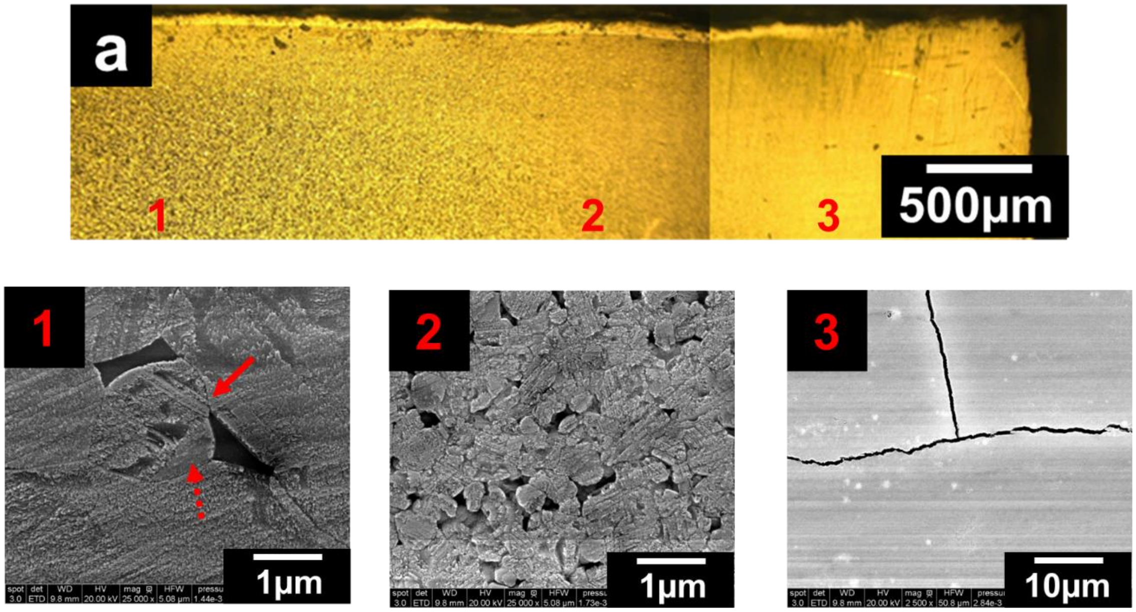

Figure 6.6 (a) Cropped optical microscope image of a vertical cross-section of nano SiC pellet processed by NFSPS (From Figure 6.5.), (1) – (3) SEM image of nano SiC pellet at a different location.

SEM and EDS were used to characterize the grain size and composition of the different locations inside the SiC pellet (Figure 6.6). Figure 6.6(a) is the cropped OM image (upper right portion of Figure 6.5). The center (region 1) of the SiC sample has the largest average grain size 2.5 μm compared with 0.5 μm average grain size of region 2. Also, twin boundaries can be observed in the grains. In particular, a twin boundary was initiated at a grain boundary (solid red arrow in region 1). Another area which is not affected by pressure from other particles remained twin free (dashed red arrow in region 2), which may indicate the observed twins are deformation twins. At the edge of the SiC sample (region 3) cracks are observed. The melting temperature of SiC is around 2700 °C. Due to the non-homogeneous temperature distribution during the NFSPS, the temperature of the powder can be higher than 2500 °C, even despite the recorded maximum temperature of the die is 1576 °C. Therefore, the edge of the sample can be melted during processing and cracked during cooling or ejection of the sample after NFSPS. EDS of region 1 and 2 indicates that the grains are composed of Si (41 at%), C (56.62 at%) and O (1.41at%). At the same time, EDS of region 3 shows Si (34.2 wt%), C (56.49 wt%), O (8.19 wt%), Ca (0.37 wt%), Mg (0.21 wt%), and Fe (0.26 wt%). The diffusion of elements from BN or graphite paper can be a possible source of these impurities.

### 6.2.3. NFSPS of Tungsten Powder

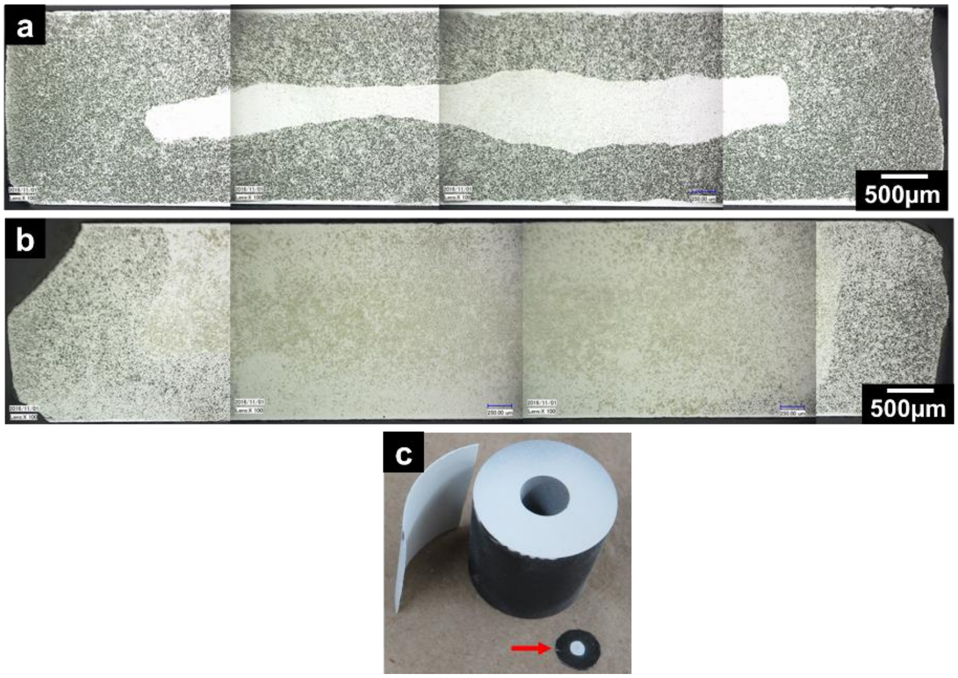

Figure 6.7 Optical microscope images of a vertical cross-section of etched nanopowder W pellet processed by NFSPS, (a) electric current concentration case, (b) electric current deflection case and (c) boron nitride coating at the center of the graphite paper (red arrow) used for the electric current deflection case.

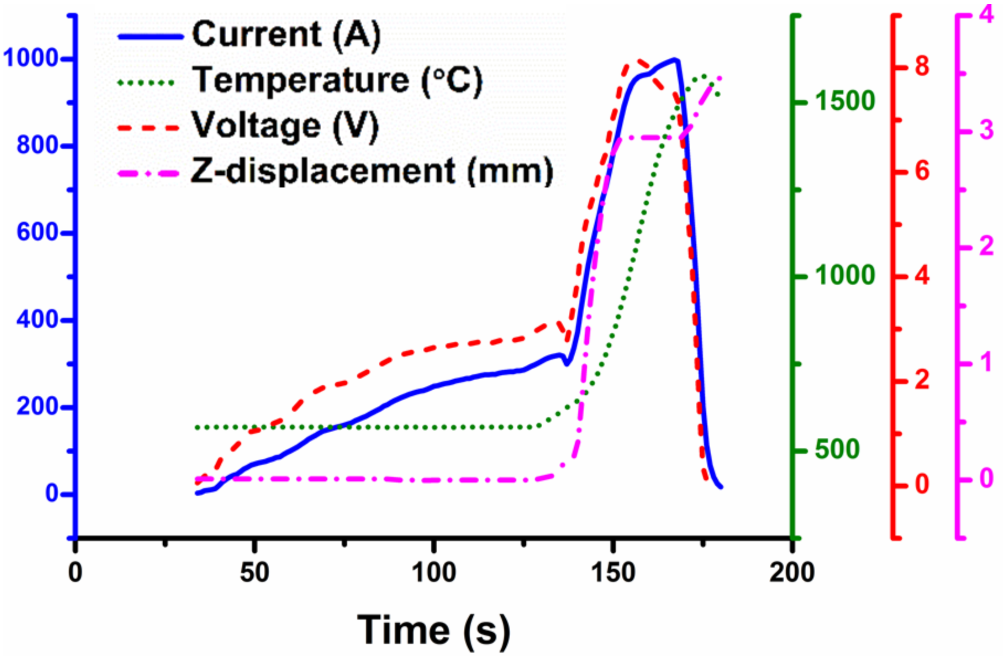

Figure 6.8 The parameter changes during nano W powder consolidation using NFSPS. (blue solid line: electric current (A), green dot line: temperature, red dash line: voltage (V) and magenta dash-dot line: Z-axis displacement (mm))

Direct heating setup (Figure 6.2(a)) was used to consolidate the nano size W powder using NFSPS with the forced mode. Under 50 MPa, nano W was densified to 90.84% with clear inhomogeneous density distribution between the center and the edge of the sample (Figure 6.7(a)). In direct heating setup, the electric current flows to the center of the powder which generates large direct Joule heating with possible electric current effects, which can help fast densification at the center. Herewith, no electric current can flow through the graphite paper surrounding the punches and the powder, therefore the external layers of the powder sample are subjected to lower temperatures. In order to deviate the electric current flow from the center to the entire sample, the center of the graphite paper located between the punches and the powder was coated by BN (Figure 6.7(c)). Previously, BN coating on a graphite punch was suggested as a thermal homogenizer for SPS [254]. Using that approach, the density distribution of the W sample became more homogenized and had a higher relative density (94.15%) under the same pressure (Figure 6.7(b)).

However, the edge of the sample was still porous compared to the center. Using the graphical area approximation by ImageJ, the dense portion of Figure 6.8(a) and (b) can be assessed as 17% and 66%, respectively. Increasing the size of the boron nitride coating on the graphite paper and increasing the holding time may improve the homogenization of the density in the W pellet.

Figure 6.8 shows the NFSPS parameter evolution during the W nanopowder consolidation using the electric current deflector (BN coating in the center of the graphite paper) (Figure 6.7(b)). The electric current was applied for 133 sec with 50 MPa. During fast heating (137s to 156s), the heating rate is around 1513.13 °C/min. The shape of the Z-displacement curve becomes flat at 153 s, yet resulting in a porous structure (94.15%).

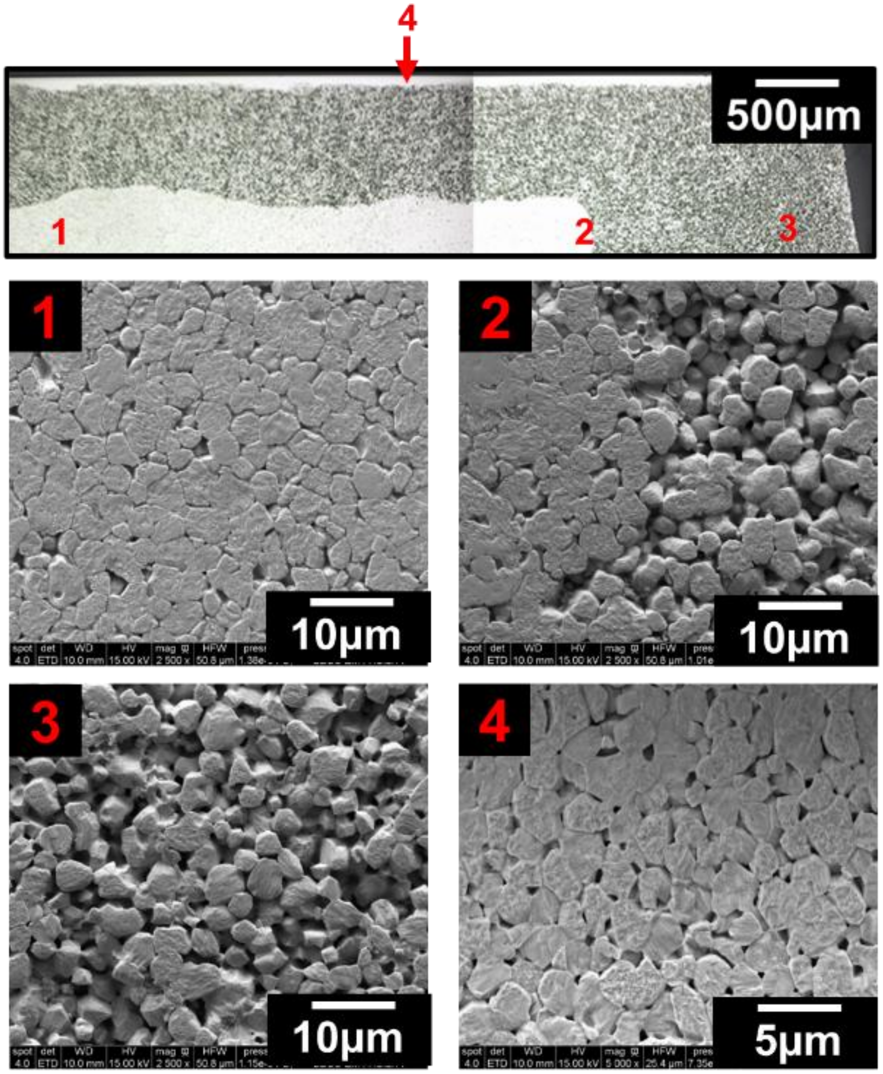

Figure 6.9 The microstructure of current concentration case of nanopowder W pellet processed by NFSPS: (a) Cropped optical microscope image of vertical cross section (From Figure 7(a).), (1) – (4) SEM images at different locations indicated by the red color numbers.

The density and grain size distribution of the compacted W pellets with and without electric current deflector were measured using SEM. For the W sample densified without an electric current deviator (Figure 6.7(a).), the center region 1 has a more densified structure compared with that of the edge region 3 with a similar average grain size of 5 μm. Clear boundary (Region 2 in Figure 6.9) between the dense and porous regions is observed. Also, the top and bottom layers of the pellet have a dense structure with a smaller grain size of 2 μm compared with another region.

If there are only thermal effects influencing the densification, a gradual density distribution from the center to the edge should be expected. The abrupt change of the density may be from the intrinsic effects of the electric current due to the concentration of the electric current flow.

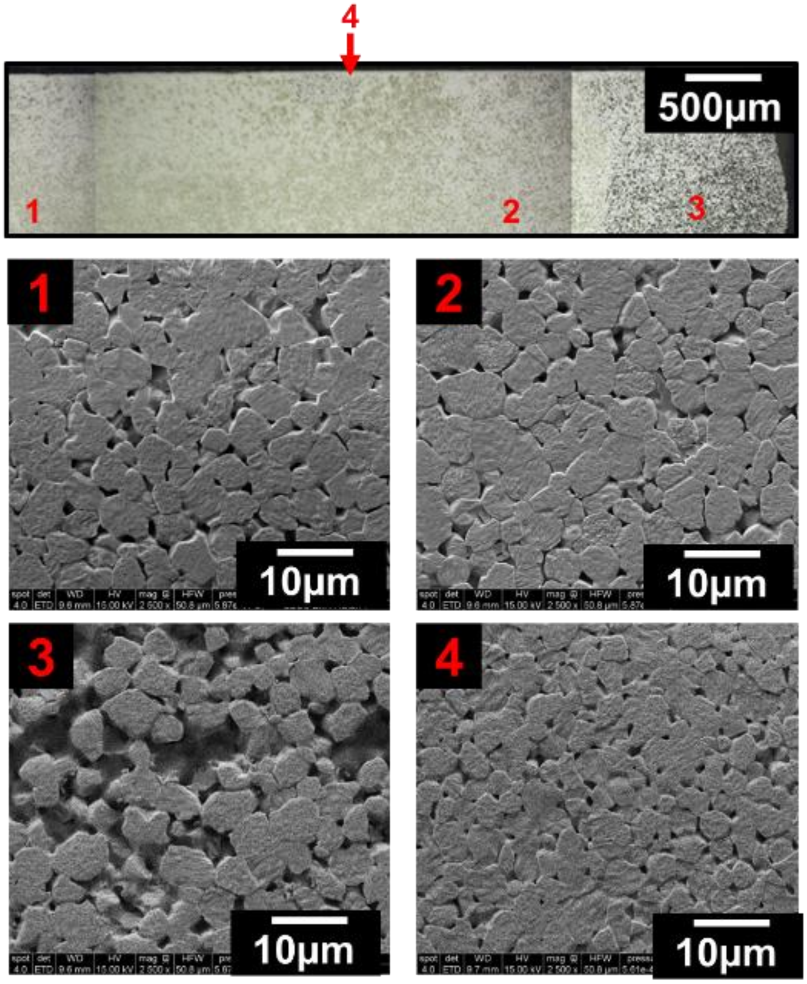

Figure 6.10 The microstructure of current deflection case of nanopowder W pellet processed by NFSPS: (a) Cropped optical microscope image of vertical cross section (From Figure 7(b).), (1) – (4) SEM images at different locations indicated by the red color numbers.

For the W sample with an electric current deviator, the boundary between the dense and the porous regions was moved to the edge side (Figure 6.10). The center regions 1 and 2 have a more dense structure compared with the edge region 3 with a similar average grain size of 7 μm.

Like in the previous case (region 4 in Figure 6.9), the upper and bottom layers of the pellet have higher density with a smaller grain size of 4 μm compared with other regions (Region 1~3).

### 6.2.4. Limitations and solution for NFSPS process

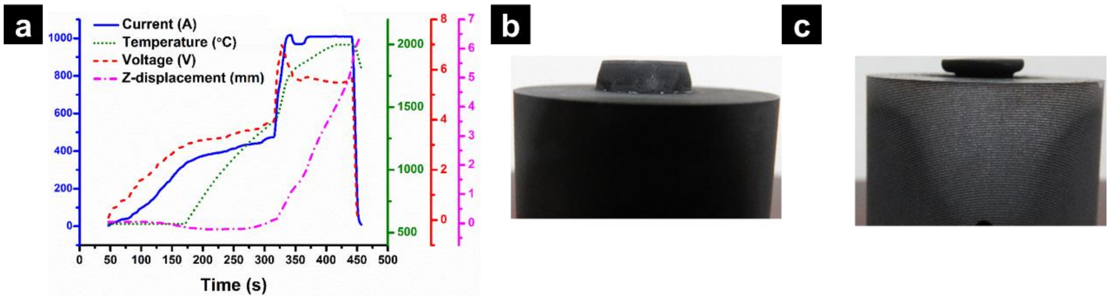

Figure 6.11 (a) The NFSPS parameter evolution during the ZrN powder consolidation. (blue solid line: electric current(A), green dot line: temperature, red dash line: voltage (V) and magenta dash-dot line: Z-axis displacement (mm)). (b) creep of the punch and (c) sublimation of the punch during the NFSPS of ZrN powder.

NFSPS method showed fast densification and net shape capability for low and medium melting temperature metal or ceramic materials. For the high sintering temperature material (refractory material), the deformation of the graphite tooling becomes problematic. Figure 6.11 represents the densification results of ZrN powder using the NFSPS direct heating mode. The ZrN powder used in this study becomes fully dense at 1700 °C, 60 MPa, 100 °C/min and 1 min holding time when processed by the regular SPS method (The data is not shown). However, when ZrN is densified under 60 MPa using NFSPS, the Z-displacement curve (Figure 6.11(a)) does not show a flat region with increasing temperature, resulting in the still porous ZrN pellet (96.92 %). This is due to the creep (Figure 6.11(b)) or sublimation (Figure 6.11(c)) of the graphite punch. The graphite punch represents the most heat accumulative region during NFSPS. The real temperature of the punch can be about 2000 °C to 3000 °C even if the pyrometer indicates that the die temperature is 2000 °C (Figure 6.11(a)).

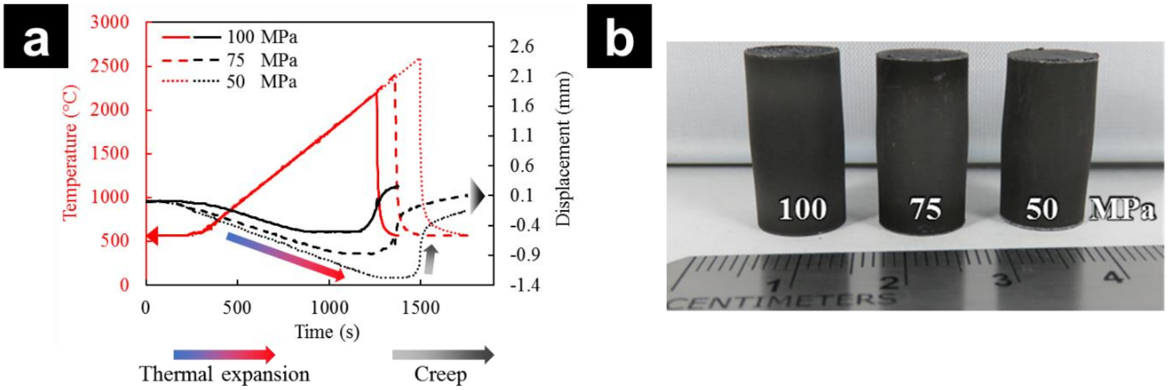

Figure 6.12 The creep test of graphite punch by SPS (a) The temperature (arrow to left) and displacement (arrow to right) change with time for the graphite punch with 3 different pressure (50 MPa, 75 MPa and 100 MPa), (b) Image of crept punches after the experiment

To prevent the creep and enhance the densification of NFSPS process, the creep behavior of graphite punch was investigated. As shown in Figure 6.12(a), higher pressure make graphite creep at the lower temperature: 50 MPa for 2300 °C, 80 MPa for 1878 °C and 100 MPa for 1587 °C. Figure 6.12(b) shows the crept punches after each creep test under 3 different pressure. With this information, two-step NFSPS was applied to nano-SiC compaction by NFSPS which will be discussed later.

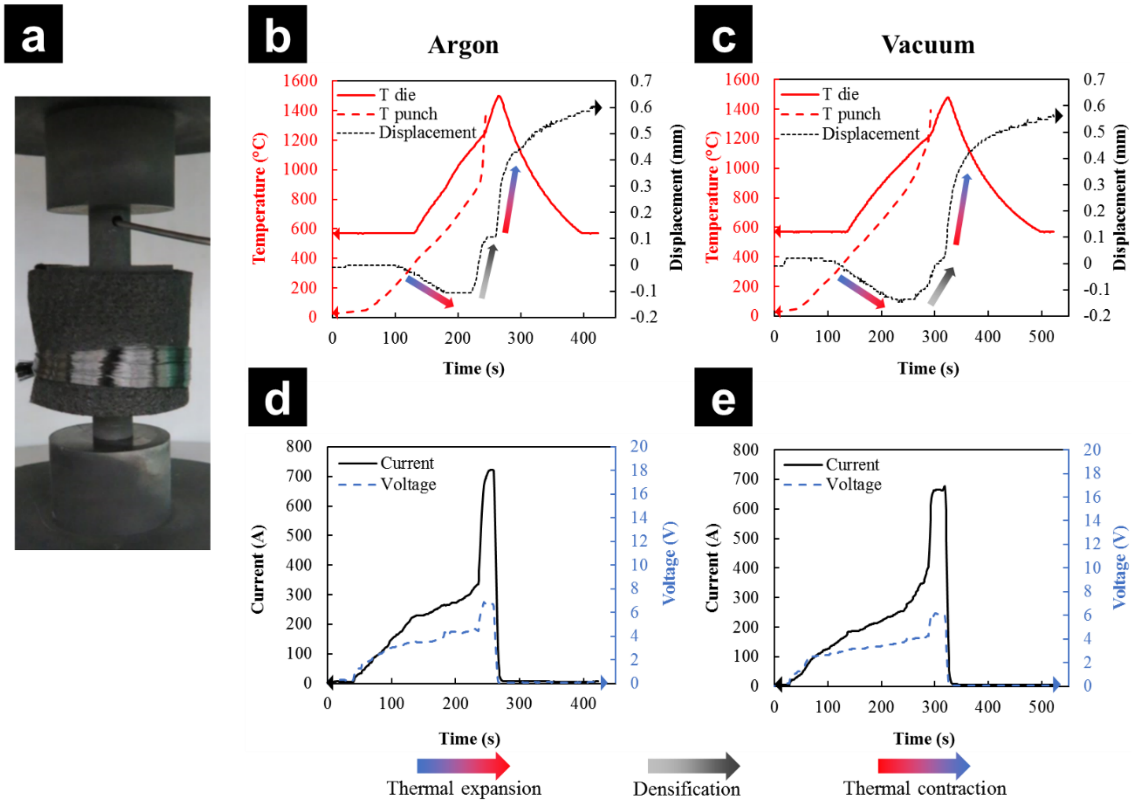

Figure 6.13 Effect of gas flow during NFSPS. (a) picture of graphite die setup during NFSPS, Die and punch temperature and displacement change with time under (b) Ar gas flow and (c) vacuum, Current and voltage change during NFSPS (d) Ar gas flow and (e) vacuum

The influence of Ar gas flow on the creep of graphite punch was investigated. The continuous flow of the Ar gas into the chamber may reduce the temperature of the graphite punch, so that the creep can be prevented. PID was governed by the temperature of the die surface, the temperature of the punch was additionally measured by a k-type thermocouple (top punch at Figure 6.13(a)). As shown in Figure 6.13(b) and (c), the temperature decrease of the punch for Ar flow case is higher than that of the punch for vacuum case, yet the difference is not significant. Figure 6.13 (d) and (e) shows the current and voltage change during the NFSPS process under Ar gas flow and vacuum, respectively. Almost similar current, voltage and holding duration were applied for both cases. Even despite the punch temperature is lower in the presence of Ar gas, the creep of the punch was observed. Also, the relative density of the SiC pellet for both conditions is similar (~ 86%) indicating that Ar flow does not affect much the creep behavior during NFSPS.

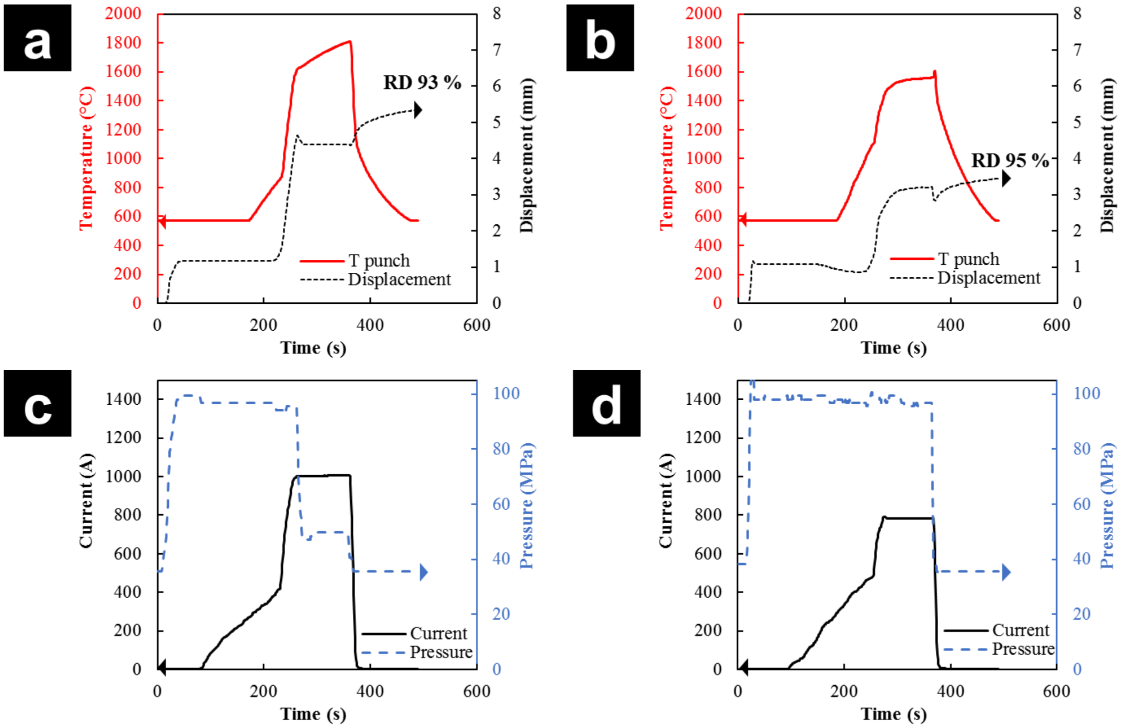

Figure 6.14 The punch temperature and displacement change with time under (a) two-step pressure NFSPS and (b) NFSPS with a smaller punch. Current and pressure change during (c) two-step pressure NFSPS and (d) NFSPS with a smaller punch

The two-step pressure NFSPS was used to compact the nano-SiC powders. The temperature of the punch was measured *in-situ* by extra thermocouple to determine when the pressure should be decreased during the NFSPS process (Figure 6.14(a)). The NFSPS process starts with the pressure of 100 MPa and this is reduced to 50MPa at before 1587 °C, which is the onset creep temperature for 100 MPa case (Figure 6.14(c)). This method renders higher density (93%) of the SiC pellet compared with the regular NFSPS approach. However, the creep of the punch occurred in spite of the two-step pressure application, which can be explained by the stable displacement during the electric current holding (black line in Figure 6.14(a)). The stable displacement does not indicate that densification is finished, instead, it shows that the punch cannot be moved due to its deformed shape.

The punch with low aspect ratio can resist creep better than the one with high aspect ratio. The height of the graphite punch was reduced from 20 mm to 15.5 mm to have a low aspect ratio. Nano SiC powder was compacted under 100MPa in Ar by NFSPS method using the 15.5mm height punch. As shown in Figure 6.14(b), initially, the slower decrease of the strain rate was observed indicating that the densification of SiC occurs during the last stage of the sintering under constantly applied pressure and without obstruction of the deformed punch. Even despite the temperature and the current applied were lower than during the two-step pressure NFSPS (Figure 6.14(a) to (d)), the relative density of SiC sample was the highest (95%) obtained in this study, indicating that low aspect ratio punch works well. After NFSPS, the creep of the punch with the lower aspect ratio was not observed.

In summary, a novel NFSPS approach enabling the achievement of fast densification similarly to flash sintering based on the spark plasma sintering process is developed. In this method, the current is concentrated in the sample, and an electrically insulated die is added to easily control the shape of the sample. Usually, the flash sintering method is applied to materials with a runaway of their electrical properties. We demonstrated that our novel approach used in different direct/hybrid configurations is applicable to nearly all materials from insulative ceramics to conductive metals. High concentration of energy inside the sample and short sintering time makes NFSPS more energy efficient compared with flash sintering.  The developed approach integrates the advantages of the SPS technology in terms of densification and microstructure control and improves the SPS industrial applicability by enabling net shaping and significantly reducing the operation time.

## 6.3. Chapter Conclusions

The developed novel NFSPS technique enables fast consolidation (< 1 min) with the net shaping of metal or ceramic components using a regular SPS machine. NFSPS can be easily carried out by utilizing the graphite paper coated by BN in the framework of EDS or RS sintering technologies. Unlike in flash sintering, for NFSPS the pre-compaction and binders are not required for the fabrication of green specimens. Thermal runaway during NFSPS was not observed possibly due to the high electric conductivity of the graphite and low voltage mode of the SPS machine. However, without thermal runaway, full or near full density samples were obtained for metal and ceramic materials. This means that while flash sintering is mostly based on just regular Joule heating phenomena, thermal runaway may not be required to achieve fast densification when the fast heating rate is imposed by the consolidation approach like NFSPS. Higher pressure can be achieved in NFSPS compared with the results of Zapata-Solvas et al. [83] who used the brittle alumina film as an insulation layer in a graphite tooling setup under 16 MPa. About 40 sec was required to make the full density TZ-3YS pellets using NFSPS. However, inhomogeneous density distribution was observed for SiC and W samples produced by NFSPS. Simple BN coating in the center of the graphite paper between the powder and the punches improves the density distribution and the final density by changing the electric current path. The creep of the graphite punch limits the application of NFSPS to high melting temperature materials. The graphite punch with low aspect ratio solves the creep problem of NFSPS successfully.

Chapter 6, in part, is a reprint of the material as it appears in *Scientific report*, 2017. C. Manière, G. Lee, and E.A. Olevsky. The dissertation/thesis author was the secondary investigator and author of this paper.

Chapter 6, in part, is currently being prepared for submission for publication of the material. C. Manière; G. Lee; J. McKittrick; A. Maximenko; E.A. Olevsky. The dissertation/thesis author was the secondary investigator and author of this paper.

# CHAPTER 7 General Conclusions

## 7.1. Achieved Goals

The research is conducted to find the influence of the electric current on the efficiency of current assisted consolidation of powder materials. We found that electric current enhances the densification kinetics of conductive powders by either changing the densification mechanism itself or changing the creep parameters like the deformability of materials. We showed also that the electric current can reduce the surface oxides or slower the grain growth. Finally, we developed a new method which uses the high concentration of the electric current to accelerate the consolidation process.

For the first time, the constitutive equation for hot pressing (HP) was modified to have electric current effects-related terms, resulting in the constitutive equation for spark plasma sintering (SPS). We used these two equations as the tools for elucidating intrinsic electric currents effects on the densification kinetics of electrically conductive powders. There are three possible changes which may be introduced by electric current effects into the SPS-specific constitutive equation: (i) the change of the creep exponent (*n* or its reciprocal *m* (strain rate sensitivity), indicating the change of the mass transfer mechanism; (ii) change of the frequency (pre-exponential) factor related to the material's deformability (this corresponds to the influence of electroplasticity); and (iii) extra terms introduced in the constitutive equation in addition to the traditional power-law creep expression (this corresponds to the possible influence of additional dissipative mechanisms, such as electromigration, oxide reduction, etc.).

The fine ZrN powder compaction by 3 SPS mode experiments conducted under different electric current density levels, and micro-sized ZrN HP vs. SPS comparative experiments showed that the electric current flow can influence the deformability of the powders and enhance the densification during electric current assisted sintering if it is assumed that there is no change of deformation mechanism under electric current.

Otherwise, if it is assumed that the electric current flow can change the deformation mechanism of the powder, the micro-sized ZrN HP vs. SPS comparative experiments indicates that the densification mechanism is different in HP and SPS. HP is based on the dislocation climb ($m$ = 0.22),  while SPS uses the dislocation glide controlled creep mechanism ($m$ = 0.33). The electric current effect such as localized heating at defects and defects generation may facilitate the diffusion of the number of barriers encountered by a mobile dislocation, which assists the removal of the obstacle. Also, a mobile dislocation that obtains energy from local Joule heating or an elastic field effect from vacancies generated by an electric current, can overcome obstacles more easily.

A comparative study of SPS and high voltage electric discharge compaction (HVEDC) methods was conducted to see the effect of high voltage on the consolidation of micro-sized ZrN. SPS enables higher density and produces more uniform microstructures compared to HVEDC, which is due to non-homogeneous electric current and corresponding temperature distributions and short sintering time of HVEDC. A constitutive model of the densification behavior was proposed and verified based on the experimental data of HVEDC, and showed that the high voltage application to ZrN powders can change the $m$ value from 0.1 to 1 when we disregard the Joule heating due to short sintering time (μs). This also validates the previous statement that the electric current affects the densification mechanism of the conductive powders during the sintering.

We showed that the densification mechanism of W consolidated by SPS was between the dislocation glide and the GBS for regular SPS; The electron backscatter diffraction (EBSD) analysis showed the removal of the grain structure orientation of W during SPS, which is related to GBS mechanism. Generally, the transition from the dislocation creep controlled by the dislocation climb to the grain boundary diffusional creep is expected for the HP of W powders, which indicating the mechanism may not be changed by electric current.

The oxide phase in the starting Mo nanopowder gives detrimental effect on the density and mechanical property of produced pellet. The densification mechanism of Mo nanopowders after melting of Mo oxide phase is revealed as the dislocation creep controlled by dislocation climb with lattice diffusion. The melted oxide phase in the grain boundary and porous area between the particles prevent the grain boundary diffusion mechanism. Two in situ oxide removal technique(The carbothermal reduction or the particle surface cleaning by electric current) during SPS results in the decrease of the oxide contents and the increase of the final density.

By hydrogen reduction and milling of $MoO_3$ micro powders, Mo nanopowders (~100 nm) without surface oxide were successfully synthesized and their densification mechanism compacted by SPS were revealed as GBS mechanism controlled by grain boundary diffusion mechanism which confirming that oxide phase in Mo nanopowders blocks the grain boundary diffusion. SPS method successfully limits the grain growth of Mo nanopowders during sintering. Although the total reflectivity of PC Mo mirror after exposure is lower than that of SC mirror, this PC Mo mirror shows lower diffuse reflectivity and higher erosion resistance under same plasma condition. Making bulk Mo mirror with nanograin size by SPS process will give clear benefit respect to the cost and life expectancy of the mirror for future optics study in the nuclear reactor.

The net shape flash spark plasma sintering (NFSPS) technique enables fast consolidation (< 1 min) with the net shaping of metal or ceramic components using a regular SPS machine.

Unlike in flash sintering, for NFSPS the pre-compaction and binders are not required for the fabrication of green specimens. High pressure used in NFSPS can be the reason for fast densification even without thermal runaway phenomena. It was shown that the creep and sublimation of the graphite punch limit the application of NFSPS to refractory materials. Reducing the height of the graphite punch successfully remove the creep problem during NFSPS.

## 7.2. Engineering & Science Novelty of the Obtained Research Results

a. The new constitutive equation of SPS taking into account the electric current effects has been developed. The electric current density change during SPS has been estimated with the consideration of the inter-particle neck area growth. It was shown that high electric current density can change either the densification mechanism or the deformability of conductive powders.
b. ZrN powders components have been consolidated using SPS and HVEDC methods. Theoretically, it was shown for the first time that the densification mechanism can be changed with applied voltages during the HVEDC process.
c. For the first time, the densification mechanism of W powders which have GBS mechanism was proved experimentally by EBSD method.
d. The densification mechanisms of the Mo nanopowders with or without the oxide phase compacted by SPS were revealed.
e. For the first time, Mo metal mirror with submicron grain size was fabricated by SPS; and the reflectivity was tested before and after the plasma exposure.
f. The developed novel NFSPS technique enables fast consolidation (< 1 min) with the net shaping of metal or ceramic components using a regular SPS machine. NFSPS is

the promising densification technique in terms of energy efficiency and sintering time. NFSPS can be easily achieved using a regular SPS machine.

## 7.3. Summary of Research Progress

A flowchart that summarizes the conducted work corresponding to the formulated research objectives and tasks in Figure 2.1 is given in Figure 7.1. It is safe to conclude here that all tasks required have been successfully achieved in this study.

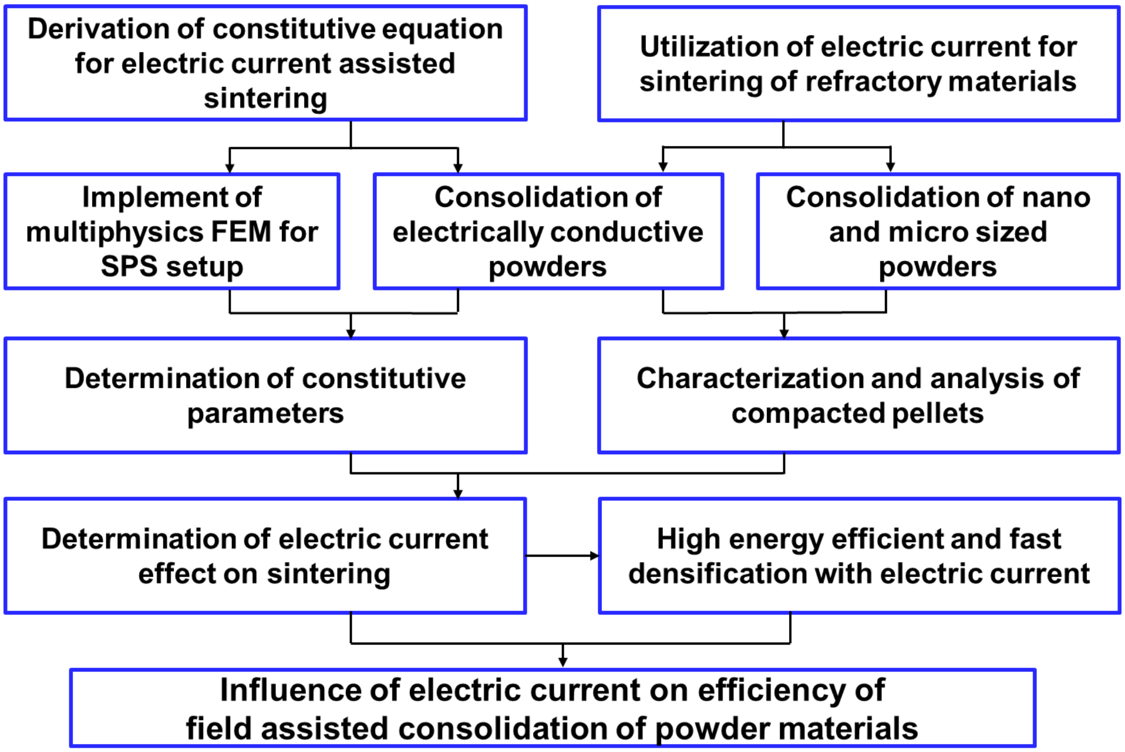

Figure 7.1 Summary of conducted work in a flowchart

# References

[1] J.E. Garay, Current-Activated, Pressure-Assisted Densification of Materials, Annual Review of Materials Research 40(1) (2010) 445-468.

[2] R. Orrù, R. Licheri, A.M. Locci, A. Cincotti, G. Cao, Consolidation/synthesis of materials by electric current activated/assisted sintering, Materials Science and Engineering: R: Reports 63(4-6) (2009) 127-287.

[3] G. Lee, M.S. Yurlova, D. Giuntini, E.G. Grigoryev, O.L. Khasanov, J. McKittrick, E.A. Olevsky, Densification of zirconium nitride by spark plasma sintering and high voltage electric discharge consolidation: a comparative analysis, Ceram. Int. 41(10, Part B) (2015) 14973-14987.

[4] M.S. Yurlova, V.D. Demenyuk, L.Y. Lebedeva, D.V. Dudina, E.G. Grigoryev, E.A. Olevsky, Electric pulse consolidation: an alternative to spark plasma sintering, J. Mater. Sci. 49(3) (2014) 952-985.

[5] D.J. Williams, W. Johnson, Neck Formation and Growth in High-Voltage Discharge Forming of Metal Powders, Powder Metall. 25(2) (1982) 85-89.

[6] D.K. Kim, H.-R. Pak, K. Okazaki, Electrodischarge compaction of nickel powders, Mat. Sci. Eng. A. 104(0) (1988) 191-200.

[7] E.G. Grigoryev, E.A. Olevsky, Thermal processes during high-voltage electric discharge consolidation of powder materials, Scripta Mater. 66(9) (2012) 662-665.

[8] Z.A. Munir, U. Anselmi-Tamburini, M. Ohyanagi, The effect of electric field and pressure on the synthesis and consolidation of materials: A review of the spark plasma sintering method, J. Mater. Sci. 41(3) (2006) 763-777.

[9] E.A. Olevsky, W.L. Bradbury, C.D. Haines, D.G. Martin, D. Kapoor, S.J. Kang, Fundamental Aspects of Spark Plasma Sintering: I. Experimental Analysis of Scalability, J. Am. Ceram. Soc. 95(8) (2012) 2406-2413.

[10] E.A. Olevsky, C. Garcia-Cardona, W.L. Bradbury, C.D. Haines, D.G. Martin, D. Kapoor, S.J. Kang, Fundamental Aspects of Spark Plasma Sintering: II. Finite Element Analysis of Scalability, J. Am. Ceram. Soc. 95(8) (2012) 2414-2422.

[11] O. Guillon, J. Gonzalez-Julian, B. Dargatz, T. Kessel, G. Schierning, J. Räthel, M. Herrmann, Field-Assisted Sintering Technology/Spark Plasma Sintering: Mechanisms, Materials, and Technology Developments, Adv. Eng. Mater. 16(7) (2014) 830-849.

[12] Z.A. Munir, D.V. Quach, M. Ohyanagi, Electric Current Activation of Sintering: A Review of the Pulsed Electric Current Sintering Process, J. Am. Ceram. Soc. 94(1) (2011) 1-19.

[13] E. Olevsky, I. Bogachev, A. Maximenko, Spark-plasma sintering efficiency control by inter-particle contact area growth: A viewpoint, Scripta Mater. 69(2) (2013) 112-116.

[14] E.A. Olevsky, S. Kandukuri, L. Froyen, Consolidation enhancement in spark-plasma sintering: Impact of high heating rates, J. Appl. Phys. 102(11) (2007) 114913.

[15] E.A. Olevsky, L. Froyen, Impact of thermal diffusion on densification during SPS, J. Am. Ceram. Soc. 92(1) (2009) S122-S132.

[16] Z.A. Munir, Analytical treatment of the role of surface oxide layers in the sintering of metals, J. Mater. Sci. 14(11) (1979) 2733-2740.

[17] K.R. Anderson, J.R. Groza, M. Fendorf, C.J. Echer, Surface oxide debonding in field assisted powder sintering, Mat. Sci. Eng. A. 270(2) (1999) 278-282.

[18] J.R. Groza, A. Zavaliangos, Sintering activation by external electrical field, Mat. Sci. Eng. A. 287(2) (2000) 171-177.

[19] J.R. Groza, M. Garcia, J.A. Schneider, Surface effects in field-assisted sintering, J. Mater. Res. 16(1) (2001) 286-292.

[20] C.S. Bonifacio, J.F. Rufner, T.B. Holland, K. van Benthem, In situ transmission electron microscopy study of dielectric breakdown of surface oxides during electric field-assisted sintering of nickel nanoparticles, Appl. Phys. Lett. 101(9) (2012).

[21] C.S. Bonifacio, T.B. Holland, K. van Benthem, Evidence of surface cleaning during electric field assisted sintering, Scripta Mater. 69(11-12) (2013) 769-772.

[22] C.S. Bonifacio, T.B. Holland, K. van Benthem, Time-dependent dielectric breakdown of surface oxides during electric-field-assisted sintering, Acta Mater. 63 (2014) 140-149.

[23] R. Marder, C. Estournès, G. Chevallier, R. Chaim, Plasma in spark plasma sintering of ceramic particle compacts, Scripta Mater. 82 (2014) 57-60.

[24] D.M. Hulbert, A. Anders, J. Andersson, E.J. Lavernia, A.K. Mukherjee, A discussion on the absence of plasma in spark plasma sintering, Scripta Mater. 60(10) (2009) 835-838.

[25] P. Asoka-Kumar, K. O’Brien, K.G. Lynn, P.J. Simpson, K.P. Rodbell, Detection of current-induced vacancies in thin aluminum–copper lines using positrons, Appl. Phys. Lett. 68(3) (1996) 406-408.

[26] J.E. Garay, S.C. Glade, U. Anselmi-Tamburini, P. Asoka-Kumar, Z.A. Munir, Electric current enhanced defect mobility in Ni3Ti intermetallics, Appl. Phys. Lett. 85(4) (2004) 573-575.

[27] J.M. Frei, U. Anselmi-Tamburini, Z.A. Munir, Current effects on neck growth in the sintering of copper spheres to copper plates by the pulsed electric current method, J. Appl. Phys. 101(11) (2007) 114914-8.

[28] N. Toyofuku, T. Kuramoto, T. Imai, M. Ohyanagi, Z.A. Munir, Effect of pulsed DC current on neck growth between tungsten wires and tungsten plates during the initial stage of sintering by the spark plasma sintering method, J. Mater. Sci. 47(5) (2012) 2201-2205.

[29] W. Chen, U. Anselmi-Tamburini, J.E. Garay, J.R. Groza, Z.A. Munir, Fundamental investigations on the spark plasma sintering/synthesis process: I. Effect of dc pulsing on reactivity, Mat. Sci. Eng. A. 394(1–2) (2005) 132-138.

[30] U. Anselmi-Tamburini, J.E. Garay, Z.A. Munir, Fundamental investigations on the spark plasma sintering/synthesis process: III. Current effect on reactivity, Mat. Sci. Eng. A. 407(1–2) (2005) 24-30.

[31] E. Olevsky, L. Froyen, Constitutive modeling of spark-plasma sintering of conductive materials, Scripta Mater. 55(12) (2006) 1175-1178.

[32] Z. Trzaska, J.-P. Monchoux, Electromigration experiments by spark plasma sintering in the silver–zinc system, J. Alloys Compd. 635(0) (2015) 142-149.

[33] E.S. Machlin, Applied voltage and the plastic properties of ``brittle" rock salt, J. Appl. Phys. 30(7) (1959) 1109-1110.

[34] H. Conrad, A.F. Sprecher, W.D. Cao, X.P. Lu, Electroplasticity—the effect of electricity on the mechanical properties of metals, JOM 42(9) (1990) 28-33.

[35] H. Conrad, Electroplasticity in metals and ceramics, Mat. Sci. Eng. A 287(2) (2000) 276-287.

[36] W.A. Salandro, J.J. Jones, C. Bunget, L. Mears, J.T. Roth, The effect of electric current on metals, Electrically assisted forming: modeling and control, Springer International Publishing, Cham, 2015, pp. 37-54.

[37] X. Song, X. Liu, J. Zhang, Neck Formation and Self-Adjusting Mechanism of Neck Growth of Conducting Powders in Spark Plasma Sintering, J. Am. Ceram. Soc. 89(2) (2006) 494-500.

[38] M.S. Siopis, B.L. Kinsey, Experimental Investigation of Grain and Specimen Size Effects During Electrical-Assisted Forming, Journal of Manufacturing Science and Engineering 132(2) (2010) 021004-021004-7.

[39] M.S. Siopis, B.L. Kinsey, N. Kota, O.B. Ozdoganlar, Effect of Severe Prior Deformation on Electrical-Assisted Compression of Copper Specimens, Journal of Manufacturing Science and Engineering 133(6) (2011) 064502-064502-5.

[40] H. Jabbar, J.-P. Monchoux, F. Houdellier, M. Dollé, F.-P. Schimansky, F. Pyczak, M. Thomas, A. Couret, Microstructure and mechanical properties of high niobium containing TiAl alloys elaborated by spark plasma sintering, Intermetallics 18(12) (2010) 2312-2321.

[41] T. Grosdidier, G. Ji, S. Launois, Processing dense hetero-nanostructured metallic materials by spark plasma sintering, Scripta Mater. 57(6) (2007) 525-528.

[42] H.J. Frost, M.F. Ashby, Deformation-mechanism maps, the plasticity and creep of metals and ceramics, Pergamon Press, Oxford, 1982.

[43] J.D. Hansen, R.P. Rusin, M.-H. Teng, D.L. Johnson, Combined-Stage Sintering Model, J. Am. Ceram. Soc. 75(5) (1992) 1129-1135.

[44] H. Su, D.L. Johnson, Master sintering curve: a practical approach to sintering, J. Am. Ceram. Soc. 79(12) (1996) 3211-3217.

[45] O. Guillon, J. Langer, Master sintering curve applied to the Field-Assisted Sintering Technique, J. Mater. Sci. 45(19) (2010) 5191-5195.

[46] G. Bernard-Granger, C. Guizard, Spark plasma sintering of a commercially available granulated zirconia powder: I. Sintering path and hypotheses about the mechanism(s) controlling densification, Acta Mater. 55(10) (2007) 3493-3504.

[47] G. Bernard-Granger, A. Addad, G. Fantozzi, G. Bonnefont, C. Guizard, D. Vernat, Spark plasma sintering of a commercially available granulated zirconia powder: Comparison with hot-pressing, Acta Mater. 58(9) (2010) 3390-3399.

[48] P. Guyot, G. Antou, N. Pradeilles, A. Weibel, M. Vandenhende, G. Chevallier, A. Peigney, C. Estournès, A. Maître, Hot pressing and spark plasma sintering of alumina: Discussion about an analytical modelling used for sintering mechanism determination, Scripta Mater. 84–85 (2014) 35-38.

[49] G. Antou, P. Guyot, N. Pradeilles, M. Vandenhende, A. Maître, Identification of densification mechanisms of pressure-assisted sintering: application to hot pressing and spark plasma sintering of alumina, J. Mater. Sci. 50(5) (2015) 2327-2336.

[50] E.A. Olevsky, Theory of sintering: from discrete to continuum, Mat Sci Eng R 23(2) (1998) 41-100.

[51] J. Langer, M.J. Hoffmann, O. Guillon, Electric field-assisted sintering and hot pressing of semiconductive zinc oxide: a comparative study, J. Am. Ceram. Soc. 94(8) (2011) 2344-2353.

[52] J. Langer, M.J. Hoffmann, O. Guillon, Electric field-assisted sintering in comparison with the hot pressing of yttria-stabilized zirconia, J. Am. Ceram. Soc. 94(1) (2011) 24-31.

[53] J. Langer, M.J. Hoffmann, O. Guillon, Direct comparison between hot pressing and electric field-assisted sintering of submicron alumina, Acta Mater. 57(18) (2009) 5454-5465.

[54] M. Demuynck, J.-P. Erauw, O. Van der Biest, F. Delannay, F. Cambier, Densification of alumina by SPS and HP: A comparative study, J. Eur. Ceram. Soc. 32(9) (2012) 1957-1964.

[55] W. Li, E.A. Olevsky, J. McKittrick, A.L. Maximenko, R.M. German, Densification mechanisms of spark plasma sintering: multi-step pressure dilatometry, J. Mater. Sci. 47(20) (2012) 7036-7046.

[56] E.V. Aleksandrova, A.M. Ilyina, E.G. Grigoryev, E.A. Olevsky, Contribution of electric current into densification kinetics during spark plasma sintering of conductive powder, J. Am. Ceram. Soc. 98(11) (2015) 3509-3517.

[57] M. Cologna, B. Rashkova, R. Raj, Flash sintering of nanograin zirconia in <5 s at 850°C, J. Am. Ceram. Soc. 93(11) (2010) 3556-3559.

[58] J.A. Downs, V.M. Sglavo, Electric Field Assisted Sintering of Cubic Zirconia at 390°C, J. Am. Ceram. Soc. 96(5) (2013) 1342-1344.

[59] R. Muccillo, E.N.S. Muccillo, An experimental setup for shrinkage evaluation during electric field-assisted flash sintering: Application to yttria-stabilized zirconia, J. Eur. Ceram. Soc. 33(3) (2013) 515-520.

[60] R. Muccillo, E.N.S. Muccillo, Electric field-assisted flash sintering of tin dioxide, J. Eur. Ceram. Soc. 34(4) (2014) 915-923.

[61] C. Schmerbauch, J. Gonzalez-Julian, R. Röder, C. Ronning, O. Guillon, Flash Sintering of Nanocrystalline Zinc Oxide and its Influence on Microstructure and Defect Formation, J. Am. Ceram. Soc. 97(6) (2014) 1728-1735.

[62] H. Yoshida, Y. Sakka, T. Yamamoto, J.-M. Lebrun, R. Raj, Densification behaviour and microstructural development in undoped yttria prepared by flash-sintering, J. Eur. Ceram. Soc. 34(4) (2014) 991-1000.

[63] J. Gonzalez-Julian, O. Guillon, Effect of Electric Field/Current on Liquid Phase Sintering, J. Am. Ceram. Soc. 98(7) (2015) 2018-2027.

[64] S.K. Jha, R. Raj, The effect of electric field on sintering and electrical conductivity of titania, J. Am. Ceram. Soc. 97(2) (2014) 527-534.

[65] E. Zapata-Solvas, S. Bonilla, P.R. Wilshaw, R.I. Todd, Preliminary investigation of flash sintering of SiC, J. Eur. Ceram. Soc. 33(13–14) (2013) 2811-2816.

[66] M. Yu, S. Grasso, R. McKinnon, T. Saunders, M.J. Reece, Review of flash sintering: materials, mechanisms and modelling, Adv Appl Ceram 116(1) (2017) 24-60.

[67] R. Raj, M. Cologna, J.S.C. Francis, D.J. Green, Influence of externally imposed and internally generated electrical fields on grain growth, diffusional creep, sintering and related phenomena in ceramics, J. Am. Ceram. Soc. 94(7) (2011) 1941-1965.

[68] M. Cologna, J.S.C. Francis, R. Raj, Field assisted and flash sintering of alumina and its relationship to conductivity and MgO-doping, J. Eur. Ceram. Soc. 31(15) (2011) 2827-2837.

[69] J. Narayan, A new mechanism for field-assisted processing and flash sintering of materials, Scripta Mater. 69(2) (2013) 107-111.

[70] J.C. M'Peko, J.S.C. Francis, R. Raj, Impedance Spectroscopy and Dielectric Properties of Flash Versus Conventionally Sintered Yttria-Doped Zirconia Electroceramics Viewed at the Microstructural Level, J. Am. Ceram. Soc. 96(12) (2013) 3760-3767.

[71] I.J. Hewitt, A.A. Lacey, R.I. Todd, A Mathematical Model for Flash Sintering, Math. Model. Nat. Phenom. 10(6) (2015) 77-89.

[72] S. Grasso, Y. Sakka, N. Rendtorff, C. Hu, G. Maizza, H. Borodianska, O. Vasylkiv, Modeling of the temperature distribution of flash sintered zirconia, J. Ceram. Soc. Jpn. 119(1386) (2011) 144-146.

[73] K.S. Naik, V.M. Sglavo, R. Raj, Field assisted sintering of ceramic constituted by alumina and yttria stabilized zirconia, J. Eur. Ceram. Soc. 34(10) (2014) 2435-2442.

[74] K.S. Naik, V.M. Sglavo, R. Raj, Flash sintering as a nucleation phenomenon and a model thereof, J. Eur. Ceram. Soc. 34(15) (2014) 4063-4067.

[75] R.I. Todd, E. Zapata-Solvas, R.S. Bonilla, T. Sneddon, P.R. Wilshaw, Electrical characteristics of flash sintering: thermal runaway of Joule heating, J. Eur. Ceram. Soc. 35(6) (2015) 1865-1877.

[76] Y. Zhang, J.-I. Jung, J. Luo, Thermal runaway, flash sintering and asymmetrical microstructural development of ZnO and ZnO–Bi2O3 under direct currents, Acta Mater. 94 (2015) 87-100.

[77] S. Grasso, T. Saunders, H. Porwal, B. Milsom, A. Tudball, M. Reece, Flash Spark Plasma Sintering (FSPS) of α and β SiC, J. Am. Ceram. Soc. 99(5) (2016) 1534-1543.

[78] S. Grasso, T. Saunders, H. Porwal, O. Cedillos-Barraza, D.D. Jayaseelan, W.E. Lee, M.J. Reece, Flash spark plasma sintering (FSPS) of pure $ZrB_2$, J. Am. Ceram. Soc. 97(8) (2014) 2405-2408.

[79] S. Grasso, E.-Y. Kim, T. Saunders, M. Yu, A. Tudball, S.-H. Choi, M. Reece, Ultra-Rapid Crystal Growth of Textured SiC Using Flash Spark Plasma Sintering Route, Crystal Growth & Design 16(4) (2016) 2317-2321.

[80] E.A. Olevsky, S.M. Rolfing, A.L. Maximenko, Flash (ultra-rapid) spark-plasma sintering of silicon carbide, Sci. Rep. 6 (2016) 33408.

[81] B. Niu, F. Zhang, J. Zhang, W. Ji, W. Wang, Z. Fu, Ultra-fast densification of boron carbide by flash spark plasma sintering, Scripta Mater. 116 (2016) 127-130.

[82] B. Román-Manso, M. Belmonte, M.I. Osendi, P. Miranzo, Effects of Current Confinement on the Spark Plasma Sintering of Silicon Carbide Ceramics, J. Am. Ceram. Soc. 98(9) (2015) 2745-2753.

[83] E. Zapata-Solvas, D. Gómez-García, A. Domínguez-Rodríguez, R.I. Todd, Ultra-fast and energy-efficient sintering of ceramics by electric current concentration, Sci. Rep. 5 (2015) 8513.

[84] E.A. Olevsky, Theory of sintering: from discrete to continuum, Materials Science and Engineering: R: Reports 23(2) (1998) 41-100.

[85] J. Campbell, Y. Fahmy, H. Conrad, Influence of an electric field on the plastic deformation of fine-grained Al2O3, Metall and Mat Trans A 30(11) (1999) 2817-2823.

[86] D. Yang, H. Conrad, Plastic deformation of fine-grained $Al_2O_3$ in the presence of an electric field, Scripta Mater. 41(4) (1999) 397-401.

[87] H. Conrad, D. Yang, Influence of an electric field on the plastic deformation of fine-grained MgO at high homologous temperatures, Acta Mater. 48(16) (2000) 4045-4052.

[88] T.G. Nieh, J. Wadsworth, O.D. Sherby, Superplasticity in metals and ceramics, Cambridge University Press, Cambridge, 1997.

[89] H. Conrad, Thermally activated plastic flow of metals and ceramics with an electric field or current, Mat. Sci. Eng. A. 322(1–2) (2002) 100-107.

[90] B. Ruszkiewicz, T. Grimm, I. Ragai, L. Mears, J.T. Roth, A Review of Electrically-Assisted Manufacturing with Emphasis on Modeling and Understanding of the Electroplastic Effect, Journal of Manufacturing Science and Engineering (2017).

[91] J.T. Roth, I. Loker, D. Mauck, M. Warner, S.F. Golovashchenko, A. Krause, Enhanced formability of 5754 aluminum sheet metal using electric pulsing, Trans. North Am. Manuf. Res. Inst. SME 36 (2008) 405-412.

[92] T. Ungár, A. Borbély, The effect of dislocation contrast on x-ray line broadening: A new approach to line profile analysis, Appl. Phys. Lett. 69(21) (1996) 3173-3175.

[93] T. Ungar, I. Dragomir, A. Revesz, A. Borbely, The contrast factors of dislocations in cubic crystals: the dislocation model of strain anisotropy in practice, J. Appl. Crystallogr. 32(5) (1999) 992-1002.

[94] S. Deng, R. Li, T. Yuan, S. Xie, M. Zhang, K. Zhou, P. Cao, Direct current-enhanced densification kinetics during spark plasma sintering of tungsten powder, Scripta Mater. 143 (2018) 25-29.

[95] K. Okazaki, M. Kagawa, H. Conrad, A study of the electroplastic effect in metals, Scripta Metallurgica 12(11) (1978) 1063-1068.

[96] W. Kang, I. Beniam, S.M. Qidwai, In situ electron microscopy studies of electromechanical behavior in metals at the nanoscale using a novel microdevice-based system, Rev. Sci. Instrum. 87(9) (2016) 095001.

[97] S.-J. Kim, S.-D. Kim, D. Yoo, J. Lee, Y. Rhyim, D. Kim, Evaluation of the Athermal Effect of Electric Pulsing on the Recovery Behavior of Magnesium Alloy, Metall and Mat Trans A 47(12) (2016) 6368-6373.

[98] V.O. Zlokazov, V.V. Potemkin, A.V. Stepanov, D.G. Chikin, Influence of structural defects on 1/f in thin niobium films, Radiophysics and Quantum Electronics 35(11) (1992) 610-613.

[99] M. Kumar, N. Umezawa, S. Ishii, T. Nagao, Examining the performance of refractory conductive ceramics as plasmonic materials: a theoretical approach, ACS Photonics 3(1) (2016) 43-50.

[100] T. Kino, T. Endo, S. Kawata, Deviations from Matthiessen's rule of the electrical resistivity of dislocations in aluminum, J. Phys. Soc. Jpn. 36(3) (1974) 698-705.

[101] D. Hull, D.J. Bacon, Chapter 10 - Strength of Crystalline Solids, Introduction to Dislocations (Fifth Edition), Butterworth-Heinemann, Oxford, 2011, pp. 205-249.

[102] C. Manière, L. Durand, A. Weibel, C. Estournès, Spark-plasma-sintering and finite element method: From the identification of the sintering parameters of a submicronic α-alumina powder to the development of complex shapes, Acta Mater. 102 (2016) 169-175.

[103] C. Manière, L. Durand, G. Chevallier, C. Estournès, A spark plasma sintering densification modeling approach: from polymer, metals to ceramics, J. Mater. Sci. 53(10) (2018) 7869-7876.

[104] H.F. Fischmeister, E. Arzt, Densification of powders by particle deformation, Powder Metall. 26(2) (1983) 82-88.

[105] A.S. Helle, K.E. Easterling, M.F. Ashby, Hot-isostatic pressing diagrams: New developments, Acta Metall. 33(12) (1985) 2163-2174.

[106] D. Holec, M. Friák, J. Neugebauer, P.H. Mayrhofer, Trends in the elastic response of binary early transition metal nitrides, Phys. Rev. B 85(6) (2012) 064101.

[107] T. Ungar, J. Gubicza, G. Ribarik, A. Borbely, Crystallite size distribution and dislocation structure determined by diffraction profile analysis: principles and practical application to cubic and hexagonal crystals, J. Appl. Crystallogr. 34(3) (2001) 298-310.

[108] J. Málek, L. Beneš, T. Mitsuhashi, Powder diffraction data and Rietveld refinement of metastable t-ZrO2 at low temperature, Powder Diffr. 12(2) (1997) 96-98.

[109] C. Manière, G. Lee, E.A. Olevsky, Proportional integral derivative, modeling and ways of stabilization for the spark plasma sintering process, Results Phys. 7 (2017) 1494-1497.

[110] R.G. Sheppard, D. Morgan, D.M. Mathes, D.J. Bray, Properties and Characteristics of Graphite, Poco Graphite, Inc., 1987.

[111] J. Adachi, K. Kurosaki, M. Uno, S. Yamanaka, Effect of porosity on thermal and electrical properties of polycrystalline bulk ZrN prepared by spark plasma sintering, J. Alloys Compd. 432(1-2) (2007) 7-10.

[112] V. Basini, J.P. Ottaviani, J.C. Richaud, M. Streit, F. Ingold, Experimental assessment of thermophysical properties of (Pu,Zr)N, J. Nucl. Mater. 344(1-3) (2005) 186-190.

[113] S. Muñoz, U. Anselmi-Tamburini, Temperature and stress fields evolution during spark plasma sintering processes, J. Mater. Sci. 45(23) (2010) 6528-6539.

[114] G. Lee, E.A. Olevsky, C. Manière, A. Maximenko, O. Izhvanov, C. Back, J. McKittrick, Effect of electric current on densification behavior of conductive ceramic powders consolidated by spark plasma sintering, Acta Mater. 144(Supplement C) (2018) 524-533.

[115] K.I. Rybakov, E.A. Olevsky, V.E. Semenov, The microwave ponderomotive effect on ceramic sintering, Scripta Mater. 66(12) (2012) 1049-1052.

[116] C. Manière, A. Pavia, L. Durand, G. Chevallier, K. Afanga, C. Estournès, Finite-element modeling of the electro-thermal contacts in the spark plasma sintering process, J. Eur. Ceram. Soc. 36(3) (2016) 741-748.

[117] X. Wei, D. Giuntini, A.L. Maximenko, C.D. Haines, E.A. Olevsky, Experimental investigation of electric contact resistance in spark plasma sintering tooling setup, J. Am. Ceram. Soc. 98(11) (2015) 3553-3560.

[118] C. Manière, L. Durand, E. Brisson, H. Desplats, P. Carré, P. Rogeon, C. Estournès, Contact resistances in spark plasma sintering: from in-situ and ex-situ determinations to an extended model for the scale up of the process, J.Eur. Ceram. Soc. 37(4) (2016) 1593-1605.

[119] R.Y. Petrykina, L.K. Shvedova, Hot pressing of transition metal nitrides and their properties, Sov Powder Metall+ 11(4) (1972) 276-279.

[120] S.L. Hayes, J.K. Thomas, K.L. Peddicord, Material property correlations for uranium mononitride: III. Transport properties, J. Nucl. Mater. 171(2–3) (1990) 289-299.

[121] G. Lee, J. McKittrick, E. Ivanov, E.A. Olevsky, Densification mechanism and mechanical properties of tungsten powder consolidated by spark plasma sintering, Int. J. Refract. Met. Hard Mater. 61 (2016) 22-29.

[122] E. Khaleghi, Y.-S. Lin, M.A. Meyers, E.A. Olevsky, Spark plasma sintering of tantalum carbide, Scripta Mater. 63(6) (2010) 577-580.

[123] J. Adachi, K. Kurosaki, M. Uno, S. Yamanaka, Thermal and electrical properties of zirconium nitride, J. Alloys Compd. 399(1-2) (2005) 242-244.

[124] G.W. Egeland, K. Wheeler, P. Peralta, K.J. McClellan, S.A. Maloy, G.M. Bond, Plastic deformation in zirconium nitride observed by nanoindentation and TEM, J. Nucl. Mater. 416(3) (2011) 253-261.

[125] K. Wheeler, P. Peralta, M. Parra, K. McClellan, J. Dunwoody, G. Egeland, Effect of sintering conditions on the microstructure and mechanical properties of ZrN as a surrogate for actinide nitride fuels, J. Nucl. Mater. 366(3) (2007) 306-316.

[126] H. Muta, K. Kurosaki, M. Uno, S. Yamanaka, Thermal and mechanical properties of uranium nitride prepared by SPS technique, J. Mater. Sci. 43(19) (2008) 6429-6434.

[127] M. Burghartz, G. Ledergerber, H. Hein, R.R. van der Laan, R.J.M. Konings, Some aspects of the use of ZrN as an inert matrix for actinide fuels, J. Nucl. Mater. 288(2-3) (2001) 233-236.

[128] M. Streit, F. Ingold, Nitrides as a nuclear fuel option, J. Eur. Ceram. Soc. 25(12) (2005) 2687-2692.

[129] S. Park, I. Han, H. Lee, S. Huh, W. Park, Microstructural evolution and grain morphology of ZrN pellets, Metals and Materials International 15(2) (2009) 187-192.

[130] Y. Arai, K. Nakajima, Preparation and characterization of PuN pellets containing ZrN and TiN, J. Nucl. Mater. 281(2-3) (2000) 244-247.

[131] A.K. Sengupta, C. Ganguly, (Pu0.7u0.3)N Fuel for Fast Breeder Test Reactor-Thermal Conductivity and Chemical Compatibility with Ss 316 and Sodium, T Indian I Metals 43(1) (1990) 31-35.

[132] R.A. Andrievskii, I.I. Spivak, K.L. Chevasheva, Effective self-diffusion coefficients in interstitial compounds, Sov Powder Metall+ 7(7) (1968) 559-562.

[133] O.V. Pshenichnaya, M.A. Kuzenkova, P.S. Kislyi, The sintering of zirconium nitride in vacuum and in nitrogen, Sov Powder Metall+ 14(12) (1975) 986-989.

[134] Y. Tang, G.-J. Zhang, J.-X. Xue, X.-G. Wang, C.-M. Xu, X. Huang, Densification and mechanical properties of hot-pressed ZrN ceramics doped with Zr or Ti, J. Eur. Ceram. Soc. 33(7) (2013) 1363-1371.

[135] N. Alexandre, M. Desmaison-Brut, F. Valin, M. Boncoeur, Mechanical properties of hot isostatically pressed zirconium nitride materials, J. Mater. Sci. 28(9) (1993) 2385-2390.

[136] H.J. Ryu, Y.W. Lee, S.I. Cha, S.H. Hong, Sintering behaviour and microstructures of carbides and nitrides for the inert matrix fuel by spark plasma sintering, J. Nucl. Mater. 352(1-3) (2006) 341-348.

[137] Y. Tang, J.-X. Xue, G.-J. Zhang, X.-G. Wang, C.-M. Xu, Microstructural differences and formation mechanisms of spark plasma sintered ceramics with or without boron nitride wrapping, Scripta Mater. 75 (2014) 98-101.

[138] C. Manière, U. Kus, L. Durand, R. Mainguy, J. Huez, D. Delagnes, C. Estournès, Identification of the norton-green compaction model for the prediction of the Ti–6Al–4V densification during the spark plasma sintering process Adv. Eng. Mater. 18(10) (2016) 1720-1727.

[139] M. Yoneya, T. Ikeshoji, A numerical calculation method advantageous for complex boundary problems -an application to the pulse discharge sintering process, Mater. Trans. 42(11) (2001) 2165-2171.

[140] N. Chawake, L.D. Pinto, A.K. Srivastav, K. Akkiraju, B.S. Murty, R.S. Kottada, On Joule heating during spark plasma sintering of metal powders, Scripta Mater. 93 (2014) 52-55.

[141] W. Cao, A.F. Sprecher, H. Conrad, Measurement of the electroplastic effect in Nb, J. Phys. E. Sci. Instrum. 22(12) (1989) 1026-1034.

[142] P.-A. Geslin, B. Appolaire, A. Finel, Multiscale theory of dislocation climb, Phys. Rev. Lett. 115(26) (2015) 265501.

[143] W. Chen, J.Z. Jiang, Elastic properties and electronic structures of 4d- and 5d-transition metal mononitrides, J. Alloys Compd. 499(2) (2010) 243-254.

[144] A.B. Riabov, V.A. Yartys, B.C. Hauback, P.W. Guegan, G. Wiesinger, I.R. Harris, Hydrogenation behaviour, neutron diffraction studies and microstructural characterisation of boron oxide-doped Zr–V alloys, J. Alloys Compd. 293–295(0) (1999) 93-100.

[145] B. Bondars, G. Heidemane, J. Grabis, K. Laschke, H. Boysen, J. Schneider, F. Frey, Powder diffraction investigations of plasma sprayed zirconia, J. Mater. Sci. 30(6) (1995) 1621-1625.

[146] D.V. Quach, H. Avila-Paredes, S. Kim, M. Martin, Z.A. Munir, Pressure effects and grain growth kinetics in the consolidation of nanostructured fully stabilized zirconia by pulsed electric current sintering, Acta Mater. 58(15) (2010) 5022-5030.

[147] X. Wei, C. Back, O. Izhvanov, O. Khasanov, C. Haines, E. Olevsky, Spark Plasma Sintering of Commercial Zirconium Carbide Powders: Densification Behavior and Mechanical Properties, Materials 8(9) (2015) 5289.

[148] P.T. Dawson, Auger and x-ray characterization of surface nitride films on Ti, Zr, and Hf, Journal of Vacuum Science and Technology 21(1) (1982) 36.

[149] J. Adachi, K. Kurosaki, M. Uno, S. Yamanaka, Porosity influence on the mechanical properties of polycrystalline zirconium nitride ceramics, J. Nucl. Mater. 358(2-3) (2006) 106-110.

[150] X.J. Chen, V.V. Struzhkin, Z. Wu, M. Somayazulu, J. Qian, S. Kung, A.N. Christensen, Y. Zhao, R.E. Cohen, H.K. Mao, R.J. Hemley, Hard superconducting nitrides, P. Natl. Acad. Sci. USA. 102(9) (2005) 3198-201.

[151] E.V. Aleksandrova, A.M. Ilyina, E.G. Grigoryev, E.A. Olevsky, Contribution of electric current into densification kinetics during spark-plasma sintering of conductive powder, J. Am. Ceram. Soc. (2015) in press.

[152] E.A. Olevsky, B. Kushnarev, A. Maximenko, V. Tikare, M. Braginsky, Modelling of anisotropic sintering in crystalline ceramics, Philos Mag 85(19) (2005) 2123-2146.

[153] M.E. Straumanis, C.A. Faunce, W.J. James, The Defect Structure and Bonding of Zirconium Nitride Containing Excess Nitrogen, Inorg. Chem. 5(11) (1966) 2027-2030.

[154] J. Luo, R. Stevens, Porosity-dependence of elastic moduli and hardness of 3Y-TZP ceramics, Ceram. Int. 25(3) (1999) 281-286.

[155] B. McWilliams, A. Zavaliangos, K. Cho, R. Dowding, The modeling of electric-current-assisted sintering to produce bulk nanocrystalline tungsten, JOM 58(4) (2006) 67-71.

[156] Y. Kim, M.-H. Hong, S. Lee, E.-P. Kim, S. Lee, J.-W. Noh, The effect of yttrium oxide on the sintering behavior and hardness of tungsten, Metals and Materials International 12(3) (2006) 245-248.

[157] B.P. Bewlay, C.L. Briant, The Formation and the Role of Potassium Bubbles in NS-Doped Tungsten, in: L.B. Lassner, W.D. Schubert, B. Lux (Eds.), The Chemistry of Non-Sag Tungsten, Pergamon, Oxford, 1995, pp. 137-159.

[158] D.M. Karpinos, A.A. Kravchenko, Y.L. Pilipovskii, V.G. Tkachenko, Y.M. Shamatov, Hot pressing of tungsten and its pseudoalloys. Part I, Sov Powder Metall+ 9(4) (1970) 287-291.

[159] M.A. Monge, M.A. Auger, T. Leguey, Y. Ortega, L. Bolzoni, E. Gordo, R. Pareja, Characterization of novel W alloys produced by HIP, J. Nucl. Mater. 386–388 (2009) 613-617.

[160] G. Jones, J.R. Groza, K. Yamazaki, K. Shoda, Plasma Activated Sintering (PAS) of Tungsten Powders, Mater. Manuf. Processes 9(6) (1994) 1105-1114.

[161] K.C. Cho, R.H. Woodman, B.R. Klotz, R.J. Dowding, Plasma Pressure Compaction of Tungsten Powders, Mater. Manuf. Processes 19(4) (2004) 619-630.

[162] R.M. German, E. Olevsky, Mapping the compaction and sintering response of tungsten-based materials into the nanoscale size range, Int J Refract Met H 23(4-6) (2005) 294-300.

[163] R.M. German, J. Ma, X. Wang, E. Olevsky, Processing model for tungsten powders and extension to nanoscale size range, Powder Metall. 49(1) (2006) 19-27.

[164] H.W. Hayden, J.H. Brophy, Low-temperature sintering of pure tungsten and tungsten-iridium, Journal of the Less Common Metals 6(3) (1964) 214-218.

[165] N.C. Kothari, Sintering kinetics in tungsten powder, Journal of the Less Common Metals 5(2) (1963) 140-150.

[166] N.C. Kothari, Grain Growth during Sintering of Tungsten, J. Appl. Phys. 38(5) (1967) 2395-2396.

[167] T. Vasilos, J.T. Smith, Diffusion Mechanism for Tungsten Sintering Kinetics, J. Appl. Phys. 35(1) (1964) 215-217.

[168] L.C. Chen, Plansee Seminar Dilatometric analysis of sintering of tungsten and tungsten with ceria and hafnia dispersions, Int. J. Refract. Met. Hard Mater. 12(1) (1994) 41-51.

[169] D.M. Karpinos, A.A. Kravchenko, Y.L. Pilipovskii, V.G. Tkachenko, Y.M. Shamatov, Hot pressing of tungsten and its pseudoalloys. II, Sov Powder Metall+ 10(5) (1971) 367-372.

[170] Z. Gao, G. Viola, B. Milsom, I. Whitaker, H. Yan, M. Reece, Kinetics of Densification and Grain Growth of Pure Tungsten During Spark Plasma Sintering, Metall and Materi Trans B 43(6) (2012) 1608-1614.

[171] D.S. Wilkinson, M.F. Ashby, Pressure sintering by power law creep, Acta Metall. 23(11) (1975) 1277-1285.

[172] S.L. Robinson, O.D. Sherby, Mechanical behavior of polycrystalline tungsten at elevated temperature, Acta Metall. 17(2) (1969) 109-125.

[173] S. Matsuyama, A. Kurumada, Y. Imamura, H. Kurishita, Y. Motohashi, Study on Superplasticity of Tungsten Materials, Proc. Ibaraki district conference 2003 (2003) 145-146.

[174] M. Garfinkle, SUPERPLASTICITY IN TUNGSTEN-RHENIUM ALLOYS Trans. Metall. AIME 2(245) (1969) 303.

[175] E. Oda, T. Ohtaki, A. Kuroda, H. Fujiwara, K. Ameyama, K. Yoshida, Thermal Stability of Nano Grain Structure Tungsten Prepared by SPD-PM Process, Advanced Materials Research 15-17 (2006) 564-569.

[176] K. Ameyama, E. Oda, H. Fujiwara, Superplasticity and high temperature deformation behaviour in nano grain Tungsten compacts, Materialwiss. Werkstofftech. 39(4-5) (2008) 336-339.

[177] P. Souvatzis, M.I. Katsnelson, S. Simak, R. Ahuja, O. Eriksson, P. Mohn, First-principles prediction of superplastic transition-metal alloys, Physical Review B 70(1) (2004) 012201.

[178] H. Kurishita, S. Matsuo, H. Arakawa, S. Kobayashi, K. Nakai, T. Takida, K. Takebe, M. Kawai, Superplastic deformation in W–0.5 wt.% TiC with approximately 0.1 μm grain size, Mat. Sci. Eng. A. 477(1–2) (2008) 162-167.

[179] E.S. Dvilis, O.L. Khasanov, V.N. Gulbin, M.S. Petyukevich, A.O. Khasanov, E.A. Olevsky, Spark Plasma Sintering of Aluminum-Magnesium-Matrix Composites with Boron Carbide and Tungsten Nano-powder Inclusions: Modeling and Experimentation, JOM 68(3) (2016) 908-919.

[180] H.E. Swanson, E. Tatge, S. United, Standard X-ray diffraction powder patterns. Vol. I, Data for 54 inorganic substances, National Bureau of Standards, Washington, D.C., 1953.

[181] T.R. Malow, C.C. Koch, Grain growth in nanocrystalline iron prepared by mechanical attrition, Acta Mater. 45(5) (1997) 2177-2186.

[182] K.G. Kreider, G. Bruggeman, GRAIN BOUNDARY DIFFUSION IN TUNGSTEN, Journal Name: Trans. Met. Soc. AIME 239 (1967) 1222-1226.

[183] H. Wang, Z. Zak Fang, Kinetic Analysis of Densification Behavior of Nano-sized Tungsten Powder, J. Am. Ceram. Soc. 95(8) (2012) 2458-2464.

[184] T.G. Nieh, J. Wadsworth,, O.D. Sherby., Superplasticity in Metals and Ceramics, Cambridge University Press1997.

[185] A.M. Korsunsky, M. Xie, N. Baimpas, X. Song, X-ray Texture Analysis and Imaging of Engineering Materials at Oxford HEX-lab, Proceedings of the International MultiConference of Engineers and Computer Scientists 2 (2012).

[186] M.T. Pérez-Prado, G. González-Doncel, O.A. Ruano, T.R. McNelley, Texture analysis of the transition from slip to grain boundary sliding in a discontinuously recrystallized superplastic aluminum alloy, Acta Mater. 49(12) (2001) 2259-2268.

[187] F.W. Crossman, M.F. Ashby, The non-uniform flow of polycrystals by grain-boundary sliding accommodated by power-law creep, Acta Metall. 23(4) (1975) 425-440.

[188] F.A. Mohamed, T.G. Langdon, Deformation mechanism maps for superplastic materials, Scripta Metallurgica 10(8) (1976) 759-762.

[189] H. Lüthy, R.A. White, O.D. Sherby, Grain boundary sliding and deformation mechanism maps, Materials Science and Engineering 39(2) (1979) 211-216.

[190] J. Almanstötter, M. Rühle, Grain growth phenomena in tungsten wire, Int. J. Refract. Met. Hard Mater. 15(5–6) (1997) 295-300.

[191] D.M. Karpinos, A.A. Kravchenko, Y.L. Pilipovskii, V.G. Tkachenko, Y.M. Shamatov, Reaction of tungsten with die material in hot pressing, Sov Powder Metall+ 9(10) (1970) 831-834.

[192] L. McCarty, R. Donelson, R. Hehemann, A diffusion model for tungsten powder carburization, Metall. Trans. A 18(13) (1987) 969-974.

[193] E. Lassner, W.-D. Schubert, Tungsten : Properties, Chemistry, Technology of the Element, Alloys, and Chemical Compounds, 1 ed., Springer US1999.

[194] Y. Jiang, J.F. Yang, Z. Zhuang, R. Liu, Y.P. Zhou, X. Wang, Q.F. Fang, Characterization and properties of tungsten carbide coatings fabricated by SPS technique, J. Nucl. Mater. 433(1–3) (2013) 449-454.

[195] B.B. Bokhonov, A.V. Ukhina, D.V. Dudina, A.G. Anisimov, V.I. Mali, I.S. Batraev, Carbon uptake during Spark Plasma Sintering: investigation through the analysis of the carbide "footprint" in a Ni-W alloy, RSC Advances 5(98) (2015) 80228-80237.

[196] E. Khaleghi, Tailored Net-Shape Powder Composites by Spark Plasma Sintering, Mechanical and Aerospace Engineering, UC San Diego, UC San Diego Electronic Theses and Dissertations, 2012.

[197] J. Ma, J. Zhang, W. Liu, Z. Shen, Suppressing pore-boundary separation during spark plasma sintering of tungsten, J. Nucl. Mater. 438(1–3) (2013) 199-203.

[198] R. Coppola, C. Ohms, J. Reiser, M. Rieth, R.C. Wimpory, Neutron diffraction stress determination in W-laminates for structural divertor applications, Nuclear Materials and Energy 3–4 (2015) 37-42.

[199] Z. Zhou, Y. Ma, J. Du, J. Linke, Fabrication and characterization of ultra-fine grained tungsten by resistance sintering under ultra-high pressure, Mat. Sci. Eng. A. 505(1–2) (2009) 131-135.

[200] T. Takida, H. Kurishita, M. Mabuchi, T. Igarashi, Y. Doi, T. Nagae, Mechanical properties of fine-grained, sintered molybdenum alloys with dispersed particles developed by mechanical alloying, Mater. Trans. 45(1) (2004) 143-148.

[201] T. Takida, M. Mabuchi, N. Nakamura, T. Igarashi, Y. Doi, T. Nagae, The role of dispersed particles in strengthening and fracture mechanisms in a Mo-ZrC alloy processed by mechanical alloying, Metall and Mat Trans A 31(3) (2000) 715-721.

[202] S.P. Chakraborty, N. Krishnamurthy, The preparation of a molybdenum based high temperature refractory alloy by powder processing route, Journal of Powder Metallurgy & Mining 2(3) (2013).

[203] I. Campos, R. Rosas, U. Figueroa, C. VillaVelázquez, A. Meneses, A. Guevara, Fracture toughness evaluation using Palmqvist crack models on AISI 1045 borided steels, Mat. Sci. Eng. A. 488(1-2) (2008) 562-568.

[204] P.K. Higgins, Z.A. Munir, Modification of the sintering kinetics of palladium by a surface oxide, Metall. Trans. B 12(3) (1981) 589-594.

[205] R.T. Begley, D.L. Harrod, R.E. Gold, High Temperature Creep and Fracture Behavior of the Refractory Metals, Springer US, Boston, MA, 1968, pp. 41-83.

[206] J.B. Conway, P.N. Flagella, Creep-rupture data for the refractory metals to high temperatures, Gordon and Breach Science Publishers1971.

[207] W.V. Green, M.C. Smith, D.M. Olson, Short-time creep-rupture behavior of molybdenum at high temperature, Trans. AIME 2215 (1959) 1061-1066.

[208] H. Carvalhinhos, B.B. Argent, The creep of molybdenum, J. Inst. Met. 95 (1967) 364-368.

[209] T. Takida, M. Mabuchi, M. Nakamura, T. Igarashi, Y. Doi, T. Nagae, Mechanical properties of a ZrC-dispersed Mo alloy processed by mechanical alloying and spark plasma sintering, Mat. Sci. Eng. A. 276(1–2) (2000) 269-272.

[210] K.B. Yoder, A.A. Elmustafa, J.C. Lin, R.A. Hoffman, D.S. Stone, Activation analysis of deformation in evaporated molybdenum thin films, J. Phys. D: Appl. Phys. 36(7) (2003) 884-895.

[211] D.S. Stone, K.B. Yoder, Division of the hardness of molybdenum into rate-dependent and rate-independent components, J. Mater. Res. 9(10) (1994) 2524-2533.

[212] L.L.Y. Chang, B. Phillips, Phase relations in refractory mtal-oygen sstems, J. Am. Ceram. Soc. 52(10) (1969) 527-533.

[213] P. Bakhru, Equilibria between $MoO_2$ and liquid molybdenum oxide, UNIVERSITY OF MISSOURI-ROLLA, 1972.

[214] H.S. Huang, K.S. Hwang, Deoxidation of molybdenum during vacuum sintering, Metall and Mat Trans A 33(3) (2002) 657-664.

[215] L. Brewer, R.H. Lamoreaux, The Mo-O system (Molybdenum-Oxygen), Bulletin of Alloy Phase Diagrams 1(2) (1980) 85-89.

[216] B.-K. Lee, J.-M. Oh, I.-J. Shon, H.-S. Kim, J.-W. Lim, Influence of Oxygen Concentration on Mechanical Properties of Molybdenum Powder During Sintering, Journal of Nanoscience and Nanotechnology (2014).

[217] J.X. Zhu, D.F. Zhou, S.R. Guo, J.F. Ye, X.F. Hao, X.Q. Cao, J. Meng, Grain boundary conductivity of high purity neodymium-doped ceria nanosystem with and without the doping of molybdenum oxide, J. Power Sources 174(1) (2007) 114-123.

[218] S. Majumdar, S. Raveendra, I. Samajdar, P. Bhargava, I.G. Sharma, Densification and grain growth during isothermal sintering of Mo and mechanically alloyed Mo–TZM, Acta Mater. 57(14) (2009) 4158-4168.

[219] W.J. Clegg, Role of carbon in the sintering of boron-doped silicon carbide, J. Am. Ceram. Soc. 83(5) (2000) 1039-1043.

[220] S. Prochazka, R.M. Scanlan, Effect of boron and carbon on sintering of SIC, J. Am. Ceram. Soc. 58(1-2) (1975) 72.

[221] M. Rączka, G. Górny, L. Stobierski, K. Rożniatowski, Effect of carbon content on the microstructure and properties of silicon carbide-based sinters, Mater. Charact. 46(2) (2001) 245-249.

[222] M.A. Rossi, M.J. Matthewson, A. Kaza, D. Niesz, R.L. Haber, Modeling of gas-phase transport and composition evolution during the initial-stage sintering of boron carbide with carbon additions, J. Am. Ceram. Soc. 93(11) (2010) 3691-3699.

[223] M. Asadikiya, C. Rudolf, C. Zhang, B. Boesl, A. Agarwal, Y. Zhong, Thermodynamic modeling and investigation of the oxygen effect on the sintering of B4C, J. Alloys Compd. 699 (2017) 1022-1029.

[224] M. Thompson, W.G. Fahrenholtz, G. Hilmas, Effect of starting particle size and oxygen content on densification of ZrB2, J. Am. Ceram. Soc. 94(2) (2011) 429-435.

[225] J.H.C. Kyoung Hun Kim, Joo Seok Park, Jong Pil Ahn and Kwang Bo Shim, Sintering behavior and mechanical properties of B4C ceramics fabricated by spark plasma sintering, Journal of Ceramic Processing Research 10(6) (2009) 716-720.

[226] M. Saghafi, A. Ataie, S. Heshmati-Manesh, SOLID STATE REDUCTION OF MoO 3 WITH CARBON VIA MECHANICAL ALLOYING TO SYNTHESIZE NANO-CRYSTALINE MoO 2, International Journal of Modern Physics: Conference Series 5 (2012) 441-447.

[227] M. Saghafi, A. Ataie, S. Heshmati-Manesh, Effects of mechanical activation of MoO3/C powder mixture in the processing of nano-crystalline molybdenum, Int. J. Refract. Met. Hard Mater. 29(4) (2011) 419-423.

[228] E. Khaleghi, Y.-S. Lin, M.A. Meyers, E.A. Olevsky, Spark plasma sintering of tantalum carbide, Scripta Materialia 63(6) (2010) 577-580.

[229] G.-S. Kim, H.G. Kim, D.-G. Kim, S.-T. Oh, M.-J. Suk, Y.D. Kim, Densification behavior of Mo nanopowders prepared by mechanochemical processing, J. Alloys Compd. 469(1–2) (2009) 401-405.

[230] R.K. Bordia, S.-J.L. Kang, E.A. Olevsky, Current understanding and future research directions at the onset of the next century of sintering science and technology, Journal of the American Ceramic Society 100(6) (2017) 2314-2352.

[231] R. Ohser-Wiedemann, U. Martin, H.J. Seifert, A. Müller, Densification behaviour of pure molybdenum powder by spark plasma sintering, Int. J. Refract. Met. Hard Mater. 28(4) (2010) 550-557.

[232] J.D. Hanawalt, H.W. Rinn, L.K. Frevel, Chemical analysis by X-Ray diffraction, Anal. Chem. 10 (1938) 475-512.

[233] H.E. Swanson, E. Tatge, S. United, Standard X-ray diffraction powder patterns. Vol. I, Data for 54 inorganic substances, National Bureau of Standards, [Washington, D.C.], 1953.

[234] A.N. Christensen, A neutron diffraction investigation on a crystal of alpha-Mo2 C, Acta Chem. Scand., Ser. A 31 (1977) 509 -511.

[235] B. Eren, L. Marot, M. Langer, R. Steiner, M. Wisse, D. Mathys, E. Meyer, The effect of low temperature deuterium plasma on molybdenum reflectivity, Nucl. Fusion 51(10) (2011) 103025.

[236] J.N. Brooks, J.P. Allain, Particle deposition and optical response of ITER motional Stark effect diagnostic first mirrors, Nucl. Fusion 48(4) (2008) 045003.

[237] B. Eren, L. Marot, A. Litnovsky, M. Matveeva, R. Steiner, V. Emberger, M. Wisse, D. Mathys, G. Covarel, E. Meyer, Reflective metallic coatings for first mirrors on ITER, Fusion Eng. Des. 86(9) (2011) 2593-2596.

[238] M. Wisse, B. Eren, L. Marot, R. Steiner, E. Meyer, Spectroscopic reflectometry of mirror surfaces during plasma exposure, Rev. Sci. Instrum. 83(1) (2012) 013509.

[239] M.S. Park, T.S. Jo, S.H. Kim, D.-G. Kim, Y.D. Kim, Two-Step Sintering of Molybdenum Nanopowder, Advances in Sintering Science and Technology, John Wiley & Sons, Inc.2010, pp. 415-420.

[240] T. Sugie, S. Kasai, M. Taniguchi, M. Nagatsu, T. Nishitani, Irradiation test of Mo- and W-mirrors for ITER by low energy deuterium ions, J. Nucl. Mater. 329-333 (2004) 1481-1485.

[241] A. Litnovsky, G. De Temmerman, K. Vukolov, P. Wienhold, V. Philipps, O. Schmitz, U. Samm, G. Sergienko, P. Oelhafen, M. Büttner, I. Orlovskiy, A. Yastrebkov, U. Breuer, A. Scholl, Investigations of single crystal and polycrystalline metal mirrors under erosion conditions in TEXTOR, Fusion Eng. Des. 82(2) (2007) 123-132.

[242] V.S. Voitsenya, M. Balden, A.F. Bardamid, V.N. Bondarenko, J.W. Davis, V.G. Konovalov, I.V. Ryzhkov, O.O. Skoryk, S.I. Solodovchenko, Z. Zhang-jian, Development of surface relief on polycrystalline metals due to sputtering, Nuclear Instruments and Methods in Physics Research Section B: Beam Interactions with Materials and Atoms 302 (2013) 32-39.

[243] A.P. Ilyin, O.B. Nazarenko, G.V. Shuvalov, I.V. Klekovkin, D.V. Tikhonov, L.O. Tolbanova, Production and characterization of molybdenum nanopowders obtained by electrical explosion of wires, Optoelectronics and Advanced Materials, Rapid Communications 4(6) (2010) 834-837.

[244] G.-S. Kim, Y.J. Lee, D.-G. Kim, Y.D. Kim, Consolidation behavior of Mo powder fabricated from milled Mo oxide by hydrogen-reduction, J. Alloys Compd. 454(1–2) (2008) 327-330.

[245] N. Ni, M. Tesconi, S.E. Tabibi, S. Gupta, S.H. Yalkowsky, Use of pure t-butanol as a solvent for freeze-drying: a case study, Int. J. Pharm. 226(1–2) (2001) 39-46.

[246] F. Swanson, Natl. Bur. Stand. (U.S), Circ, 539(3) (1954) 30.

[247] D.M. Goebel, G. Campbell, R.W. Conn, Plasma surface interaction experimental facility (PISCES) for materials and edge physics studies, J. Nucl. Mater. 121 (1984) 277-282.

[248] A. Pavia, L. Durand, F. Ajustron, V. Bley, G. Chevallier, A. Peigney, C. Estournès, Electro-thermal measurements and finite element method simulations of a spark plasma sintering device, J. Mater. Process. Technol. 213(8) (2013) 1327-1336.

[249] D.D. Avrov, A.S. Bakin, S.I. Dorozhkin, A.O. Lebedev, V.P. Rastegaev, Electrical Conductivity of Single-Crystalline Bulk 6H-SiC and Epitaxial Layers of AIN in the Temperature Range 300-2300 K, 1998.

[250] K. Motzfeldt, High Temperature Experiments in Chemistry and Materials Science, John Wiley & Sons, Chichester, UK, 2012.

[251] O. Yamamoto, Y. Arati, Y. Takeda, N. Imanishi, Y. Mizutani, M. Kawai, Y. Nakamura, Electrical conductivity of stabilized zirconia with ytterbia and scandia, Solid State Ionics 79 (1995) 137-142.

[252] J.S.C. Francis, R. Raj, J. Halloran, Influence of the Field and the Current Limit on Flash Sintering at Isothermal Furnace Temperatures, J. Am. Ceram. Soc. 96(9) (2013) 2754-2758.

[253] S. Hayun, V. Paris, R. Mitrani, S. Kalabukhov, M.P. Dariel, E. Zaretsky, N. Frage, Microstructure and mechanical properties of silicon carbide processed by Spark Plasma Sintering (SPS), Ceram. Int. 38(8) (2012) 6335-6340.

[254] D. Giuntini, J. Raethel, M. Herrmann, A. Michaelis, E.A. Olevsky, Advancement of Tooling for Spark Plasma Sintering, J. Am. Ceram. Soc. 98(11) (2015) 3529-3537.